

## Plasma-assisted catalysis for air purification

***Citation for published version (APA):***

Chirumamilla, V. R. (2018). *Plasma-assisted catalysis for air purification*. [Phd Thesis 1 (Research TU/e / Graduation TU/e), Electrical Engineering]. Technische Universiteit Eindhoven.

***Document status and date:***

Published: 23/04/2018

***Document Version:***

Publisher's PDF, also known as Version of Record (includes final page, issue and volume numbers)

***Please check the document version of this publication:***

- A submitted manuscript is the version of the article upon submission and before peer-review. There can be important differences between the submitted version and the official published version of record. People interested in the research are advised to contact the author for the final version of the publication, or visit the DOI to the publisher's website.
- The final author version and the galley proof are versions of the publication after peer review.
- The final published version features the final layout of the paper including the volume, issue and page numbers.

[Link to publication](#)

***General rights***

Copyright and moral rights for the publications made accessible in the public portal are retained by the authors and/or other copyright owners and it is a condition of accessing publications that users recognise and abide by the legal requirements associated with these rights.

- Users may download and print one copy of any publication from the public portal for the purpose of private study or research.
- You may not further distribute the material or use it for any profit-making activity or commercial gain
- You may freely distribute the URL identifying the publication in the public portal.

If the publication is distributed under the terms of Article 25fa of the Dutch Copyright Act, indicated by the "Taverne" license above, please follow below link for the End User Agreement:

[www.tue.nl/taverne](http://www.tue.nl/taverne)

***Take down policy***

If you believe that this document breaches copyright please contact us at:

[openaccess@tue.nl](mailto:openaccess@tue.nl)

providing details and we will investigate your claim.

# **Plasma-assisted catalysis for air purification**

PROEFSCHRIFT

ter verkrijging van de graad van doctor aan de  
Technische Universiteit Eindhoven, op gezag van de  
rector magnificus prof.dr.ir. F.P.T. Baaijens, voor een  
commissie aangewezen door het College voor  
Promoties, in het openbaar te verdedigen  
op maandag 23 april 2018 om 11.00 uur

door

Vindhya Rani Chirumamilla

geboren te Guntur, India

Dit proefschrift is goedgekeurd door de promotoren en de samenstelling van de promotiecommissie is als volgt:

voorzitter:	prof.dr.ir. A.B. Smolders
promotor:	prof.dr.ing. A.J.M. Pemen
copromotor:	dr.ir. T. Huiskamp
leden:	prof.dr. Christopher Whitehead (University of Manchester) prof.dr. Crisitina Paradisi (University of Padova) prof.dr. Volker Hessel
adviseur:	dr.ir. W.L.F.M. Hoeben

dr. R.A.H. Engeln neemt plaats als reservelid

Het onderzoek dat in dit proefschrift wordt beschreven is uitgevoerd in overeenstemming met de TU/e Gedragscode Wetenschapsbeoefening.

This work has been supported by the Eniac JU project 324284 Environmental Sensors for Energy Efficiency (ESEE), coordinated by Infineon.



Printed by Ipskamp Drukkers, Enschede.

ISBN: 978-94-028-1006-6

A catalogue record is available from the Eindhoven University of Technology library.

Copyright © 2018 by V.R. Chirumamilla.

All right reserved. No part of the material protected by this copyright notice may be reproduced or utilised in any form or by any means, electronic or mechanical, including photocopying, recording or by any information storage and retrieval system, without the prior permission of the author.



*To my husband and to my daughter.*



---

---

# CONTENTS

---

## Contents

<b>Summary</b>	<b>i</b>
<b>1 Introduction</b>	<b>1</b>
1.1 Research goals . . . . .	4
1.2 Organisation of the thesis . . . . .	4
<b>2 Experimental setup</b>	<b>7</b>
2.1 Reactor configuration . . . . .	7
2.1.1 DBD reactor . . . . .	7
2.2 Catalyst preparation . . . . .	8
2.3 Power modulator topology . . . . .	10
2.3.1 Microsecond ( $\mu$ s) pulse source . . . . .	10
2.3.2 Nanosecond (ns) pulse source . . . . .	12
2.3.3 Electrical measurements . . . . .	13
2.4 Gas concentration measurements . . . . .	15
2.5 Impedance measurements . . . . .	17
<b>3 Investigation on the effect of electrical parameters on NO<sub>x</sub> removal</b>	<b>21</b>
3.1 Introduction . . . . .	21
3.2 Effect of applied peak-voltage . . . . .	22
3.2.1 Plasma-alone configuration . . . . .	22
3.2.2 In-plasma configuration . . . . .	26
3.2.3 Post-plasma configuration . . . . .	30
3.3 Effect of pulse polarity . . . . .	33
3.3.1 Plasma-alone configuration . . . . .	34



## CONTENTS

3.3.2	In-plasma configuration . . . . .	34
3.3.3	Post-plasma configuration . . . . .	38
3.4	Effect of pulse rise-time . . . . .	38
3.4.1	Plasma-alone configuration . . . . .	40
3.4.2	In-plasma configuration . . . . .	42
3.4.3	Post-plasma configuration . . . . .	44
3.5	Summary and conclusions . . . . .	45
<b>4</b>	<b>Investigation on the effect of operational parameters for NO<sub>x</sub> removal</b>	<b>51</b>
4.1	Introduction . . . . .	51
4.2	Effect of NO input concentration . . . . .	52
4.2.1	Plasma-alone configuration . . . . .	52
4.2.2	In-plasma configuration . . . . .	55
4.2.3	Post-plasma configuration . . . . .	59
4.3	Effect of flow rate . . . . .	61
4.3.1	Plasma-alone configuration . . . . .	62
4.3.2	In-plasma configuration . . . . .	64
4.3.3	Post-plasma configuration . . . . .	66
4.4	Effect of temperature . . . . .	70
4.4.1	In-plasma configuration . . . . .	71
4.4.2	Post-plasma configuration . . . . .	74
4.5	Summary and conclusions . . . . .	77
<b>5</b>	<b>Screening of catalytic materials for NO<sub>x</sub> removal</b>	<b>79</b>
5.1	Introduction . . . . .	79
5.2	In-plasma catalytic configuration . . . . .	81
5.2.1	Effect of catalytic support . . . . .	81
5.2.2	Effect of wt% of metal-oxide loading . . . . .	87
5.3	Post-plasma catalytic configuration . . . . .	90
5.3.1	Effect of catalytic support . . . . .	90
5.3.2	Effect of wt% of metal-oxide loading . . . . .	93
5.4	Conclusions . . . . .	94
<b>6</b>	<b>SDBD reactor for on-demand air purification</b>	<b>99</b>
6.1	Introduction . . . . .	99
6.2	Experimental setup . . . . .	100
6.2.1	Design of SDBD plate . . . . .	101
6.2.2	Synthesizing the catalyst plate . . . . .	101
6.3	Electrical characterization . . . . .	106
6.3.1	Power modulator Topolgy . . . . .	106
6.3.2	Modulator specifications . . . . .	106
6.4	Chemical characterization . . . . .	107
6.4.1	NO removal in the pulsed-SDBD reactor . . . . .	107

## CONTENTS

6.4.2	Ethylene removal in the pulsed-SDBD reactor . . . . .	113
6.5	Conclusions . . . . .	116
<b>7</b>	<b>Conclusions and Recommendations</b>	<b>119</b>
7.1	Research goals . . . . .	119
7.2	Investigation on the effect of electrical parameters on NO <sub>x</sub> removal . . . . .	121
7.3	Investigation on the effect of operational parameters on NO <sub>x</sub> removal . . . . .	122
7.4	Screening of catalytic materials for NO <sub>x</sub> removal . . . . .	123
7.5	SDBD reactor for on-demand air purification . . . . .	124
7.6	Recommendations for future work . . . . .	125
<b>Appendix</b>		<b>127</b>
A1.	Supplementary data for the experimental setup . . . . .	127
	Characterization of catalytic materials . . . . .	127
	FTIR spectra and calibration . . . . .	130
A2.	Effect of the NO input concentration . . . . .	133
A3.	SDBD reactor for on-demand air purification . . . . .	136
A4.	Plasma-catalytic interactions: Effect of dielectric constant . . . . .	137
	Introduction . . . . .	137
	Experimental setup . . . . .	137
	Effect of applied peak-voltage on discharge intensity in plasma reactor . . . . .	138
	Discharge behaviour in DBD-plasma reactor packed with TiO <sub>2</sub> . . . . .	140
	Conclusions . . . . .	147
<b>Bibliography</b>		<b>149</b>
<b>List of publications</b>		<b>163</b>
<b>Acknowledgement</b>		<b>167</b>
<b>Curriculum Vitae</b>		<b>169</b>



---

---

## SUMMARY

---

This thesis focusses on combining non-thermal plasma (NTP) technology and catalysts for air purification applications. NTP technology has been researched for the past few decades for environmental remediation, bio-medical and surface engineering applications. For the NTP technology, to get commercialize, it should be made energy efficient at low cost with minimum size requirements. Recent studies have indicated that combining the plasma reactor with catalytic materials can improve the energy efficiency and product selectivity. There have been various arrangements proposed in the literature to combine the plasma reactor with catalysts: namely the in-plasma configuration (IPC) and the post-plasma configuration (PPC). In practical applications, the exhaust gases contains various pollutants at different concentrations and under various conditions (such as temperature, humidity, flow rate, hydrocarbons and so on). In order to improve the performance efficiency of a DBD reactor, one has to understand the effect of the various parameters and choose an appropriate catalytic material depending on the type of the pollutants. Thus, one of the main purpose of this work is to identify the influence of various parameters on the NO<sub>x</sub> removal efficiency and screening for various suitable catalytic materials.

The thesis can be divided in to three main parts. The first part is to understand the effect of various electrical and operational parameters on the performance of the DBD reactor. The second part is to look at various catalytic materials and understand the interaction between the plasma and the catalytic materials. The third part is to develop an SDBD based plasma-catalytic reactor which could easily be scaled-up and scaled-down for industrial applications.

In the first part of the study, to investigate the influence of electrical and operational parameters, we have used a pulsed DBD-plasma reactor and combined this with various commonly used support materials such as Al<sub>2</sub>O<sub>3</sub>, TiO<sub>2</sub>, zeolites and SiO<sub>2</sub>. We performed a systematic study using the three reactor configurations: plasma-alone, IPC and PPC configurations. From the study on the effect of electrical parameters on NO<sub>x</sub> removal, we observed that

the  $\text{NO}_x$  removal efficiency depends more on the energy density than on the applied peak-voltage. With increasing energy density, the conversions and the formation of by-products increases. With increase in applied peak-voltage, the energy costs increases. The optimal performance in terms of conversion, by-products formation and energy costs is delivered at low applied peak-voltages. With increase in the applied peak-voltage, the energy deposition per pulse increases. This high energy deposition leads to the increased microdischarges but on the other hand also leads to the increased energy losses due to heating up of the gas. All the three reactor configurations that we have tested showed the similar results.

Irrespective of the reactor arrangement configurations, positive polarity pulses show better NO and  $\text{NO}_x$  conversion. The reason for the increased conversion with positive pulses might be due to increased reactive species production with positive pulses as compared to the negative pulses. Few studies have indicated that the negative polarity pulses produces less streamer volume. The formation of by-products are not significantly effected by the pulse polarity. The study on the effect of rise time of the pulses shows that the short rise-time pulses perform better with respect to NO conversion but at the expense of increased by-products formation. Short rise-time pulses generates the high energetic electrons leading to increased radicals production. The better performance of the short rise-time pulses for NO conversion is observed in all the three tested reactor configurations.

The  $\text{NO}_x$  conversion decreases with increasing input concentrations due to the reduced availability of active species. This is applicable to all the three configurations that we have tested. The effect of flow rate on  $\text{NO}_x$  removal efficiency depends on the reactor configuration. With increasing flow rate, the NO conversion decrease for the plasma-alone and for the PPC configuration. The IPC configuration does not show significant dependance up to a certain flow rate and above that flow rate lower NO conversions are observed. This is probably due to transport limitations of the catalytic reactions. The higher conversions at lower gas flow rates comes at the expense of higher  $\text{N}_2\text{O}$  and  $\text{O}_3$  concentrations. With increase in temperature, the by-products formation can be suppressed. PPC configuration showed a similar behaviour to that of the conventional thermal catalysis which means, higher conversions can be achieved at higher temperatures. The IPC configuration show reduced NO conversion with increase in temperature which could be due to the favourable conditions for the back reaction of  $\text{NO}_2$  to NO in the presence of atomic oxygen. The addition of additives such as hydrocarbons, ammonia may enhance the performance of the DBD reactor at higher temperatures.

In the second part of the study, we performed screening of catalytic materials for  $\text{NO}_x$  removal. We did this by loading various metal oxides on  $\text{TiO}_2$  and  $\text{Al}_2\text{O}_3$  supports and by using them in a IPC and in a PPC configuration in combination with a pulsed DBD reactor. The effect of metal loading on the support materials is studied by loading various amounts of metal oxides on  $\text{TiO}_2$  and  $\text{Al}_2\text{O}_3$  supports. We studied the role of catalytic material in changing the plasma discharge characteristics. We did this by considering the voltage-current waveforms and correlating them to the corresponding dielectric constant of the catalytic materials. We showed that the discharge activity is changed significantly with introduction of the catalytic material inside the plasma reactor. For the plasma-alone

reactor, the capacitance of the reactor is low, resulting in a higher discharge current and more discharge activity. The microdischarge activity is much lower when the reactor is packed with  $\text{TiO}_2$  as compared to the  $\text{Al}_2\text{O}_3$  packing. These differences in microdischarge activity can be explained by the different capacitances due to the different dielectric constants of the two materials. The intense microdischarge activity of the plasma-alone configuration might have led to the increased NO conversions,  $\text{NO}_2$  and by-products concentrations. The by-products were greatly reduced with the catalytic materials in both the IPC and the PPC configurations.

In the third part of the study, as a part of the environmental sensors for energy efficiency (ESEE)- EU project, we have developed a modular plasma-catalytic surface-dielectric-barrier-discharge (SDBD) reactor to handle large flows which could be scaled-up and scaled-down easily. We have evaluated the performance of the SDBD reactor for  $\text{NO}_x$  and VOC removal. We have used ethylene as a model compound for VOC due to its interest in the food and floral industry. In general, DBD performed better than SDBD with respect to NO and  $\text{NO}_x$  conversions. This probably might be due to the high energy deposition per pulse by the SDBD modulator. We have observed in our parametric study that high energy deposition per pulse leads to high energy losses and thus high energy costs. To reduce the by-products formation, we used  $\text{TiO}_2$  coated  $\text{Al}_2\text{O}_3$  plates as a catalyst in parallel to the SDBD plates (electrode plates). With the use of the catalytic plates the NO and  $\text{C}_2\text{H}_4$  conversions, CO and  $\text{CO}_2$  selectivities have been marginally improved. The by-products formation have been slightly reduced by combining the SDBD plates with catalytic plates. Although, we observed better performance of the SDBD reactor with the catalytic plates, it is not clear whether the catalytic plates acts more like a catalyst to increase the product selectivity or behave like walls to quench the reactions. Probably, if we can increase the thickness of  $\text{TiO}_2$  coating from 60 nm to few  $\mu\text{m}$  thickness then we can understand the role of these catalytic plates.



---

# INTRODUCTION

---

One of the main sources of air pollution is the transportation sector. Motor vehicles emissions include unburned hydrocarbons (UHCs), carbon monoxide (CO), carbon dioxide (CO<sub>2</sub>), nitrogen oxides (NO and NO<sub>2</sub>), sulfur oxides (SO<sub>x</sub>) and particulate matter (PM). According to the European Environment Agency 2017 data (EEA-32), the transportation sector contributes around 41%, 49%, 12% and 20% of NO<sub>x</sub>, SO<sub>x</sub>, PM<sub>2.5</sub> and PM<sub>10</sub> emissions respectively [1]. These emissions are significant as they have a negative impact on human health. With increasing concerns about these impacts, the introduction of emission control standards has been started. With increasingly stringent regulations, the lower limits of the emissions standards can be reached by applying gas purification techniques for the efficient reduction of UHCs, NO<sub>x</sub>, SO<sub>x</sub>, and PMs coming from the exhaust.

Non-thermal plasma appears to be a promising technology for decomposition of gaseous pollutants with relatively low energy consumption [2–9]. The high energy electrons produced in non-thermal plasma collide with the gas molecules to generate radicals such as reactive oxygen species, metastables and ions by electron-impact dissociation and ionization. The mentioned reactive oxygen species induce oxidative degradation of the pollutants.

In this thesis we aim to combine non-thermal plasma (NTP) technology and catalysts and screening for various suitable catalytic materials for NO<sub>x</sub> removal. Non-thermal plasma is able to oxidize NO to NO<sub>2</sub> which is further converted to HNO<sub>3</sub> and HNO<sub>2</sub> in the presence of water vapor [10–13]. Without the help of a catalyst, NO<sub>x</sub> cannot be reduced to N<sub>2</sub> just with electrical discharges. From literature, it is understood that using a catalyst with a plasma reactor can enhance the product selectivity and the energy efficiency [14–18]. Yamamoto *et al.* concluded that the operating cost of a plasma-chemical hybrid system is approximately 15 times more economical compared to the conventional selective catalytic reduction process [19]. Hence, plasma-assisted catalysis is a promising way for improved pollutant removal efficiency and selectivity. Also, the production of unwanted by-products can be minimized. Non-thermal plasma can be generated at atmospheric pressure and



at ambient temperature with various techniques such as with corona discharges, pulsed-corona discharges, dielectric barrier discharges (DBDs), microwave and radio frequency discharges [20–22]. DBDs are widely used for VOCs and NO<sub>x</sub> reduction [23–32].

We believe that there are two main approaches to improve the performance efficiency of a DBD reactor for the purpose of NO<sub>x</sub> removal. The first approach would be to optimize the discharge characteristics. The second approach is to combine the plasma reactor with catalysts. The first approach includes optimizing the reactor configuration and the power source. The major parameters of the power source that should be tuned to improve the efficiency of the plasma are the frequency, applied peak-voltage, waveform of the voltage, polarity, pulse rise-time and the pulse duration. Puchkarev *et al.* stated in their study on energy-efficient plasma processing of gaseous emission that the efficiency of NO<sub>x</sub> reduction is a complex function of parameters as the pulse width, pulse polarity, current density, repetition rate, and reactor design. Careful optimization of all these parameters is required to reach cost effective NO<sub>x</sub> reduction [33].

The second approach is to combine plasma with appropriate catalysts. Combining a plasma reactor with a catalytic reactor can help in reducing the NO and NO<sub>2</sub> to molecular nitrogen with minimum by-products if the plasma operating conditions are selected carefully [34, 35]. There have been various arrangements proposed in the literature to combine a plasma reactor with a catalytic reactor such as a one-stage configuration, or in-plasma catalytic configuration (IPC), and a two-stage configuration, or post-plasma catalytic configuration (PPC) [36–38]. In both of these configurations, different catalysts have been tested and an overview of the published papers on NO<sub>x</sub> removal is presented in table 1.1. From this table, we can see that  $\gamma$ -Al<sub>2</sub>O<sub>3</sub> [34, 39], TiO<sub>2</sub> [40], Al<sub>2</sub>O<sub>3</sub> loaded with different metals such as Ag [41], Pd [40], and In [42], TiO<sub>2</sub> loaded with BaTiO<sub>3</sub> [43] and V<sub>2</sub>O<sub>5</sub>-WO<sub>3</sub> [44] and zeolites [45] are among the various catalysts that have been tested with non-thermal plasma. Although, there happens to be a lot of work done on NO<sub>x</sub> removal using plasma and plasma-catalytic configuration explaining the effect of operating conditions, a systematic parametric study on NO<sub>x</sub> removal using similar reactor configuration operating under similar conditions is never performed. Such a study is needed to get more insights on how these parameters influence the performance efficiency so that we can obtain the optimum performance of the reactor.

In this thesis, we have applied these two approaches to optimize the performance of the DBD reactor in a systematic manner. We have used a pulsed non-thermal DBD reactor at atmospheric pressure. We have studied the effect of applied peak-voltage, polarity and the pulse waveform of the voltage by varying pulse repetition rate (we used this as a factor to vary the energy density). The pulsed DBD reactor is combined with catalysts such as TiO<sub>2</sub>, Al<sub>2</sub>O<sub>3</sub> and metal-oxides loaded on TiO<sub>2</sub>, Al<sub>2</sub>O<sub>3</sub> to study the synergy between the plasma and the catalysts in terms of removal efficiency and energy efficiency. These two approaches led us to formulate the following research goals and also enabled us to achieve a systematic study using the commonly used support materials with the configurations.

Reactor configuration	Conditions	Catalyst	NO <sub>x</sub> Conversion	Energy density	Ref
DBD	T: 773 K V: 3-16 kV Addition of primary alcohols	Indium doped $\gamma$ -Al <sub>2</sub> O <sub>3</sub>	Approx. 60% @ 473 K >90% @ 623 K > 80% @ 773 K	700 J/L 100 J/L 100 J/L	[42]
SDBD	Wet gas Initial NO conc: 100 ppm	$\gamma$ -Al <sub>2</sub> O <sub>3</sub>	Approx 60%	133 J/L	[39]
Packed DBD	60 Hz AC power supply Initial NO conc: 200 ppm	BaTiO <sub>3</sub>	Approx 96%	55.5 J/L	[34]
Packed DBD	Initial NO conc: 300 to 500 ppm NO <sub>2</sub> : 15 to 50 ppm frequency: 300-350 pulses per sec Addition of methanol as additive (1000ppm) T: 150 °C	$\gamma$ -Al <sub>2</sub> O <sub>3</sub> BaTiO <sub>3</sub> + $\gamma$ -Al <sub>2</sub> O <sub>3</sub> (1:5 ratio) $\gamma$ -Al <sub>2</sub> O <sub>3</sub> + TiO <sub>2</sub> (1:1 ratio) Co- ZSM-5 post-plasma	Approx 66% 60% 21% 78%	140 J/L 140 J/L 140 J/L 60 J/L	[43]
Packed DBD	Initial NO conc: 570 ppm frequency: 900 Hz pulse per sec @ 9 kV Gas flow rate: 5 L/min T: 298 K	Degussa P-25 PCVD method	80% 58%		[46]
DBD	Initial NO conc: 500 ppm NH <sub>3</sub> : 500 ppm Gas flow rate: 25 L/min T: 100–250 °C	V <sub>2</sub> O <sub>5</sub> -WO <sub>3</sub> /TiO <sub>2</sub> Ethene as additive	55% @ 100 °C 70% @ 100 °C	80 J/L	[44]
DBD	Initial NO conc: 500 ppm Propene: 0-2000 ppm Gas flow rate: 1 L/min	Al <sub>2</sub> O <sub>3</sub> TiO <sub>2</sub> ZrO <sub>2</sub> Alumosilicate Pd/Al <sub>2</sub> O <sub>3</sub> Ag/mordenite	60% @ 300 °C 15% @ 350 °C 55% @ 300 °C 20% @ 300 °C 10% @ 230 °C 30% @ 325 °C		[40]
Cylindrical DBD	T: 250 °C Initial NO conc: 400 ppm	Cu-ZSM-5	Approx. 40% @ 273 K Approx. 25% @ 473 K	3.5 W 3.5 W	[47]
Coaxial-type DBD	Initial NO conc: 360 ppm T: 110 °C	$\gamma$ -Fe <sub>2</sub> O <sub>3</sub>	Approx. 44%	50 J/L	[48]
DBD	Initial NO conc: 1200 ppm	Ag/ Al <sub>2</sub> O <sub>3</sub>	> 50% @ 250 °C > 74% @ 250 °C > 90% @ 350 °C	60 J/L 180 J/L 60 J/L	[41]
DBD	Initial NO conc:245 ppm C <sub>3</sub> H <sub>6</sub> : 520 ppm Gas flow rate: 2.1 L/min	NaY 5% NH <sub>3</sub> loaded on NaY 40%NH <sub>3</sub> loaded on NaY 80%NH <sub>3</sub> loaded on NaY	59% @ 200 °C 68% @ 200 °C 80% @ 200 °C 82% @ 200 °C	10 J/L	[49]
DBD	Initial NO conc: 400 ppm T: 220 °C	V <sub>2</sub> O <sub>5</sub> -WO <sub>3</sub> /TiO <sub>2</sub>	Approx. 68%	40 J/L	[50]
DBD	Initial NO conc:200 ppm Initial NO conc:300 ppm Initial NO conc:400 ppm	V <sub>2</sub> O <sub>5</sub> /TiO <sub>2</sub>	Approx. 90% Approx. 85% Approx. 80%	40 J/L	[51]
DBD	Initial NO <sub>x</sub> conc:300 ppm T: 220 °C	V <sub>2</sub> O <sub>5</sub> /TiO <sub>2</sub> Cr <sub>2</sub> O <sub>3</sub> /TiO <sub>2</sub>	Approx. 85% Approx. 42%	50 J/L 60 J/L	[52]
DBD	Initial NO <sub>x</sub> conc:241 ppm T: 170 °C Gas flow rate: 2 L/min	Ba-Y	Approx. 90%	15 J/L	[53]
DBD	Initial NO <sub>x</sub> conc:550 ppm CO: 720 ppm NO <sub>2</sub> : 80 ppm Aldehydes: 80 ppm THC: 1700 ppm	V <sub>2</sub> O <sub>5</sub> /TiO <sub>2</sub>	Approx. 90% @ 200 °C Approx. 80% @ 200 °C Approx. 71% @ 200 °C	98 J/L	[54]
DBD	Initial NO <sub>x</sub> conc:500 ppm T: 300 °C Gas flow rate: 520 L/min	Co-HZSM-5	Approx. 94%	144 J/L	[55]
DBD	Initial NO <sub>x</sub> conc:550 ppm Gas flow rate: 2.1 L/min	NaY Ba-Na-Y(20%) Ba-Na-Y(40%) Ba-Na-Y(60%) Ba-Na-Y(80%) Ba-Y	Approx. 59% @ 200 °C Approx. 65% @ 200 °C Approx. 70% @ 200 °C Approx. 70% @ 200 °C Approx. 72% @ 200 °C Approx. 78% @ 200 °C	98 J/L	[56]
DBD	Initial NO <sub>x</sub> conc:445 ppm C <sub>2</sub> H <sub>4</sub> : 6000 ppm Gas flow rate: 500 mL/min	Ag/Al <sub>2</sub> O <sub>3</sub>	Approx. 90% @ 200 °C	703 J/L	[57]

**Table 1.1** – Literature review on NO<sub>x</sub> removal with plasma-catalysis.

## 1.1 Research goals

In this thesis, we investigated the combination of non-thermal plasma (NTP) technology and catalysts for air purification applications and the effect of various parameters on the plasma and plasma-catalytic processing efficiency.  $\text{NO}_x$  have been taken as target pollutant and the effect of various parameters on its removal efficiency have been researched using a pulsed-DBD and SDBD reactor. The main goals of this research were:

- To systematically study the effect of various electrical and operational parameters on  $\text{NO}_x$  removal and to optimize the performance of our DBD configuration.
- To understand the plasma-catalytic interactions by studying the physical interaction of the plasma with the catalyst and to correlate this interaction with the chemical processing efficiency.
- To develop an on-demand air purifier which could be scaled-up and scaled-down easily by using plasma-catalytic technology.

## 1.2 Organisation of the thesis

**Chapter 2** In this chapter, we describe the experimental setup that we have used in major parts of our research study. Over the course of time, we have adapted the experimental setup for some particular series of experiments and the details will be presented in the related chapters.

**Chapter 3** In this chapter, we investigated the optimization of electrical parameters to obtain energy efficient  $\text{NO}_x$  remediation. We have varied the electrical parameters such as applied peak voltage, pulse polarity and pulse rise-time to study the degree of removal of NO and  $\text{NO}_x$ , by-products formation and energy consumption in the DBD reactor. We have used all the three configurations: plasma-alone, in-plasma catalytic configuration (IPC) and post-plasma catalytic configuration (PPC). Commonly used catalyst support materials such as  $\text{TiO}_2$ ,  $\text{Al}_2\text{O}_3$ , zeolites and  $\text{SiO}_2$  have been used in the IPC and the PPC configuration.

**Chapter 4** In this chapter, we analyzed the influence of various operational parameters such as input NO concentrations, gas flow-rate, and temperature on the efficiency of  $\text{NO}_x$  removal. We have evaluated the performance by considering the increase in the  $\text{NO}_x$  removal and decrease in the by-products formation. First, we have studied the effect of operational parameters with the plasma-alone configuration and then we have packed the reactor with the catalytic materials to use it in the IPC and the PPC configurations to investigate the efficiency of  $\text{NO}_x$  removal with minimum by-products formation. Commonly used catalyst support materials such as  $\text{TiO}_2$ ,  $\text{Al}_2\text{O}_3$ , zeolites and  $\text{SiO}_2$  have been used in the IPC and the PPC configuration.

**Chapter 5** In this chapter, we have studied  $\text{NO}_x$  removal by loading various metal oxides on  $\text{TiO}_2$  and  $\text{Al}_2\text{O}_3$  using a pulsed DBD reactor. The metal-oxides that we have used in this

study are NiO, MnO, CuO, Fe<sub>3</sub>O<sub>4</sub>, Co<sub>3</sub>O<sub>4</sub>. To understand the effect of support material, we have loaded 3% of these metal oxides both on TiO<sub>2</sub> and Al<sub>2</sub>O<sub>3</sub> and looked into the NO conversion, NO<sub>x</sub> concentration and by-products formation using both the in-plasma configuration (IPC) and post-plasma configuration (PPC). It is followed by the study on the effect of metal loading where we have compared the performance of 3 wt% and 5 wt% of these metal oxides loaded on TiO<sub>2</sub> and Al<sub>2</sub>O<sub>3</sub> with both the IPC and PPC. We have attempted to study the role of catalytic material in changing the plasma discharge characteristics by looking into the voltage-current waveforms and measuring the dielectric constants of these materials to correlate them to the discharge characteristics.

**Chapter 7** In this chapter, we have developed a modular plasma-catalytic surface-dielectric-barrier-discharge (SDBD) reactor to handle large flows which could be scaled-up and scaled-down easily. A SDBD power modulator was developed to generate 7-kV high-voltage pulses with microsecond duration that can power two SDBD reactor plates at a maximum of 5 kHz pulse repetition rate. The developed reactor can accommodate up to 20 SDBD plates and thus 10 such SDBD driver units are needed to deliver high power to treat larger flows. The electrical and chemical characterization of this developed SDBD reactor is done and discussed in detail in this chapter. The operational efficiency of the developed SDBD has been investigated by studying the removal of NO<sub>x</sub> and ethylene. Finally, we combined the SDBD plasma reactor with catalyst by placing the Al<sub>2</sub>O<sub>3</sub> plates without TiO<sub>2</sub> coating and with TiO<sub>2</sub> coating alternatively to the SDBD plates in a parallel arrangement.

**Chapter 8** In this chapter, we present the conclusions and recommendations for future work.



---

## EXPERIMENTAL SETUP

---

The description of the entire experimental setup is presented in this chapter. We present the complete description of the catalytic materials, reactor and reactor configurations, chemical and electrical diagnostics, and pulsed power supply that we have used. The experimental setup can be explained in four main parts. The DBD reactor, the gas feeding system, the electrical part (pulse source and electrical measurements) and the gas diagnostics as shown in Fig. 2.1.

### 2.1 Reactor configuration

#### 2.1.1 DBD reactor

The DBD-plasma reactor is made of quartz glass with a diameter of approximately 14 mm and with a wall thickness of 2 mm. The reactor consists of two electrodes, a high-voltage electrode and a grounded electrode. The high-voltage electrode which is connected to the high-voltage power source is made up of a stainless-steel rod with a diameter of 1.5 mm and is mounted at the center of the reactor. The steel mesh around the reactor acts as the grounded electrode. We have used two DBD reactors in this study. The difference between these two reactors are the length of the reactor. The short reactor measures 220 mm in length and the long reactor measures 300 mm in length. The material of construction, thickness, inside and outside diameter are kept the same. We use a short reactor in most part of our study due to the ease in synthesizing less catalytic materials. The cross-sectional view along with the detailed dimensions of both the DBD reactors operating at ambient temperature and atmospheric pressure are shown in the Fig. 2.2. We have used the long reactor only in the study on the effect of the rise time in the Chapter 3. This reactor is designed and developed in our group by dr.ir. F.J.C.M. Beckers and dr.ir. W.F.L.M. Hoeben.

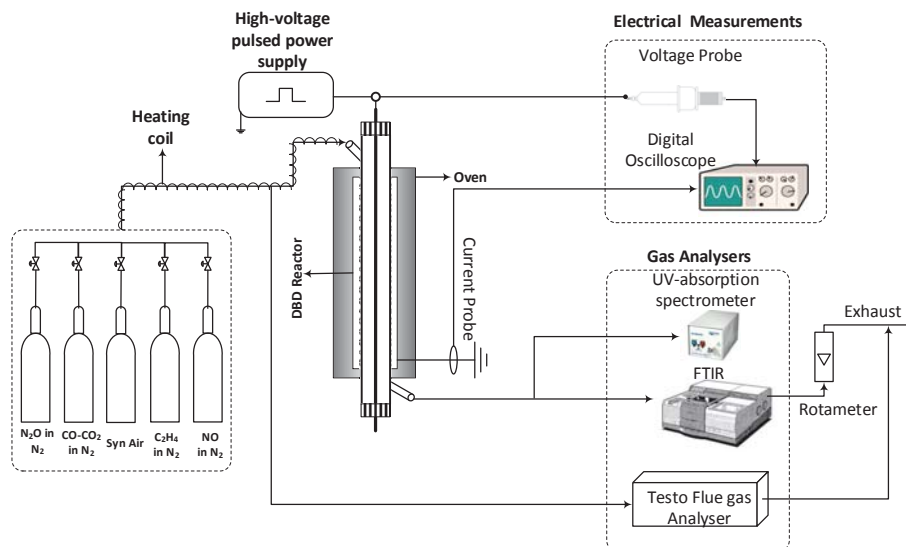


**Figure 2.1** – Schematic overview of the experimental setup with pulsed DBD reactor for NO<sub>x</sub> removal.

Throughout our study, we have used two configurations for placing the catalytic materials: The in-plasma configuration (IPC) and the post-plasma configuration (PPC). The IPC and the PPC configurations of the DBD reactor used in the experiments are shown in the Fig. 2.3.

## 2.2 Catalyst preparation

The most commonly used catalyst support materials such as TiO<sub>2</sub>, Al<sub>2</sub>O<sub>3</sub>, zeolites (NaY) and silica have been used in this study to compare the various electrical and operational parameters. Despite many studies on NO<sub>x</sub> removal using these support materials, a systematic study where these support materials are compared under the similar conditions such as reactor geometry, operating conditions and gas concentrations, has never been reported. In this thesis, we report on a systematic study on these commonly used support materials to study the effect of various parameters on removal. We have observed that silica is not a suitable support as the NO<sub>x</sub> concentration remains high despite high NO conversions. Thus, we have loaded metal-oxides on TiO<sub>2</sub> and Al<sub>2</sub>O<sub>3</sub> supports and studied the effect of various metal-oxides and various wt% of metal-oxides on NO<sub>x</sub> removal.

Catalysts precursors were obtained from Sigma-Aldrich: cobalt nitrate hexahydrate (Co(NO<sub>3</sub>)<sub>2</sub> · 6H<sub>2</sub>O), copper nitrate trihydrate (Cu(NO<sub>3</sub>)<sub>2</sub> · 3H<sub>2</sub>O), manganese nitrate tetrahydrate (Mn(NO<sub>3</sub>)<sub>2</sub> · 4H<sub>2</sub>O), iron(III) nitrate nonahydrate (Fe(NO<sub>3</sub>)<sub>3</sub> · 9H<sub>2</sub>O), nickel nitrate hexahydrate (Ni(NO<sub>3</sub>)<sub>2</sub> · 6H<sub>2</sub>O). A series of TiO<sub>2</sub> (Degussa P-25) and Al<sub>2</sub>O<sub>3</sub> based catalysts with different metals were prepared by using wet impregnation method. The desired amount

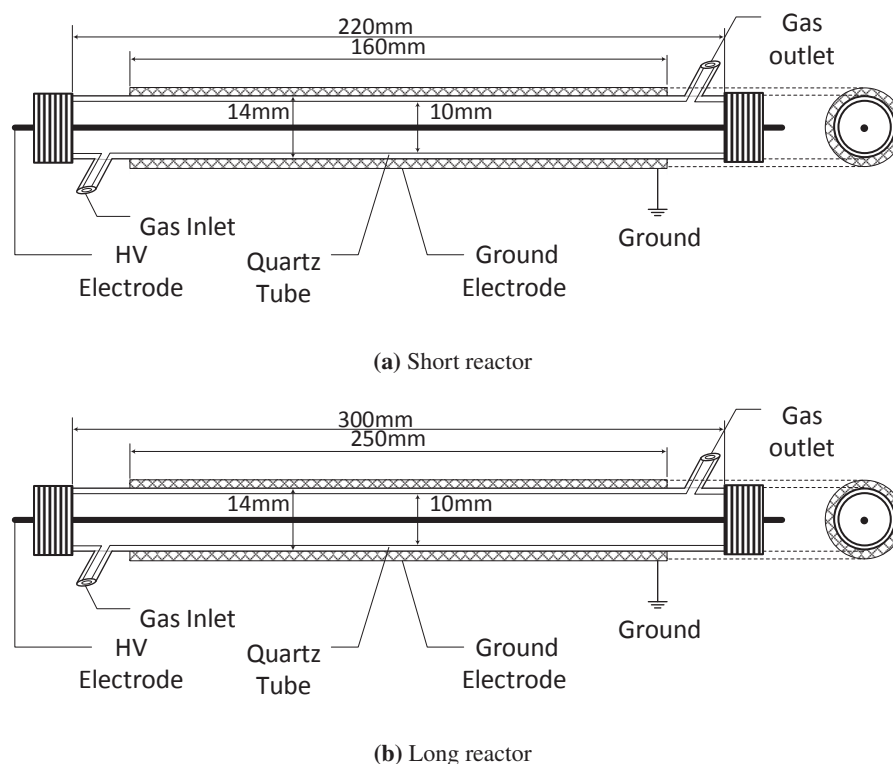


**Figure 2.2** – Cross-sectional view of the cylindrical quartz tube DBD reactor operating at ambient temperature and atmospheric pressure. Short reactor is used in most parts of our study. We have used the long reactor only in the study on the effect of rise time on  $\text{NO}_x$  removal.

of metal nitrates and  $\text{CeZrO}_4$  were dissolved in deionized water and stirred for 2 hours. Then water was removed by means of a rotary evaporator. The catalysts were dried at  $110^\circ\text{C}$  in air and then calcined at  $350^\circ\text{C}$ . The specifications of the various catalytic materials that are being used in this study are given in table 2.1. The crystalline structure of the catalysts was confirmed by recording X-ray diffraction (XRD) patterns with a Bruker D4 Endeavor diffractometer using  $\text{Cu-K}\alpha$ -radiation in the  $2\theta$  range of  $10$ – $80^\circ$  with a step length of  $0.01^\circ$  and step time of  $0.2$  s. The XRD of the catalytic materials is presented in Appendix 7.6 in Fig. A.1 and Fig. A.2. To determine how well the metal particles are dispersed on the support surface, we performed Transmission electron microscopy (TEM) imaging for the selected catalytic materials, which are presented in Appendix 7.6 in Fig. A.3. From the TEM images and XRD patterns, we can say that the metal particles are very well dispersed on the  $\text{Al}_2\text{O}_3$  support. On  $\text{TiO}_2$  support material, we have observed little peaks of  $\text{TiO}_2$  on the  $\text{Fe}_3\text{O}_4$  and  $\text{CuO}$  loaded on  $\text{TiO}_2$  in XRD pattern which means that the metal particles may not be completely dispersed.



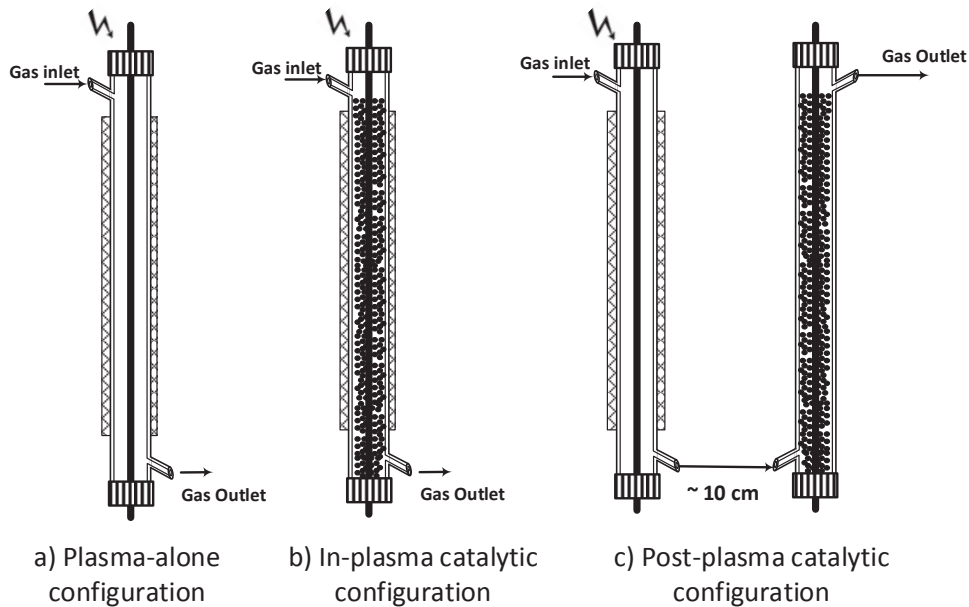


**Figure 2.3** – Schematic overview of the plasma alone configuration and the two plasma-catalytic configurations that are used in the experiments of this paper. (note: in (c), the catalytic reactor is not powered)

## 2.3 Power modulator topology

### 2.3.1 Microsecond ( $\mu\text{s}$ ) pulse source

The schematic representation of the MOSFET-based solid state microsecond pulse power source is shown in Fig. 2.4. The buffer capacitor  $C_1$  of the circuit is directly charged to 250 V via a 1:1 transformer and a rectifier. Capacitor  $C_2$  will be continuously charged to approximately 300 V via  $C_1$ - $L_1$ - $D_1$ . A pulse cycle starts by closing MOSFET  $M_1$ . Now a linearly increasing current flows via  $C_2$  and the primary winding  $L_{pri}$  of the pulse transformer. When the MOSFET is now closed, this current is interrupted in a very short time  $dt$  (depending of the switch off time of the MOSFET which is around 10 ns). Consequently, this very fast  $dI/dt$  results in the induction of a voltage pulse at the secondary side of the transformer. The magnitude of this high-voltage pulse depends on the  $dI/dt$  and is set to 17 kV. The duration of this high-voltage pulse depends on the  $dt$  and is set to  $2 \mu\text{s}$ . The pulse rise time is  $0.9 \mu\text{s}$ . The maximum repetition rate ( $f$ ) of the source is 1000 pulses per second. The typical voltage and discharge current for the microsecond pulse source is shown in Fig. 2.5a and the power and energy per pulse is shown in Fig. 2.5b respectively.

Catalyst	size (mm)	BET surface area (m <sup>2</sup> /g)	Composition
TiO <sub>2</sub>	1.5	50	75% anatase
CuO-MnO <sub>2</sub> -TiO <sub>2</sub>	1.5	50	3wt% CuO, 6.8wt% MnO <sub>2</sub>
CuO-MnO <sub>2</sub> -Al <sub>2</sub> O <sub>3</sub>	2	80	30wt% Cu-/mn-oxide
TiO <sub>2</sub> (p-25)	1-2	50	75% anatase
NiO-TiO <sub>2</sub>	1-2	50	3wt% Ni-Oxide
MnO-TiO <sub>2</sub>	1-2	50	3wt% mn-oxide
Fe <sub>3</sub> O <sub>4</sub> -TiO <sub>2</sub>	1-2	50	3wt% Fe-oxide
CuO-TiO <sub>2</sub>	1-2	50	3wt% Cu-oxide
Co <sub>3</sub> O <sub>4</sub> -TiO <sub>2</sub>	1-2	50	3wt% Co-oxide
Al <sub>2</sub> O <sub>3</sub>	1.5	120	
NiO-Al <sub>2</sub> O <sub>3</sub>	1-2	120	3wt% Ni-Oxide
Fe <sub>3</sub> O <sub>4</sub> -Al <sub>2</sub> O <sub>3</sub>	1-2	120	3wt% Fe-oxide
CuO-Al <sub>2</sub> O <sub>3</sub>	1-2	120	3wt% Cu-oxide
Co <sub>3</sub> O <sub>4</sub> -Al <sub>2</sub> O <sub>3</sub>	1-2	120	3wt% Co-oxide
NiO-TiO <sub>2</sub>	1-2	50	5wt% Ni-Oxide
MnO-TiO <sub>2</sub>	1-2	50	5wt% mn-oxide
Fe <sub>3</sub> O <sub>4</sub> -TiO <sub>2</sub>	1-2	50	5wt% Fe-oxide
CuO-TiO <sub>2</sub>	1-2	50	5wt% Cu-oxide
Co <sub>3</sub> O <sub>4</sub> -TiO <sub>2</sub>	1-2	50	5wt% Co-oxide
SiO <sub>2</sub>	1-2	200	
zeolites	1-2	1700	2.6 mol% SiO <sub>2</sub> / mol%Al <sub>2</sub> O <sub>3</sub>

**Table 2.1** – Specifications of the catalysts that are used in the experiments of this study.

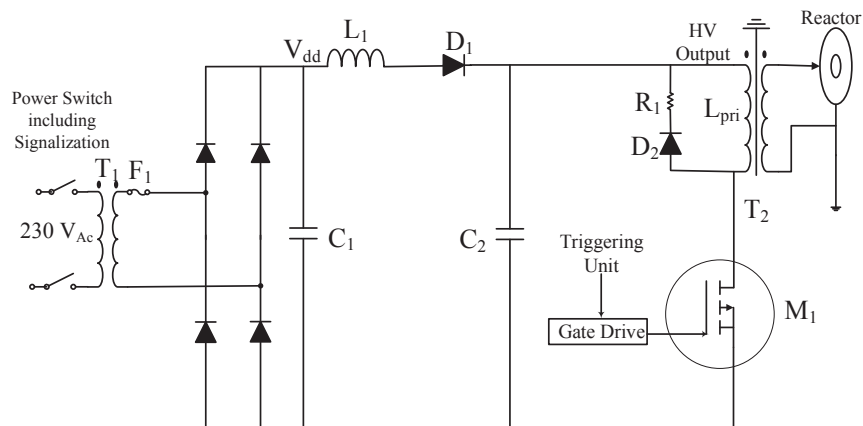


**Figure 2.4** – Schematic overview of the MOSFET based solid state microsecond pulse power source. This power source has been designed and developed by dr.ir. F.J.C.M. Beckers.

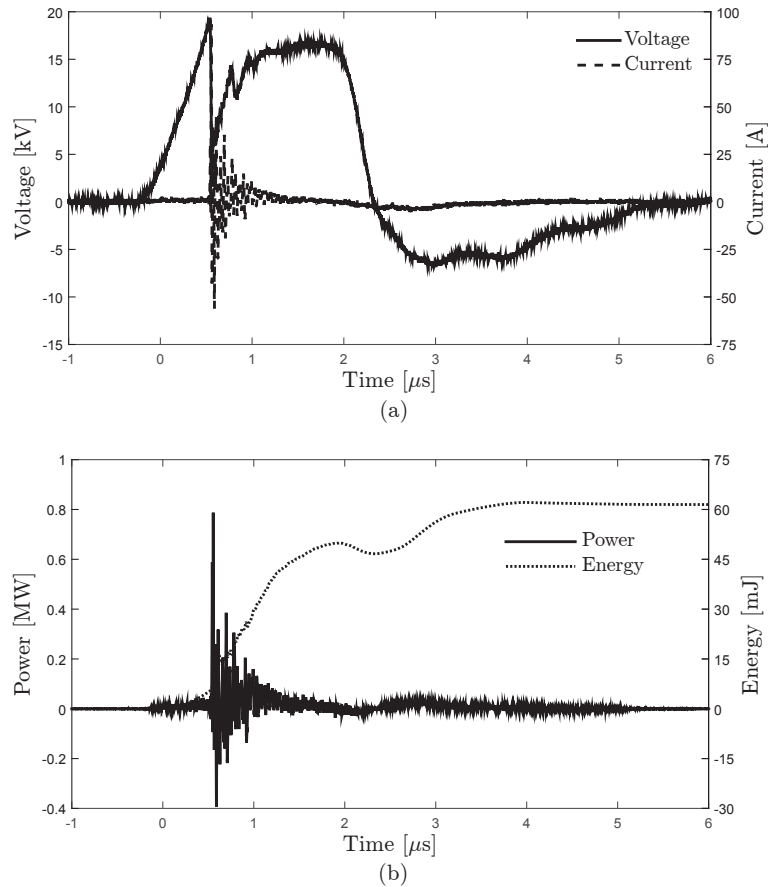


**Figure 2.5** – Typical waveforms in the DBD reactor with the  $\mu\text{s}$  pulse source: (a) Applied voltage and discharge current (b) Power and energy deposited per pulse.

### 2.3.2 Nanosecond (ns) pulse source

The schematic of the spark-gap based high-voltage nanosecond pulse circuit is shown in Fig. 2.6. Pulse generation is realized by first charging capacitor  $C_1$  in less than 10 ms by a 60-kV DC power supply. Resistor  $R_1$  limits the charging current and prevents a near short circuit of the power supply output when the spark gap fires. The spark gap is a multiple-gap spark gap consisting of three disc-shaped electrodes (two gaps) [58]. A trigger unit applies a 30-kV trigger pulse ( $\mu\text{s}$  rise-time) to the center electrode which causes the right pair of electrodes to fire. The current path of the trigger discharge is via  $D_1$ - $R_2$ -SG- $R_3$ . The full

voltage on  $C_1$  will now be over the left and the center electrode causing the full spark-gap to fire. Capacitor  $C_1$  will be rapidly discharged (in less than 100 ns) into the 50  $\Omega$  coaxial cable, creating the high-voltage pulse on the output of the cable.  $R_2$  is added to protect the trigger unit from transient voltages and possible voltage reversal on  $C_1$ . The energy transfer to the reactor stops after the plasma in the reactor quenches after the pulse voltage has dropped below the plasma extinction voltage. The spark gap remains conducting until all energy remaining in the circuit is consumed. The spark-gap channel and resistor  $R_3$  dissipate the remaining energy in the circuit, including the energy due to reflections of the pulse voltage due to improper impedance matching between the reactor and the coaxial cable. Resistor  $R_3$  has a high impedance ( $R_3 \gg Z_{cable}$ ) and consumes only a small amount of energy during the pulse generation. The maximum repetition rate of the pulse source is 100 pulses per second. The typical voltage and discharge current for the nanosecond pulse source is shown in Fig. 2.7a and the power and energy per pulse is shown in Fig. 2.7b respectively. Both the  $\mu$ s pulse source and the ns pulse source was developed by dr.ir. F.J.C.M. Beckers.

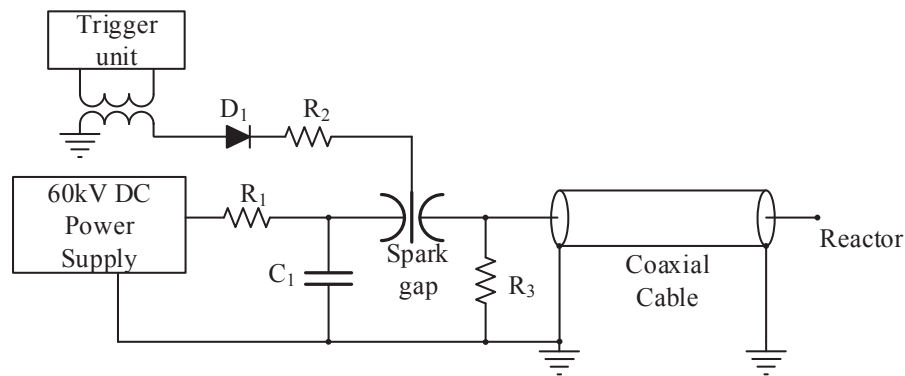


**Figure 2.6** – Schematic overview of the spark-gap based high-voltage nanosecond pulse circuit. This power source has been designed and developed by dr.ir. F.J.C.M. Beckers.

### 2.3.3 Electrical measurements

A Northstar PVM-5 high-voltage probe and a Pearson 6600 current probe were used to measure the voltage over the reactor and the discharge current respectively. These two probes were connected to a Lecroy Wavesurfer 454 oscilloscope to record the signals and to calculate the power and the energy of a pulse.

For all experiments, the magnitude of the high voltage pulse was kept constant (unless otherwise mentioned). For both pulse sources, the pulse repetition rate was varied for the energy density. The pulse repetition rate for the  $\mu$ s pulse-source and ns pulse-source can be

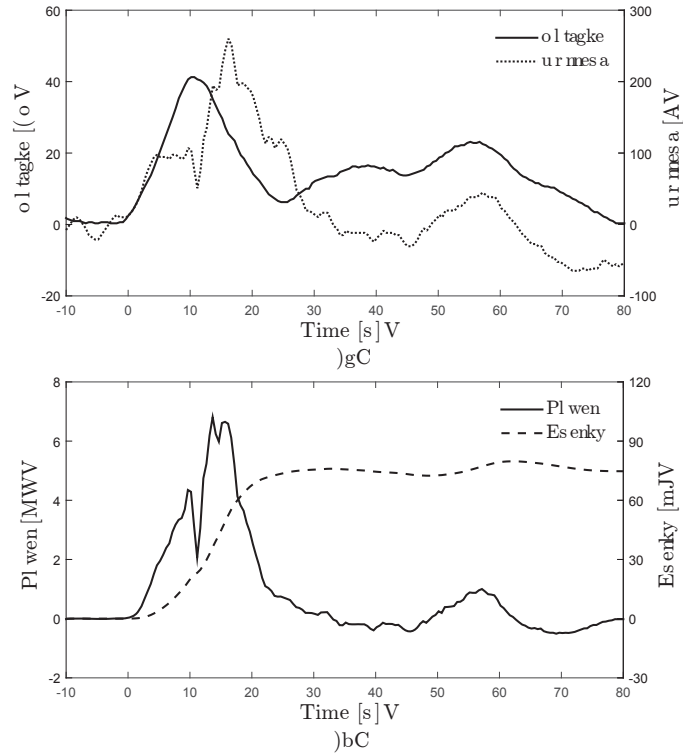


**Figure 2.7** – Typical waveforms in the DBD reactor with the ns pulse source: (a) Applied voltage and discharge current (b) Power and energy deposited per pulse.

varied from 1 Hz–1 kHz and 1 Hz–100 Hz respectively . The energy per pulse ( $E_p$ , [J]) is calculated by using equation (2.1).

$$E_p = \int_{pulse} V(t)I(t)dt \quad (2.1)$$

$V(t)$  and  $I(t)$  in equation (2.1) represent the measured pulse-voltage and current respectively. The energy measurements were taken after the voltage and current reach a stable end value. It can be observed in Fig. 2.7a that oscillations occur in the nanosecond voltage and current waveforms. These oscillations and reflections might occur due to the mismatch between the output impedance of the power source (which is 50 ohm) and the reactor impedance (which is expected to be a few hundred ohm).

The plasma energy density ( $\epsilon$ , [J/L]) was used as the main parameter to compare the efficiency of treatment with different plasma-catalytic configurations and at varying electrical

and operational parameters. The plasma energy density is defined as the energy deposited into the gas per unit volume and can be calculated by using equation (2.2).  $F$  in equation (2.2) is the volumetric gas flow through the reactor (L/s),  $E_p$  is the energy-per-pulse [J] and  $f$  is the pulse repetition rate [Hz].

$$\varepsilon = \frac{fE_p}{F} \quad (2.2)$$

The energy yield for removing one molecule of NO is represented by the W-value in eV/NO molecule and the removal efficiency of NO is represented by G-value in mol/J. These parameters are determined by equations (2.3) and (2.4) respectively.

$$\text{Energy cost (W-value)} = \frac{V_m \times \varepsilon}{\Delta[\text{NO}] \times 10^{-6} \times N_a \times e} \quad (\text{eV/NO molecule}) \quad (2.3)$$

$$\text{Energy yield (G-value)} = \frac{\Delta[\text{NO}] \times 10^{-6}}{V_m \times \varepsilon} \quad (\text{mol/J}) \quad (2.4)$$

where  $\Delta[\text{NO}]$  is the amount of NO removed in ppm.  $V_m$  is the molar volume which is 24.48 L/mol at 20 °C and 1 atm.  $N_a$  is the Avagadro number and  $e$  is the charge of the electron.

## 2.4 Gas concentration measurements

The gas used in our experiments consists of a mixture of synthetic air with NO in N<sub>2</sub> (1% of NO in N<sub>2</sub> base), or of a mixture of synthetic air with C<sub>2</sub>H<sub>4</sub> (1% of C<sub>2</sub>H<sub>4</sub> in N<sub>2</sub> base). We have used ethylene (C<sub>2</sub>H<sub>4</sub>) as a model compound for testing the removal of VOCs with our developed SDBD reactor in Chapter 6. The 1% NO in N<sub>2</sub> mixture is diluted with synthetic air (less than 3 ppm of H<sub>2</sub>O content), using mass flow controllers to get the desired initial concentrations for the experiments. All experiments were done at room temperature and atmospheric pressure. The initial composition of the gas is tested with a Testo 350 XL flue gas analyser and the flow was controlled by mass flow controllers. The Testo 350 XL flue gas analyser is calibrated periodically and is used only when the plasma is turned off to determine the input concentration of NO and NO<sub>2</sub> and to calibrate the FTIR. The treated gas from the DBD reactor was sampled out to a Fourier Transform Infrared Spectrometer (FTIR, BRUKER Tensor 27) with a 20-cm optical path gas cell to measure the exit gas concentration.

For quantitative measurements, the FTIR was calibrated for NO, NO<sub>2</sub>, N<sub>2</sub>O, O<sub>3</sub>, C<sub>2</sub>H<sub>4</sub>, CO and CO<sub>2</sub>. NO and NO<sub>2</sub> calibration was done by varying the respective input concentrations and measuring the absorbance area of the FTIR at each concentration. A calibration factor can be obtained by plotting the absorbance area versus concentration. This calibration factor can be multiplied with the absorbance area to calculate the unknown concentrations

of NO and NO<sub>2</sub>. Similarly, N<sub>2</sub>O calibration was done by using a calibration gas-mixture of 1% N<sub>2</sub>O in N<sub>2</sub>. CO and CO<sub>2</sub> calibration was done by means of 1% CO-CO<sub>2</sub> in N<sub>2</sub> calibration gas mixture. The typical FTIR calibration curves for various gases is given in the Appendix. A.6. The typical FTIR spectra for plasma-off and plasma-on for NO<sub>x</sub> removal experiments and C<sub>2</sub>H<sub>4</sub> experiments is presented in Appendix 7.6 in the figures A.4 and A.5. The measured compositions in our experiments falls in the linearity range. For O<sub>3</sub> calibration, we used UV-absorption spectrometry to calibrate the FTIR spectrometer. For UV absorption measurements, we have used a 11-mm optical path cell and the optic fibers connect this path cell with the UV source and the spectrometer. We have used Micropack D-2000 as UV source and Ocean Optics HR2000 spectrometer. The detailed description of the UV-absorption spectrometry can be seen in the thesis of Winands, Huiskamp and Beckers [59–61].

The resulting spectra from the FTIR are used to determine the reactor-outlet concentrations of NO, NO<sub>2</sub>, O<sub>3</sub> and N<sub>2</sub>O. With these concentrations, the removal efficiency of the DBD reactor could be calculated. The conversions of NO, NO<sub>x</sub> and C<sub>2</sub>H<sub>4</sub> are determined with:

$$\text{NO conversion}[\%] = \frac{[\text{NO}]_i - [\text{NO}]_o}{[\text{NO}]_i} \times 100 \quad (2.5)$$

$$\text{NO}_x \text{ conversion}[\%] = \frac{[\text{NO}_x]_i - [\text{NO}_x]_o}{[\text{NO}_x]_i} \times 100 \quad (2.6)$$

$$\text{C}_2\text{H}_4 \text{ conversion}[\%] = \frac{[\text{C}_2\text{H}_4]_i - [\text{C}_2\text{H}_4]_o}{[\text{C}_2\text{H}_4]_i} \times 100 \quad (2.7)$$

where [NO]<sub>i</sub> and [NO]<sub>o</sub> are the reactor-inlet concentration of NO and the reactor-outlet concentration of NO respectively. [NO<sub>x</sub>]<sub>i</sub> and [NO<sub>x</sub>]<sub>o</sub> are the inlet concentration of NO<sub>x</sub> and the outlet concentration of NO<sub>x</sub> respectively. [C<sub>2</sub>H<sub>4</sub>]<sub>i</sub> and [C<sub>2</sub>H<sub>4</sub>]<sub>o</sub> are the inlet concentration of C<sub>2</sub>H<sub>4</sub> and the outlet concentration of C<sub>2</sub>H<sub>4</sub> respectively.

The selectivity towards CO and CO<sub>2</sub> is defined as the percentage of the total amount of C<sub>2</sub>H<sub>4</sub> that is being converted to CO and CO<sub>2</sub> respectively. The selectivity towards CO and CO<sub>2</sub> in C<sub>2</sub>H<sub>4</sub> measurements are determined with :

$$S_{\text{CO}}[\%] = \frac{[\text{CO}]_o}{2 \times ([\text{C}_2\text{H}_4]_i - [\text{C}_2\text{H}_4]_o)} \times 100 \quad (2.8)$$

$$S_{\text{CO}_2}[\%] = \frac{[\text{CO}_2]_o}{2 \times ([\text{C}_2\text{H}_4]_i - [\text{C}_2\text{H}_4]_o)} \times 100 \quad (2.9)$$

where [CO]<sub>o</sub> and [CO<sub>2</sub>]<sub>o</sub> are the outlet concentrations of CO and CO<sub>2</sub> from the reactor respectively.

## 2.5 Impedance measurements

One of the parameters that is expected to influence the discharge behaviour is the dielectric constant of the catalytic material that is packed in the discharge reactor. Therefore, in this section we measure the dielectric constants of the various catalytic materials that we have used. Also, it is analyzed if the dielectric constant of the catalyst varies with the type and amount of the metal oxide loading on both the  $\text{TiO}_2$  and the  $\text{Al}_2\text{O}_3$  supports. The dielectric constants have been measured by means of a Keysight 16451B Dielectric Test Fixture [62]. This instrument can measure the permittivity in the frequency range of 100 Hz - 10 MHz [123]. The test kit consists of a test cell having parallel electrodes with a diameter of 5 mm and the distance between the two electrodes can be varied up to 10 mm. The capacitance of the test kit, filled with a catalytic material, is measured by the HIOKI 3532-50 LCR HiTESTER which can measure impedances in the frequency range from 42 Hz - 5 MHz [63].

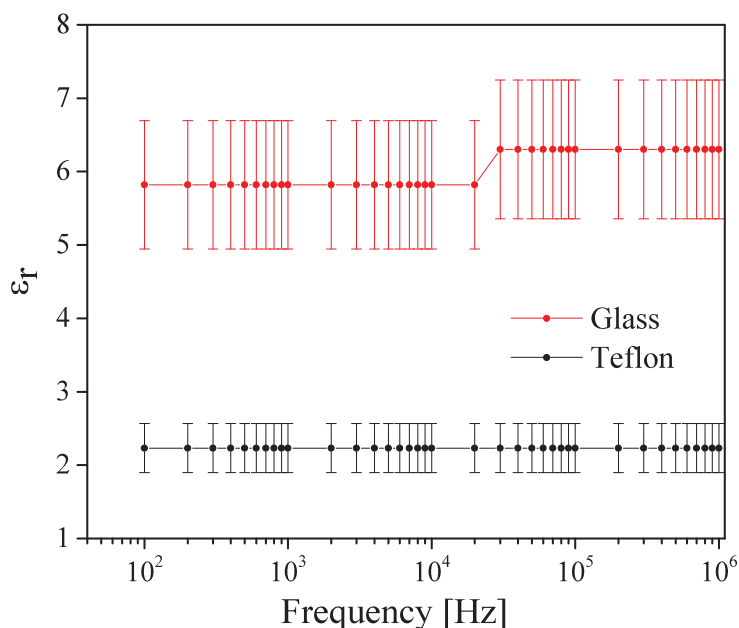


**Figure 2.8** – Dielectric constant of reference materials as a function of frequency measured at ambient temperature.

The synthesis and characterization of the catalytic materials are mentioned in section 2.2. The catalytic materials were made into pellets of diameter 5 mm with a known thickness varying from 2-3 mm. After pelletizing, the catalytic materials were kept in oven at 400 °C overnight to avoid moisture content. Moisture content in the samples may vary their dielectric properties. Every sample was taken from the oven and immediately tested for its dielectric property, thus avoiding moisture content in the sample as much as possible just as in the



experiments with the IPC and the PPC configurations. All the measurements were repeated 5-times to check for the reproducibility. It is observed that the error is high at low frequencies up to 1 kHz. As this probe is a parallel plate probe, the dielectric constant can be calculated by the formula :

$$\epsilon_r = \frac{d \times C_p}{A \times \epsilon_0} \quad (2.10)$$

where  $\epsilon_r$  is the relative dielectric constant (permittivity) of the material of interest,  $d$  is the thickness of test material [m],  $C_p$  is the capacitance of the parallel plate [F],  $A$  is the area of the electrode [m<sup>2</sup>] and  $\epsilon_0$  is the vacuum permittivity which is  $8.854 \times 10^{-12}$  [F/m].

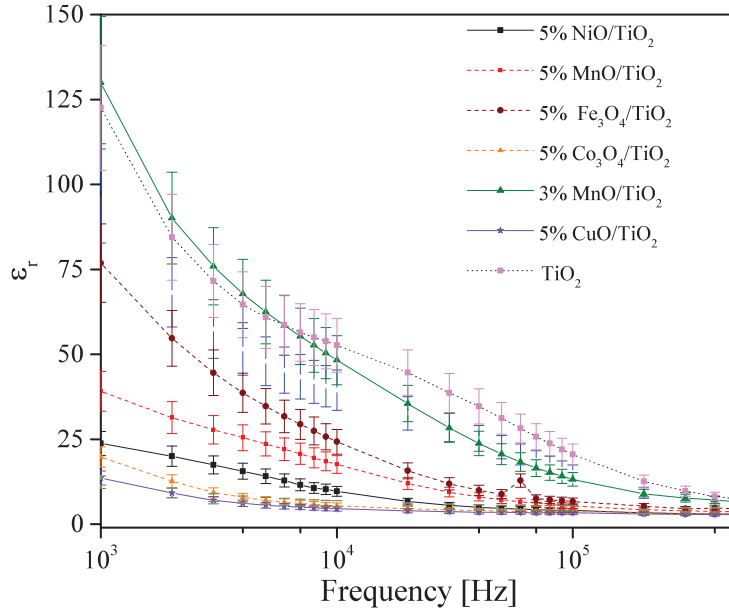


**Figure 2.9** – Dielectric constant of TiO<sub>2</sub> and metal oxides loaded on TiO<sub>2</sub> as a function of frequency measured at ambient temperature.

Before testing our catalytic materials, we have tested reference materials to check the performance of the probe. We have used glass (microscopic slide) and teflon as reference materials as their dielectric constants are well known, do not vary with frequency (atleast until the tested frequency of 1 GHz) and have much lower loss factor. The measured dielectric constants of the glass and Teflon as a function of frequency are shown in the Fig. 2.8. It can be seen that the dielectric constants are almost constant for both the materials over the

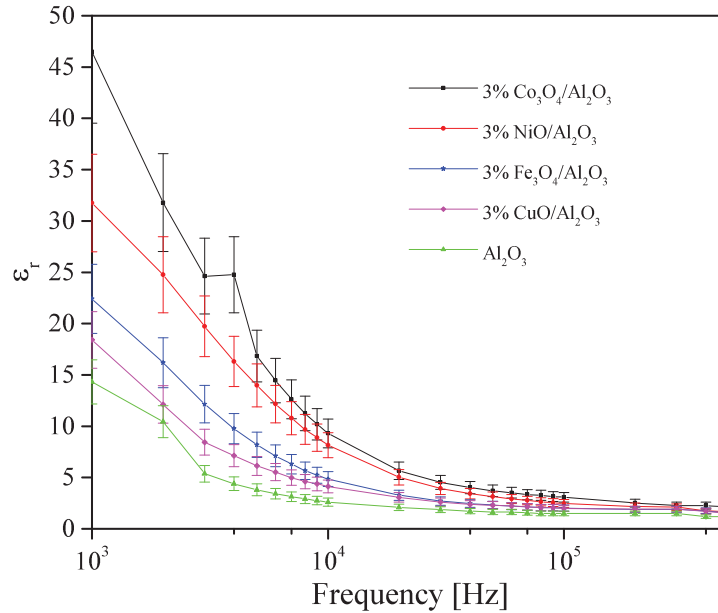


**Figure 2.10** – Dielectric constant of Al<sub>2</sub>O<sub>3</sub> and metal oxides loaded on Al<sub>2</sub>O<sub>3</sub> measured at ambient temperature.

tested frequency range. Also the measured values are in agreement with reference values as reported in literature [64–66].

The measured dielectric constant as a function of frequency for TiO<sub>2</sub>, with and without metal oxides loaded on the TiO<sub>2</sub>, is shown in Fig. 2.9. The results for Al<sub>2</sub>O<sub>3</sub>, with and without metal-oxides loaded on Al<sub>2</sub>O<sub>3</sub> are shown in Fig. 2.10. As the rise-time of the pulses in most of our experiments is 0.9 μs, the frequency that is more important for our pulses is upto 0.4 MHz. It can be seen from Fig. 2.9 that the dielectric constant of TiO<sub>2</sub> decreases when metal-oxides were loaded on this material. In literature, it is reported that different phases of TiO<sub>2</sub> have different dielectric constants [67]. 3% MnO/TiO<sub>2</sub> showed a slightly higher dielectric constant than unloaded TiO<sub>2</sub> at low frequencies. At low frequencies, the error bars are also quite high and so at this point it is unclear to comment whether 3% MnO/TiO<sub>2</sub> shows a higher dielectric constant or not. When comparing the dielectric constants of 3% MnO/TiO<sub>2</sub> with the values for 5% MnO/TiO<sub>2</sub>, It can be seen that 3% MnO/TiO<sub>2</sub> showed higher dielectric constant values than 5% MnO/TiO<sub>2</sub> at all frequencies. Thus, we may say that with increase in the metal-oxide loading, the dielectric constant decreases. Gafoor *et al.*, in their study on AC conductivity and diffuse reflectance studies of Ag-TiO<sub>2</sub> nanoparticles, investigated the effect of Ag nanoparticles on dielectric constant of TiO<sub>2</sub> as function of frequency [68]. They observed that an increasing metal loading resulted in a decrease of

the dielectric constant. They attributed this decrease in dielectric constant to the increase in thickness of grain boundaries in case that a metal loading is present. The thicker the grain boundary the less polarized the material becomes and hence resulting in lower dielectric constants.

The dielectric constant as a function of frequency for  $\text{Al}_2\text{O}_3$  showed a different dependence on the metal oxides as compared to the results for  $\text{TiO}_2$ . The measured dielectric constants for  $\text{Al}_2\text{O}_3$  increase when the  $\text{Al}_2\text{O}_3$  is loaded with metal-oxides. The difference in the values of the dielectric constants was reducing from 10 kHz and above 100 kHz. For all the metal oxides on  $\text{Al}_2\text{O}_3$ , the dielectric constant converged to a value of 2.5-3.0. A similar trend for dielectric constants of  $\text{Al}_2\text{O}_3$  loaded with  $\text{ZrO}_2$  were observed in [69]. The difference in the behavioural trend of the dielectric constant for metal-oxides loaded on  $\text{TiO}_2$  and  $\text{Al}_2\text{O}_3$  needs further understanding of material chemistry.

---

## INVESTIGATION ON THE EFFECT OF ELECTRICAL PARAMETERS ON NO<sub>x</sub> REMOVAL

---

### 3.1 Introduction

During plasma treatment, highly active radicals and ions are produced by energetic electrons which initiate the chemical reactions to decompose pollutants. To obtain efficient remediation these active radicals and ions should be utilized in a effective way to improve the selectivity and to reduce the by-products formation. For this, careful optimization of electrical parameters and operational parameters is required to obtain energy efficient NO<sub>x</sub> remediation irrespective of using a plasma-alone configuration or plasma combined with catalysts. In this chapter, we have varied the electrical parameters such as applied peak voltage, pulse polarity and pulse rise-time to study the degree of removal of NO<sub>x</sub> (sum of NO and NO<sub>2</sub>), by-products formation and energy consumption in the DBD reactor. By varying the electrical parameters, the energy cost and yield change considerably. A useful parameter to optimize the energy consumption and removal efficiency in the NTP reactor is the energy cost [7, 70] which is defined as the energy transferred to the plasma per mol of NO or NO<sub>x</sub> removed from the gas stream. By varying the applied-voltage, energy deposition per pulse in the reactor changes which in turn effects the energy costs. To study the effect of the electrical parameters all the three configurations that were discussed in Chapter 2: plasma-alone, in-plasma catalytic configuration(IPC) and post-plasma catalytic configuration (PPC) were used. Commonly used support materials such as TiO<sub>2</sub>, Al<sub>2</sub>O<sub>3</sub>, NaY and SiO<sub>2</sub> have been used in the IPC and the PPC configuration.

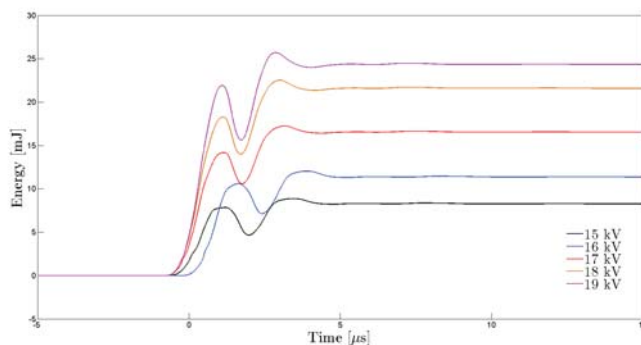


**Figure 3.1** – Energy deposited per pulse in the DBD reactor for different applied peak-voltages.

### 3.2 Effect of applied peak-voltage

In this section, we studied the effect of applied peak-voltage on the NO and NO<sub>x</sub> removal efficiency and by-products formation. The main by-products that we have reported here are N<sub>2</sub>O and O<sub>3</sub>, although also N<sub>2</sub>O<sub>5</sub> was observed at high energy densities. We varied the applied peak-voltage from 15 kV to 19 kV with an interval of 1 kV. Below 15 kV, there is no plasma generation in our DBD reactor. By increasing the applied peak-voltage, the energy deposition per pulse in the reactor increases from 8 mJ to 24 mJ, as seen in Fig. 3.1. For each input voltage, the pulse repetition rate was varied to vary the energy density. The input NO concentration is 200 ppm diluted in 5 slm of dry synthetic air. Experiments were conducted at atmospheric pressure and room temperature. All the experiments in this chapter were performed for 4 times and are reproducible within +/- 5% error margin.

#### 3.2.1 Plasma-alone configuration

Figure 3.2 shows the effect of applied-voltage on the NO and NO<sub>2</sub> concentrations at various energy densities. It can be observed that with increasing energy density, NO concentration reduces to below 6 ppm for all the applied voltages. Thus we can say that the NO conversion does not depend on the applied peak-voltage but is a function of energy density. Few other researchers also reported the same [71–73]. The NO<sub>2</sub> concentration keeps increasing up to 40 J/L and then starts to reduce. The amount of radicals production scales linearly with energy density which in turn leads to higher density of radicals and in this case, production of more O and N atoms as shown in equation (3.1) and (3.3). Thus the produced atomic oxygen and atomic nitrogen react with O<sub>2</sub> and NO<sub>2</sub> to produce O<sub>3</sub> and N<sub>2</sub>O respectively as shown in the equation (3.4) to (3.7). NO<sub>3</sub> is a transient species and reacts with NO<sub>2</sub> to form N<sub>2</sub>O<sub>5</sub> by the reaction (3.10). Although NO<sup>+</sup>, H<sub>3</sub>O<sup>+</sup> ions are major ions in air plasmas, the ion densities are relatively small and are not chemically active in the NO<sub>x</sub> removal process [74]. Therefore, we have not considered ions in our reaction pathways.

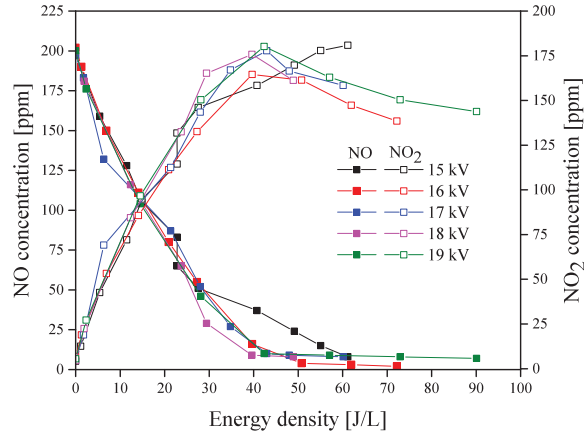


**Figure 3.2** – NO and NO<sub>2</sub> concentrations as a function of energy densities for various applied voltages for input NO concentration of 200 ppm and gas flow rate of 5 L/min.



With increasing energy densities, the collisions between the electrons and the neutrals are more frequent which leads to the production of more O and N atoms as shown in equation (3.1) and (3.3) which leads to increasing removal efficiency but also increases the by-products formation. Increasing the energy densities also increases energy costs; i.e. the energy needed to remove one mol of NO or NO<sub>x</sub>.

When the energy cost for NO and NO<sub>x</sub> is plotted as a function of applied voltage at various energy densities as shown in Fig. 3.4a and Fig. 3.4b, it is observed that with increasing applied voltage the energy cost first decreases to a minimum at 16 kV and then

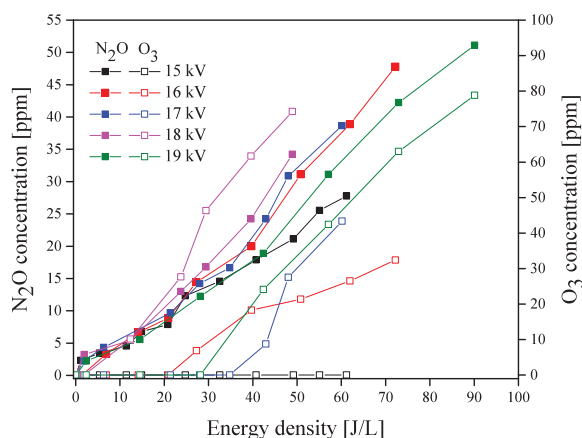
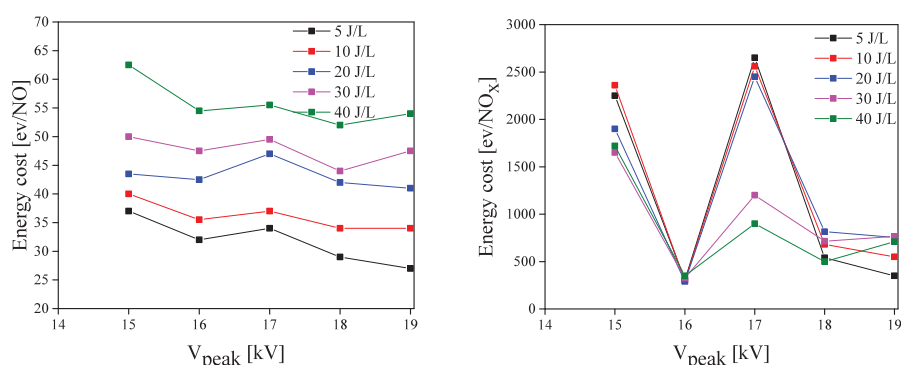


**Figure 3.3** – N<sub>2</sub>O and O<sub>3</sub> concentrations as a function of energy densities for various applied voltages for input NO concentration of 200 ppm and gas flow rate of 5 L/min.



(a) Energy cost per molecule of NO removed.

(b) Energy cost per molecule of NO<sub>x</sub> removed.

**Figure 3.4** – Energy cost for NO and NO<sub>x</sub> removed as a function of energy density for various applied voltages for input NO concentration of 200 ppm and gas flow rate of 5 L/min in a plasma-alone configuration.

increases for all energy densities. A similar trend is observed when energy cost for NO<sub>x</sub> molecule is plotted as a function of applied voltage. The energy costs for NO<sub>x</sub> molecule first decreases to a minimum at 16 kV and then increases at 17 kV and above this applied peak-voltage, the energy costs decreases again. We observed high energy costs at 17 kV upto an energy density of 20 J/L. This is probably due to high energy deposition per pulse at 17 kV as compared to 16 kV leading to high energy density and higher NO conversions. But this applied energy density is just enough to convert NO to NO<sub>2</sub> giving rise to lower NO<sub>x</sub> removal. This lower NO<sub>x</sub> removal and high energy per pulse might have lead to higher

energy costs below 20 J/L. Above 20 J/L, the NO conversions are high and the produced NO<sub>2</sub> is consumed to form N<sub>2</sub>O and N<sub>2</sub>O<sub>5</sub> resulting in higher NO<sub>x</sub> removal and leading to low energy costs at energy densities of 30 J/L and 40 J/L for applied voltage of 17 kV. For applied voltages of 18 kV and 19 kV, the energy cost for NO<sub>x</sub> removal is observed to be low. This is because, at this energy density, NO<sub>2</sub> is being consumed to form N<sub>2</sub>O<sub>5</sub>.

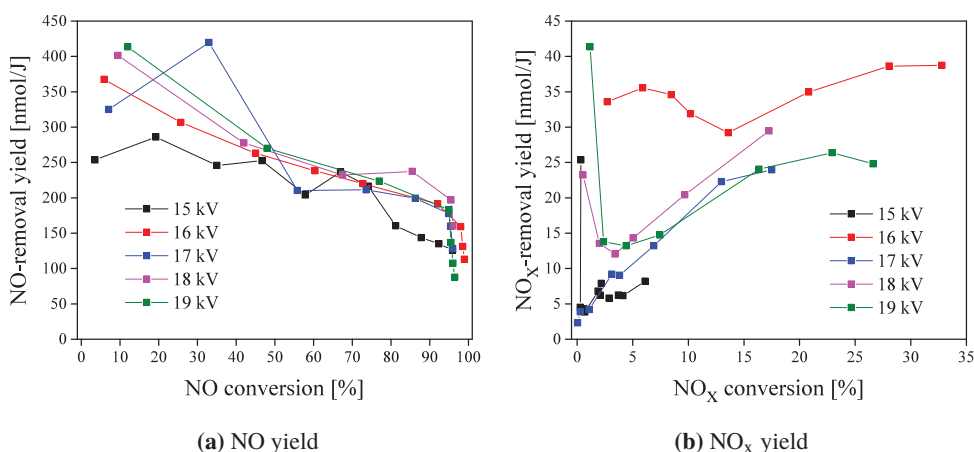


**Figure 3.5** – NO and NO<sub>x</sub> removal yield as a function of NO and NO<sub>x</sub> removal efficiency respectively for various applied voltages for input NO concentration of 200 ppm and gas flow rate of 5 L/min in a plasma-alone configuration.

When the removal yields for NO and NO<sub>x</sub> are plotted as a function of NO and NO<sub>x</sub> conversion respectively, it is observed that the removal yields (i.e. the mol of NO removed per Joule) increase with increasing applied voltage at lower energy densities which can be seen in Fig. 3.5. With increasing energy density as the NO is removed significantly, the removal yields are almost the same irrespective of the increase in applied voltage. At such high energy densities, NO is already consumed and gets converted to NO<sub>2</sub>. The term NO<sub>x</sub> conversion was used here to illustrate the yields with respect to the sum of NO and NO<sub>2</sub> concentrations for the convenience despite mixing the fact that NO<sub>2</sub> is present in small amounts (in the range of 5-10 ppm) in the input gas concentration. This small concentrations of NO<sub>2</sub> is due to mixing with synthetic air and subsequent NO-NO<sub>2</sub> equilibrium. The removal yield for NO<sub>x</sub> at 15 kV is far less than that of the removal yields at other applied voltages as seen in the Fig. 3.5. At this applied-voltage, the rate of NO conversion is low as the input energy per pulse is low and thus NO<sub>2</sub> concentration gradually increases. On the other hand, this energy per pulse is not enough to convert NO<sub>2</sub> to N<sub>2</sub>O and thus we can see lesser concentrations of N<sub>2</sub>O and O<sub>3</sub> compared to higher applied voltages. With the increasing removal of NO<sub>x</sub>, the removal yield first decreased and then increased for all the applied voltages and again starts to decrease at higher NO<sub>x</sub> removal. Higher NO<sub>x</sub> removal rates are obtained at an applied voltage of 16 kV. The removal yield for an applied voltage of 16 kV started to reduce from 34 nmol/J to 28 nmol/J until the NO<sub>x</sub> conversion reaches 13%



and after this 13% NO<sub>x</sub> removal, the NO<sub>x</sub> removal yields started to increase and reaches a maximum of 38%. The trend is same for all the other applied peak-voltages. In the study on the effect of electrode shape in dielectric barrier discharge plasma reactor for NO<sub>x</sub> removal by Koichi Takaki *et al.* [72], suggests that with the increase in applied peak-voltage, the number of microdischarges and capacitive current increases. This increase in capacitive current leads to the increased energy losses in the dielectric barrier which in turn reduces the energy efficiency.

### 3.2.2 In-plasma configuration

The effect of the plasma combined with catalyst in an in-plasma (IPC) configuration for NO and NO<sub>x</sub> removal as a function of energy density for various applied peak-voltages is shown in Fig. 3.6 and Fig. 3.7 respectively. For plasma-alone, NO conversion reaches 99% at an energy density of around 30 J/L for all the applied peak-voltages whereas when the catalyst materials are introduced in to the plasma reactor, the NO removal rate is lower than that of the plasma-alone configuration which was also observed by Jeon *et al.* [75]. 99% conversion of NO is achieved above 40 J/L for all the materials that are used here. The plasma-alone configuration showed that the NO conversion does not depend much on the applied peak-voltages but depends mainly on the energy densities whereas in the IPC configuration, NO removal is function of both applied peak-voltages as well as the energy density. For TiO<sub>2</sub>, the maximum NO conversion is achieved at 35 J/L for an applied peak-voltage of 16 kV. With increasing applied peak-voltage, NO conversion started to slightly decrease. All the other materials showed the same trend except the clear distinction of NO removal at 16 kV.

As shown in Fig. 3.7, the maximum NO<sub>x</sub> removal with TiO<sub>2</sub> and Al<sub>2</sub>O<sub>3</sub> was also achieved at 16 kV but at different energy densities. For TiO<sub>2</sub> and Al<sub>2</sub>O<sub>3</sub>, 38% NO<sub>x</sub> removal was obtained at 47 J/L and 80 J/L respectively. There appeared to be a clear distinction in the NO<sub>x</sub> removal at this applied peak-voltage with TiO<sub>2</sub> and Al<sub>2</sub>O<sub>3</sub> whereas the NaY and SiO<sub>2</sub> does not show a big difference with varied applied peak-voltage. With increasing applied peak-voltage, NaY showed negative NO<sub>x</sub> conversion at 18 kV and 19 kV applied peak-voltage as NO<sub>x</sub> is produced intrinsically. SiO<sub>2</sub> showed increasing NO<sub>x</sub> conversion with increasing applied-voltage. The maximum NO<sub>x</sub> conversion achieved was 46% at 69 J/L.

Thus different materials reacted differently to the applied peak-voltage but what is the impact of the applied peak-voltage on by-products formation? Do all the materials follow same trend or do they perform differently? To answer that, N<sub>2</sub>O concentration and O<sub>3</sub> concentrations as a function of energy density for various applied peak-voltages have been plotted as shown in Fig. 3.8. Al<sub>2</sub>O<sub>3</sub> showed higher by-products formation at applied peak voltage of 16 kV despite its high NO and NO<sub>x</sub> removal at this voltage. For TiO<sub>2</sub>, NaY and silica, it is observed that with increasing applied peak-voltage the amount of by-products formation increased. But this increase in by-products may be due to high energy densities that are applied at higher applied peak-voltages. With increasing applied peak-voltage, at low energy densities, the N<sub>2</sub>O concentrations are low but increase with increasing energy density. Whereas O<sub>3</sub> concentration showed the opposite trend. O<sub>3</sub> concentration tend to increase with increasing applied peak-voltage and energy densities.

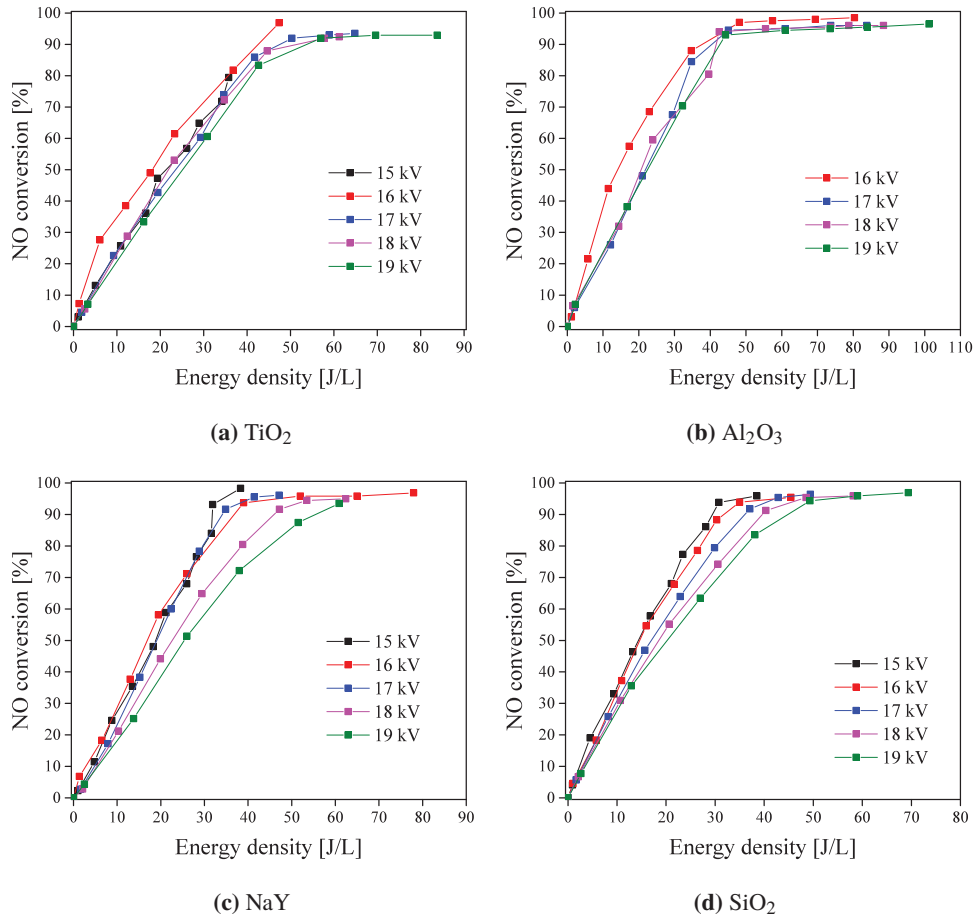


**Figure 3.6** – NO conversion as a function of energy density for various applied voltages for input NO concentration of 200 ppm and gas flow rate of 5 L/min in an IPC configuration.

When looking at the energy costs as a function of applied peak-voltages for plasma-alone and plasma combined with catalyst in the IPC configuration, it can be seen from Fig. 3.9 that the energy cost for NO removal is less for plasma-alone configuration at all applied peak-voltages. This comparison of energy costs was done at an energy density of 30 J/L as at least 80% conversion of the NO has been reached before 30 J/L for all the materials. The energy cost for NO removal at 16 kV is almost the same for TiO<sub>2</sub>, Al<sub>2</sub>O<sub>3</sub> and NaY and it is lower compared to other peak-voltages. At an applied peak-voltage of 15 kV to 16 kV, there is a dip in energy cost as more NO is converted to NO<sub>2</sub> and from 16 kV to 17 kV, the energy cost seems to rise because of the slight intrinsic production of NO and above 17 kV, the conversion

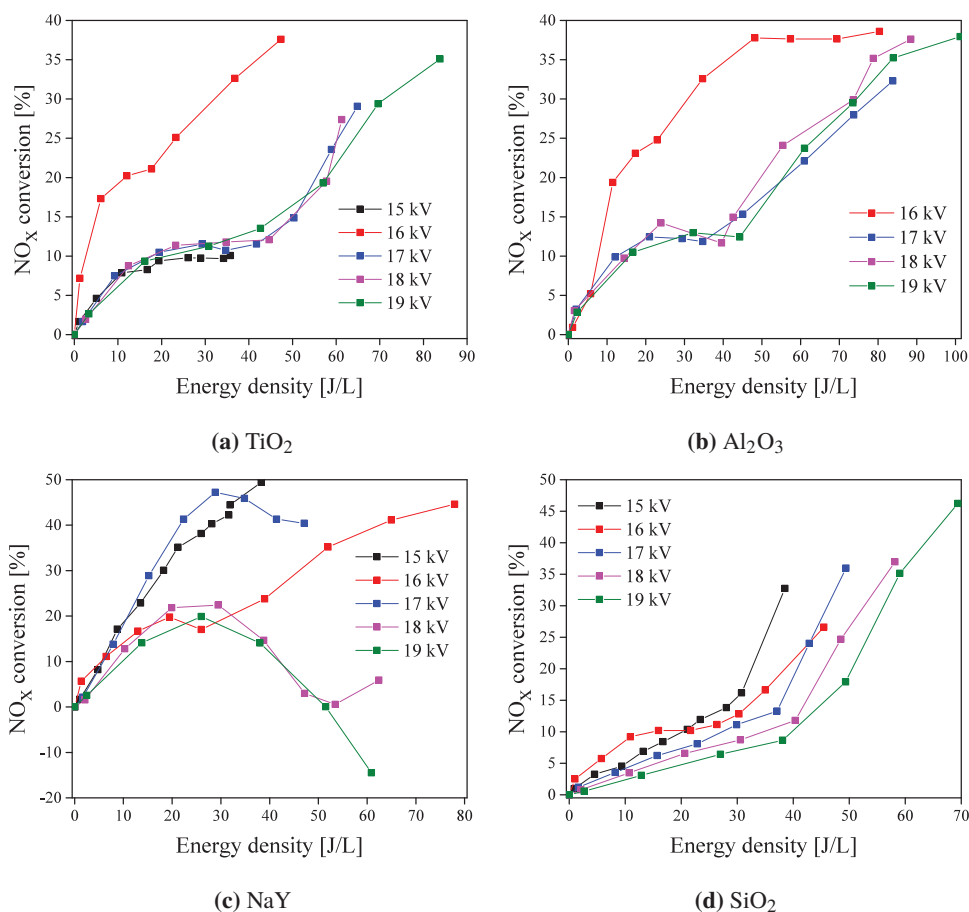


**Figure 3.7** – NO<sub>x</sub> conversion as a function of energy density for various applied peak-voltages for input NO concentration of 200 ppm and gas flow rate of 5 L/min in an IPC configuration.

of NO<sub>2</sub> to N<sub>2</sub>O<sub>5</sub> dominates thus reducing the energy costs again. But when looking at the energy costs for NO<sub>x</sub> removal, plasma-alone configuration has higher costs compared to all the tested IPC-configurations. To summarize, the energy costs for NO removal using the IPC configuration are in the order of plasma-alone < NaY (up to 17 kV) < Al<sub>2</sub>O<sub>3</sub> < Silica < TiO<sub>2</sub> and the energy costs for NO<sub>x</sub> removal using the IPC configuration are in the order of NaY < Al<sub>2</sub>O<sub>3</sub> = TiO<sub>2</sub> < Silica < Plasma-alone. The plasma-alone configuration showed lower energy costs for NO removal because of its efficiency to convert NO to NO<sub>2</sub> at low energy density while the IPC configuration requires slightly higher energy densities for complete conversion of NO.

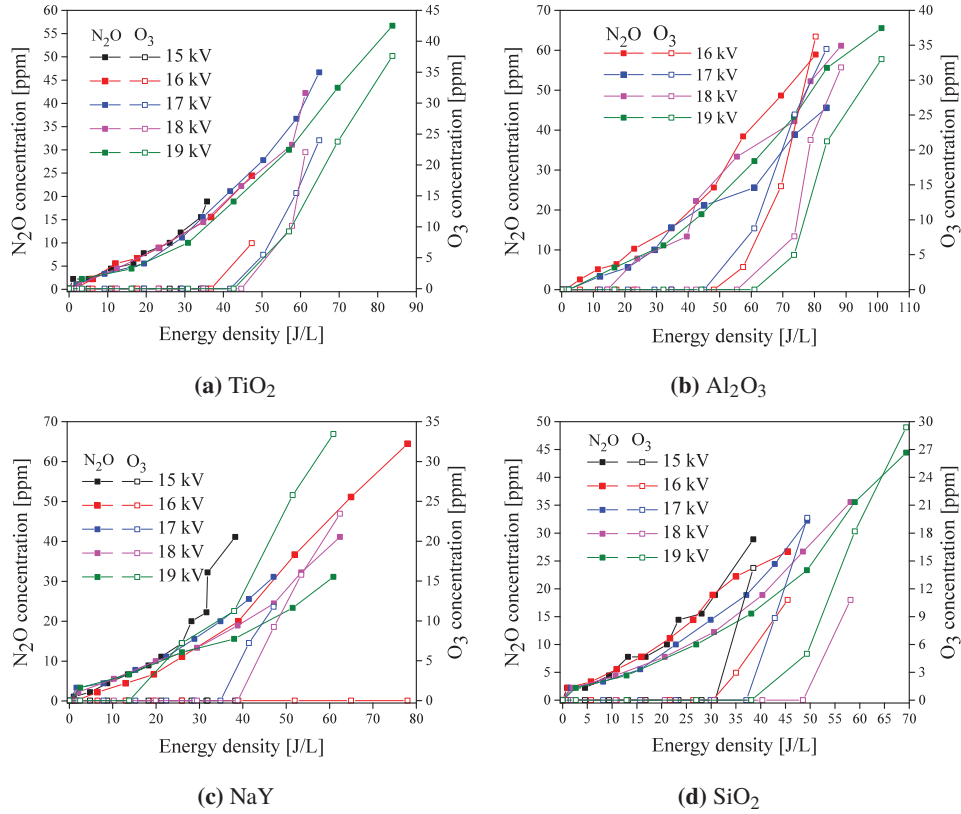


**Figure 3.8** – By-products formation as a function of energy density for various applied peak-voltages for input NO concentration of 200 ppm and gas flow rate of 5 L/min in an IPC configuration.

Previously, we have shown that with increase in the applied peak-voltage, the energy deposition per pulse increases. This increases the plasma energy density which in turn increases the radicals production. Gentile *et al.* in their study on the reaction chemistry and optimization of plasma remediation of N<sub>x</sub>O<sub>y</sub> [74] have stated that the rates of majority of remediation reactions (such as reactions 3.5 and 3.6) scale linearly with radical concentrations and the rate of radical recombination reactions (such as reaction 3.2) scale non-linear with the radical concentrations. At low energy densities, the radicals will be more utilized in the remediation reactions and less in radical recombination reactions. The more the radicals utilized in the remediation reactions, the more efficient will be the remediation process. Thus, the low applied peak-voltages provide better remediation due to less energy deposition per pulse. As an applied peak-voltage of 16 kV showed better results with respect to removal efficiency, energy costs and by-products formation, the rest of the experiments

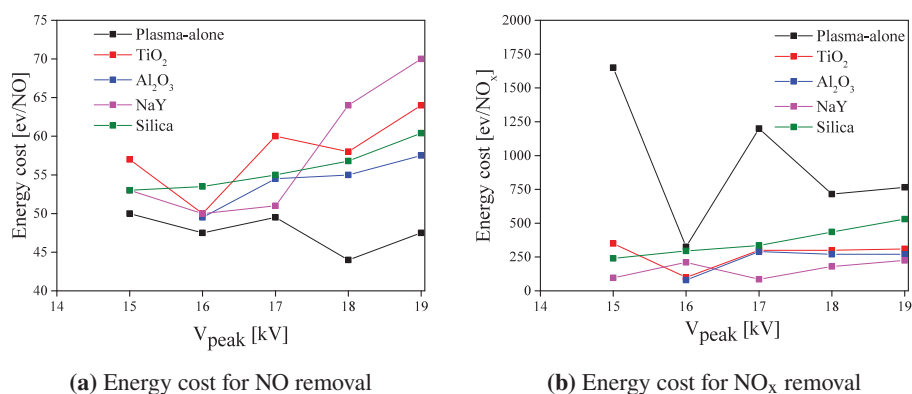


**Figure 3.9** – Energy costs for NO and NO<sub>x</sub> removal as a function of applied peak-voltages in an IPC configuration for input NO concentration of 200 ppm with gas flow rate of 5 L/min and at an energy density of 30 J/L.

were conducted at this peak-voltage unless otherwise mentioned.

### 3.2.3 Post-plasma configuration

The effect of plasma combined with catalyst in a post-plasma (PPC) configuration for NO and NO<sub>x</sub> removal as a function of energy density for various applied peak-voltages is shown in Fig. 3.10 and Fig. 3.11. As observed in the plasma-alone configuration and in the IPC configuration, the PPC configuration also shows that the NO conversion does not depend much on the applied peak-voltages but depends only on the energy densities. To obtain 90% NO conversion, energy densities higher than 50 J/L are required for all the materials that are used here whereas plasma-alone configuration achieved 99% conversion at 35 J/L. Thus for higher NO conversions, PPC configurations requires more than 1.5 times of higher energy densities compared to the plasma-alone configuration.

When looking into the NO<sub>x</sub> conversion for various applied peak-voltages as a function of energy density, PPC configurations performed better than the plasma-alone configuration. The PPC configuration with NaY showed higher NO<sub>x</sub> removal at 19 kV as compared with plasma-alone, IPC configurations and to other materials that have been used in the PPC configuration. NaY achieved 71% NO<sub>x</sub> removal at approximately 70 J/L for the applied peak-voltage of 19 kV. Ogata *et al.* [76] also observed that the formation of NO<sub>x</sub> was suppressed by combining the plasma reactor with NaY. Adelman *et al.* [76] made a temperature-programmed desorption (TPD) study on the adsorption capacity of NO<sub>x</sub> on different zeolites and have reported that in the presence of O<sub>2</sub> much of the NO<sub>x</sub> can be adsorbed on the NaY zeolites. The zeolites are also able to convert NO to N<sub>2</sub>O and N<sub>2</sub>O<sub>3</sub> which is called as a disproportionation reaction as is reported in [77].

When the N<sub>2</sub>O and O<sub>3</sub> concentrations are plotted as a function of energy density as in

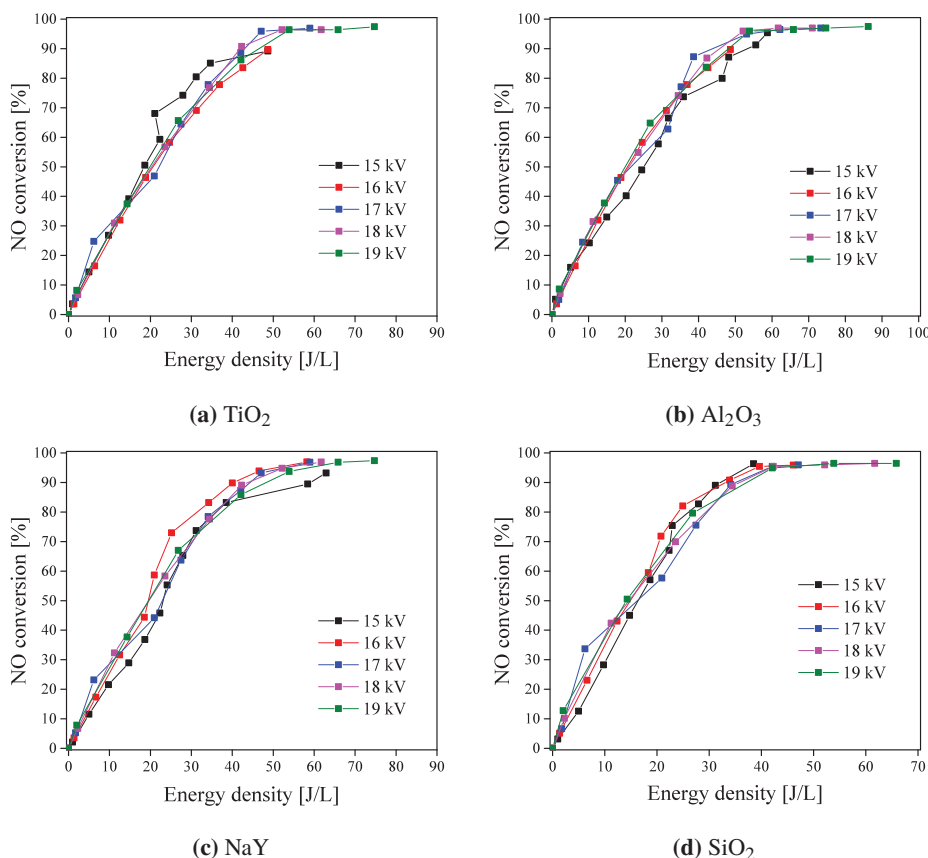


**Figure 3.10** – NO conversion as a function of energy density for various applied voltages for input NO concentration of 200 ppm and gas flow rate of 5 L/min in a PPC configuration.

Fig. 3.12, it can be seen that  $\text{Al}_2\text{O}_3$  and NaY produced higher  $\text{N}_2\text{O}$  concentrations than  $\text{TiO}_2$  and silica. On the other hand,  $\text{O}_3$  formation was less for NaY compared with  $\text{Al}_2\text{O}_3$ ,  $\text{TiO}_2$  and silica at all applied peak-voltages. In the PPC configuration, the by-products formation does not depend on applied peak-voltage but varied significantly with varying energy densities which follows the same trend as the NO-removal. In general, the by-products formation is less for PPC configurations compared to IPC and plasma-alone configurations especially with regard to  $\text{O}_3$  concentrations.

The energy costs for NO and  $\text{NO}_x$  removal as a function of the applied peak-voltages for the PPC configuration can be seen in Fig. 3.13. The energy cost for NO removal is less for plasma-alone configuration at all applied peak-voltages than with the plasma-combined with catalysts which has the same trend as seen in the IPC configurations. The increase

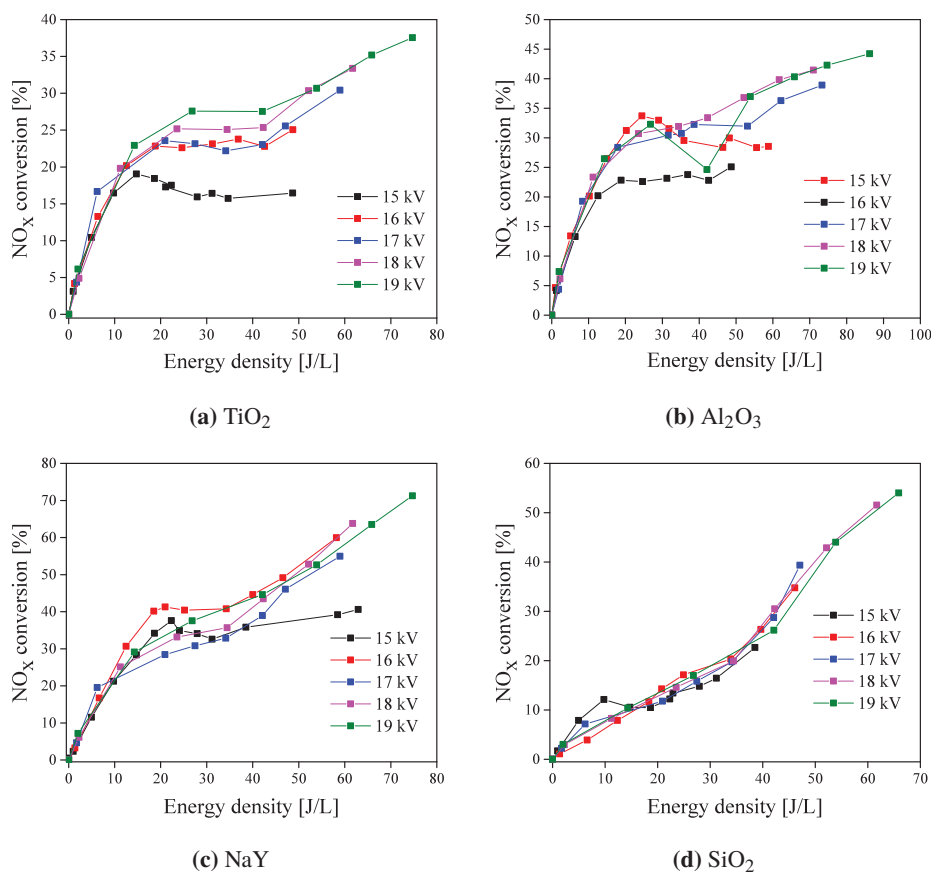


**Figure 3.11** – NO<sub>x</sub> conversion as a function of energy density for various applied voltages for input NO concentration of 200 ppm and gas flow rate of 5 L/min in a PPC configuration.

and decrease of energy costs at various applied peak-voltages followed the same trend as mentioned earlier for the IPC configuration. When a comparison is made between the energy cost for NO<sub>x</sub> removal using the plasma-alone and the PPC configurations, it can be seen that the energy costs per mol of NO<sub>x</sub> removal is much higher for the plasma-alone configuration as the NO<sub>2</sub> concentrations are higher. To summarize, the energy costs for NO removal using the PPC configuration are in the order of plasma-alone < NaY < Silica < TiO<sub>2</sub> < Al<sub>2</sub>O<sub>3</sub> and the energy costs for NO<sub>x</sub> removal using the PPC configuration are in the order of NaY < Al<sub>2</sub>O<sub>3</sub> < TiO<sub>2</sub> < Silica < Plasma-alone.

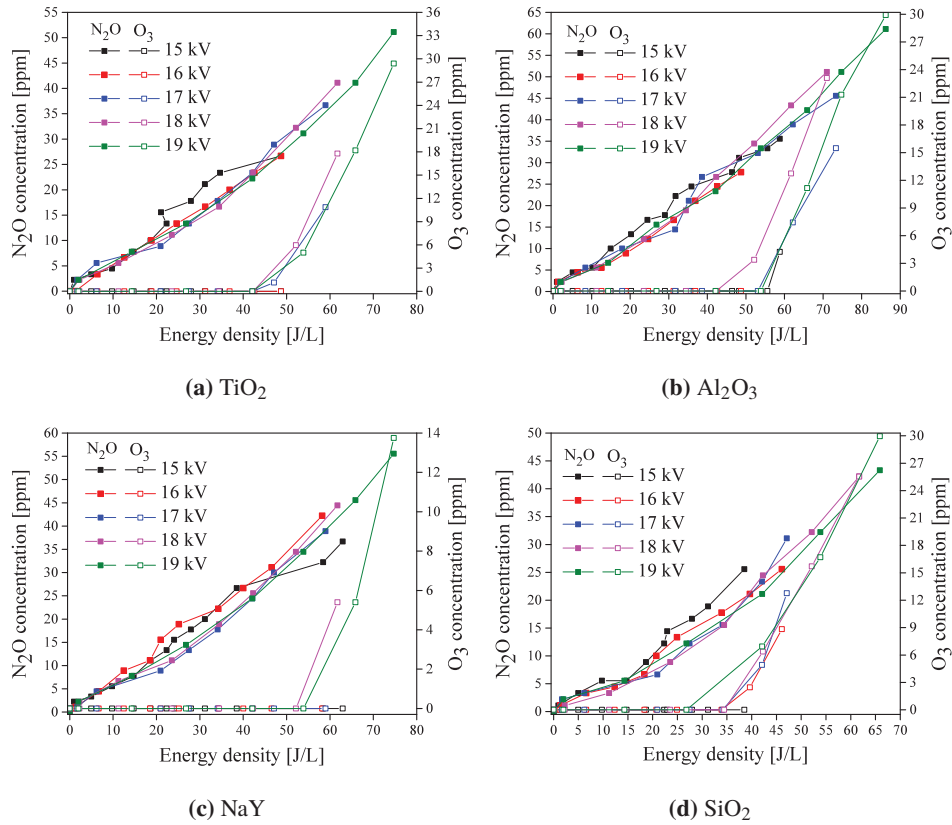


**Figure 3.12** – By-products formation as a function of energy density for various applied voltages for input  $NO$  concentration of 200 ppm and gas flow rate of 5 L/min in a PPC configuration.

### 3.3 Effect of pulse polarity

From the literature, it can be found that the plasma processing depends on the polarity of the applied high-voltage pulses [60, 78, 79]. In the study on control of  $NO_x$  by positive and negative pulsed corona discharges by Masuda *et al.* [78], they stated that positive pulsing produces more reactive species as compared to the negative pulsed corona. In the study by Huiskamp *et al.* [73, 80], study was done on the streamer development and propagation with positive and negative polarity pulses. The positive and negative streamers were studied by ICCD fast imaging. He observed that the negative pulses produced less streamer volume compared to positive pulses and hence less  $O_3$ . Muaffaq *et al.* [79] also reported that for dielectric barrier discharges, positive pulses lead to a formation of large number of positive streamers with a high electric field region at their heads. They also observed that



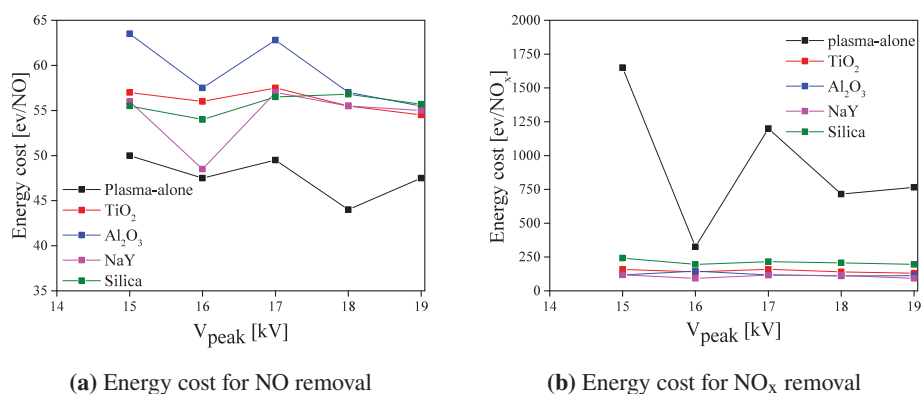


**Figure 3.13** – Energy costs for NO and NO<sub>x</sub> removal as a function of applied peak-voltages in PPC configuration for input NO concentration of 200 ppm with gas flow rate of 5 L/min and at an energy density of 30 J/L.

the NO<sub>x</sub> removal is higher with positive pulses than with negative pulses. Thus, different configurations showed different effects with positive and negative pulses and it will be interesting to see how the pulse polarity affects the NO<sub>x</sub> removal in our configuration. In this section, we have investigated the effect of polarity on NO<sub>x</sub> removal in the dielectric barrier discharge reactor. The experiments were conducted at applied peak-voltage of 16 kV and an initial NO concentration of 200 ppm. The pulse repetition rate was varied from 10 Hz–1 kHz to vary the energy density. We have used TiO<sub>2</sub>, Al<sub>2</sub>O<sub>3</sub>, NaY, and SiO<sub>2</sub> in the IPC and the PPC configurations.

### 3.3.1 Plasma-alone configuration

The effect of pulse-polarity on the NO and NO<sub>x</sub> removal as function of energy density is shown in Fig. 3.14. The negative polarity pulses showed slightly better NO conversion whereas the positive polarity pulses showed a bit better NO<sub>x</sub> conversion. The NO<sub>2</sub> concentrations are observed to be higher with negative polarity which resulted in lower NO<sub>x</sub> conversions. Similar results were obtained in [81] where the authors have studied the effect of polarity on NO<sub>x</sub> removal in a coaxial corona discharge reactor and they have also observed that at higher temperatures, the negative polarity resulted in higher NO<sub>x</sub> removal. There happens to be no significant difference in the by-products formation with the positive polarity pulses and negative polarity as seen in Fig. 3.15.

### 3.3.2 In-plasma configuration

The effect of pulse-polarity on the plasma combined with catalyst in a IPC for NO and NO<sub>x</sub> conversion as a function of energy density is shown in Fig. 3.16. The positive pulses show

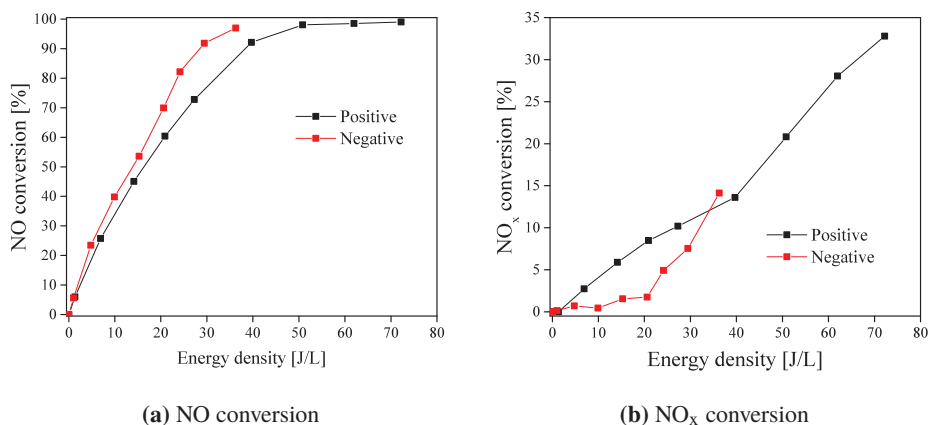


**Figure 3.14** – NO and NO<sub>x</sub> conversion as a function of energy density for the positive polarity pulses and the negative polarity pulses for input NO concentration of 200 ppm and gas flow rate of 5 L/min in a plasma-alone configuration.

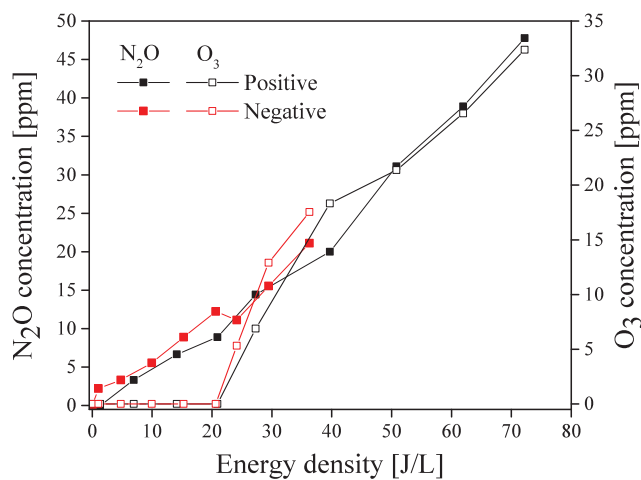


**Figure 3.15** – N<sub>2</sub>O and O<sub>3</sub> concentrations as a function of energy density for the positive polarity pulses and the negative polarity pulses for input NO concentration of 200 ppm and gas flow rate of 5 L/min in a plasma-alone configuration.

better conversion especially with regard to NO<sub>x</sub> for TiO<sub>2</sub>, Al<sub>2</sub>O<sub>3</sub>, and NaY. It is interesting to see the effect of polarity on NO<sub>x</sub> conversion with NaY as the difference between positive and negative pulses is quite obvious above 20 J/L. The maximum NO<sub>x</sub> conversion for NaY with negative pulse is approximately 17% whereas a conversion of approximately 45% is

achieved with positive pulses which is around 2.5 times higher than that for the negative pulses. This behaviour is also observed with TiO<sub>2</sub> and Al<sub>2</sub>O<sub>3</sub>. For TiO<sub>2</sub>, the NO<sub>x</sub> conversion was approximately 39% with positive pulses but only 11% with negative pulses. For Al<sub>2</sub>O<sub>3</sub>, 38% of NO<sub>x</sub> conversion was achieved with positive pulses and 15% with negative pulses. It can be seen that for both Al<sub>2</sub>O<sub>3</sub> and TiO<sub>2</sub>, the NO<sub>x</sub> conversion started to increase above 40 J/L. This is due to the consumption of NO<sub>2</sub> to form N<sub>2</sub>O<sub>5</sub>. In contrast, silica showed better NO<sub>x</sub> conversion with negative pulses than positive pulses above 15 J/L.

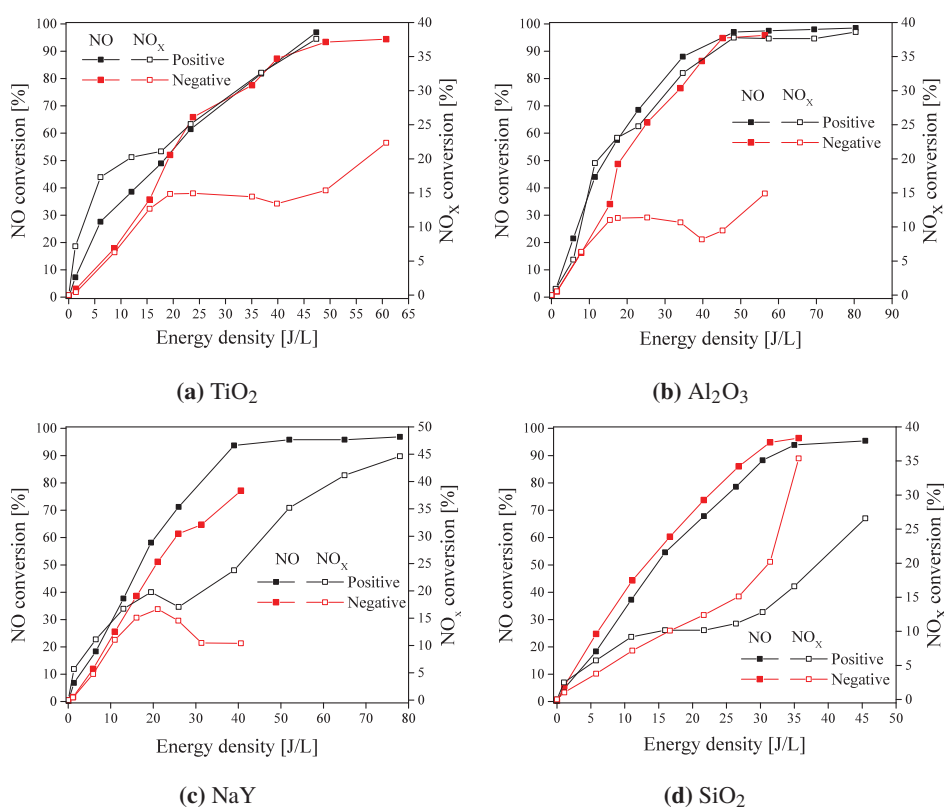


**Figure 3.16** – NO and NO<sub>x</sub> conversion as a function of energy density for the positive polarity pulses and the negative polarity pulses in the IPC configuration for input NO concentration of 200 ppm and gas flow rate of 5 L/min.

The effect of polarity on by-products formation is shown in the Fig.3.17. It can be observed that TiO<sub>2</sub> does not show any significant difference of N<sub>2</sub>O concentrations with polarity but showed higher O<sub>3</sub> concentrations with positive pulses and no O<sub>3</sub> formation was observed for negative pulses. On the other hand, Al<sub>2</sub>O<sub>3</sub> did not exhibit any considerable difference in both N<sub>2</sub>O and O<sub>3</sub> concentrations with change in the polarity. For NaY, the

change in polarity does not appear to effect the  $N_2O$  concentration but a small concentration of  $O_3$  (7 ppm) can be noticed with negative pulses. The performance of silica is in-line with NaY where the polarity did not show significant effect on  $N_2O$  concentrations but positive pulses give better results with respect to  $O_3$  concentrations. As mentioned earlier, in the study by Huiskamp [73, 80], lesser  $O_3$  yields were observed with negative pulses and in our case it is in-line with performance of  $TiO_2$  and contradicts with NaY and silica. Though there is no clear evidence on why these materials behaved differently with change in polarity, an in-depth study on the amount of micro-discharges formed with different materials for different polarities with ICCD imaging or optical spectrum measurements to investigate the electron energies with streamer for positive pulses and negative pulses may give a clue for this difference in the performance.

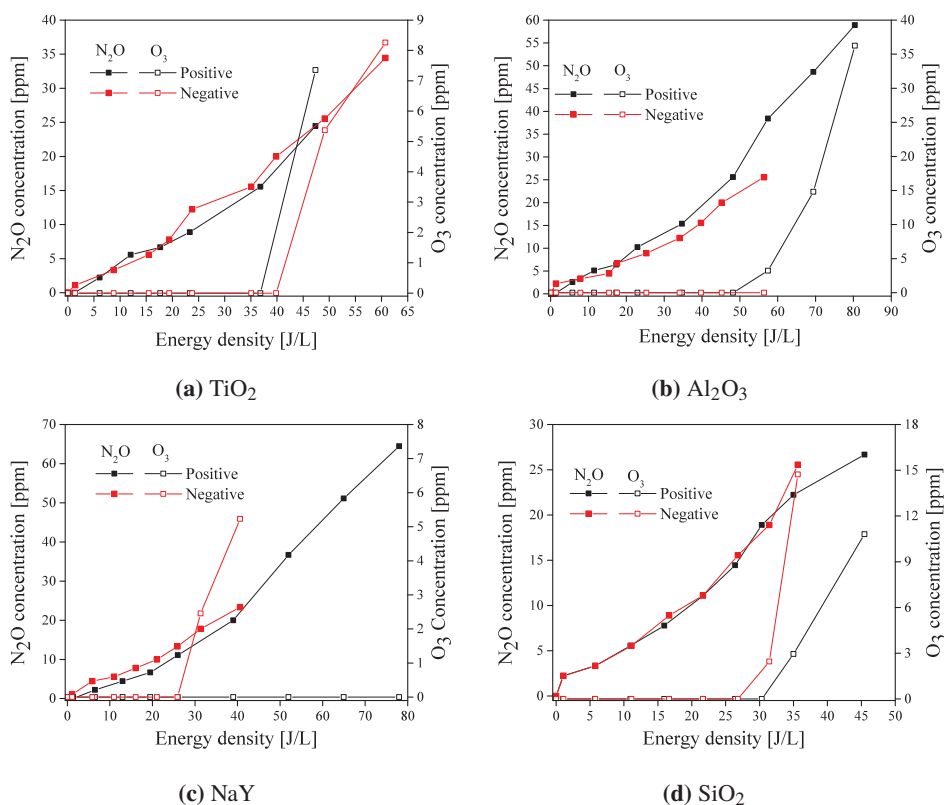


**Figure 3.17** – By-products formation as a function of energy density for the positive polarity pulses and the negative polarity pulses in the IPC configuration for input NO concentration of 200 ppm and gas flow rate of 5 L/min.

### 3.3.3 Post-plasma configuration

Figure 3.18 shows the effect of polarity of the pulses when the plasma is combined with catalysts in a PPC configuration. With TiO<sub>2</sub>, the negative pulses show higher NO conversion whereas a higher conversion for NO<sub>x</sub> was obtained with the positive pulses. For the negative pulses, NO<sub>x</sub> conversion started to fall above 25 J/L. Al<sub>2</sub>O<sub>3</sub> showed slightly higher NO conversion with the negative pulses above 15 J/L but again the positive pulses showed better NO<sub>x</sub> conversion similar to the behaviour of TiO<sub>2</sub>. A maximum NO<sub>x</sub> conversion of 11% is achieved with the negative pulses whereas the positive pulses achieved a maximum of 23% for Al<sub>2</sub>O<sub>3</sub>. NaY showed better NO and NO<sub>x</sub> conversions with the positive pulses whereas silica achieved better NO conversion with positive pulses. Higher NO<sub>x</sub> conversion for silica was achieved with positive pulses up to 15 J/L and above 34 J/L and in between 15–34 J/L, the negative pulses performed better in terms of NO<sub>x</sub> removal. When the IPC and PPC configurations are compared with respect to NO and NO<sub>x</sub> conversions, regardless of the polarities, the NO conversion achieved by the PPC configuration is less than that of the plasma-alone and IPC configuration. Whereas the NO<sub>x</sub> conversions are better in the PPC configuration than the plasma-alone configuration but bit lower compared to the IPC configurations.

The effect of pulse-polarity on the by-products formation is shown in Fig. 3.19. Regardless of the polarities, O<sub>3</sub> formation has been suppressed in the PPC configuration and in general the N<sub>2</sub>O concentrations were less with PPC configurations with all the materials that have been used in this study. For TiO<sub>2</sub>, N<sub>2</sub>O concentration is observed to be higher for negative pulses especially above the energy density of 20 J/L. No ozone was observed with TiO<sub>2</sub> for both the positive pulses and the negative pulses. Al<sub>2</sub>O<sub>3</sub> exhibited the similar behaviour as in the IPC configuration which means that no significant difference was observed for both the N<sub>2</sub>O concentrations and O<sub>3</sub> concentrations. N<sub>2</sub>O concentrations are appeared to be higher with positive pulses for NaY. 5 ppm of O<sub>3</sub> was observed with negative pulses for NaY which is was also the approximate O<sub>3</sub> concentration that was observed in IPC configuration with the negative pulses. Similar to the behaviour of NaY, silica also exhibited higher N<sub>2</sub>O concentrations with positive pulses. O<sub>3</sub> concentrations was observed to be higher with positive pulses for silica.

## 3.4 Effect of pulse rise-time

In this section, the effect of pulse rise-time was studied by using a microsecond pulse source with 0.9- $\mu$ s rise time and 2- $\mu$ s pulse width (referred to as  $\mu$ s pulse) and a nanosecond pulse source with 10-ns rise time and 16-ns pulse width (referred to as ns pulse). So the

---

The contents of this section have been published previously as [9]:

- V.R. Chirumamilla, W.F.L.M. Hoeben, F.J.C.M. Beckers, T. Huiskamp, E.J.M. Van Heesch, and A.J.M. Pemen, "Experimental investigation on the effect of a microsecond pulse and a nanosecond pulse on NO removal using a pulsed DBD with catalytic materials," *Plasma Chemistry and Plasma Processing*, vol.36(2), pp. 487-510, Mar 2016.

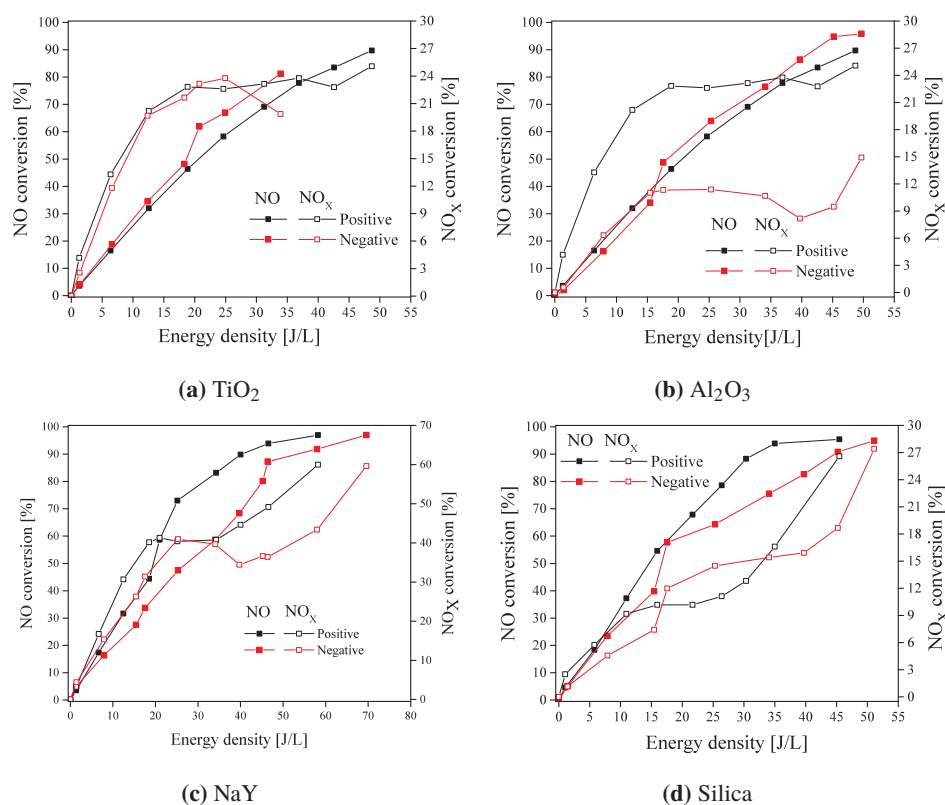


**Figure 3.18** – NO and NO<sub>x</sub> conversion as a function of energy density for the positive polarity pulses and the negative polarity pulses in the PPC configuration for input NO concentration of 200 ppm and gas flow rate of 5 L/min.

rise-times and the pulse-width of the two pulses varied by about 2 orders of magnitude. A pulsed non-thermal DBD reactor is combined with TiO<sub>2</sub>, CuO-MnO<sub>2</sub>-TiO<sub>2</sub>, CuO-MnO<sub>2</sub>-Al<sub>2</sub>O<sub>3</sub> to study the effect of rise-time on the NO removal efficiency, energy efficiency and the by-products formation for plasma-alone, in-plasma (IPC) and post-plasma (PPC) configurations. The characteristics of the catalytic materials are mentioned in Chapter 2. The reactor that has been used in this section is slightly longer than that of the reactor that has been used previously and is explained in the Chapter 2 in the Fig. 2.2b. The microsecond pulse power source that has been used here is as described in the Chapter 2 in the Fig. 2.4 and the schematic overview of the nano-second pulse-power source that has been used in this section can be found in the Fig. 2.6. The typical applied voltage and discharge current and the subsequent energy per pulse and power for the nanosecond source are shown in the Fig. 2.7 and and for the microsecond pulse power source these parameters were shown in the

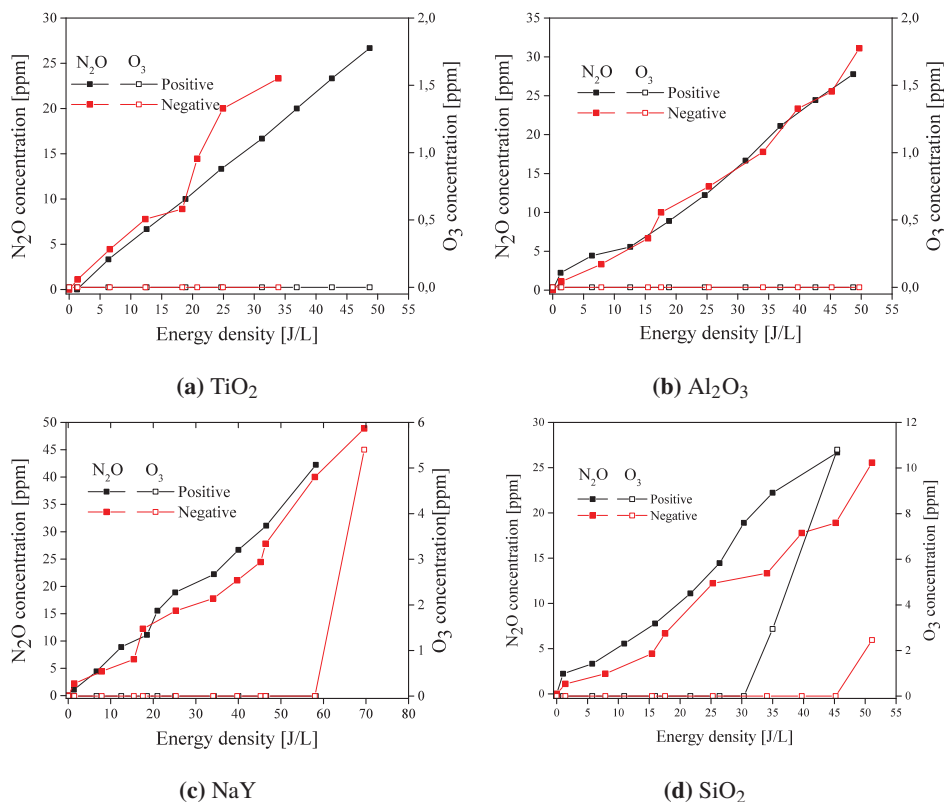


**Figure 3.19** – By-products formation as a function of energy density for the positive polarity pulses and the negative polarity pulses in the PPC configuration for input NO concentration of 200 ppm and gas flow rate of 5 L/min.

Fig. 2.5. The voltage was kept constant (17 kV for the  $\mu$ s pulse source and 40 kV for the ns pulse source) and the pulse repetition rate was used as the operating parameter to vary the energy densities.

### 3.4.1 Plasma-alone configuration

Figure 3.20 shows the effect of the microsecond and nanosecond pulse energization on the NO conversion. It can be seen that for the ns-pulse the NO conversion is near 100% at much lower energy densities as compared to the  $\mu$ s-pulse. An energy density of approximately 60 J/L and 130 J/L were required for 100% NO conversion using the ns and the  $\mu$ s-pulse respectively. This 100% conversion of NO by the ns-pulse at low energy densities is due to the ability of the short rise times to produce high E/N values, where E is the electric field

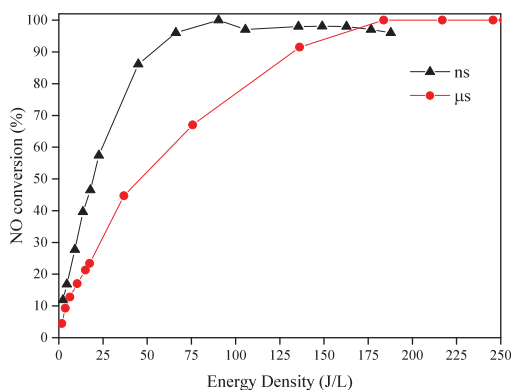


**Figure 3.20** – NO conversion as a function of the energy density with the nanosecond-pulse source and the microsecond-pulse source.

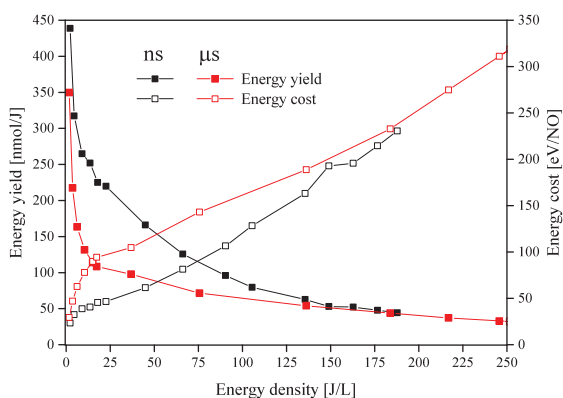


**Figure 3.21** – W-value and G-value as a function of energy density with the nanosecond-pulse source and the microsecond-pulse source.

and  $N$  is the density of the gas in the reactor [82].

The Energy cost W-value (i.e. the energy required to remove one mol of NO) are 90 and 184 eV/NO molecule respectively for the ns-pulse and the  $\mu$ s-pulse and the energy yield G-value (i.e. the amount of NO removed per Joule of energy supplied) are 100 and 200 nmol/J at 25 J/L as seen in Fig. 3.21. The results of Fig. 3.21 also show that with increasing energy density, the W-value increases and keeps increasing even after 100% NO removal while the G-value decreases to a minimum of 50 nmol/J at an energy density of 50 J/L and then remains almost constant. The increase in the W-value even after 100% NO conversion is due to the fact that there is no NO left for further conversion and the energy input to the reactor is used in other reactions such as the production of  $O_3$ ,  $N_2O$  and other unwanted by-products formation. The input energy is also dissipated in the form of light and heat.



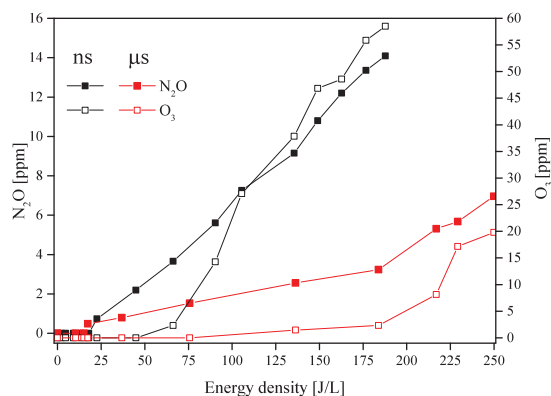


**Figure 3.22** – N<sub>2</sub>O and O<sub>3</sub> formation as a function of the energy density with the nanosecond-pulse source and the microsecond-pulse source.

The effect of the energy density on the by-products formation such as O<sub>3</sub> and N<sub>2</sub>O are studied with respect to the rise time as shown in Fig. 3.22. With increasing energy density, the by-products formation increases with both the  $\mu$ s-pulse and ns-pulse. The production of by-products is more pronounced with the ns-pulse rise time compared to the  $\mu$ s-pulse. It is observed that for 100% NO conversion, approximately 6 ppm and 14 ppm of N<sub>2</sub>O and O<sub>3</sub> is generated respectively for the ns-pulse. Whereas for the  $\mu$ s-pulse, N<sub>2</sub>O and O<sub>3</sub> formation is 3 ppm and 2 ppm respectively. The ns-pulse is efficient in converting 100% NO at low energy densities but at the expense of higher by-products formation. This is due to the possibility of generating the plasma at a much higher voltage with a ns-pulse. This leads to higher energy densities which in turn leads to the production of more O and N atoms consequently producing more O<sub>3</sub> and N<sub>2</sub>O as described in sec. 3.2

### 3.4.2 In-plasma configuration

A pulsed DBD reactor is combined with catalysts such as TiO<sub>2</sub>, CuO-MnO<sub>2</sub>-TiO<sub>2</sub> and CuO-MnO<sub>2</sub>-Al<sub>2</sub>O<sub>3</sub> to study the a possible benefit from combining plasma with catalysts in terms of the NO removal efficiency and its energy efficiency. From Fig. 3.23, NO conversion as a function of the energy density, it can be seen that CuO-MnO<sub>2</sub>-TiO<sub>2</sub> catalyst is capable of removing 100% NO at low energy densities as compared to CuO-MnO<sub>2</sub>-Al<sub>2</sub>O<sub>3</sub> and TiO<sub>2</sub>. The ns-pulse shows better removal efficiency with both the plasma alone configuration and for the IPC. But, as mentioned earlier, higher NO conversion at lower energy densities is at the expense of higher by-products formation which can be observed in the Fig. 3.24.

Figure 3.24a and Fig. 3.24b show the production of N<sub>2</sub>O and O<sub>3</sub> respectively as a function of the energy density. It can be noticed that the by-products formation is reduced with an IPC configuration as compared to the plasma-alone configuration irrespective of the  $\mu$ s-pulse or a ns-pulse input. However, the ns-pulse produces higher amounts of N<sub>2</sub>O and O<sub>3</sub>

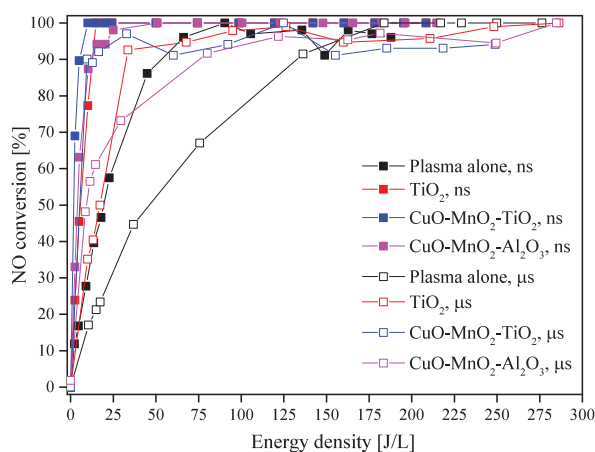
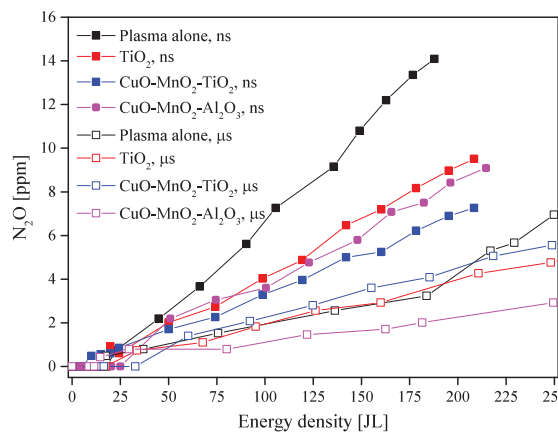


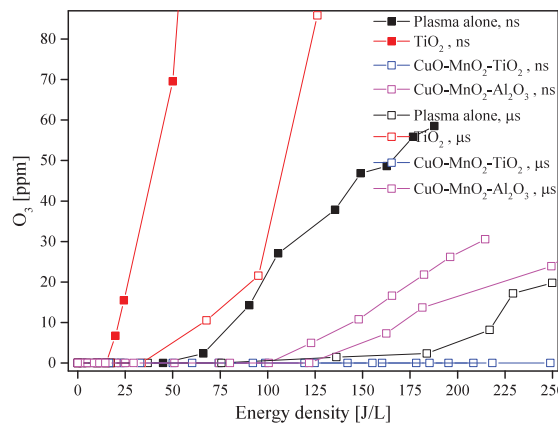
**Figure 3.23** – NO conversion as a function of energy density for various catalysts with in-plasma catalytic configuration with the nanosecond-pulse source and the microsecond-pulse source.

compared to the  $\mu\text{s}$ -pulse. The trend is slightly different for  $\text{TiO}_2$  and  $\text{CuO-MnO}_2\text{-Al}_2\text{O}_3$  as these catalysts produced higher amounts of  $\text{N}_2\text{O}$  and  $\text{O}_3$  with the  $\mu\text{s}$  pulse for 100% NO conversion compared with the ns-pulse. It is also observed that  $\text{TiO}_2$  produced higher amounts of  $\text{O}_3$  compared to the plasma alone configuration,  $\text{CuO-MnO}_2\text{-TiO}_2$ ,  $\text{CuO-MnO}_2\text{-Al}_2\text{O}_3$  catalysts.

The  $\text{MnO}_x$ -based catalysts showed better performance with respect to ozone decomposition as compared to the other materials. This may be due to the in-situ decomposition of ozone into atomic oxygen on the surface, where this atomic oxygen will be present on the  $\text{MnO}_x$  surface in the form of  $\text{O} (^3\text{P})$ . This in turn might oxidize NO to  $\text{NO}_2$  which might be the possible reason for the better performance of the  $\text{MnO}_x$ -based catalysts with respect to ozone decomposition. As mentioned in [83], the better performance of  $\text{CuO-MnO}_2\text{-TiO}_2$  can be attributed to the synergy between the plasma excitation and the photocatalytic behaviour of  $\text{TiO}_2$ . Even though  $\text{MnO}_x$ -based catalysts proved to be efficient in ozone decomposition, it is also observed from the results of this study that  $\text{CuO-MnO}_2\text{-Al}_2\text{O}_3$ , at higher densities failed to decompose ozone. This may be due to the difference in the support materials. With a change in the dielectric constant of the support material, there could be a change in the plasma distribution or plasma discharges or in the adsorption-desorption effects of the molecules. The effect of catalyst support was studied in [84] where the authors investigated the effect of the catalyst support in the degradation of odorous compounds by the plasma and found out that there were differences in the electric behaviour and the space development of the plasma with different supports.



(a) N<sub>2</sub>O formation as a function of energy density for various catalysts with the nanosecond-pulse source and the microsecond-pulse source.



(b) O<sub>3</sub> formation as a function of energy density for various catalysts with the nanosecond-pulse source and the microsecond-pulse source.

**Figure 3.24** – By-products formation as a function of energy density for various catalysts with in-plasma catalytic configuration with the nanosecond-pulse source and the microsecond-pulse source.

### 3.4.3 Post-plasma configuration

The effect of the energy density on the removal efficiency for the PPC configuration is shown in Fig. 3.25. It is observed that, the CuO-MnO<sub>2</sub>-TiO<sub>2</sub> catalyst showed better performance with both the IPC and the PPC configurations with respect to both NO removal efficiency

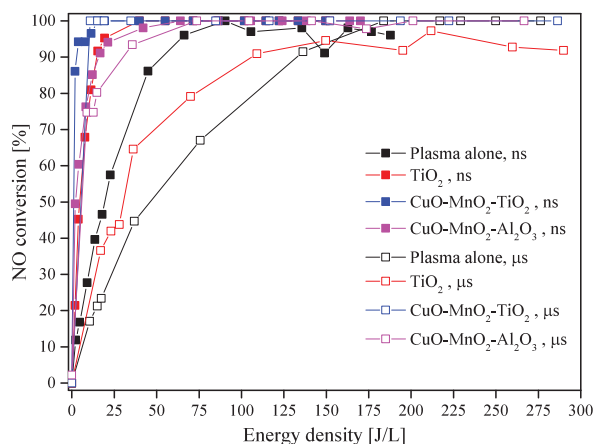
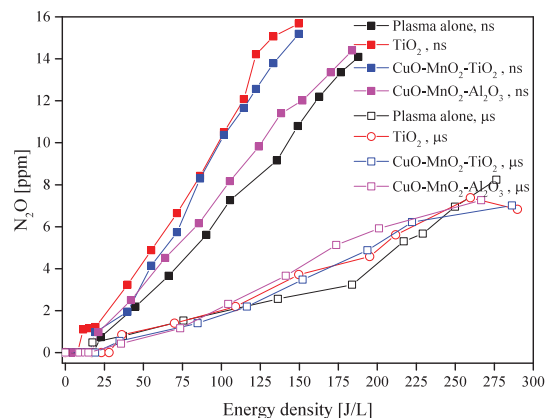


**Figure 3.25** – NO conversion as a function of energy density for various catalysts with post-plasma catalytic configuration with the nanosecond-pulse source and the microsecond-pulse source.

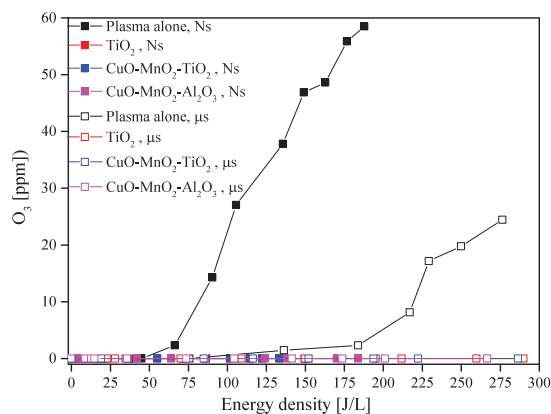
and by-products formation. CuO-MnO<sub>2</sub>-TiO<sub>2</sub> catalyst is capable of removing 100% NO at low energy density with both the  $\mu$ s and the ns pulses compared with CuO-MnO<sub>2</sub>-Al<sub>2</sub>O<sub>3</sub> and TiO<sub>2</sub>. Nanosecond-pulses showed better performance with the PPC configuration with respect to removal efficiency but at the expense of by-products formation which showed the same trend as with the IPC configuration. Figure 3.26a and Fig. 3.26b shows the effect of energy density on by-products formation. Nanosecond-pulse showed higher N<sub>2</sub>O and O<sub>3</sub> formation than the  $\mu$ s-pulse. TiO<sub>2</sub> showed higher amounts of N<sub>2</sub>O formation with the IPC compared to the PPC with both the  $\mu$ s and the ns-pulses whereas CuO-MnO<sub>2</sub>-Al<sub>2</sub>O<sub>3</sub> showed higher N<sub>2</sub>O formation with the PPC with the ns-pulse only. In general, the PPC performed better with both the  $\mu$ s and the ns-pulse with respect to the by-products formation irrespective of the catalysts used.

### 3.5 Summary and conclusions

To obtain efficient remediation of NO<sub>x</sub>, careful optimization of electrical parameters and operational parameters is required. In this chapter we have studied the effect of electrical parameters on the NO and NO<sub>x</sub> removal, and the by-products formation using a pulsed dielectric-barrier-discharge reactor. The electrical parameters that are varied in this study are the applied peak-voltage, pulse polarity and pulse rise-time. To study the effect of the electrical parameters, we have used three plasma reactor configurations: plasma-alone, in-plasma catalytic configuration (IPC) and post-plasma catalytic configuration (PPC). Commonly used support materials such as TiO<sub>2</sub>, Al<sub>2</sub>O<sub>3</sub>, NaY and SiO<sub>2</sub> have been used in both the IPC and the PPC configuration. The main by-products that we have reported here are N<sub>2</sub>O and O<sub>3</sub> although N<sub>2</sub>O<sub>5</sub> was only observed at high energy densities.



(a) N<sub>2</sub>O formation as a function of energy density for various catalysts with the nanosecond-pulse source and the microsecond-pulse source.



(b) O<sub>3</sub> formation as a function of energy density for various catalysts with the nanosecond-pulse source and the microsecond-pulse source.

**Figure 3.26** – By-products formation as a function of energy density for various catalysts with post-plasma catalytic configuration with the nanosecond-pulse source and the microsecond-pulse source.

**Effect of applied peak-voltage** We varied the applied peak-voltage from 15 kV to 19 kV with an interval of 1 kV. It is observed that the conversions and by-products formation depend more on energy density than on applied peak-voltage. The lower applied peak-voltages show better removal efficiency because of low energy density. At low energy densities, the radicals will be more utilized in the remediation reactions and less in radical recombination

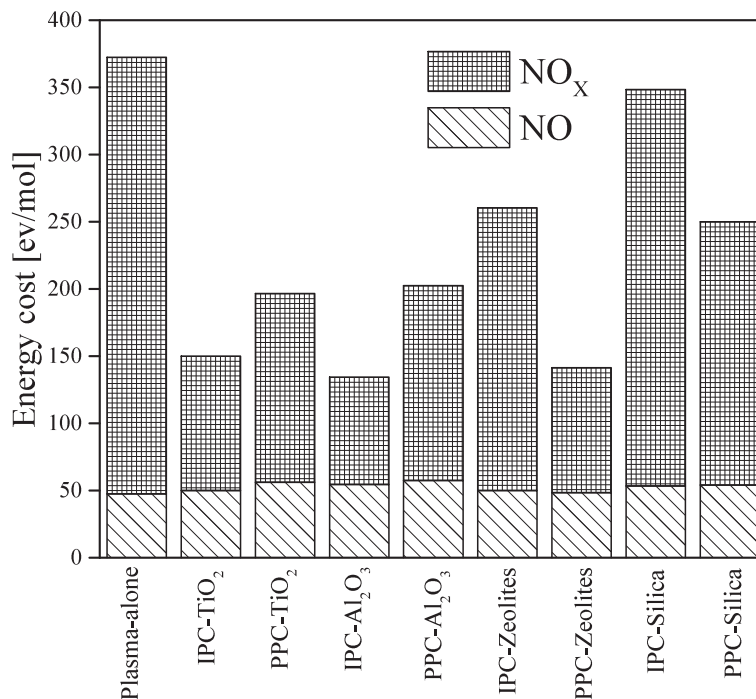


**Figure 3.27** – Comparison of energy costs for NO and NO<sub>x</sub> removal in plasma-alone, In-plasma and post-plasma configurations at the applied peak-voltage of 16 kV and at an energy density of 30 J/L.

reactions. The more the radicals utilized in the remediation reactions, the more efficient the NO<sub>x</sub> removal. Thus, the low applied peak-voltages provide better remediation due to the low energy per pulse deposition thus providing the low plasma energy density. As an applied peak-voltage of 16 kV showed better results with respect to removal efficiency, energy costs and by-products formation, the rest of the experiments were conducted at this peak-voltage unless otherwise mentioned.

By varying the applied peak-voltage, the energy cost and the yield changes considerably. A useful parameter to optimize the energy consumption and removal efficiency in the NTP reactor is the energy cost which is defined as the energy transferred to the plasma per mol of NO or NO<sub>x</sub> removed from the gas stream. An overview of the energy costs for NO and NO<sub>x</sub> removal in the plasma-alone, IPC and the PPC configurations at an applied peak-voltage of 16 kV and energy density of 30 J/L (as more than 80% conversion is obtained for all the three configuration at this energy density) is shown in Fig. 3.27. It can be seen that the energy costs for NO removal remains almost the same for all the three configurations and the energy costs for NO<sub>x</sub> removal varies significantly. Plasma-alone configuration has higher energy costs for NO<sub>x</sub> removal followed by silica in IPC configuration. Al<sub>2</sub>O<sub>3</sub> in IPC configuration showed low energy costs for NO<sub>x</sub> removal followed by NaY in PPC configuration.

Configuration	NO conversion	NO <sub>x</sub> conversion	N <sub>2</sub> O formation	O <sub>3</sub> formation
Plasma-alone	+	-	○	○
IPC-TiO <sub>2</sub>	○	-	○	+
PPC-TiO <sub>2</sub>	○	○	-	○
IPC-Al <sub>2</sub> O <sub>3</sub>	-	-	+	+
PPC-Al <sub>2</sub> O <sub>3</sub>	-	-	○	○
IPC-NaY	-	-	-	-
PPC-NaY	+/-	+/-	+	-
IPC-SiO <sub>2</sub>	+	+	○	-
PPC-SiO <sub>2</sub>	-	+/-	+	+

**Table 3.1** – Performance of negative-pulse polarity as compared to the positive-pulse polarity on NO and NO<sub>x</sub> removal and the by-products formation with all the three configurations. The symbols indicates that the negative-pulse polarity showed increased performance (+), decreased performance (-), no significant effect (○) and may have positive or negative effect (+/-).

**Effect of pulse polarity** From the literature, we studied that different discharge configurations showed different effects on NO and NO<sub>x</sub> removal with positive and negative pulses which triggered us to investigate how this polarity effects the NO<sub>x</sub> removal in our configuration. In summary, the performance of negative-pulse polarity as compared to the positive-pulse polarity on NO and NO<sub>x</sub> removal and the by-products formation with all the three configurations is shown in table 3.1. The symbols in table 3.1 indicates that compared to the positive pulse polarity, the negative pulse polarity showed increased performance (+), decreased performance (-), no significant effect (○) and may have positive or negative effect (+/-).

In general, positive pulses performed better than negative pulses with respect to NO<sub>x</sub> which could be due to increased reactive species production with positive pulses as compared to the negative pulses. The positive pulses also showed better NO<sub>x</sub> conversions for TiO<sub>2</sub>, Al<sub>2</sub>O<sub>3</sub> and NaY with both the IPC and the PPC configurations. There is no significant difference observed in the N<sub>2</sub>O formation for the plasma-alone and the IPC configuration with both the positive and negative pulses whereas the negative pulses showed low O<sub>3</sub> concentrations. This decrease in O<sub>3</sub> concentrations can be attributed to the less streamer volume with negative pulses as compared to the positive pulses. The positive polarity pulses have been chosen for further experiments.

**Effect of pulse rise-time** A  $\mu$ s-pulse with a rise time of 0.9- $\mu$ s and width of 2- $\mu$ s and a ns-pulse source with a rise time of 10-ns and width of 16-ns were used to study the effect of pulse parameters on the NO conversion and the by-products formation. A comparison has been made between different plasma-catalytic configurations such as an in-plasma catalytic configuration and a post-plasma catalytic configuration as shown in table 3.2. Where the symbols in table 3.2 indicates that the specific configuration showed best performance (++) ,

Configuration	NO <sub>x</sub> removal		O <sub>3</sub> concentration [ppm]		N <sub>2</sub> O concentration [ppm]	
	$\mu$ s	ns	$\mu$ s	ns	$\mu$ s	ns
Plasma-alone	o	+	-	-	-	-
IPC-TiO <sub>2</sub>	o	++	-	-	+	-
IPC-CuO-MnO <sub>2</sub> -TiO <sub>2</sub>	-	++	++	++	++	+
IPC-CuO-MnO <sub>2</sub> -Al <sub>2</sub> O <sub>3</sub>	-	+	+	+	+	-
PPC-TiO <sub>2</sub>	+	-	++	++	o	-
PPC-CuO-MnO <sub>2</sub> -TiO <sub>2</sub>	++	+	++	++	+	+
PPC-CuO-MnO <sub>2</sub> -Al <sub>2</sub> O <sub>3</sub>	+	+	+	-	o	-

**Table 3.2** – Comparison between different plasma-catalytic configurations on NO<sub>x</sub> removal and by-products formation with the nanosecond pulse source and the microsecond pulse source at 90% NO conversion. The symbols in the table indicates that the specific configuration showed best performance (++), + (good performance), satisfactory performance (+/-) and poor performance (-).

+ (good performance), satisfactory performance (+/-) and poor performance (-).

With regard to the  $\mu$ s-pulse and ns-pulse energization, we have observed that the ns pulse showed higher conversions but at the expense of higher by-products formation for the given energy density. The high conversions and the increased by-products formation with the ns-pulse energization is possibly due to the plasma generation at much higher voltages as compared to the  $\mu$ s-pulse energization. To conclude, the short duration pulses are efficient for NO conversion but produces more by-products. This by-products formation can be reduced by placing an appropriate catalyst either in the IPC configuration or in the PPC configuration. We have observed that MnO<sub>x</sub>-based catalyst showed reduced O<sub>3</sub> concentrations with both the IPC and the PPC which might be due to the insitu decomposition of ozone into atomic oxygen on the surface of the catalyst.

The optimum electrical parameters that we have observed for our configuration with the given power modulator topologies is to use  $\mu$ s-pulse energization with 16 kV applied peak-voltage with positive polarity pulses. Nevertheless, there is a slight variation in the performance of the system with the catalytic materials in the IPC and the PPC configurations.





---

# INVESTIGATION ON THE EFFECT OF OPERATIONAL PARAMETERS FOR NO<sub>x</sub> REMOVAL

---

## 4.1 Introduction

The efficiency of NO<sub>x</sub> removal depends on both the electrical parameters and operational parameters. By optimizing the electrical parameters, the discharge activity is tuned to obtain optimum removal efficiency. In the previous chapter, we have discussed how electrical parameters (the applied peak-voltage, the pulse-polarity and the rise time of the applied high-voltage pulse) affects the energy efficiency of NO conversion with a pulsed DBD reactor with and with-out catalytic materials.

In this chapter, we analyze the influence of various operational parameters, such as the input NO concentrations, the gas flow-rate, and the gas temperature, on the efficiency of NO<sub>x</sub> removal. We have evaluated the performance of the NO<sub>x</sub> removal process by considering the increase in energy efficiency and the decrease in by-products formation. First, we have studied the effect of operational parameters with the plasma-alone configuration. Next, we also studied two combined plasma/catalytic combinations, namely a IPC and a PPC configuration, and their effect on the efficiency of NO<sub>x</sub> removal and the formation of by-products. The performance of the three configurations is assessed by means of the following two parameters: the energy yield and the energy cost, both as a function of the energy density. The energy yield and energy costs are calculated by equations 2.3 and 2.4 respectively.

Various studies are available to evaluate the performance of NTP systems by means of the parameters energy cost and energy yield, reporting results for various materials under different conditions [85–89]. With change in the reactor conditions, these performance parameters vary considerably. This makes it difficult to compare the efficiency of NO<sub>x</sub> removal

with our reactor configuration with the results from these studies. Thus we have performed a systematic performance evaluation of our DBD reactor, combined with TiO<sub>2</sub>, Al<sub>2</sub>O<sub>3</sub>, NaY and SiO<sub>2</sub> at various operating conditions, while keeping the electrical parameters unchanged. The pulse repetition rate was varied in order to vary the plasma energy density. The detailed characterization of these catalytic materials is presented in Chapter 2. All the experiments in this chapter were performed for 4 times and are reproducible within +/- 5% error margin.

## 4.2 Effect of NO input concentration

In this section, we have studied the effect of NO input concentrations on NO<sub>x</sub> removal by varying the input concentrations from 100 ppm to 300 ppm, for three reactor configurations: a DBD plasma-alone, a IPC configuration and a PPC configurations. The applied-peak voltage was kept constant at 16 kV and positive-polarity pulses have been used. The reason for choosing this voltage and polarity have been discussed in Chapter 3. The pulse repetition rate was varied (from 10 Hz to 600 Hz) to vary the plasma energy density from 0 to 110 J/L, for 5 slm gas flow rate). The gas flow-rate was kept constant at 5 slm and the reactor was operated at ambient conditions.

### 4.2.1 Plasma-alone configuration

The effect of the input NO concentrations on the NO conversion and the formation of by-products is examined here. Figure 4.1 shows the NO conversion as a function of energy density for various input NO concentrations. It can be observed that the NO conversion increased with increasing energy density, irrespective of the input NO concentrations. However, with increasing input concentrations, the conversion is found to decrease significantly. The same trend has also been observed in [73, 89, 90]. At lower input concentrations, complete conversion requires low energy densities, while with increasing input concentrations, the required energy density for complete conversion increases. For an input NO concentration of 300 ppm, we could not obtain 100% conversion.

To study the kinetics, the pollutant concentration is expressed as an exponential function of the energy density applied to the DBD reactor, as shown in Eq. (4.1) and as stated by many researchers [89–93].

$$\frac{[C]}{[C]_0} = e^{-K_E E_d} \quad (4.1)$$

In this equation, C<sub>0</sub> is the input concentration in ppm and C is the output concentration in ppm. The energy constant K<sub>E</sub> is defined as 1/E<sub>0</sub>, where E<sub>0</sub> is the specific applied plasma energy density, and has the unit L/J. The specific energy E<sub>0</sub> (or sometimes referred to as β) [91, 94], is defined as the amount of energy required to remove 63% of the NO.

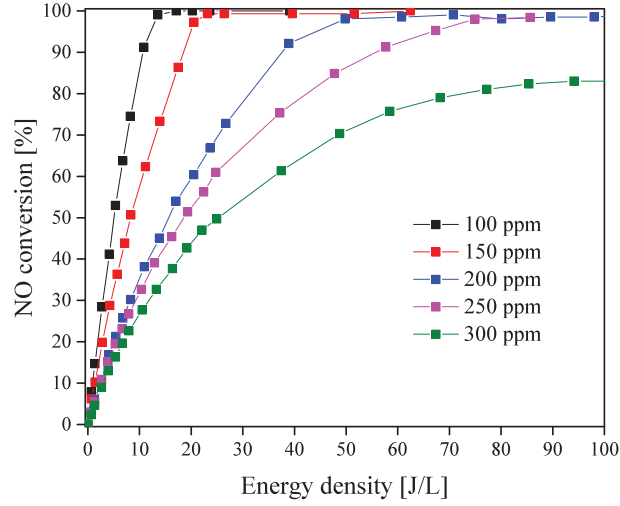


**Figure 4.1** – NO conversion as a function of energy density for various input NO concentrations for the plasma-alone configuration at a gas flow-rate of 5 slm.

The conversion  $X$  is defined as:

$$X = 1 - \frac{C}{C_0} \quad (4.2)$$

By combining equations 4.1 and 4.2, we can write

$$\ln\left(\frac{C}{C_0}\right) = \ln(1 - X) = -K_E E_d \quad (4.3)$$

Thus when we plot a graph for  $\ln(1-X)$  as a function of the energy density, the slope of this graph represents the energy constant.

A graph of  $\ln(1-X)$  as a function of energy density for various concentrations can be seen in Fig. 4.2a. This graph is shown only for the lower energy densities where  $\ln(1-X)$  linearly depends on the energy density. At higher energy densities, the slope is not any more linear and becomes more steep [95]. Interestingly, this linear relationship was observed until the NO conversion was approximately 70% which is in line with the definition of  $K_E$  being a constant of an exponential function. It can be noted that the energy constant values decrease with increasing input concentrations. Which, from our definition means that the energy efficiency of the NO conversion process is higher for low input concentrations. When the energy constant is plotted as a function of the input NO concentration, we can notice that the energy constant decreases exponentially with concentration as seen in Fig. 4.2b. This indicates that more energy is required to remove higher input NO concentrations.

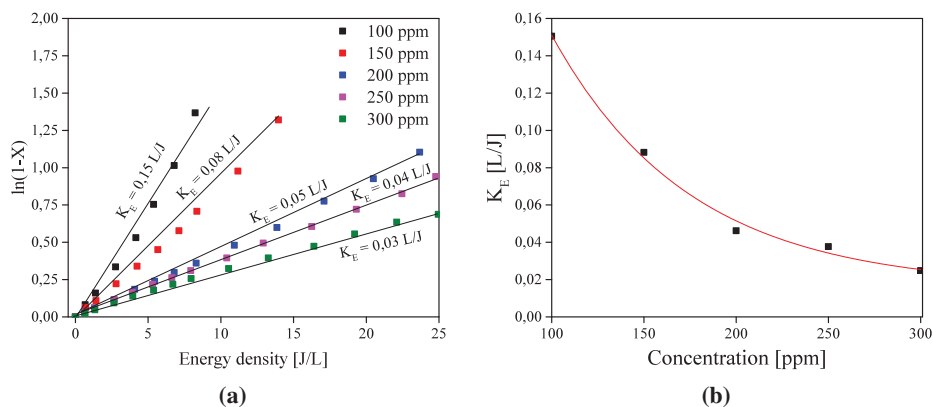


**Figure 4.2** – First order kinetic plot to understand the effect of the input NO concentration on the removal efficiency by calculating the energy constants for plasma-alone configuration.  $K_E$  values obtained from (a) are plotted against concentration in (b) to study the effect of the input concentration on the energy constant for plasma-alone configuration at a gas flow-rate of 5slm and at ambient temperature.

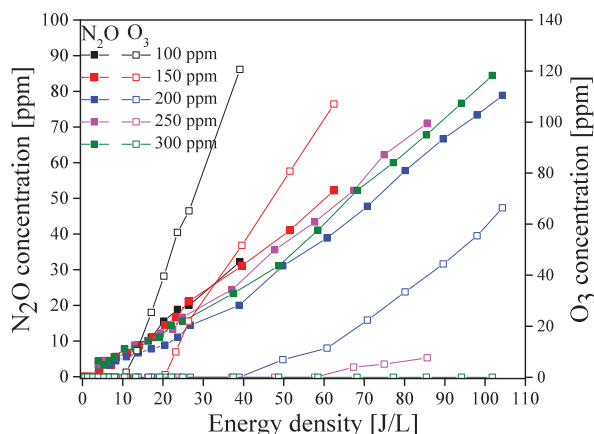


**Figure 4.3** – By-products formation as a function of energy density for various input NO concentrations for the plasma-alone configuration at a gas flow-rate of 5 slm.

The effect of the initial concentration on the by-products formation can be seen in Fig. 4.3. At increasing energy density, both the N<sub>2</sub>O and the O<sub>3</sub> concentration increase as well. At lower energy densities, the NO conversion is lower and thus we have more NO available. In this case, the atomic oxygen will primarily react with NO to form NO<sub>2</sub> rather than forming O<sub>3</sub>. Whereas at higher energy densities, as most of the NO is converted (at least 70%), the amount of NO available to react with atomic oxygen is less and thus

remaining atomic oxygen combine with  $O_2$  to form  $O_3$  as mentioned in the reaction 3.4. At further higher energy densities, the dissociation of  $N_2$  to atomic N also increases resulting in converting  $NO_2$  to  $N_2O$  and releasing further some more atomic oxygen as per reaction 3.7. Also these atomic oxygen will further aid the formation of  $O_3$ , which eventually reacts with  $NO_2$  to form  $N_2O_5$  as per reactions 3.9 and 3.10. Therefore, for the lower NO input concentrations,  $O_3$  formation starts already at lower energy densities as compared to higher input concentrations. Formation of  $O_3$  decreases with increasing input NO concentration. For an input concentration of 300 ppm, no  $O_3$  can be observed for the energy densities applied in these experiments, since complete conversion of NO has not been reached yet. On the other hand,  $N_2O$  concentration keeps increasing linearly with energy density for all the input NO concentrations because of the availability of  $NO_2$ .

#### 4.2.2 In-plasma configuration

In this section, we have studied the effect of input concentration on NO removal by placing catalytic materials inside the plasma reactor; an in-plasma or an IPC configuration. We have packed the DBD reactor with the following catalytic materials:  $TiO_2$ ,  $Al_2O_3$ , zeolites (NaY) and  $SiO_2$ . During the experiments, the energy density has been varied by varying the pulse repetition rate. The other parameters have been kept constant: the gas flow rate and applied peak-voltage were 5 slm and 16 kV respectively.

The effect of input NO concentration as a function of energy density for various input NO concentrations for the various catalytic materials is shown in Fig. 4.4. As already observed in the previous section for the plasma-alone configuration, also for the IPC configuration, the NO conversion decreases with increasing NO input concentrations for all the catalytic materials. Higher NO input concentrations require higher energy densities to obtain complete NO conversion. It also can be observed that with all the catalytic materials, complete conversion for all the input NO concentrations can be achieved. An exception are the results obtained with  $Al_2O_3$  catalyst. In the case of  $Al_2O_3$ , for an input NO concentration of 300 ppm, a maximum NO conversion of 80% could be realized even at high energy density of 90 J/L.

The decrease in the NO concentration and increase in the  $NO_2$  concentration as a function of the energy density for all the catalytic materials can be found in Appendix 7.6 in Fig. A.7.

Observing Fig. 4.4, it can be seen that the NO removal vs energy density graphs for IPC follow an exponential relation and thus the NO removal process follows first order kinetics behaviour for all the catalytic materials. Thus, we can obtain the characteristic energy for the IPC configuration and for all the catalytic materials by plotting the parameter  $\ln(1-X)$  versus the energy density, in the same manner as mentioned in the previous section for the plasma-alone configuration. The graphs of  $\ln(1-X)$  as a function of energy density for various initial NO concentrations and for the various catalytic materials are given in Appendix 7.6 in Fig. A.8. As observed for the plasma-alone configuration, also for the IPC configuration the slopes of these curves are linear at least up to 75% conversion. This shows that the effect of energy density on the characteristic energy is limited and that the characteristic energy is mainly influenced by the NO input concentrations. For all the catalytic materials the slope

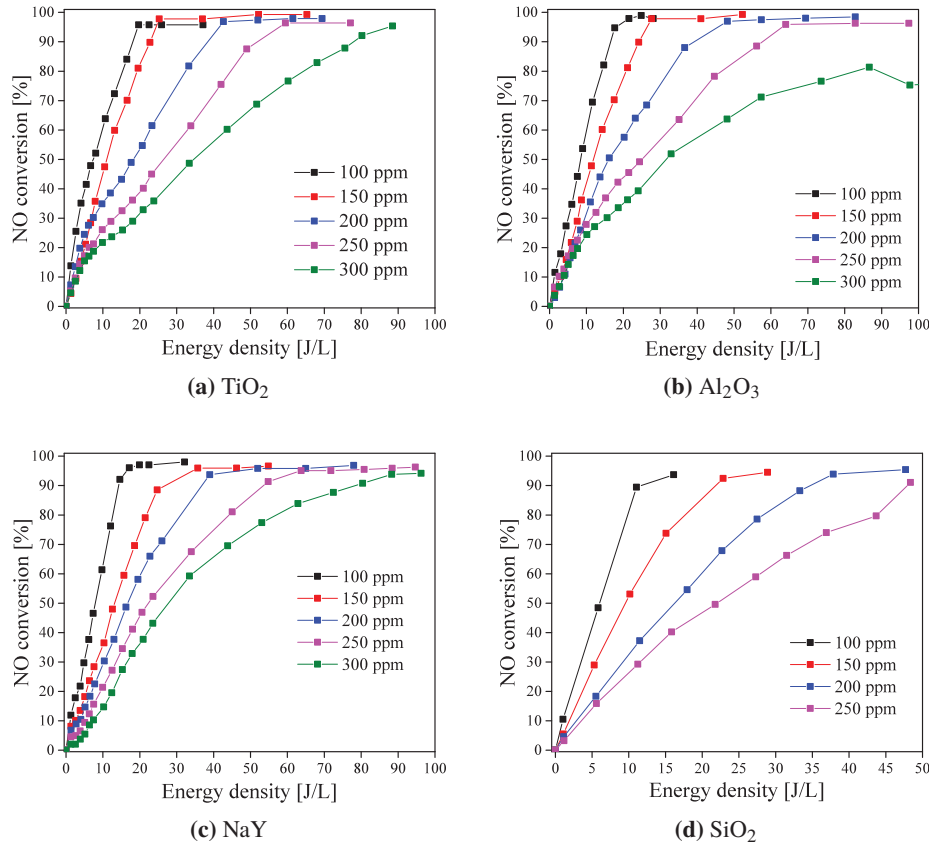


**Figure 4.4** – NO conversion as a function of energy density for various NO input concentrations at a gas flow-rate of 5 slm for an IPC configuration.

becomes steeper at low input concentrations and the slope reduces as the concentration increases.

Figure 4.5 shows a comparison of the effect of the input concentrations on the energy constant for the plasma-alone configuration and for the IPC configuration experiments with all the catalytic materials that we have used in this study. All values of the energy constants are given in table 4.1. It can be seen that the energy constant depends exponentially on the NO input concentration for all the catalytic materials. The plasma-alone configuration shows higher energy constants up to 200 ppm as compared to the IPC configuration. This is because, the plasma-alone configuration is efficient in converting NO to NO<sub>2</sub> at low energy density resulting in complete NO conversions. On the other hand, the IPC configuration needs a bit higher energy density to obtain complete NO conversion as compared to plasma-alone configuration. Hence, we observe that the energy constant values of the IPC configurations

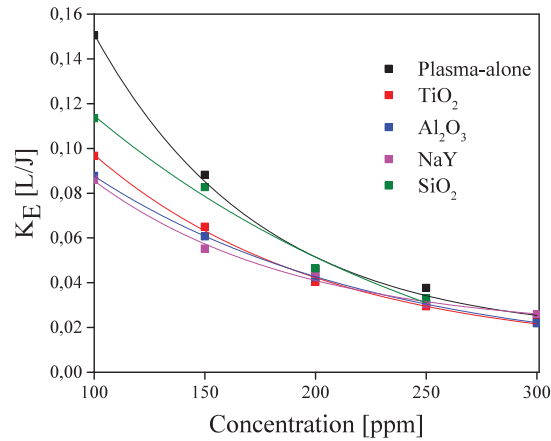


**Figure 4.5** – Comparison of the effect of energy constant on the input concentration for all the catalytic materials that we have used in this study for IPC configuration at a gas flow-rate of 5 slm and at ambient temperature.

are slightly lower than that of plasma-alone configuration at low NO input concentrations. The energy constants significantly depend on the type of the catalytic material, however for higher input concentrations, e.g. at 300 ppm, there is no significant difference in the energy constant values irrespective of the catalysts or the configuration. Plasma-alone and IPC configurations showed approximately the same energy constant values. Which means that even the plasma-alone configuration requires a bit higher energy density to convert NO to NO<sub>2</sub> for high NO input concentrations. Therefore, the performance of the plasma-alone configuration and the IPC configuration is almost the same with respect to NO conversions for high NO input concentrations.

Configuration	NO concentration [ppm]				
	100	150	200	250	300
Plasma-alone	0.15	0.09	0.05	0.04	0.02
TiO <sub>2</sub>	0.01	0.07	0.04	0.03	0.02
Al <sub>2</sub> O <sub>3</sub>	0.09	0.06	0.04	0.023	0.02
NaY	0.09	0.06	0.04	0.03	0.03
SiO <sub>2</sub>	0.11	0.08	0.05	0.03	

**Table 4.1** – Summary of the values of energy constants [L/J] for all the catalytic materials that we have used in this study at various input concentrations.

The other important criteria for performance analysis is the by-product formation. N<sub>2</sub>O and O<sub>3</sub> formation as function of energy density for all the catalytic materials that we have used is shown in the Fig.4.6. With increasing energy density, both the N<sub>2</sub>O and O<sub>3</sub>



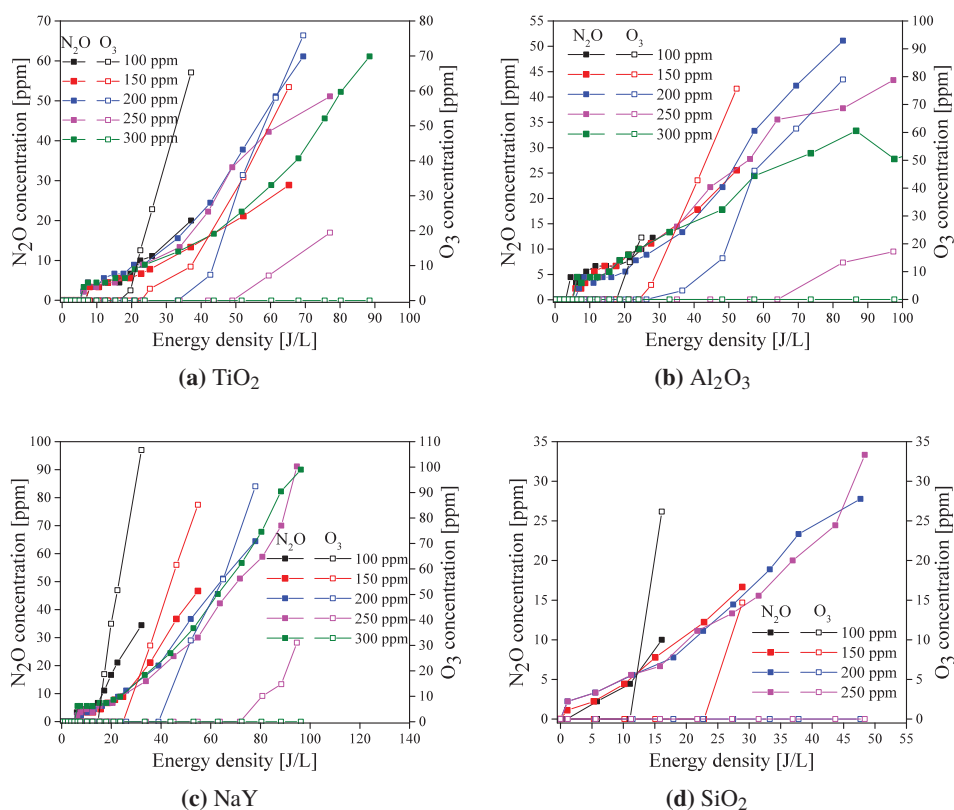


**Figure 4.6** – By-products formation as a function of energy density for various NO input concentrations at a gas flow-rate of 5 slm for IPC configuration.

formation increases. It can be seen that N<sub>2</sub>O concentrations does not significantly depend on the NO input concentration, and mainly depend on energy density. On the other hand, the O<sub>3</sub> formation does strongly depend on both the input concentration as well as on the energy density. This is because, at low input concentration, the NO is completely converted already at low energy density, resulting in excess atomic oxygen that will be utilized for O<sub>3</sub> formation. At high initial NO concentrations, the complete NO conversions requires higher energy densities, leaving less excess atomic oxygen for O<sub>3</sub> formation. That is the reason, O<sub>3</sub> is not observed for 250 and 300 ppm for all the catalysts.

Comparing the results at an energy density of 50 J/L, the highest concentration of N<sub>2</sub>O is observed for the plasma-alone configuration. By order of N<sub>2</sub>O formation at 50 J/L, the order of the performance of the various catalytic materials is as follows: plasma-alone > NaY > SiO<sub>2</sub> > TiO<sub>2</sub> > Al<sub>2</sub>O<sub>3</sub>. In the same manner, the order for O<sub>3</sub> formation is as follows: plasma-alone > NaY > TiO<sub>2</sub> > Al<sub>2</sub>O<sub>3</sub> > SiO<sub>2</sub>.

To summarize, the plasma-alone configuration showed better results for NO removal but at the cost of maximum by-products formation. The by-products formation can be reduced by applying an IPC configuration, but at the cost of higher energy requirements for the NO removal. For the IPC configurations tested, SiO<sub>2</sub> showed better results for both NO conversion and for reducing O<sub>3</sub> formation but produced higher N<sub>2</sub>O concentrations. Al<sub>2</sub>O<sub>3</sub> and TiO<sub>2</sub> showed optimum performance for NO removal with minimum by-products formation.

### 4.2.3 Post-plasma configuration

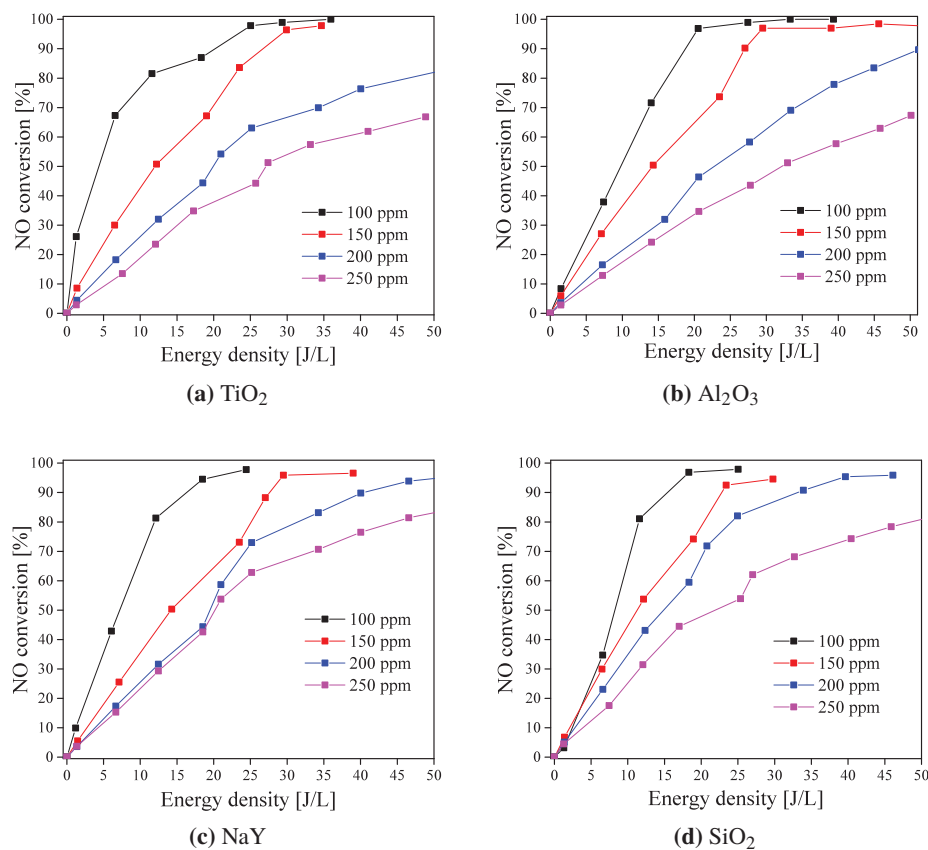
In this section, we have studied the effect of the input concentration on NO removal for a configuration where a catalytic reactor is positioned downstream of the plasma reactor: a so called post-plasma configuration (PPC). We have packed the catalytic reactor with TiO<sub>2</sub>, Al<sub>2</sub>O<sub>3</sub>, zeolites (NaY) and SiO<sub>2</sub>. We have varied the input NO concentrations between 100 ppm and 250 ppm keeping all the other operational parameters constant. Under these conditions, we studied the effect on the NO removal and the formation of by-products as a function of the applied plasma energy density. The energy density was varied by varying the pulse repetition rate.

Figure 4.7 shows the effect of the NO input concentrations on the NO conversion as a function of the energy density. As can be seen, for input concentrations higher than 150 ppm, for none of the catalytic materials complete NO conversion could be achieved, even at high energy densities. The curves of all graphs seems to flatten at high energy densities, indicating that complete NO conversion is apparently not possible with the PPC configurations tested in this work.

Comparing the achieved conversions with the results of the IPC configuration as discussed in the previous section, significant difference can be observed between the performance of TiO<sub>2</sub> and Al<sub>2</sub>O<sub>3</sub> for the PPC configuration as compared to the IPC configuration. For both materials, only 67% of NO conversion was achieved at an energy density of 48 J/L for the PPC configuration, while complete conversion was observed for the IPC configuration at approximately 60 J/L. On the contrary, NaY showed better NO conversion and lower NO<sub>2</sub> concentrations for the PPC configuration as compared to the IPC configuration. Also, SiO<sub>2</sub> showed better conversions up to 200 ppm of input concentration, as compared to the IPC results. But despite the better NO conversion, SiO<sub>2</sub> showed higher NO<sub>2</sub> concentrations which means higher NO<sub>x</sub> concentrations.

The measured NO and NO<sub>2</sub> concentrations as a function of energy density for various NO input concentrations and for all the catalytic materials can be found in Appendix 7.6 in Fig. A.9. In general, the IPC configuration showed better performance with regard to NO conversion as compared to PPC. But on the other hand, the PPC configuration showed lower NO<sub>2</sub> concentrations and in turn lower NO<sub>x</sub> concentrations than with the IPC configuration.

The effect of the input NO concentration on the by-products formation as a function of energy density for TiO<sub>2</sub>, Al<sub>2</sub>O<sub>3</sub>, zeolites (NaY), SiO<sub>2</sub> is shown in Fig. 4.8. In general, less by-products are formed for the PPC configuration as compared to the IPC configuration. At a given energy density, there is not a notable difference in the concentration of N<sub>2</sub>O for various



**Figure 4.7** – NO conversion as a function of energy density for various NO input concentrations at a gas flow-rate of 5 slm for the PPC configuration.

NO input concentrations. N<sub>2</sub>O concentrations mainly depend on the energy density, which is also the case for the IPC configuration. In comparison to the IPC configuration, the O<sub>3</sub> concentrations for the PPC configurations are nearly two times less. In the PPC configuration, the plasma and catalyst are separated from each other and there is no interaction between the plasma and the catalyst. The composition of the gas is modified in the plasma reactor and the outlet gas from the plasma reactor along with long lived species enter the catalytic reactor for further decomposition. From the plasma reactor, as seen in the plasma-alone configuration, we obtain higher NO<sub>2</sub> concentrations but when this gas with high NO<sub>2</sub> concentration is fed to the catalytic reactor in the PPC configuration, we observed less NO<sub>2</sub> concentrations which suggests that adsorption plays an important role in the PPC configuration.

To summarize, higher NO conversions are obtained with the plasma-alone configuration

but at the expense of high  $\text{NO}_x$ ,  $\text{N}_2\text{O}$  and  $\text{O}_3$  concentrations. On the other hand, the PPC configurations show exactly the opposite behaviour. The PPC configuration showed lower  $\text{NO}$  conversions but also less  $\text{NO}_x$ ,  $\text{N}_2\text{O}$  and  $\text{O}_3$  concentrations. The performance of the IPC configuration lies somewhere in between the performance of the plasma-alone and the PPC configurations. The IPC configuration showed higher  $\text{NO}$  conversions with moderate  $\text{NO}_x$ ,  $\text{N}_2\text{O}$  and  $\text{O}_3$  concentrations.

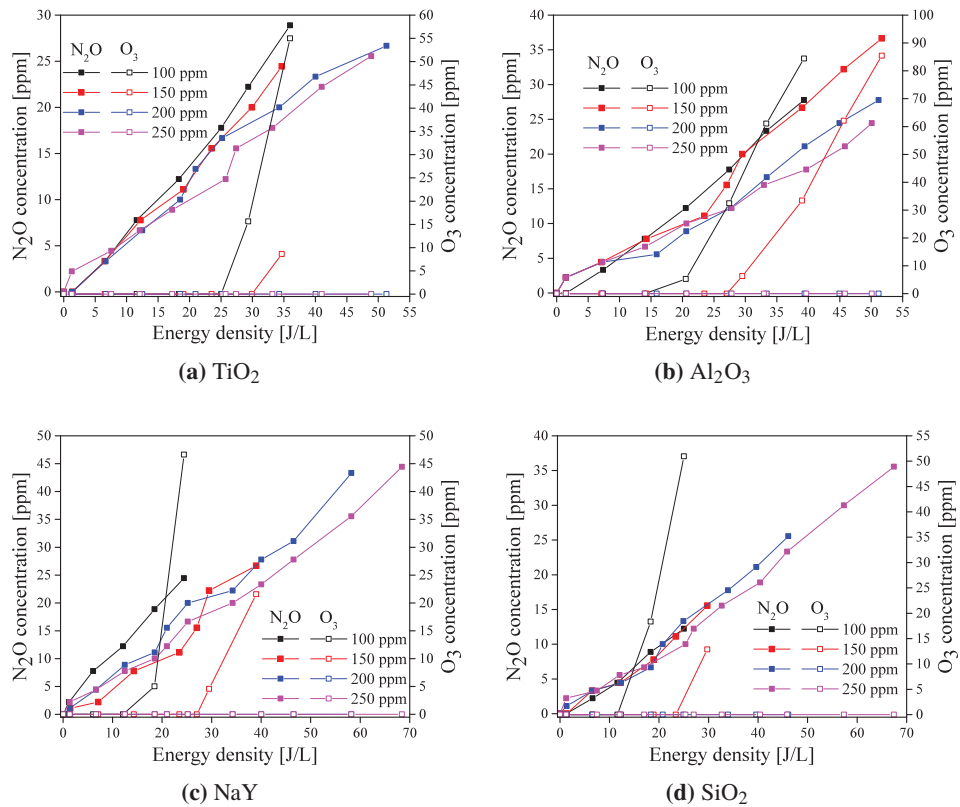


**Figure 4.8** – By-products formation as a function of energy density for various  $\text{NO}$  input concentrations at a gas flow-rate of 5 slm for PPC configuration.

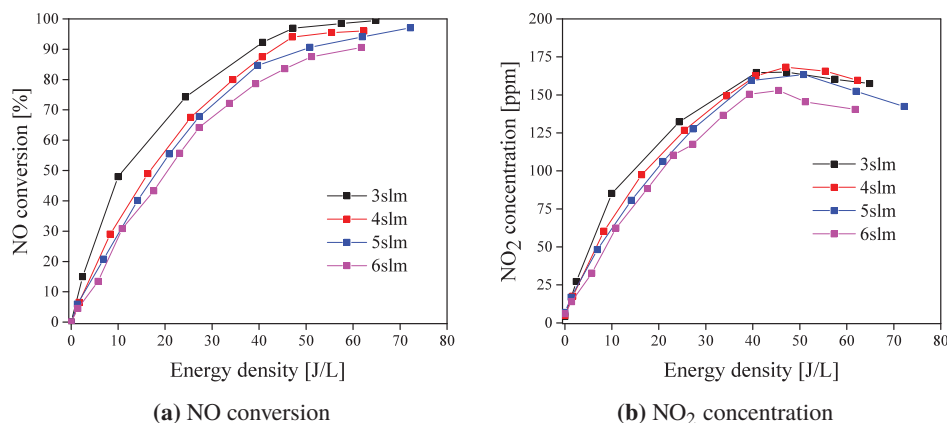
### 4.3 Effect of flow rate

Gas flow rate is an important parameter for the performance of the reactor as it varies the residence time. By varying the residence time, the decomposition rates of various pollutants can vary, which in turn can effect the removal efficiency and by-products formation. In

particular for a catalytic reactor, the pollutant molecule must spend a certain time in the reactor to interact with the catalytic surface and to obtain optimum conversion and lesser by-products formation. In this section, we have studied the effect of gas flow rate on NO<sub>x</sub> removal and by-products formation by varying the gas flow rate from 3 slm to 6 slm for the three configurations: the plasma-alone, a IPC configuration and the PPC configuration. The applied flow rates of 3 slm, 4 slm, 5 slm and 6 slm correspond to the reactor residence times of 0.5 s, 0.375 s, 0.3 s and 0.25 s respectively. All the experiments were done at input NO concentration of 200 ppm.

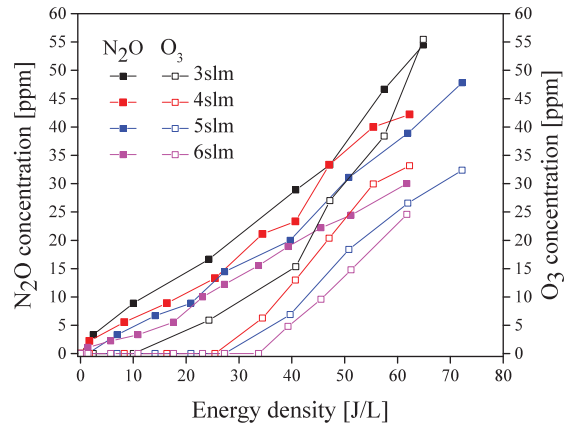
### 4.3.1 Plasma-alone configuration

Figure 4.9 shows the effect of the gas flow rate on the NO conversion and on the NO<sub>2</sub> concentration for gas flow rates of 3 slm, 4 slm, 5 slm and 6 slm, for the plasma-alone configuration, and for an input NO concentration of 200 ppm. It can be observed from Fig. 4.9a that the NO conversion increases with increasing energy density for all the gas flow rates. Also the NO conversion slightly depends on the gas flow rate: at a certain energy density, the NO conversion slightly decreases with increasing the gas flow rate. The same trend was also observed by [26, 96].



**Figure 4.9** – NO conversion and NO<sub>2</sub> concentration as a function of energy density at various flow rates for the input NO concentration of 200 ppm and at ambient temperature for the plasma-alone configuration.

When the gas flow rate increases, the residence time in the reactor decreases. In other words, the time spent by a NO molecule in the reactor decreases. Increasing the residence time increases the probability of collisions between the electrons and the gas molecules will likely result in a higher generation of N and atomic oxygen at a given energy density. With more atomic oxygen and atomic nitrogen, the NO conversion increases according to



**Figure 4.10** – By-products formation as a function of energy density at various flow rates for the input NO concentration of 200 ppm and at ambient temperature for the plasma-alone configuration.

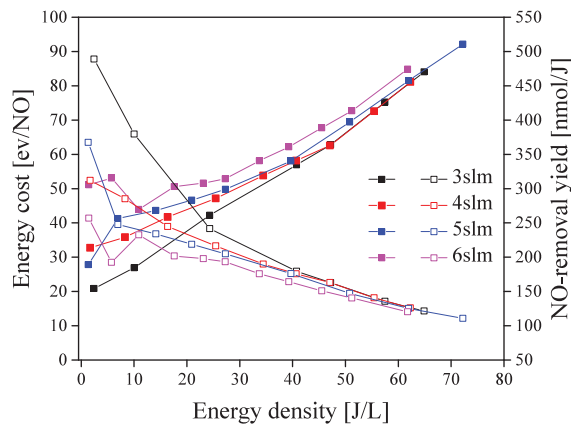


**Figure 4.11** – Energy cost per mol of NO removed and NO-removal yield as a function of energy density at various flow rates for the input NO concentration of 200 ppm and at ambient temperature for the plasma-alone configuration. The closed markers represent energy cost and the open markers represent NO-removal yield.

eq. 3.7. But on the other hand, also the formation of  $N_2O$  and  $O_3$  increases according to equations. 3.8 and 3.9 .

Figure 4.9b shows that lower gas flow rates result in slightly higher  $NO_2$  concentrations. For lower gas flow rates, a bit lower energy density is needed to obtain the same conversion rate as compared to a higher gas flow rate. As the NO is completely converted at low flow rates, the  $NO_2$ ,  $N_2O$  and  $O_3$  concentrations are higher for low gas flow rates.

The by-products formation as a function of energy density for various gas flow rates and for an input NO concentration of 200 ppm is shown in Fig. 4.10. With increasing energy density, the by-products formation increases as well for all the gas flow rates. The formed N<sub>2</sub>O concentration increases nearly linearly with the applied energy density. The formation of O<sub>3</sub> at low energy densities is only observed for lower gas flow rates (3 slm), for other flow rates at least 30 J/L is needed to have some O<sub>3</sub> formation. The concentration of O<sub>3</sub> is higher for lower gas flow rates. So lower gas flow rates result into higher concentrations of N<sub>2</sub>O and O<sub>3</sub>. As mentioned before, this might be due to the increased number of collisions between electrons and N<sub>2</sub> and O<sub>2</sub> molecules resulting in more atomic oxygen and atomic nitrogen which in turn affect the by-products formation. Thus, in summary, though the effects of flow rates are small, we observe that at low gas flow rate results in higher NO conversion and removal yields at lower energy densities but at the expense of increased by-products formation.

When considering the energy cost and the energy yield for NO removal for various gas flow rates, it can be observed from Fig. 4.11 that the energy cost decreases and that the energy yield increases with energy density for all the gas flow rates. With increasing gas flow rate, the energy cost per mol of NO removed increases and the NO removal yield decreases.

#### 4.3.2 In-plasma configuration

The influence of the gas flow rate on the NO conversion and on the by-products formation as a function of energy density is studied in this section by packing the plasma reactor with the following catalytic materials: TiO<sub>2</sub>, Al<sub>2</sub>O<sub>3</sub>, NaY and SiO<sub>2</sub>, such a configuration referred to as an in-plasma configuration (IPC). The effect of gas flow rate on the NO conversion for various flow rates on the NO conversion obtained with the IPC configuration for an input NO concentration of 200 ppm is shown in the Fig. 4.12. It can be observed that the NO conversion depends on the applied plasma energy density and to a much lesser extent on the gas flow rate. At higher energy densities, the NO conversions obtained with all the catalytic materials are almost the same for all the adjusted flow rates. At least up to a flow rate of 5 slm, the effect on the NO conversion is very small for all the catalytic materials, while for flow rates above 5 slm (i.e., at 6 slm), a bit lower NO conversions are observed.

When comparing the NO conversion obtained with the IPC configuration with the results for plasma-alone configuration, a slightly different trend can be observed. The plasma-alone configuration showed higher NO conversion rates at lower flow rates whereas for the IPC configuration, the NO conversion remained almost constant up to 5 slm and above 5 slm, the NO conversion starts to slightly decrease. A similar trend has been observed by [50, 51, 97, 98].

For conventional thermal catalysis, the conversions are strongly affected by the gas residence time whereas in the results on plasma-catalysis as obtained in this section, it is interesting to note that the NO conversion is not influenced significantly by the residence time at a given energy density. This is probably due to the strong dependence of the generation of radicals and atomic species on the applied plasma energy density. The higher the energy density the more generation of radicals and atomic species are generated. These radicals

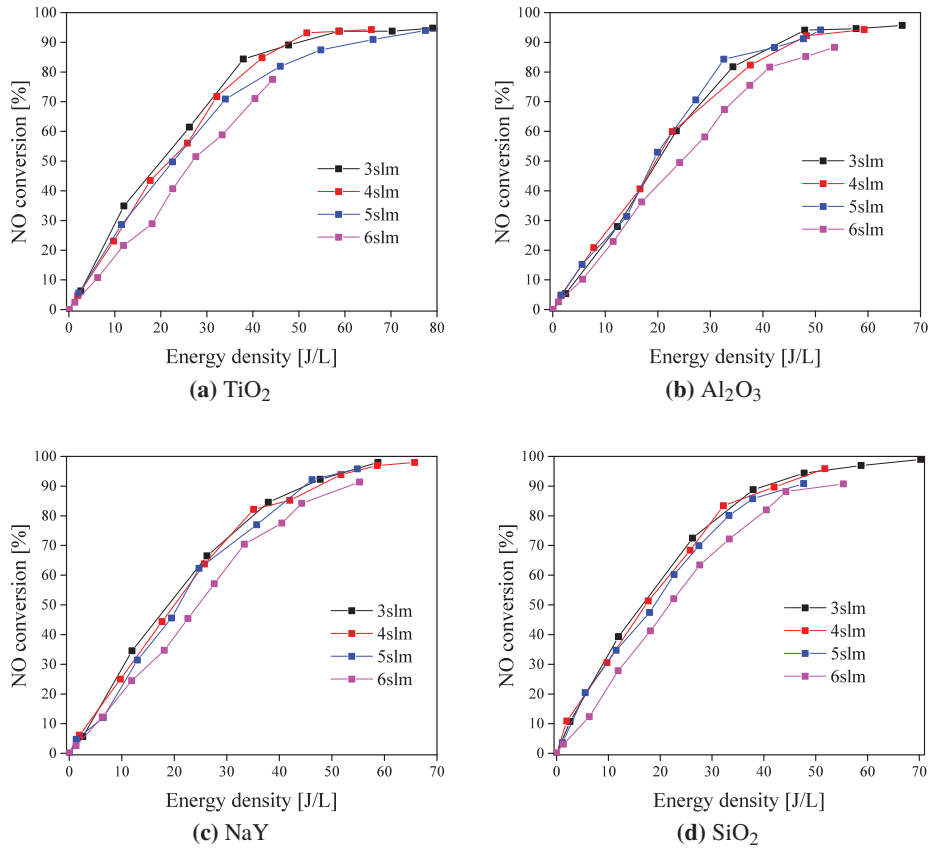


**Figure 4.12** – NO conversion as a function of energy density at various flow rates for the input NO concentration of 200 ppm and at ambient temperature for an in-plasma configuration.

and atomic species have a very short life time and quickly terminate. Consequently, the flow rate is expected not to have a strong effect on the conversion as long as the energy density is kept constant. The decrease of the NO conversion at the higher flow rate of 6 slm could be due to transport limitations of the catalytic reactions as mentioned in [97].

Thus, when we plot the NO conversion at a given energy density as a function of the flow rate as shown in Fig. 4.13, the NO conversion falls is almost constant up to a flow rate of 5 slm, while above 5 slm, the NO conversion drops.

Figure 4.13 summarizes the results of the NO conversion for various flow rates at an energy density of 20 J/L for all the catalytic materials that we have used in this part of the study and for the plasma-alone configuration. It is interesting to see that the NO conversion as a function of flow rate for SiO<sub>2</sub> closely follows the results for the plasma-alone configuration. This probably could be due to comparable energy constant values of SiO<sub>2</sub> with plasma-alone



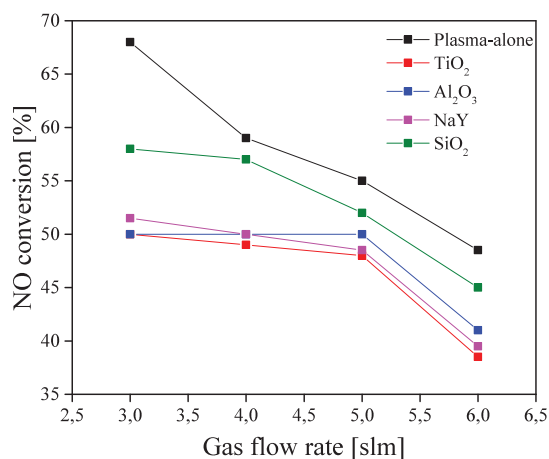


**Figure 4.13** – NO conversion as a function of the residence time for the input NO concentration of 200 ppm, at ambient temperature and at an energy density of 20 J/L for an IPC configuration which is packed with TiO<sub>2</sub>, Al<sub>2</sub>O<sub>3</sub>, NaY and SiO<sub>2</sub>.

configuration as discussed in sec. 4.2.2.

The by-products formation as a function of energy density for various flow rates at an input concentration of 200 ppm for the IPC configuration is shown in Fig. 4.14. The N<sub>2</sub>O and O<sub>3</sub> concentrations show a similar trend as that of the NO conversion as a function of energy density for various flow rates. The N<sub>2</sub>O concentration increases with increasing energy density for all the flow rates. The difference in the N<sub>2</sub>O concentration is less pronounced for flow rates from 3 slm to 5 slm, while at 6 slm, the difference is more pronounced. This could be due to the low NO conversion at 6 slm which is attributed to the transport limitations of the catalytic reactions. Low NO conversion means low NO<sub>2</sub> concentrations which will impact the N<sub>2</sub>O concentrations, since they depend on the NO<sub>2</sub> and on the nitrogen radicals concentrations. The same explanation also holds for the O<sub>3</sub> concentrations as function of energy density for various flow rates.

### 4.3.3 Post-plasma configuration

This section describes the results for a post-plasma configuration (PPC) on the effect of the gas flow rate on the NO conversion and on the by-products formation as a function of energy density for gas flow rates of 3 slm, 4 slm, 5 slm and 6 slm. For this configuration, the catalytic reactor is packed with TiO<sub>2</sub>, Al<sub>2</sub>O<sub>3</sub>, NaY and SiO<sub>2</sub> catalysts. The input NO concentration was maintained at 200 ppm for all the adjusted flow rates. The effect of the gas flow rate on the NO conversion for various flow rates for an input NO concentration of 200 ppm is shown in Fig. 4.15.

In Chapter 3 and in the previous section 4.2, we have seen that with the PPC configuration NO conversion rates can be realized up to maximum of 90% conversion. For the experiments

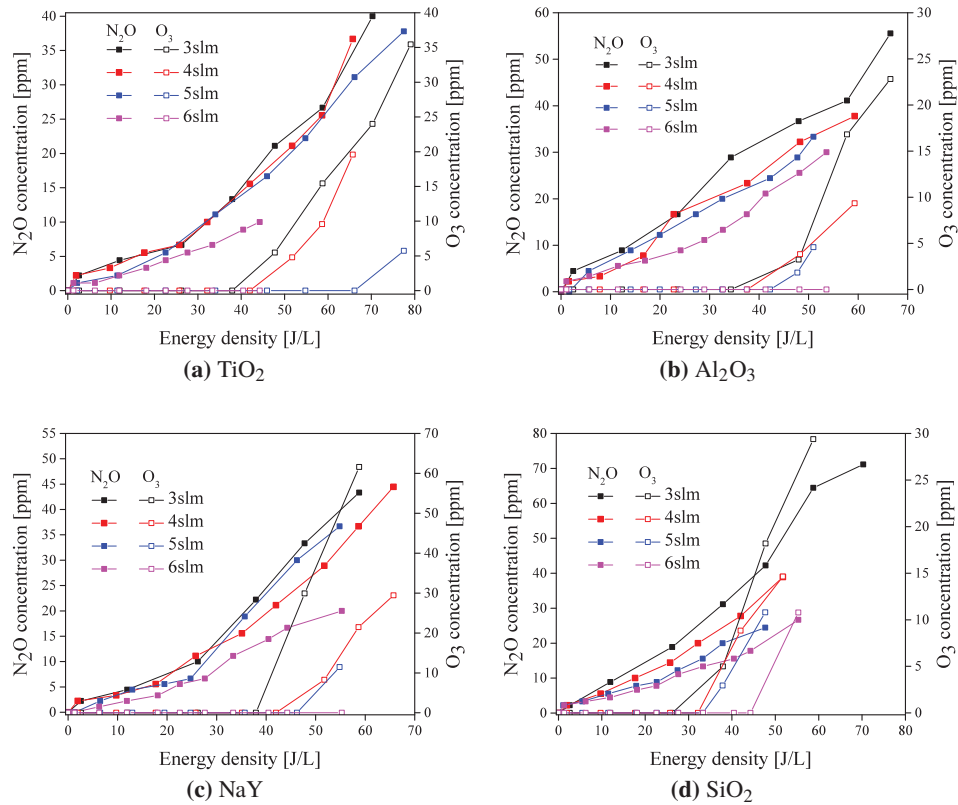


**Figure 4.14** – By-products formation as a function of energy density at various flow rates for the input NO concentration of 200 ppm and at ambient temperature for an in-plasma configuration.

described in this section, conversions obtained at a flow rate below 3 slm are larger than 95% or all the catalytic materials. In conventional catalysis, usually, the conversion rate increases with increasing residence time and thus at lower flow rates. This behaviour can also be observed for the PPC configuration. As mentioned earlier, the NO conversion strongly depends on the plasma energy density. With increasing energy density the NO conversion increases for all the flow rates and for all the catalytic materials.

When comparing the results with the results obtained with the IPC configuration, at higher energy densities the conversions obtained with the IPC configuration were similar for all the catalytic materials and for all the flow rates. However, for the PPC configuration the results are different since NO conversions now do depend on the flow rate. The NO conversion decreases with increasing flow rate for all the catalytic materials. This behaviour is similar to the behaviour of the plasma-alone configuration. The NO conversions obtained

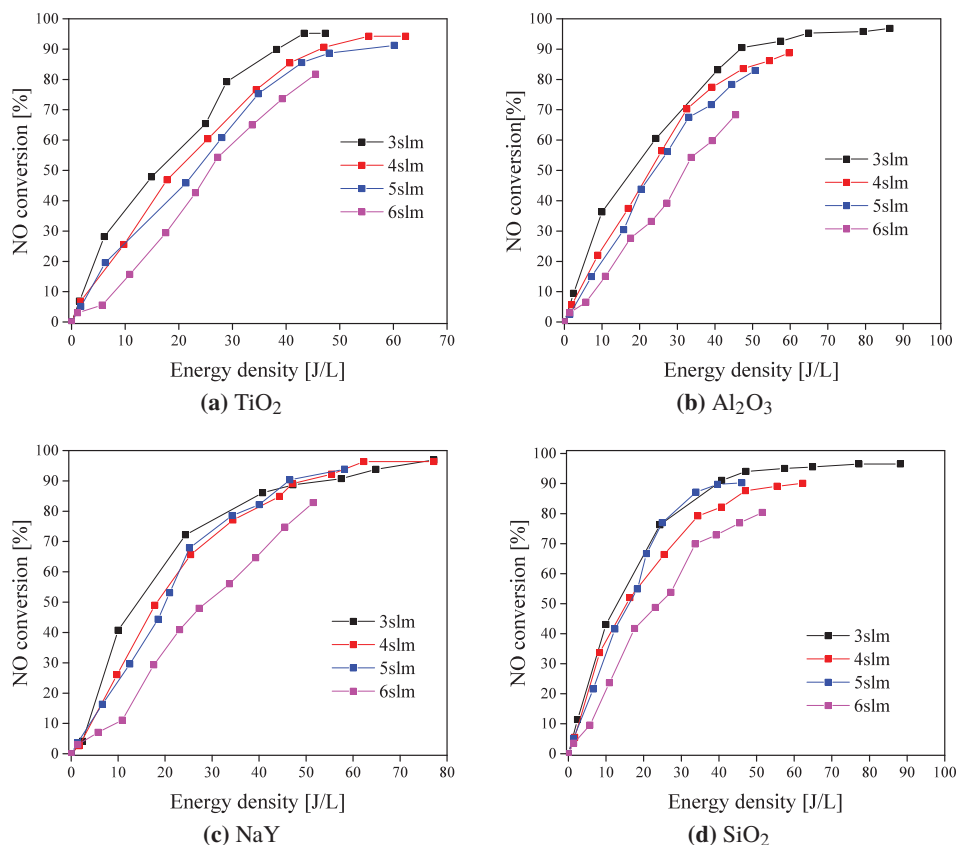


**Figure 4.15** – NO conversion as a function of energy density at various flow rates for the input NO concentration of 200 ppm and at ambient temperature for the post-plasma configuration.

with the PPC configuration at higher energy densities for a flow rate of 6 slm for TiO<sub>2</sub>, Al<sub>2</sub>O<sub>3</sub>, NaY and SiO<sub>2</sub> are 80%, 69%, 83%, and 81% respectively.

The by-products formation as a function of energy density for various flow rates at an input concentration of 200 ppm for the PPC configuration is shown in Fig. 4.16. In general, the PPC configuration showed slightly lower N<sub>2</sub>O concentrations as compared to the IPC configuration at low gas flow rates. The N<sub>2</sub>O and O<sub>3</sub> concentrations increase linearly with energy density for all the flow rates and for all the catalytic materials. The maximum N<sub>2</sub>O concentrations for 3 slm of gas flow rate obtained by TiO<sub>2</sub>, Al<sub>2</sub>O<sub>3</sub>, NaY and SiO<sub>2</sub> were 48 ppm, 67 ppm, 49 ppm and 65 ppm respectively. For the higher flow rate of 6 slm, these concentrations are 20 ppm, 20 ppm, 17 ppm and 36 ppm respectively. With increasing flow rate the N<sub>2</sub>O concentration is observed to decrease for all the catalytic materials.

When looking to the O<sub>3</sub> concentrations, the PPC configuration showed almost no for-

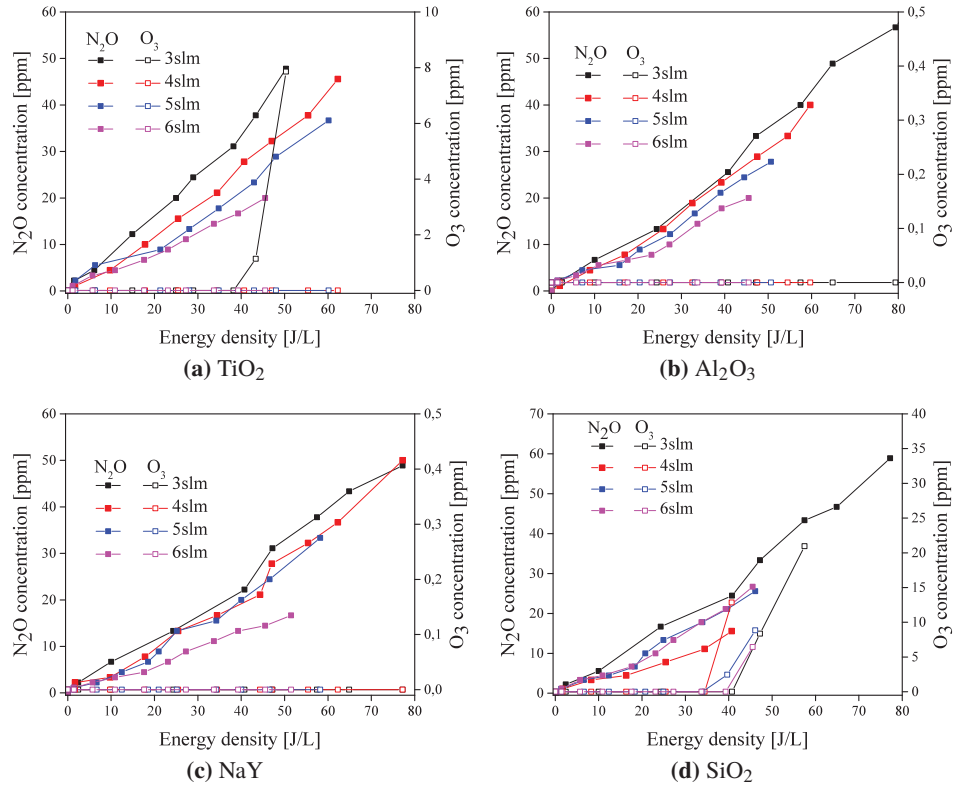


**Figure 4.16** – By-products formation as a function of energy density at various flow rates for the input NO concentration of 200 ppm for the post-plasma configuration.

mation of ozone, except when using the SiO<sub>2</sub> catalyst. Nevertheless, the O<sub>3</sub> concentrations produced with the SiO<sub>2</sub> catalyst in the PPC configuration is less than in the IPC configuration. So, clearly the O<sub>3</sub> formation is almost suppressed by the catalytic materials in the PPC configuration. This can be explained by the fact that the input gas to the PPC configuration is the output gas from the plasma reactor containing concentrations of NO<sub>2</sub>, N<sub>2</sub>O and O<sub>3</sub> along with long lived reactive species and intermediates. Ozone from the plasma reactor entering the catalytic reactor, might get adsorbed on the active site of the catalyst and gets decomposed into oxygen and an active O radical. This active oxygen decomposes into oxygen leaving the active site of the catalyst. The reaction pathways or the plausible mechanisms of O<sub>3</sub> decomposition on a catalytic surface are mentioned in [99, 100].

To summarize, for the PPC configuration, with increasing flow rate, the NO conversion decreases. This behaviour is similar to the behaviour of the plasma-alone configuration. On the contrary, the IPC configuration does not show significant dependence of the NO conversion on the flow rate, for flow rates up to 5 slm. At 6 slm flow rate, lower NO

conversions are observed, probably due to the transport limitation of the catalytic reactions. The higher conversions at lower gas flow rates come at the expense of higher N<sub>2</sub>O and O<sub>3</sub> concentrations. The catalytic materials in the PPC configuration managed to suppress the O<sub>3</sub> formation and thus no O<sub>3</sub> was observed at all the flow rates. By-products formation for the PPC configuration was significantly lower as compared to the IPC and the plasma-alone configuration for all the flow rates.

#### 4.4 Effect of temperature

The performance of the NTP process can be influenced by temperature as it can change the reaction kinetics. It also changes gas density which in turn can effect the local reduced electric field value ( $E/N$ ) [101]. There are very few NTP studies on the effect of temperature on NO<sub>x</sub> removal and by-products formation [89, 102–109]. Harling *et al.* [102] studied the effect of temperature on NO<sub>x</sub> removal and on the destruction of DCM using non-thermal, atmospheric plasma-assisted catalysis using TiO<sub>2</sub> and Al<sub>2</sub>O<sub>3</sub> catalysts. They have observed that the NO<sub>x</sub> generated by the plasma increases with temperature and that adding a catalyst showed a higher destruction of NO<sub>x</sub> with both a single-stage (what we refer here as IPC) as well as a two-stage (referred here as PPC) configuration. Ravi *et al.* [103] studied the temperature effect on hydrocarbon enhanced nitric oxide conversion using a dielectric barrier discharge reactor, using ethylene, acetylene, n-hexane as additives. They have observed that with increasing temperature, the discharge power increases as well and attribute this effect to the increased ionization at higher temperatures. Their results show that adding ethylene and n-hexane results in higher NO removal efficiency and that the temperature has no effect. Whereas when adding acetylene, the performance improves performance only at higher temperature. Wang *et al.* [104] in their study on NO and SO<sub>2</sub> removal using dielectric barrier discharge plasma at different temperatures mentioned that the  $E/N$  increases with increasing temperature and that electronic excitations play an important role in NO removal. They also observed that with increasing in temperature the NO conversion decreases. Kim *et al.* [89] observed that the energy constant value decreases exponentially with increase in temperature. Unfortunately, in most of these references the by-products formation is not discussed.

In this section, we have studied the NO removal and the by-products formation by varying the temperature from 50 °C to 200 °C using both the in-plasma configuration (IPC) and the post-plasma configuration (PPC). Unfortunately, we have not performed the experiments with plasma-alone configuration in this section. We have used the following catalytic materials: TiO<sub>2</sub>, Al<sub>2</sub>O<sub>3</sub> and NaY. The input NO concentration used in this part of the experiments is 200 ppm. The flow rate is maintained constant at 5 slm. The applied-peak voltage was kept constant at 16 kV and positive polarity pulses have been used. The pulse repetition rate was varied to vary the energy density. To study the effect of temperature, the reactor filled with catalytic materials is placed in a temperature-controlled oven which can be heated up to 400 °C. The input gas to the reactor can be preheated up to 200 °C in the gas mixing line before entering the reactor.

#### 4.4.1 In-plasma configuration

In this section, we have studied the effect of temperature on the NO conversion and by-products formation by varying the energy density for the IPC configuration. The plasma reactor is packed with  $\text{TiO}_2$ ,  $\text{Al}_2\text{O}_3$ , and  $\text{NaY}$ . Figure 4.17 shows the effect of temperature on the NO conversion for  $\text{TiO}_2$ ,  $\text{Al}_2\text{O}_3$  and  $\text{NaY}$  at energy density values of 20 J/L, 30 J/L and 40 J/L.

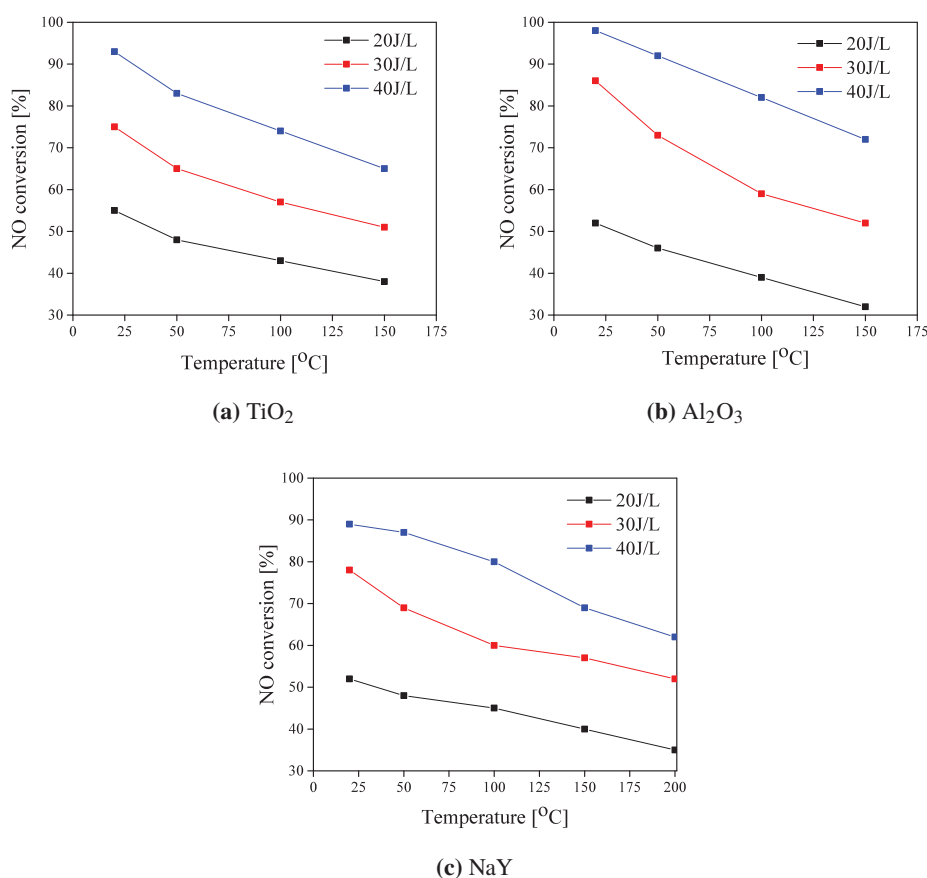
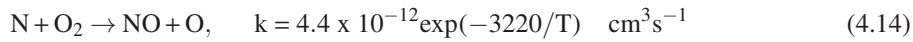
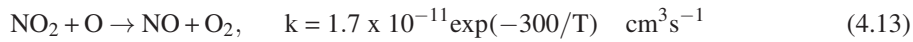
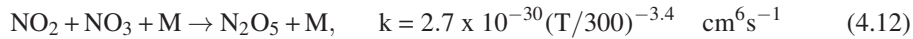
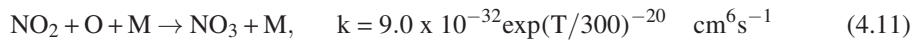
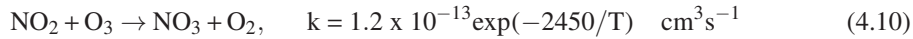
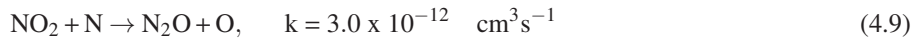
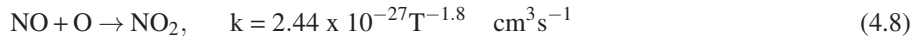
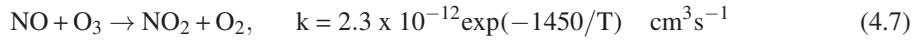
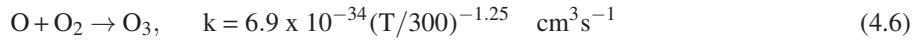
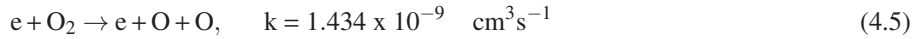
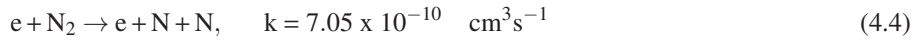


**Figure 4.17** – NO conversion as a function of temperature at various energy densities for the input NO concentration of 200 ppm and gas flow rate of 5 slm for the in-plasma configuration.

It can be observed that, at 20 J/L, using  $\text{TiO}_2$  showed a slightly higher NO conversion as compared to  $\text{Al}_2\text{O}_3$  and  $\text{NaY}$ . While at 40 J/L, using  $\text{Al}_2\text{O}_3$  performed better than  $\text{TiO}_2$  and  $\text{NaY}$ . This difference between the various catalytic materials can also be observed in Fig. 4.18 where the energy constant is plotted as a function of temperature for  $\text{TiO}_2$ ,  $\text{Al}_2\text{O}_3$  and  $\text{NaY}$ .

The strong temperature dependence when using TiO<sub>2</sub> might be due to the creation of more oxidative sites on the TiO<sub>2</sub> surface when exposed to plasma [110]. With more oxidative sites, the back formation of NO might have been facilitated through reactions 4.13 and 4.14. The better performance of Al<sub>2</sub>O<sub>3</sub> as compared to TiO<sub>2</sub> and NaY at higher temperatures could be due to the limitation in the back-reduction of NO<sub>2</sub> to NO on the surface of Al<sub>2</sub>O<sub>3</sub> as mentioned in [111].

We restate here the reactions mentioned in Chapter 3 along with their rate constants. In addition with reactions we consider, these reactions (reactions 4.8, 4.10, 4.13, 4.14) are important to understand the effect of temperature on NO conversion and by-products formation. All the reactions that we consider here are obtained from [112–115]. From Fig. 4.17 it can be seen that at all the energy densities, the NO conversion decreases with increasing temperature for all the catalytic materials. A similar trend has been observed by [104, 105]. NO is oxidized to NO<sub>2</sub> mainly through reactions 4.7 and 4.8. At higher temperatures, ozone is decomposed easily to oxygen and atomic oxygen through reaction 4.6. Thus apparently, reaction 4.7 is not important at higher temperatures. With increasing temperature, the rate of reaction 4.8 decreases and thus less NO conversions are observed. The effect of temperature depends on the nature of the pollutant, eventual additives and the catalysts used.



N<sub>2</sub>O concentration as a function of energy density for various temperatures at an input NO concentration of 200 ppm at a gas flow rate of 5 slm is shown in Fig. 4.19. The N<sub>2</sub>O concentration increases with increasing energy density for all the temperatures considered

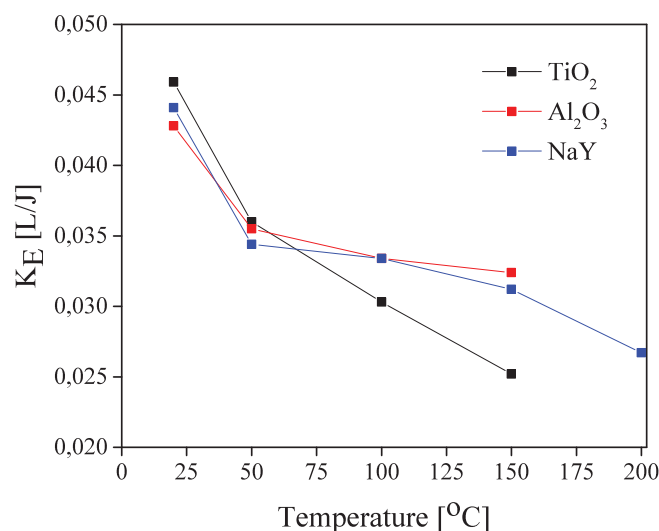


**Figure 4.18** – Comparison of the energy constant value as a function of temperature for TiO<sub>2</sub>, Al<sub>2</sub>O<sub>3</sub>, and NaY in the IPC configuration for an input NO concentration of 200 ppm at a gas flow rate of 5 slm.

here. As already observed in this section, the NO conversion decreases with increasing temperature. The same trend is noticed for the N<sub>2</sub>O formation. Despite of the back formation of NO at higher temperatures, NO<sub>2</sub> concentration increases with increase in temperature due to the higher reaction rate constants of reaction 4.5 as compared to the rate of reaction 4.4. Also the higher dissociation of O<sub>3</sub> at higher temperatures through reaction 4.6 will play a role. Thus, we expect at higher temperatures that most of the energy is used for producing more atomic oxygen than atomic nitrogen which leads to higher NO<sub>2</sub> concentrations and lower N<sub>2</sub>O concentrations at higher temperatures. Thus, we observe lower N<sub>2</sub>O concentrations with increase in temperature. As mentioned earlier, we have not considered ions in our reaction pathways although NO<sup>+</sup>, H<sub>3</sub>O<sup>+</sup> ions are major ions in air plasmas because the ion densities are relatively small and are not chemically active in the NO<sub>x</sub> removal process [74].

When comparing the catalytic materials, TiO<sub>2</sub> produces lower N<sub>2</sub>O concentrations as compared to Al<sub>2</sub>O<sub>3</sub> and NaY at all temperatures. This probably could be due to the lower NO conversion and thus comparatively less NO<sub>2</sub> is available to get consumed by reaction 4.9 to produce N<sub>2</sub>O. The lower NO conversion with TiO<sub>2</sub> is due to the increase in the oxidative sites when the TiO<sub>2</sub> is exposed to the plasma, thus facilitating the back formation of NO through reactions 4.13 and 4.14 as mentioned earlier. As the ozone decomposition increases with increasing temperature, we have not observed any ozone formation for the temperatures between 50 °C to 200 °C.



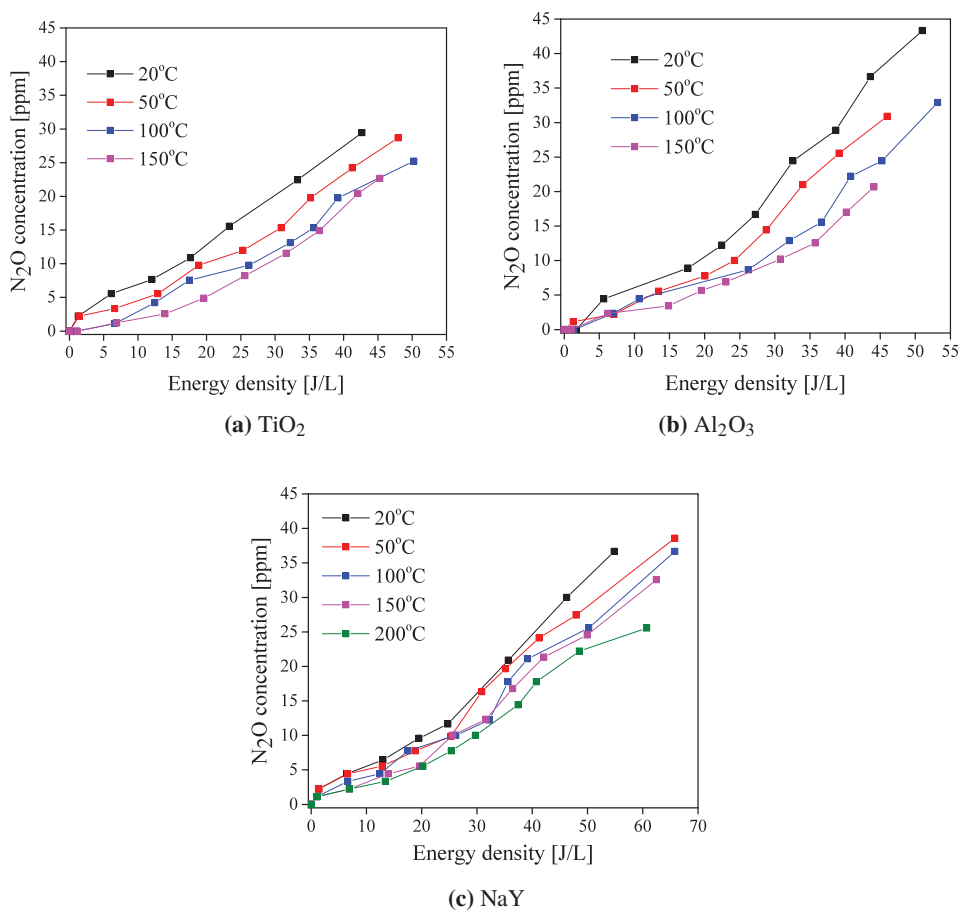


**Figure 4.19** – N<sub>2</sub>O concentration as a function of energy density for various temperatures for the input NO concentration of 200 ppm at gas flow rate of 5 slm for the in-plasma configuration.

#### 4.4.2 Post-plasma configuration

We have studied the effect of temperature on the NO conversion and by-products formation by varying the plasma energy density. The catalytic reactor is packed with TiO<sub>2</sub>, Al<sub>2</sub>O<sub>3</sub>, and NaY and is positioned downstream to the plasma reactor in a post-plasma configuration (PPC) arrangement. To study the effect of temperature, this catalytic reactor downstream to the plasma reactor is placed in a temperature-controlled oven which can be heated up to 400 °C. In this configuration, only the catalytic reactor was heated up to the desired temperature, the plasma reactor remained at room temperature.

Fig. 4.20 shows the effect of temperature on the NO conversion for TiO<sub>2</sub>, Al<sub>2</sub>O<sub>3</sub> and NaY

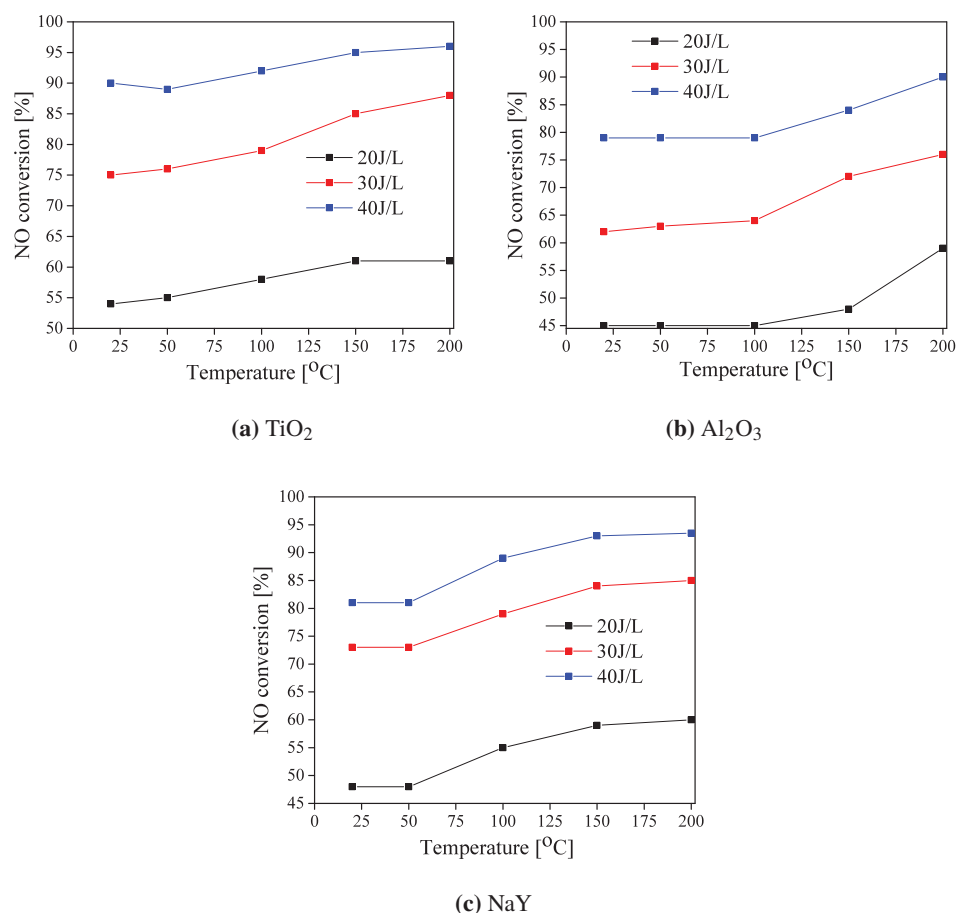


**Figure 4.20** – NO conversion as a function of temperature at various energy densities for the input NO concentration of 200 ppm and gas flow rate of 5 slm for the post-plasma configuration.

at energy density values of 20 J/L, 30 J/L and 40 J/L. It is observed that the NO conversion remains almost constant up to 50 °C for TiO<sub>2</sub> and NaY and up to 100 °C for Al<sub>2</sub>O<sub>3</sub> at all the energy densities. TiO<sub>2</sub> performed better at the energy densities of 30 J/L and 40 J/L at all temperatures while NaY performed better at low energy density of 20 J/L. For all the catalytic materials, the maximum NO conversions are at 40 J/L and at 200 °C. The maximum conversion achieved by TiO<sub>2</sub>, Al<sub>2</sub>O<sub>3</sub> and NaY are 96%, 90% and 94% respectively.

Figure 4.20 shows that the NO conversion is a function of both the plasma energy density and the temperature. With increase in temperature, the NO conversion increases. This is opposite to what has been observed for the IPC configuration in the previous section. For the IPC configuration, NO conversion decreased with increase in temperature whereas in

the PPC configuration the NO conversion remained constant up to a certain temperature depending on the material and starts to increase for higher temperatures. This behaviour is similar to the behaviour of the conventional selective catalytic reduction process of NO in dry conditions with additives [116–119].

Typically, all the catalytic materials showed distinct behaviour from 150 °C on which suggests that the catalytic material is activated thermally from this temperature. It is not clear from the available measurement data that if this increase in NO conversion further increases with increase in temperature at even higher temperatures beyond 200 °C. Nevertheless, the tendency of NO conversion is similar to that of the thermal catalysis. Also a similar temperature dependence has been observed for toluene and benzene destruction using NTP and catalysts [102, 120].

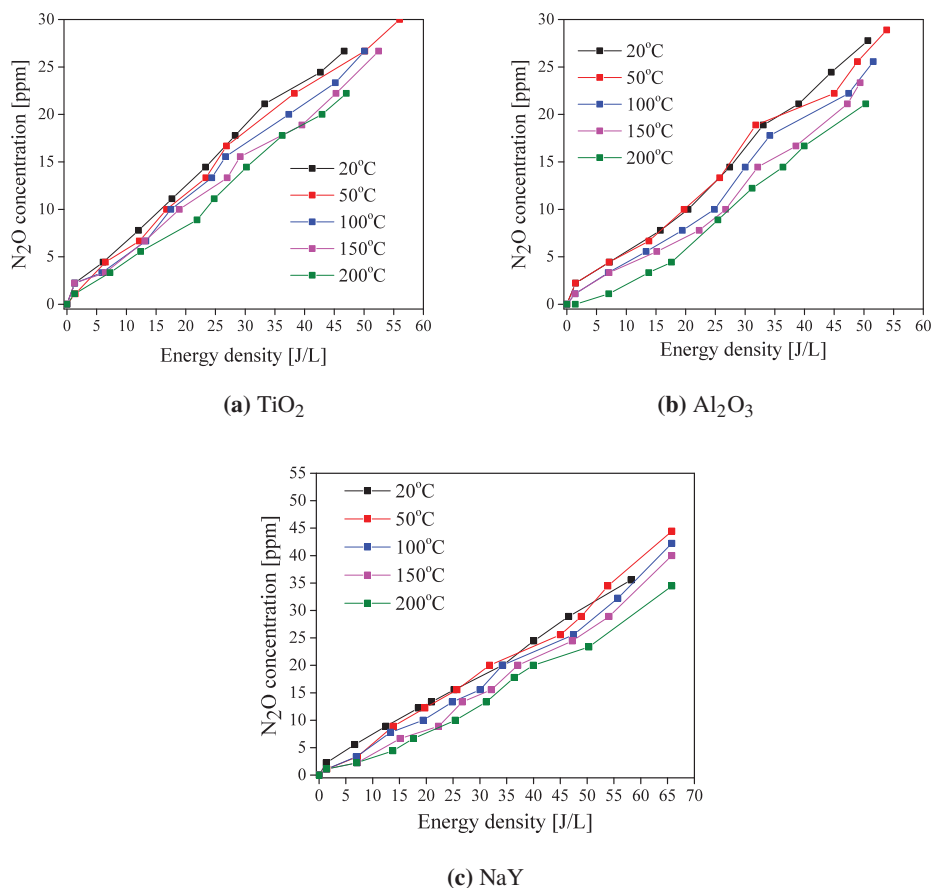


**Figure 4.21** – N<sub>2</sub>O concentration as a function of energy density for various temperatures for the input NO concentration of 200 ppm at gas flow rate of 5 slm for the post-plasma configuration.

We have studied the effect of temperature on  $N_2O$  concentration as a function of energy density for the PPC configuration. In the previous sections we have observed that the PPC configuration produced little or no ozone. At higher temperatures  $O_3$  gets easily dissociated to  $O_2$  and atomic oxygen. Thus, also in this section, no  $O_3$  formation occurred at all the temperatures. The  $N_2O$  concentration as a function of energy density for various temperatures is shown in Fig. 4.21. It can be observed that the  $N_2O$  concentration for  $TiO_2$ ,  $Al_2O_3$  and NaY increases with increase in the energy density for all the temperatures that we have used in this part of the study. At low energy densities, no significant change is observed in the  $N_2O$  concentration for  $TiO_2$ ,  $Al_2O_3$  and NaY for all the temperatures. NaY showed higher  $N_2O$  concentrations as compared to  $TiO_2$  and  $Al_2O_3$ . This might be due to the higher plasma energy density required by NaY to obtain maximum conversion. High energy densities leads to high  $N_2O$  concentrations because of the increased atomic nitrogen formation. Although the  $N_2O$  concentrations does not show a strong dependence of temperature in the PPC configuration, it can be observed that an increasing temperature leads to a slight reduction of the  $N_2O$  concentrations for  $TiO_2$ ,  $Al_2O_3$  and NaY. Therefore the PPC configuration performed better as compared to the IPC configuration showing high NO conversion and less by-products formation at higher temperatures.

## 4.5 Summary and conclusions

In this chapter, we have investigated the effect of operational parameters on  $NO_x$  removal using plasma-alone, in-plasma (IPC) and post-plasma (PPC) configurations. The operational parameters that we have studied here are the input NO concentration, flow rate and temperature. We have used the following catalytic materials:  $TiO_2$ ,  $Al_2O_3$ , NaY and  $SiO_2$  both in a IPC and a PPC configuration for all the parameters except in the study on the effect of temperature where we have not performed the experiments with plasma-alone configuration and also we have not used  $SiO_2$  in both the IPC and the PPC configuration.

A summary of the effect of these parameters on the NO conversion and on the by-products formations is shown in the table 4.2. The '+'-symbol indicates a better performance (higher NO conversion and lower by-products formation) with an increase of the stated parameter, while the symbol '-'-indicates that the reactor configuration performs worse with an increase of the stated parameter, the symbol '+/-'-indicates that the performance may either increase or decrease and finally a 'o'-indicates that the system does not show any significant dependence on the parameter.

**Effect of NO input concentration** With increase in the input NO concentration all the three configurations showed lower NO conversion but on the other hand the by-products formation was lowered. Higher NO conversions are obtained with plasma-alone configuration but at the expense of high  $NO_x$ ,  $N_2O$  and  $O_3$  concentrations, while on the other hand the PPC configuration showed the opposite trend. The PPC configuration showed lower NO conversions but also less  $NO_x$ ,  $N_2O$  and  $O_3$  concentrations. The performance of the IPC configuration lies somewhere in between the plasma-alone and the PPC configurations.

	Plasma-alone			In-plasma			Post-plasma		
	NO	N <sub>2</sub> O	O <sub>3</sub>	NO	N <sub>2</sub> O	O <sub>3</sub>	NO	N <sub>2</sub> O	O <sub>3</sub>
Concentration	-	+/-	+	-	+	+	-	+	+
Flow rate	+/-	+	+	+/-	+	+	-	+	+
Temperature				-	+	+	+	○	+

**Table 4.2** – A summary of the effect of the operational parameters on NO conversion and by-products formation. The symbols indicate that the reactor configuration performs better (+), worse (-), may either increase or decrease (+/-) and does not show any significant dependence (○) with an increase of the stated parameter.

The IPC configuration showed higher NO conversions with moderate NO<sub>x</sub>, N<sub>2</sub>O and O<sub>3</sub> concentrations.

**Effect of flow rate** With increasing flow rate, the NO conversion decrease for the plasma-alone and for the PPC configuration. The IPC configuration does not show significant dependence of the NO conversion with flow rate up to a 5 slm, while at 6 slm, lower NO conversions are observed. This probably could be due to transport limitations of the catalytic reactions. The higher conversions at lower gas flow rates comes with the expense of higher N<sub>2</sub>O and O<sub>3</sub> concentrations. The catalytic materials in the PPC configuration managed to suppress the O<sub>3</sub> formation and thus no O<sub>3</sub> was observed at all the flow rates. Lower by-products formation was observed for the PPC configuration as compared to the IPC and the plasma-alone configuration for all the flow rates.

**Effect of temperature** With increasing temperature, the NO conversion decreases for the IPC configuration whereas the PPC configuration showed increasing NO conversions with increasing temperatures. No ozone was observed for the PPC configuration, while for the IPC configuration, above 50 °C no ozone formation has been observed. In both the configurations, N<sub>2</sub>O concentrations slightly decreased with increasing temperature. Thus both the configurations performed better in terms of minimum by-products formation at higher temperatures. The PPC configuration showed the best performance results with respect to both NO conversion and N<sub>2</sub>O concentration at higher temperatures.

---

## SCREENING OF CATALYTIC MATERIALS FOR NO<sub>x</sub> REMOVAL

---

### 5.1 Introduction

In plasma-catalysis, the important task is to choose an appropriate catalyst. Choosing a proper catalyst in the case of a PPC configuration is rather straight forward. The plasma reactor converts the NO to NO<sub>2</sub> before passing on to the catalytic reactor. The role of the catalyst is then to decompose the ozone that is formed by the plasma and to adsorb or selectively reduce the NO<sub>2</sub> to N<sub>2</sub>. This role of the catalyst is comparable to the catalytic function for the conventional selective catalytic reduction (SCR) process after the plasma reactor has changed the gas composition. On the other hand, choosing an appropriate catalyst for a IPC configuration is more complicated as the catalytic material is placed inside the plasma reactor and the properties of the catalytic material such as size, shape, surface area, pore size, dielectric constant and many currently unknown parameters influence the performance of both the plasma and the pollutant removal. Thus, it is important to investigate whether the catalyst changes the discharge characteristics and vice-versa, if the plasma changes the physical and chemical characteristics of the catalyst for the IPC configuration.

Noble metals and transition metal-oxides have been found to be effective for ozone decomposition. When noble metals are used as a catalysts, it is reported that their catalytic activity decreases with time due to poisoning of the catalyst by adsorbed O atoms [121]. The metal-oxide catalysts are considered as an alternative to the noble metal catalysts as the activity of metal-oxide catalysts is higher compared to the metal catalysts [122]. In the case of transition metal oxides being used, it is reported that surface defects such as vacancies and dislocations alter the local oxygen bonding which turns out to be the active sites for the catalytic reactions. A general characterization of the behavior of transition metal-oxides catalysts is presented in [123–126]. Transition metal oxides have been used

in combination with non-thermal plasma for NO<sub>x</sub> and VOC removal by many researchers [48, 99, 100, 127–132]. In this chapter, we have performed experiments with various metal-oxides from the first transition period namely: NiO, MnO, CuO, Fe<sub>3</sub>O<sub>4</sub>, Co<sub>3</sub>O<sub>4</sub> supported on TiO<sub>2</sub> and Al<sub>2</sub>O<sub>3</sub>.

Yamamoto *et al.* in their study on the transition metal oxide catalysts for diesel PM removal [133], have plotted catalytic oxidation rate as a function of formation enthalpy for various transition metal oxides. This plot suggested that the Fe<sub>2</sub>O<sub>3</sub> has high catalytic oxidation rate at moderate formation enthalpy. Wojciechowska *et al.* in their study on the nitrogen oxides removal by catalytic materials [121] made an excellent review on the NO reduction using various catalytic materials and using various additives. They stated that the activity of the metal-oxides loaded on Al<sub>2</sub>O<sub>3</sub> for NO reduction by CO is as follows: Fe > Cu > Cr > Ni > Co > Mn > V. From Sabatier's principle, for an optimum rate of reaction, the interaction between the adsorbates should neither be too weak nor too strong. There is a clear trend in the activation energy energies, heats of desorption and catalytic activity for this first transition period of elements that we have chosen. The activation energies of oxygen desorption from oxides showed a increasing trend along the first transition period while the heats of oxygen desorption shows a decreasing trend with the exception of Fe<sub>2</sub>O<sub>3</sub>. On the other hand, the catalytic activity showed a decreasing trend along the period for oxidation of ammonia, ethylene, methane and other hydrocarbons as mentioned in [134]. Thus, it will be interesting to study how these materials perform when combined with plasma for NO<sub>x</sub> removal.

Not much literature is available on a systematic study on the comparison between IPC and PPC configurations for these various catalytic materials for NO<sub>x</sub> removal. Various studies state that the IPC configuration achieved better NO<sub>x</sub> removal efficiencies whereas the PPC configuration showed lesser by-products formation.

In this chapter, we study the role of catalytic material in changing the plasma discharge characteristics by considering the voltage-current waveforms and by measuring the dielectric constants of these catalytic materials and to correlate the dielectric constant values with the discharge characteristics. We have studied NO<sub>x</sub> removal by loading various metal oxides on TiO<sub>2</sub> and Al<sub>2</sub>O<sub>3</sub> supports and by using them in a IPC and in a PPC combination with a pulsed DBD reactor. The metal-oxides that we have used in this study are NiO, MnO, CuO, Fe<sub>3</sub>O<sub>4</sub>, and Co<sub>3</sub>O<sub>4</sub>. To understand the effect of the support material, we have loaded 3% of these metal oxides both on TiO<sub>2</sub> and Al<sub>2</sub>O<sub>3</sub> and compared the NO conversion, NO<sub>x</sub> concentration and by-products formation for both supports using both the in-plasma configuration (IPC) and post-plasma configuration (PPC). Next, the effect of metal loading on the support materials is studied, where we have compared the performance of 3wt% and 5wt% of these metal oxides loaded on TiO<sub>2</sub> and Al<sub>2</sub>O<sub>3</sub> for both the IPC and PPC.

The experimental setup, energy density measurements and gas measurements for these experiments are described in Chapter 2. The characteristics of all the catalytic materials was done and were mentioned in detail in Chapter 2. The particle size of all the catalytic materials used here is 1-2 mm. All the experiments were conducted with an input NO concentration of 200 ppm and a gas flow of 5 slm.

All the catalytic materials were pre-treated before conducting the experiments. The

reactor is filled with catalytic materials and then placed in an oven. The reactor is then heated up to 400 °C with a continuous flow of synthetic air at a flowrate of 1 slm. This pre-treatment was done to ensure that there is no adsorbed H<sub>2</sub>O or CO<sub>2</sub> on the catalytic materials. All the experiments were performed for 3 times and are reproducible within +/- 5% error margin.

## 5.2 In-plasma catalytic configuration

### 5.2.1 Effect of catalytic support

In this section, we have performed experiments with 3wt% of NiO, MnO, CuO, Fe<sub>3</sub>O<sub>4</sub>, Co<sub>3</sub>O<sub>4</sub> loaded on to TiO<sub>2</sub> and Al<sub>2</sub>O<sub>3</sub> supports. These catalytic materials were placed inside the plasma reactor, as a IPC configuration. Figure 5.1a shows the effect of the various metal oxides loaded on TiO<sub>2</sub> on NO conversion. For all the catalytic materials, the NO conversion increases with increasing energy density. In case of TiO<sub>2</sub> substrate, the NO conversion is always higher using the plasma-alone configuration as compared to using the IPC configuration. The same trend was observed in the previous chapters and was also reported by other researchers [45, 75, 105].

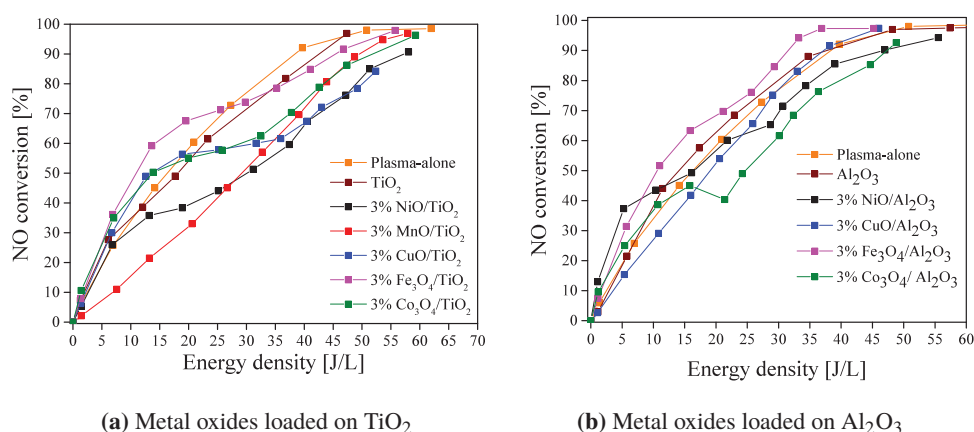
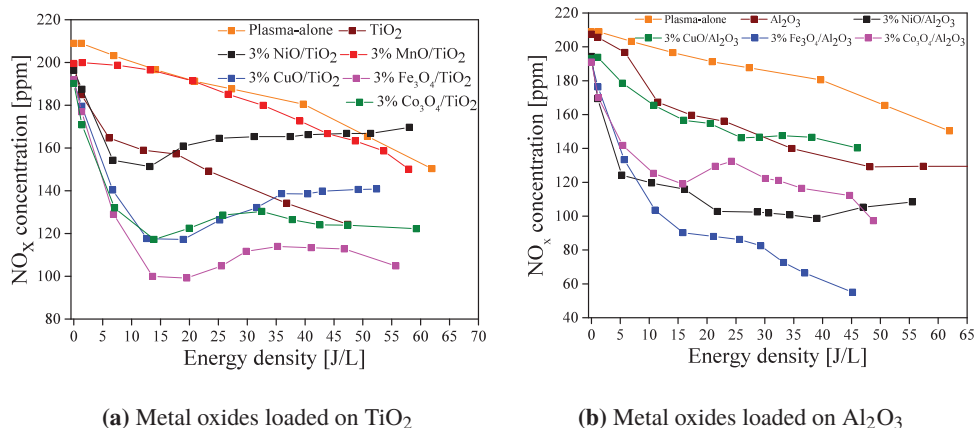


**Figure 5.1** – NO conversion for various metal-oxides loaded on TiO<sub>2</sub> and Al<sub>2</sub>O<sub>3</sub> for an IPC configuration for an input NO concentration of 200 ppm and at a flow-rate of 5 slm.

When looking at the various catalytic materials, at low energy densities, up to 30 J/L, Fe<sub>3</sub>O<sub>4</sub> showed higher NO conversion whereas MnO and NiO showed poor conversion. CuO showed better NO conversion at lower energy density (up to 30 J/L) than at high energy density.

When the metal oxides are loaded on Al<sub>2</sub>O<sub>3</sub> instead of TiO<sub>2</sub>, different NO conversion behaviour can be observed. NO conversion as a function of plasma energy density for various metal oxides loaded on Al<sub>2</sub>O<sub>3</sub> is shown in Fig. 5.1b. 3% Fe<sub>3</sub>O<sub>4</sub> showed higher

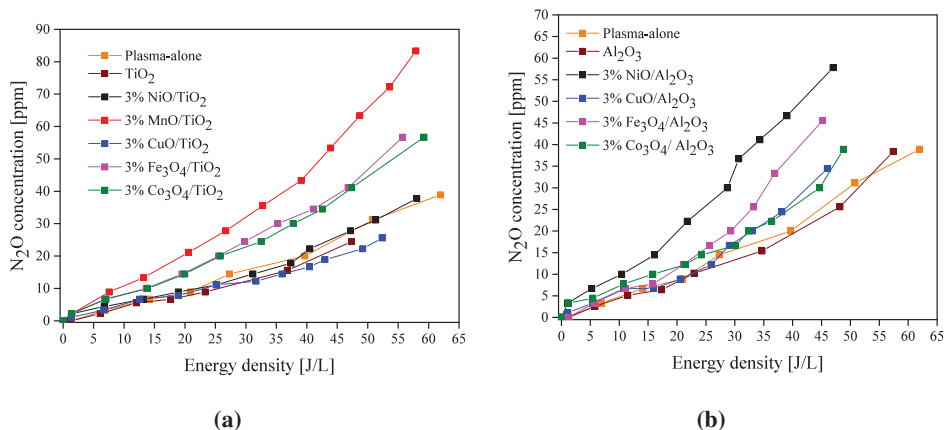




**Figure 5.2** – NO<sub>x</sub> concentration for various metal-oxides loaded on TiO<sub>2</sub> and Al<sub>2</sub>O<sub>3</sub> for an IPC configuration for an input NO concentration of 200 ppm and at a flow-rate of 5 slm.

NO conversion than plasma-alone and also than the IPC-TiO<sub>2</sub> configuration. And 3% NiO showed poor NO conversion when loaded on TiO<sub>2</sub> whereas when this NiO is loaded on Al<sub>2</sub>O<sub>3</sub>, the NO conversion is better.

Considering the NO<sub>x</sub> concentrations as a function of the plasma energy density, as shown for TiO<sub>2</sub> in Fig. 5.2a, it can be observed that NO<sub>x</sub> concentrations decrease with increasing energy density initially, while increasing again at high energy densities for metal oxides loaded on TiO<sub>2</sub>. This increases in NO<sub>x</sub> concentration at higher energy densities is attributed to the NO<sub>2</sub> concentrations that increase with increasing energy density. The plasma-alone and the MnO catalyst showed the highest NO<sub>x</sub> concentrations. Low NO<sub>x</sub> concentrations were obtained with Fe<sub>3</sub>O<sub>4</sub> followed by Co<sub>3</sub>O<sub>4</sub> and CuO.



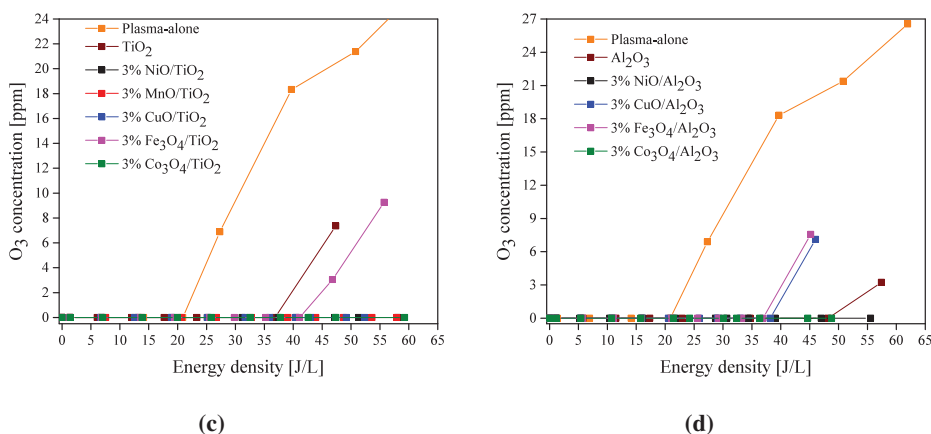


**Figure 5.3** – By-products formation as a function of energy density for various metal-oxides loaded on TiO<sub>2</sub> and Al<sub>2</sub>O<sub>3</sub> for an IPC configuration for an input NO concentration of 200 ppm and at a flow-rate of 5 slm. (a) N<sub>2</sub>O concentration with metal oxides loaded on TiO<sub>2</sub> (b) N<sub>2</sub>O concentration with metal oxides loaded on Al<sub>2</sub>O<sub>3</sub> (c) O<sub>3</sub> concentration with metal oxides loaded on TiO<sub>2</sub> (d) O<sub>3</sub> concentration with metal oxides loaded on Al<sub>2</sub>O<sub>3</sub>.

So, MnO and NiO showed poor performance with respect to both NO and NO<sub>x</sub> concentrations. Though the NiO catalyst loaded on TiO<sub>2</sub> performed poorly, the performance of this catalytic materials was enhanced significantly when loaded on to Al<sub>2</sub>O<sub>3</sub> as seen in Fig. 5.3d. For metal-oxides loaded on Al<sub>2</sub>O<sub>3</sub>, NO<sub>x</sub> concentration was observed to reduce with increasing energy density as seen in Fig. 5.3d. We have studied the NO<sub>x</sub> concentrations only up to 60 J/L since all the catalytic materials showed above 95% NO conversion at this energy density. Further increase in energy density will be a mere waste of energy and also will show a further increase in the by-products formation. Fe<sub>3</sub>O<sub>4</sub> showed low NO<sub>x</sub> concentration when loaded both on TiO<sub>2</sub> as well as on Al<sub>2</sub>O<sub>3</sub>. The NO<sub>x</sub> concentration at 45 J/L for the plasma-alone configuration is approximately 170 ppm whereas using the Fe<sub>3</sub>O<sub>4</sub> catalyst resulted in only 55 ppm. So Fe<sub>3</sub>O<sub>4</sub> showed more than 30% NO<sub>x</sub> removal efficiency. CuO showed reasonably better NO conversion but poor NO<sub>x</sub> concentrations.

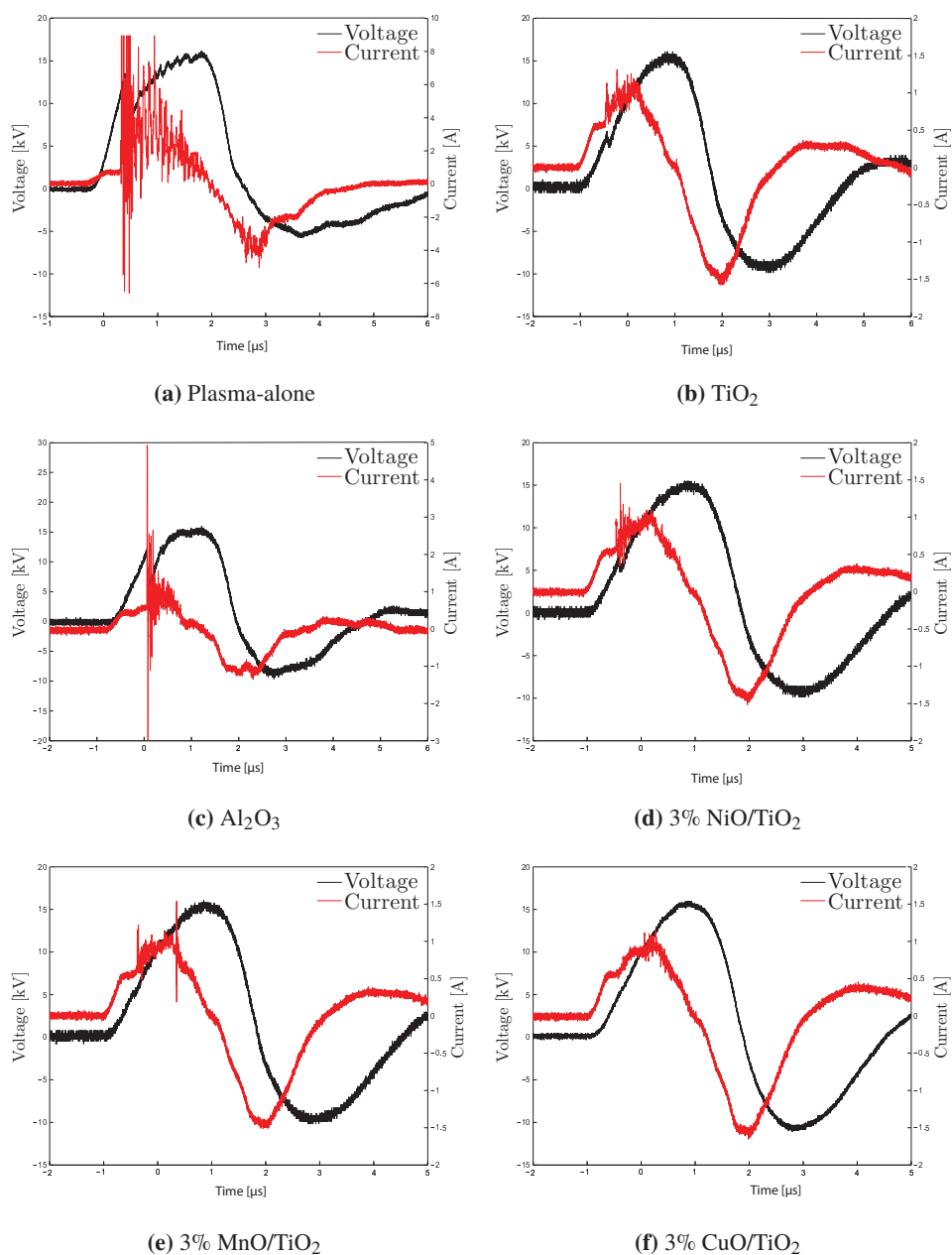


**Figure 5.4** – Voltage-current waveforms for plasma-alone, TiO<sub>2</sub>, metal oxides loaded on TiO<sub>2</sub>, Al<sub>2</sub>O<sub>3</sub> and metal oxides loaded on TiO<sub>2</sub> at a frequency of 300 Hz for an input NO concentration of 200 ppm and for a gas flow-rate of 5 slm.

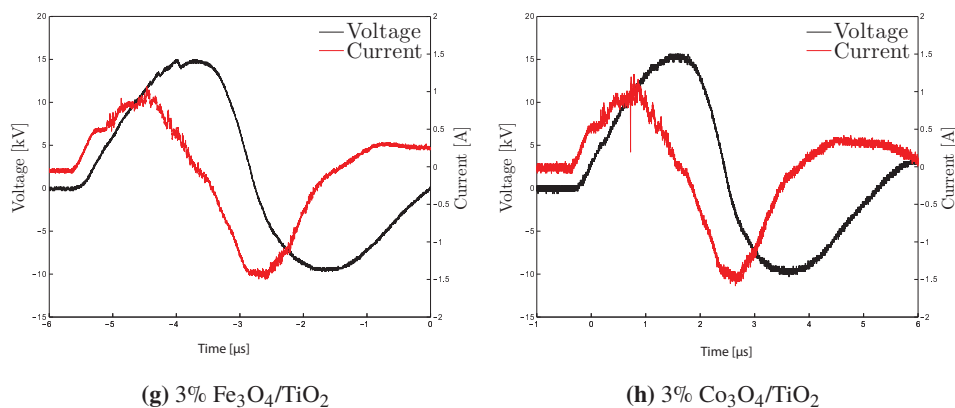


**Figure 5.4** – Voltage-current waveforms for plasma-alone,  $\text{TiO}_2$ ,  $\text{Al}_2\text{O}_3$  and metal oxides loaded on  $\text{TiO}_2$  at a frequency of 300 Hz for an input NO concentration of 200 ppm and for a gas flow-rate of 5 slm.

The main purpose of combining the catalysts with the plasma reactor is to reduce the formation of by-products. In order to compare the performance of the various catalytic materials and the two support materials, we have plotted the  $\text{N}_2\text{O}$  and  $\text{O}_3$  concentrations as a function of energy density and compared these results  $\text{N}_2\text{O}$  and  $\text{O}_3$  concentrations as generated with the plasma-alone configuration. These results are shown in Fig. 5.3. It can be seen from Fig. 5.3a that using the MnO catalyst, results in significantly higher  $\text{N}_2\text{O}$  concentrations than for the plasma-alone configuration and also compared to the other catalytic materials. All the metal oxides loaded on  $\text{TiO}_2$  result in higher  $\text{N}_2\text{O}$  concentrations as compared to the plasma-alone configuration, except for the CuO catalyst. The same behaviour is observed with metal oxides loaded on  $\text{Al}_2\text{O}_3$ , with the exception that CuO produced higher  $\text{N}_2\text{O}$  concentrations than the plasma-alone configuration. Despite its moderate performance with respect to NO conversion and  $\text{NO}_x$  concentration, NiO loaded on  $\text{Al}_2\text{O}_3$  showed higher  $\text{N}_2\text{O}$  concentrations than any other metal oxide catalyst. The lower  $\text{N}_2\text{O}$  concentrations obtained with the plasma-alone configuration could be attributed to the higher concentrations of  $\text{NO}_2$  which reacts with  $\text{O}_3$  to form  $\text{NO}_3$  and  $\text{N}_2\text{O}_5$ . A  $\text{N}_2\text{O}_5$  peak is observed in the FTIR spectrum with the plasma-alone configuration and not when using catalytic materials. We have not further discussed the  $\text{N}_2\text{O}_5$  formation in this thesis as we have not calibrated the FTIR to quantify the  $\text{N}_2\text{O}_5$  concentrations.

Another important by-product that is of our interest is  $\text{O}_3$ . Almost all the catalytic materials showed no ozone formation whereas the plasma-alone configuration showed increasing  $\text{O}_3$  concentrations with increasing energy density. Small concentrations of  $\text{O}_3$  were observed with  $\text{Fe}_3\text{O}_4$  on  $\text{TiO}_2$  and with  $\text{Fe}_3\text{O}_4$  and CuO on  $\text{Al}_2\text{O}_3$  when the energy densities are above 45 J/L. But at such high energy densities, NO is already completely converted and thus  $\text{O}_3$  appears.

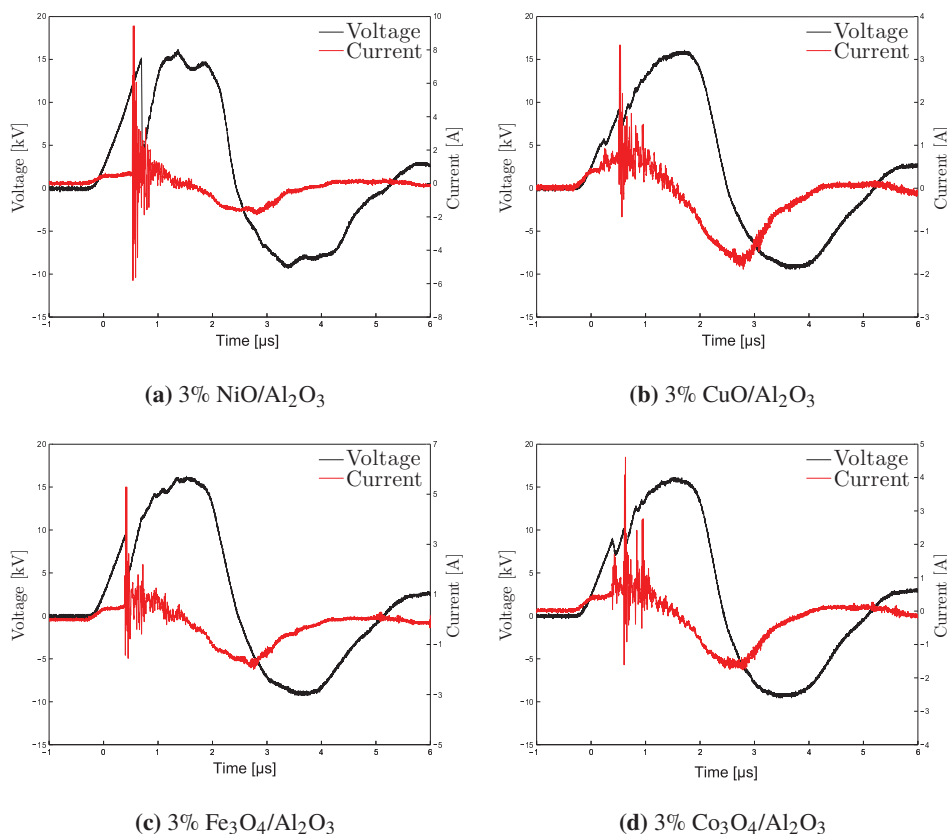


**Figure 5.5** – Voltage-current waveforms for metal oxides loaded on Al<sub>2</sub>O<sub>3</sub> at a frequency of 300 Hz for an input NO concentration of 200 ppm and for a gas flow-rate of 5 slm.

To summarize, the plasma-alone configuration produced less N<sub>2</sub>O compared to all the metal oxides loaded on both TiO<sub>2</sub> as well as on Al<sub>2</sub>O<sub>3</sub>. This is attributed to the formation of other by-products such as NO<sub>3</sub> and N<sub>2</sub>O<sub>5</sub>. On the other hand, O<sub>3</sub> formation showed a different trend. All the catalytic materials suppressed the formation of O<sub>3</sub>.

We tried to understand the difference in the different performance of the various metal oxides loaded on either TiO<sub>2</sub> or Al<sub>2</sub>O<sub>3</sub> substrates by comparing the voltage-current waveforms for all these configurations. Figure 5.4 shows the voltage and current waveforms for the plasma-alone, as well as for TiO<sub>2</sub>, TiO<sub>2</sub> loaded with 3 wt% of NiO, MnO, CuO, Fe<sub>3</sub>O<sub>4</sub>, Co<sub>3</sub>O<sub>4</sub> and fig. 5.5 shows the voltage and current waveforms for Al<sub>2</sub>O<sub>3</sub> and Al<sub>2</sub>O<sub>3</sub> loaded with 3 wt% of NiO, CuO, Fe<sub>3</sub>O<sub>4</sub>, Co<sub>3</sub>O<sub>4</sub>. For all the waveform, the pulse repetition rate was 300 Hz. The applied peak-voltage, the input NO concentration and operational conditions

were kept constant for all the materials.

For the plasma-alone configuration, the current waveform show intense spikes which means, as expected for a DBD configuration, intense microdischarge activity. When a catalytic material is introduced inside the plasma reactor, the current waveform and thus the discharge activity is changed significantly. When  $\text{Al}_2\text{O}_3$  is placed inside the reactor, the current waveform shows microdischarge activity but with slightly lower magnitude as compared to the plasma-alone reactor. Similarly when the plasma reactor is packed with  $\text{TiO}_2$ , the current waveform shows much less microdischarge activity. These differences in microdischarge activity can be explained by the different capacitances due to the different dielectric constants of the two materials. For the plasma-alone reactor, the capacitance of the reactor is low, resulting in a higher discharge current and more discharge activity. When the catalytic material is placed inside the reactor, the capacitance of the reactor is increased and consequently the current magnitude reduces. Of the two materials,  $\text{TiO}_2$  has the highest dielectric constant and thus the highest capacitance. Due to the higher dielectric constant the electric field in the air cavities around the catalyst enhances, eventually leading to more discharges on the surface of the catalytic material [135–137].

When the metal oxides are loaded on the  $\text{TiO}_2$  support, the discharge activity is slightly less intense which could be correlated again to their dielectric constants. In Chapter 2, we have derived values for the dielectric constant for the various catalytic materials. When  $\text{TiO}_2$  is loaded with metal oxides, the dielectric constant is decreased, thus producing reasonably higher microdischarge activity as compared to  $\text{TiO}_2$  with out metal oxides.

The positive and negative half cycle of the voltage-current waveform are fairly different from each other and this difference depends on the catalytic material. When using  $\text{Fe}_3\text{O}_4$  and  $\text{NiO}$  on  $\text{Al}_2\text{O}_3$  support, intense spikes are observed on the current waveforms, which could be related to increased microdischarge activity. The peak current for both of these materials is higher as compared to the other catalytic materials that we have used in our study. This increase in microdischarge activity might have led to the increased conversions obtained with these materials. In order of  $\text{NO}$  conversion rate,  $\text{Fe}_3\text{O}_4$  loaded on  $\text{Al}_2\text{O}_3$  showed highest  $\text{NO}$  conversion followed by  $\text{NiO}$  and  $\text{CuO}$  on  $\text{Al}_2\text{O}_3$ . The increased peak currents and microdischarge activity when metal oxides are loaded on  $\text{Al}_2\text{O}_3$  are expected to be the main reason for the increased  $\text{NO}$  conversion. Other parameters of the catalytic material such as particle size, shape, surface roughness, conductivity might affect the conversion efficiency as well. For all the experiments, we have used catalytic materials with particle size 1-2 mm and thus the different performance of the various materials cannot be attributed to the effect of particle size. The plasma development along the surface of these catalytic materials is studied using ICCD imaging in the Appendix 7.6.

### 5.2.2 Effect of wt% of metal-oxide loading

To study the effect of metal oxide loading,  $\text{TiO}_2$  was loaded with 3 wt% and 5 wt% of  $\text{CuO}$ ,  $\text{Fe}_3\text{O}_4$  and  $\text{Co}_3\text{O}_4$ . Figure 5.6 shows the effect of metal oxide loading on  $\text{NO}$  conversion and  $\text{NO}_x$  concentration as a function of energy density. When increasing the wt% of metal oxide loading on  $\text{TiO}_2$ , the  $\text{NO}$  conversions increase notably. There is also a significant

difference in the NO<sub>x</sub> concentration. Loading a metal oxide on the TiO<sub>2</sub> always results in lower NO<sub>x</sub> concentrations as for TiO<sub>2</sub> alone, except for Fe<sub>3</sub>O<sub>4</sub>. For this catalyst, 5% Fe<sub>3</sub>O<sub>4</sub> results in higher NO<sub>x</sub> concentrations as compared to 3% Fe<sub>3</sub>O<sub>4</sub>. On the contrary, for CuO, 5% CuO showed much lesser NO<sub>x</sub> concentrations as compared to 3% CuO. No significant difference was observed for Co<sub>3</sub>O<sub>4</sub>. To conclude, increasing the metal oxide loading on the TiO<sub>2</sub> support results in increased conversion of NO.

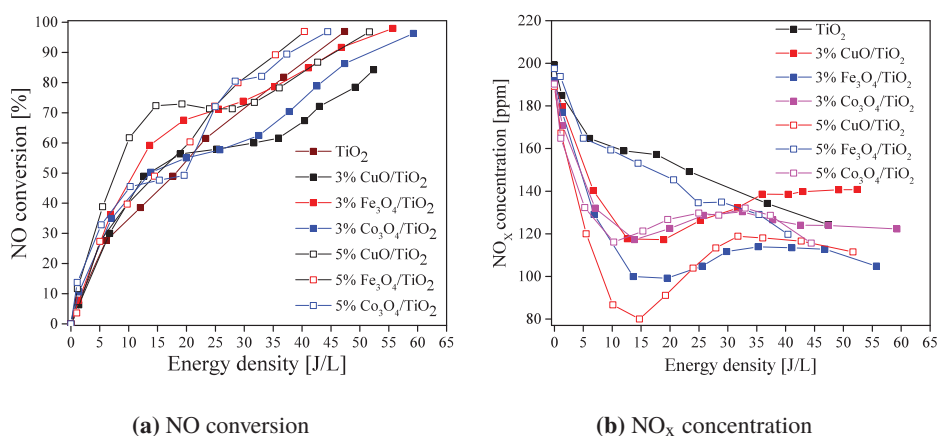


**Figure 5.6** – NO conversion and NO<sub>x</sub> concentrations for various metal-oxides loaded on TiO<sub>2</sub> for an IPC configuration for an input NO concentration of 200 ppm and at a flow-rate of 5 slm.

N<sub>2</sub>O formation as a function of energy densities for the various metal oxide loadings is shown in Fig. 5.7. With increasing energy density, the N<sub>2</sub>O concentration increases for all the metal oxide loadings. When increasing the metal oxide loading on the TiO<sub>2</sub>, the N<sub>2</sub>O concentration shows a considerable difference at higher energy densities. A higher metal oxide loading results in higher N<sub>2</sub>O concentrations at higher energy densities. While at low energy densities, up to 25 J/L, the metal oxide loading has no significant effect on the N<sub>2</sub>O concentration. Loading of 5% and 3% of Fe<sub>3</sub>O<sub>4</sub> on TiO<sub>2</sub> results in similar N<sub>2</sub>O concentrations. This might be due to the presence of higher concentrations of NO<sub>2</sub>, which reacts with atomic nitrogen to form N<sub>2</sub>O. Higher NO<sub>2</sub> concentrations leads to higher N<sub>2</sub>O concentrations.

When looking at the O<sub>3</sub> formation, higher metal oxide loadings completely suppressed the O<sub>3</sub> formation even at high energy densities. No O<sub>3</sub> has been observed.

To conclude, the CuO catalyst with 5% loading on TiO<sub>2</sub> performed better, for both the NO<sub>x</sub> removal as well as with low by-products formation.

With increase in metal oxide loading both the physical properties and the electrical properties of the catalytic material may change. The change in physical properties is related to the increase in the active sites of the materials. Varying the metal oxide loading may also vary the discharge activity. The V-I waveforms for 3% metal oxide loading and 5%

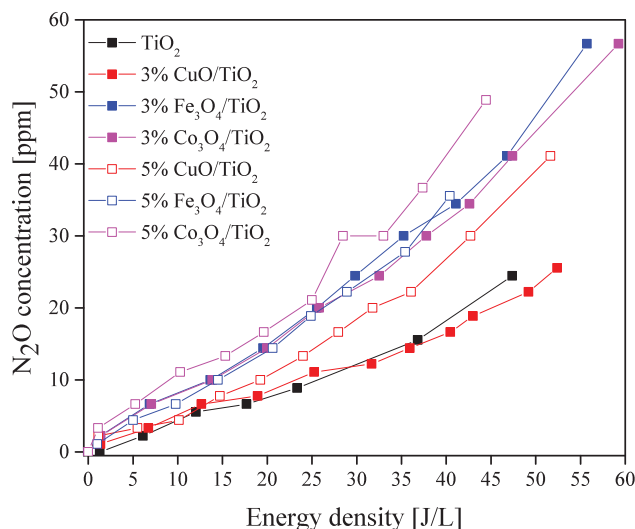


**Figure 5.7** – N<sub>2</sub>O concentration as a function of energy density for various wt% of metal-oxides loaded on TiO<sub>2</sub> for an IPC configuration for an input NO concentration of 200 ppm and at a flow-rate of 5 slm.

metal oxide loading on TiO<sub>2</sub> are shown in Fig. 5.8. The voltage waveforms do not show any significant difference and the input peak-voltage for all the materials is same. However, some interesting observation can be made from the current waveforms. With increasing metal oxide loading, the number of spikes in the current waveform increase, indicating an increase in microdischarges. This increase in microdischarges may lead to increased reactive species production since more energy is deposited in the discharge. With increased reactive species production, the conversions and by-products formation will also be different. Thus we obtain an increase of the NO conversion with increased metal oxide loading, but at the expense of higher N<sub>2</sub>O formation.

The observed differences in discharge current, and thus in discharge behaviour, might be due to the difference in the dielectric constant for the various metal-oxide loading concentrations. In Chapter 2, we have discussed the difference in the dielectric constants with increased metal oxide loading. With increasing dielectric constant, the local electric field strength between the catalytic pellets increases, which apparently effects the NO conversions. With different metal oxide loading, the intensity of plasma varies and the observations of this variation in plasma discharges after placing the catalytic materials in the plasma reactor will be presented in Chapter 7.6.



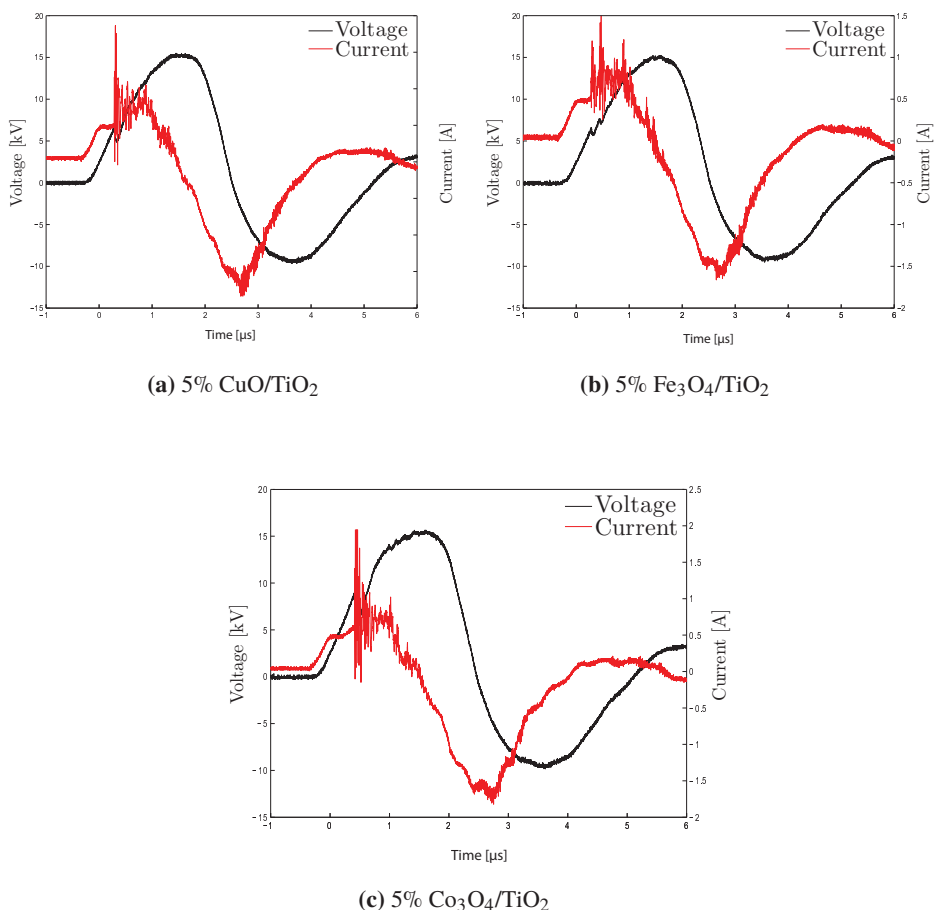


**Figure 5.8** – Voltage-current waveforms for 5% metal oxides loading on TiO<sub>2</sub> at a frequency of 300 Hz for an input NO concentration of 200 ppm and for a gas flow-rate of 5 slm.

### 5.3 Post-plasma catalytic configuration

#### 5.3.1 Effect of catalytic support

In this section, we have studied the effect of the metal oxide loading when supporting the metal-oxide catalyst by either TiO<sub>2</sub> or by Al<sub>2</sub>O<sub>3</sub>, by performing experiments with 3wt% of NiO, MnO, CuO, Fe<sub>3</sub>O<sub>4</sub>, Co<sub>3</sub>O<sub>4</sub> loaded on to the two support materials and when using a PPC configuration. Figure 5.9 shows the effect of various metal oxides loaded on TiO<sub>2</sub> (Fig. 5.9a) and Al<sub>2</sub>O<sub>3</sub> (Fig. 5.9b) on NO conversion.

From the Fig. 5.9a, it can be seen that the NO conversion is notably higher for the plasma-

alone configuration than for a PPC configuration with metal oxides loaded on  $\text{TiO}_2$ . Even at higher energy densities, the catalytic materials were not able to realize NO conversion above 90% with PPC configuration. While in comparison, with the IPC configuration as shown in the previous section, all the materials achieved more than 90% NO conversion for energy densities above 50 J/L. However, for the PPC configuration, MnO showed moderate NO conversion whereas CuO showed poor conversion in comparison with the results for these materials for the IPC configuration. There was not a significant difference in NO conversion between the IPC and the PPC configurations for the material MnO,  $\text{Fe}_3\text{O}_4$  and  $\text{Co}_3\text{O}_4$ .

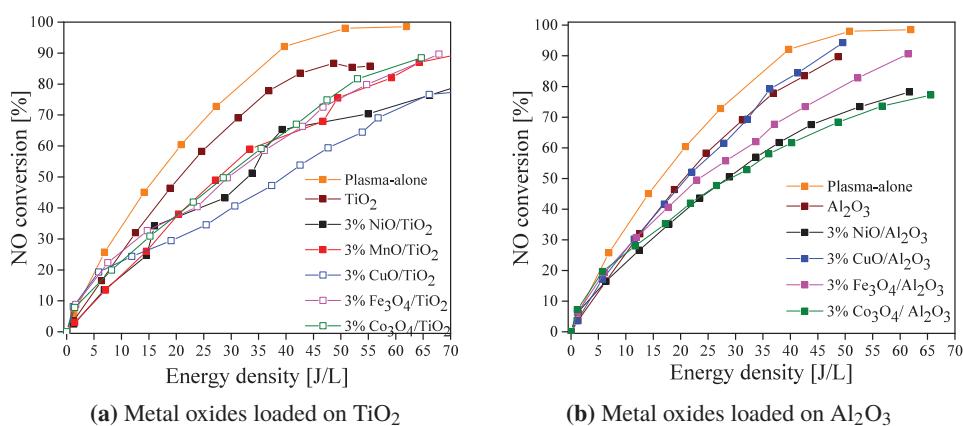


**Figure 5.9** – NO conversion as a function of energy density for various metal-oxides loaded on  $\text{TiO}_2$  and  $\text{Al}_2\text{O}_3$  in the PPC configuration for an input NO concentration of 200 ppm and a flow-rate of 5 slm.

The metal oxides loaded on  $\text{Al}_2\text{O}_3$  showed better conversions than the metal oxides loaded on  $\text{TiO}_2$  as can be observed in Fig. 5.9b. Comparing these results with the results obtained with the IPC configuration in the previous section, with the catalytic materials applied in the PPC configuration, lower NO conversions are obtained as with the plasma-alone configuration. For the PPC configuration, CuO showed better NO conversion compared to all the other catalytic materials whereas  $\text{Co}_3\text{O}_4$  obtained low NO conversion.

The order of NO conversions obtained with metal oxides loaded on  $\text{TiO}_2$  is plasma-alone >  $\text{TiO}_2$  > MnO  $\approx$   $\text{Fe}_3\text{O}_4$   $\approx$   $\text{Co}_3\text{O}_4$  > CuO. In a same way, the order of NO conversion obtained with metal oxides loaded on  $\text{Al}_2\text{O}_3$  is plasma alone > CuO  $\approx$   $\text{Al}_2\text{O}_3$  >  $\text{Fe}_3\text{O}_4$  > NiO  $\approx$   $\text{Co}_3\text{O}_4$ . MnO showed better conversions in the PPC configuration than in the IPC configuration. Huang *et al.* also observed higher conversions and lower  $\text{O}_3$  concentrations with MnO in the PPC configuration compared to the IPC configuration [138].

With increasing energy density,  $\text{NO}_x$  concentrations started to reduce for all the catalytic materials. Applying catalytic materials always results in much lower  $\text{NO}_x$  concentrations in PPC configuration as compared to the plasma-alone configuration. However, the IPC configuration as described in the previous section, results in substantially lower  $\text{NO}_x$  con-

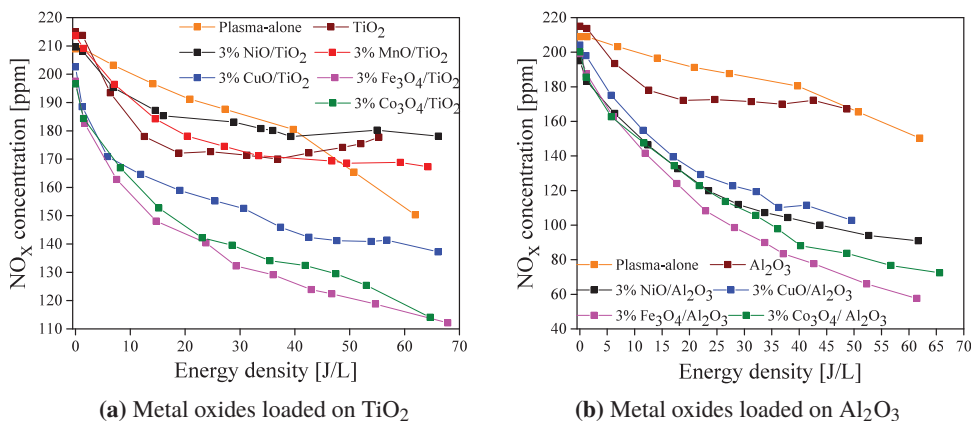


**Figure 5.10** – NO<sub>x</sub> concentration for various metal-oxides loaded on TiO<sub>2</sub> and Al<sub>2</sub>O<sub>3</sub> for the PPC configuration for an input NO concentration of 200 ppm and at a flow-rate of 5 slm.

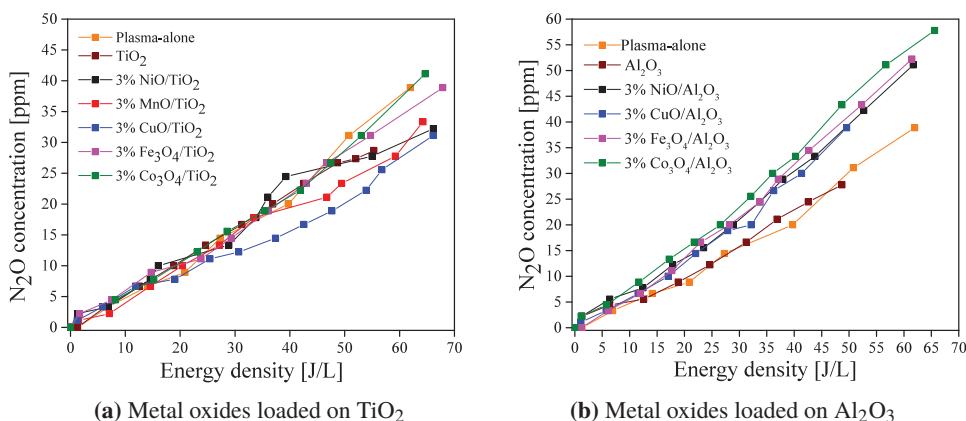


**Figure 5.11** – N<sub>2</sub>O concentration as a function of energy density for various metal-oxides loaded on TiO<sub>2</sub> and Al<sub>2</sub>O<sub>3</sub> for the PPC configuration for an input NO concentration of 200 ppm and at a flow-rate of 5 slm.

concentrations than the PPC configurations. Metal oxides loaded on Al<sub>2</sub>O<sub>3</sub> showed significantly lower NO<sub>x</sub> concentrations as compared to loading the metal oxides on TiO<sub>2</sub>. MnO and NiO showed higher NO<sub>x</sub> concentrations when loaded on TiO<sub>2</sub> both for the IPC and the PPC configuration whereas NiO loaded on Al<sub>2</sub>O<sub>3</sub> provided much less NO<sub>x</sub> concentrations. Fe<sub>3</sub>O<sub>4</sub> showed low NO<sub>x</sub> concentrations both for TiO<sub>2</sub> and Al<sub>2</sub>O<sub>3</sub> supports. Finally, Co<sub>3</sub>O<sub>4</sub> also obtained lower NO<sub>x</sub> concentrations both on TiO<sub>2</sub> and Al<sub>2</sub>O<sub>3</sub> supports despite of its poor

performance with regard to NO conversion.

The by-products formation as a function of energy density for metal oxides loaded on TiO<sub>2</sub> and Al<sub>2</sub>O<sub>3</sub> is shown in Fig. 5.11. We do not show the O<sub>3</sub> concentrations because we have not observed O<sub>3</sub> concentrations for all the metal oxides in the PPC configuration. Therefore we show and discuss only the N<sub>2</sub>O concentrations. It can be observed that with increasing energy density, the N<sub>2</sub>O concentrations increase in a similar way as for the plasma-alone and for the IPC configuration. Thus, the N<sub>2</sub>O formation is a strong function of the plasma energy density. In general, metal oxides loaded on Al<sub>2</sub>O<sub>3</sub> result in slightly higher N<sub>2</sub>O concentrations as compared to loading metal oxides on TiO<sub>2</sub>. This is reasonable because, metal oxides loaded on Al<sub>2</sub>O<sub>3</sub> obtained higher NO conversions than metal oxides loaded on TiO<sub>2</sub> for the given energy density.

CuO loaded on TiO<sub>2</sub> showed low N<sub>2</sub>O concentrations both with IPC and PPC configurations. The result of this lower N<sub>2</sub>O concentrations might be because of lower NO<sub>2</sub> concentration, while NO<sub>2</sub> is required to react with nitrogen radicals to form N<sub>2</sub>O. Apart from CuO, the other metal oxides on TiO<sub>2</sub> did not show significant effect on the N<sub>2</sub>O formation. A similar effect is observed with metal oxides loaded on Al<sub>2</sub>O<sub>3</sub>. There is also not a significant difference in N<sub>2</sub>O formation between the different metal oxides loaded on Al<sub>2</sub>O<sub>3</sub>. Overall, the PPC configuration showed lower conversions as compared to the IPC configuration, but resulted in lower by-product formation.

### 5.3.2 Effect of wt% of metal-oxide loading

In this section, we have studied the effect of metal oxide loading on the NO<sub>x</sub> removal and by-products formation by loading 3wt% and 5wt% of CuO, Fe<sub>3</sub>O<sub>4</sub> and Co<sub>3</sub>O<sub>4</sub> on TiO<sub>2</sub>. The effect of metal loading on NO conversion and NO<sub>x</sub> concentration as a function of energy density is shown in Fig. 5.16. It can be observed that with increase in metal loading higher NO conversions and lower NO<sub>x</sub> concentrations were obtained. The NO conversion is moderately increased by increasing the metal oxide loading of Fe<sub>3</sub>O<sub>4</sub> while CuO and Co<sub>3</sub>O<sub>4</sub> showed significant difference.

The increase in NO conversion for the PPC configuration could be due to the increase in surface area with increasing metal oxide loading. Fe<sub>3</sub>O<sub>4</sub> and CuO showed considerably lower NO<sub>x</sub> concentrations with increasing metal oxide loading while moderately less concentrations were observed with Co<sub>3</sub>O<sub>4</sub>. In general, increasing the metal oxide loading led to higher conversions in both IPC and PPC configurations.

As O<sub>3</sub> formation is completely suppressed in the PPC configuration, we only looked at the N<sub>2</sub>O concentration to study the by-products formation. The N<sub>2</sub>O concentration as a function of energy density for various metal oxide loadings on TiO<sub>2</sub> is shown in Fig. 5.13. With increase in metal oxide loading, the N<sub>2</sub>O concentration increased with energy density for all the metal oxides. Thus the increase of NO conversions and the reduced NO<sub>x</sub> concentrations with an increase in metal oxide loading, comes at the expense of increased by-products formation. The N<sub>2</sub>O concentrations produced with 5% Fe<sub>3</sub>O<sub>4</sub> in PPC configuration is comparable to the performance of the 5% Fe<sub>3</sub>O<sub>4</sub> loading in the IPC configuration. This is striking, because, the main advantage of using the PPC configuration is the reduced by-

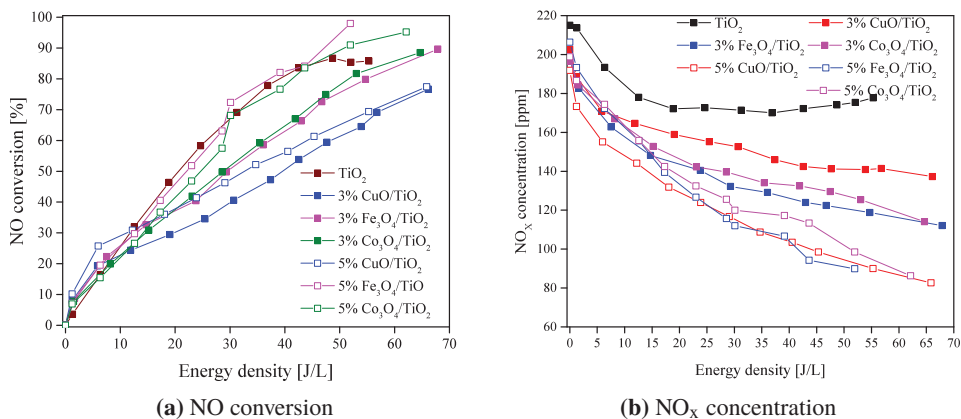


**Figure 5.12** – NO conversion for various metal-oxides loaded on TiO<sub>2</sub> for PPC configuration for an input NO concentration of 200 ppm and at a flow-rate of 5 slm.

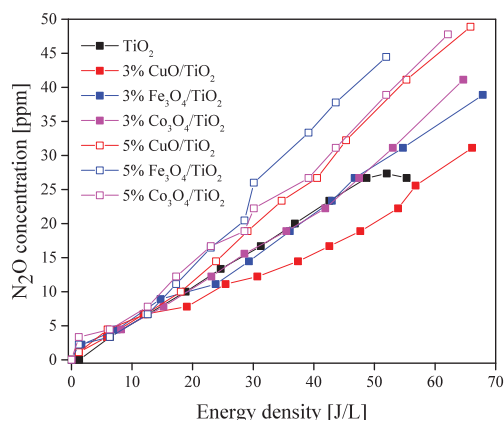


**Figure 5.13** – N<sub>2</sub>O concentration as a function of energy density for various wt% of metal-oxides loaded on TiO<sub>2</sub> for PPC configuration for an input NO concentration of 200 ppm and at a flow-rate of 5 slm.

products formation. Increasing the metal oxide loading seems to curb this advantage of the PPC configuration.

## 5.4 Conclusions

DBDs are widely used for VOCs and NO<sub>x</sub> removal. Two main arrangements are generally proposed in the literature to combine a plasma reactor with a catalytic reactor: an in-plasma

catalytic configuration (IPC), and a post-plasma catalytic configuration (PPC). In both of these configurations, different catalysts such as NaY, noble metals and transition metal oxides supported on  $\text{TiO}_2$  and on  $\text{Al}_2\text{O}_3$  have been tested. Transition metal oxides were preferred over noble metal metals for economic reason.

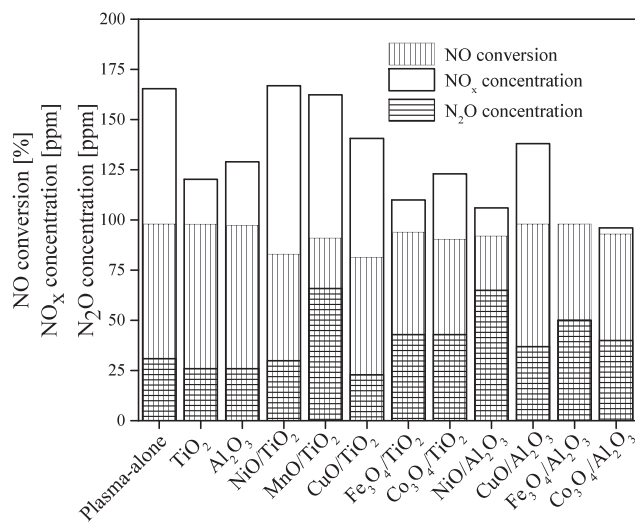


**Figure 5.14** – Comparison of the performance of various metal-oxides loaded on  $\text{TiO}_2$  and  $\text{Al}_2\text{O}_3$  for an IPC configuration for an input  $\text{NO}$  concentration of 200 ppm, at a flow-rate of 5 slm and for the energy density of 50 J/L.

In this chapter, we have studied  $\text{NO}_x$  removal by loading various metal oxides on  $\text{TiO}_2$  and on  $\text{Al}_2\text{O}_3$  using a pulsed DBD reactor. The metal-oxides that we have used in this study are NiO,  $\text{MnO}_x$ , CuO,  $\text{Fe}_3\text{O}_4$ ,  $\text{Co}_3\text{O}_4$ . To understand the effect of support material, we have loaded 3% of these metal oxides both on  $\text{TiO}_2$  and  $\text{Al}_2\text{O}_3$  and compared the  $\text{NO}$  conversion,  $\text{NO}_x$  concentration and by-products formation using both the in-plasma configuration (IPC) and post-plasma configuration (PPC). Also the effect is studied on the amount of metal-oxide loading on both support materials, where we have compared the performance of 3wt% and 5wt% of these metal oxides loaded on  $\text{TiO}_2$  and  $\text{Al}_2\text{O}_3$  for both the IPC and PPC. We studied the role of catalytic material in changing the plasma discharge characteristics by looking into the voltage-current waveforms and measuring the dielectric constants of these materials to correlate them to the discharge characteristics.

A comparison of the performance of various metal oxides loaded on  $\text{TiO}_2$  and on  $\text{Al}_2\text{O}_3$  with respect to  $\text{NO}$  conversion,  $\text{NO}_x$  concentration and  $\text{N}_2\text{O}$  concentrations at an energy density of 50 J/L for an IPC and for the PPC configuration is given in Fig. 5.14 and Fig. 5.15 respectively. In general, the metal oxides loaded on  $\text{Al}_2\text{O}_3$  performed well for both the IPC and PPC configuration. The increase in performance of  $\text{Al}_2\text{O}_3$  and metal oxides supported on  $\text{Al}_2\text{O}_3$  for the IPC configuration might be due to the formation of more

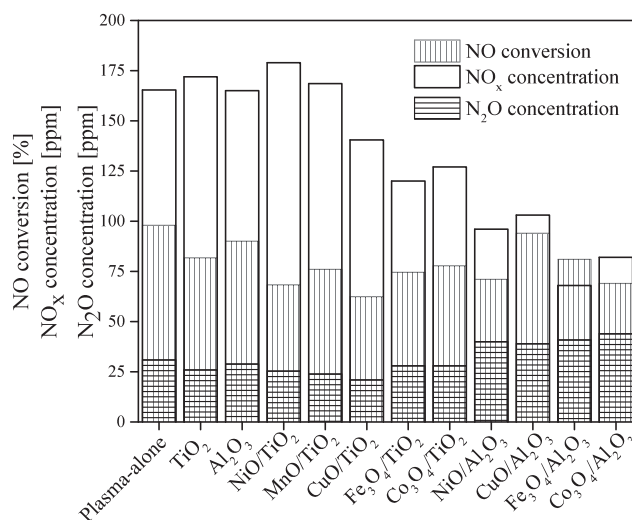
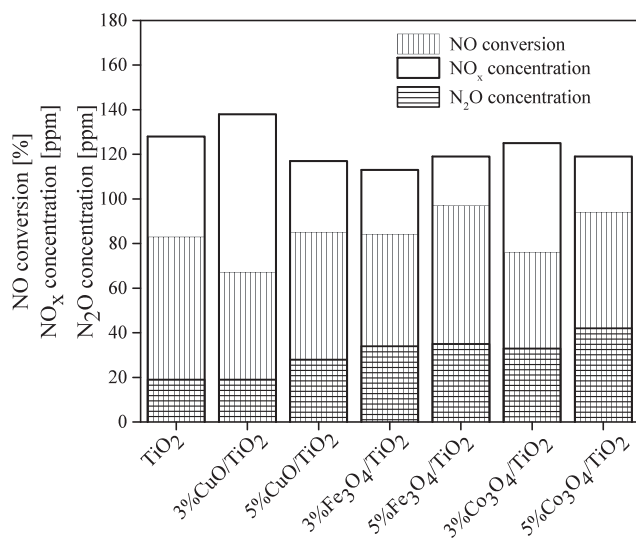


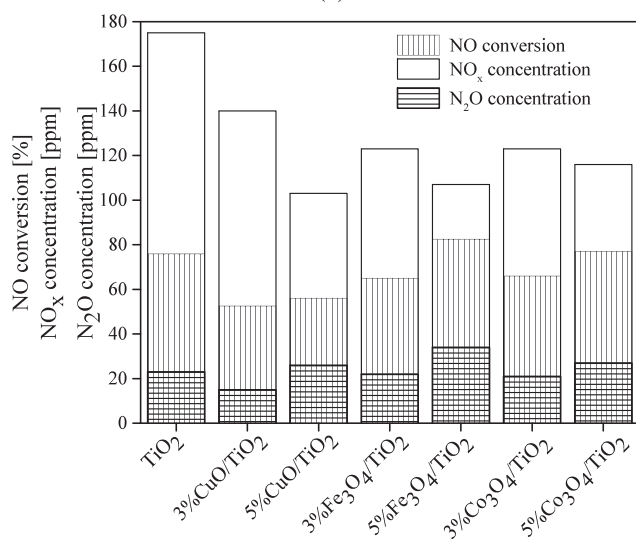
**Figure 5.15** – Comparison of the performance of various metal-oxides loaded on TiO<sub>2</sub> and Al<sub>2</sub>O<sub>3</sub> for the PPC configuration for an input NO concentration of 200 ppm, at a flow-rate of 5 slm and for the energy density of 50 J/L.

intense microdischarges, as has been observed in the current waveforms. These more intense microdischarges might be related to the higher dielectric constants: the higher the dielectric constant, the less intense the current waveform and thus the related plasma.

Comparison of the performance of various amounts of metal oxide loading on TiO<sub>2</sub> with respect to NO conversion, NO<sub>x</sub> concentration and N<sub>2</sub>O concentrations at an energy density of 40 J/L is given in Fig. 5.16. Higher metal oxide loading showed higher conversion but at the expense of higher by-products formation. 5% CuO/TiO<sub>2</sub> showed the most optimum performance for both the IPC and the PPC configuration. With increase in metal oxide loading, the surface area increases and thus improved conversions can be expected.



(a)



(b)

**Figure 5.16** – Comparison of the performance of various metal-oxides loading on  $\text{TiO}_2$  for an input NO concentration of 200 ppm, at a flow-rate of 5 slm and for the energy density of 40 J/L. (a) IPC-configuration (b) PPC-configuration.





---

## SDBD REACTOR FOR ON-DEMAND AIR PURIFICATION

---

### 6.1 Introduction

Although the main focus of our work is on understanding DBDs for air purification applications, we have also developed an Surface-dielectric-barrier-discharge (SDBD) reactor for on-demand air purification as a part of Environmental Sensors for Energy Efficiency (ESEE) project funded by EU. SDBDs have become popular recently due to their wide range of applications such as ozone generation, surface treatments and air-pollutants removal [139–145]. An important advantage of SDBD plasma is that only relatively low high-voltage pulses ( $< 10$  kV) are needed to generate the plasma [139]. They are effective in removing a wide range of pollutants. Non-thermal plasma is generated as a thin plasma layer along a dielectric surface at room temperature and atmospheric pressure. Despite the fact that the generation of homogenous plasma is relatively simple, the challenge lies in scaling-up of SDBD reactors.

In this chapter, we have developed a modular plasma-catalytic surface-dielectric-barrier-discharge (SDBD) reactor to handle large flows and which can be scaled-up and scaled-down easily. A SDBD power modulator was developed to generate 7-kV high-voltage pulses with microsecond duration that can power two SDBD-reactor plates at a maximum of 5 kHz pulse repetition rate. The developed reactor can accommodate up to 20 SDBD plates and thus 10 such SDBD driver units are needed to power these SDBD plates and to treat larger flows.

In this study, we have used three SDBD drivers connected in parallel to 6 SDBD plates. The applied power can be controlled by means of the adjustable pulse-repetition rate. The electrical and the chemical characterization of this developed SDBD reactor will both be discussed in detail in this chapter. The operational efficiency of the developed SDBD has been investigated by studying the removal of  $\text{NO}_x$  and ethylene. The removal efficiency of

$\text{NO}_x$  and ethylene are determined as a function of energy density and operational parameters such as initial concentration and gas flow rate. Finally, we combined the SDBD plasma reactor with catalyst by placing the  $\text{Al}_2\text{O}_3$  plates without  $\text{TiO}_2$  coating and with  $\text{TiO}_2$  coating alternatively to the SDBD plates in a parallel arrangement.

## 6.2 Experimental setup

The schematic representation of the experimental setup used to study the SDBD reactor performance can be found in Fig. 6.1. The flow of gas was controlled by using Bronkhorst mass flow controllers. The gas used in the experiments discussed in this chapter consists of a mixture of  $\text{NO}$  in  $\text{N}_2$  (10000 ppm of  $\text{NO}$  in  $\text{N}_2$  base),  $\text{C}_2\text{H}_4$  in  $\text{N}_2$  (1000 ppm of  $\text{C}_2\text{H}_4$  in  $\text{N}_2$  base) and synthetic air. Synthetic air (less than 3 ppm of  $\text{H}_2\text{O}$  content) is used to dilute  $\text{NO}$  and  $\text{C}_2\text{H}_4$  to get the desired input concentrations. The gas mixture is dosed at room temperature and at atmospheric pressure.

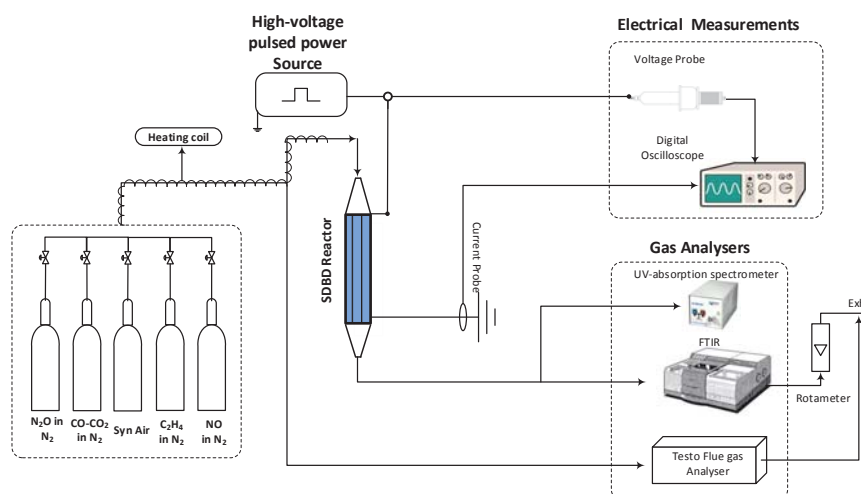


**Figure 6.1** – Schematic representation of the experimental set-up using SDBD reactor.

The treated gas from the SDBD reactor was sampled out to a Fourier Transform Infrared Spectrometer (FTIR, BRUKER Tensor 27) with a 20-cm optical path gas cell to measure the exit gas concentration. The resulting spectra from the FTIR are used to calculate the varying concentrations of  $\text{NO}$ ,  $\text{NO}_2$ ,  $\text{O}_3$ ,  $\text{N}_2\text{O}$ ,  $\text{C}_2\text{H}_4$ ,  $\text{CO}$  and  $\text{CO}_2$ . Ozone concentrations were measured with a UV-absorption spectrometer. For UV absorption measurements, we have used a 11-mm optical path cell and the optic fibers connect this path cell with the UV source and the spectrometer. We have used Micropack D-2000 as UV source and Ocean Optics

HR2000 spectrometer. A pulsed-power SDBD modulator is used to produce the discharges. Pulse repetition rate was varied from 0-300 Hz to vary the energy density. We have explained in Chapter 2 about the gas compositions and the formulas that we have used to calculate the conversions and selectivities. All the experiments in this chapter were performed for 6 times and are reproducible within  $\pm 5\%$  error margin.

The SDBD plasma-catalytic reactor consists mainly of two components: 1. Electrode plates and 2. catalytic plates. The detailed description of the design of the electrode plate and the synthesis of the catalytic plate are found in the following sections.

### 6.2.1 Design of SDBD plate

The electrode plate, from here on is referred as the SDBD plate. The SDBD plate consists of a thin ceramic dielectric plate plated with copper strip electrodes on both the sides. The layout of the copper electrode strips on the ceramic plate is shown in Fig. 6.2. In our research, alumina is used as a dielectric plate and the metallic strips are copper coated with gold to avoid corrosion when the plasma is ignited. The dimensions of the ceramic plate are 150 x 100 x 1 mm. These tracks of copper strips are produced by pcb-production technique as shown in Fig. 6.3a. The copper strips have a width of 2.3 mm and the distance between the tracks is 2.5 mm. The distance between the top edge of the dielectric plate to the copper strip is 11.5 mm and from the side edge is 10 mm. Each side of the plate consists of 16 parallel copper strips. At one side of a plate, all electrode strips are connected to the high voltage and all strips at the other side are grounded. When high-voltage (up to several kV) is applied to the metal strips, discharges initiates from the electrode along the dielectric surface of the plate. Plasma is generated on both sides of the planar SDBD plate as shown in Fig. 6.3b. These SDBD plates were manufactured for us by Accent PCB Nederland B.V. An extensive optical characterization study on this SDBD plates can be found in [146].

### 6.2.2 Synthesizing the catalyst plate

In a reactor, dielectric plates coated with a catalytic material can be positioned in parallel to SDBD plates. An example of a possible combination is shown in Fig. 6.4. The catalyst plate was made by depositing  $\text{TiO}_2$  on a ceramic plate ( $\text{Al}_2\text{O}_3$ ) with the dimensions similar to that of the SDBD plate. This deposition of  $\text{TiO}_2$  as a thin film was made by means of a chemical deposition method. The deposition method used is the sol-gel technique where the ceramic plates were dip coated in the sol-gel [147].

#### 6.2.2.1 Synthesizing $\text{TiO}_2$ thin films by sol-gel method:

A thin film of  $\text{TiO}_2$  was deposited on the ceramic plate by sol-gel method in the following steps.

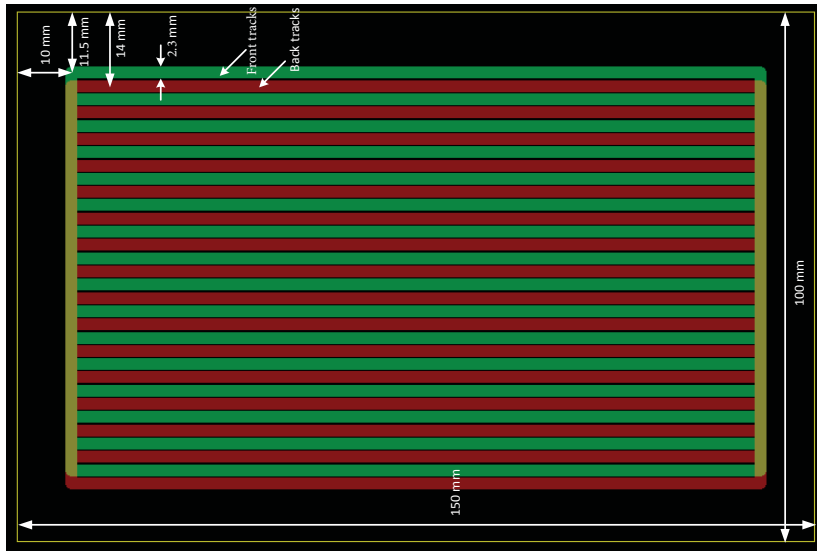
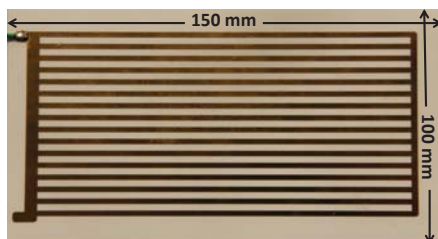
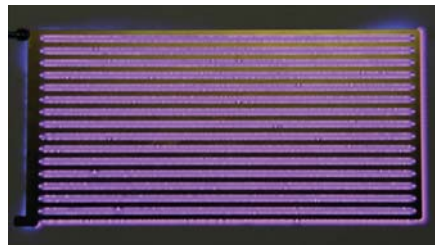


**Figure 6.2** – SDBD plate with copper metal electrodes with gold deposited on the top of copper strips. Green tracks represent the front side tracks while the red tracks represent the back side tracks



(a) Plasma-off



(b) Plasma-on

**Figure 6.3** – SDBD-plate with copper tracks coated with gold to avoid corrosion. The dimensions of the SDBD plate are 150 x 100 x 1 mm. (a): with-out plasma and (b) with plasma-on at 7-kV applied voltage.

Step 1: For the deposition of  $\text{TiO}_2$  thin film, the ceramic plates were initially cleaned with distilled water and acetone and then dried in the oven at  $100^\circ\text{C}$  to ensure that the surface is very clean with out any impurities.

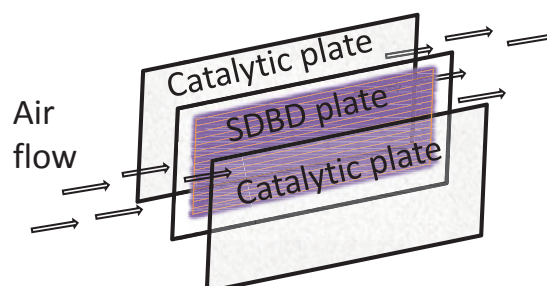


**Figure 6.4** – Planar arrangement of catalytic plates in parallel to a SDBD plate. The air flow is along the surface of all the plates.

- Step 2: Titanium (IV) tetraisopropoxide (1.77 g) is hydrolyzed with deionized water (100 ml). An ultrasonic bath was used for effective stirring up to 20 min at room temperature.
- Step 3: The resulting titanium hydroxide precipitate is separated by centrifugation. The procedure is repeated until the alcohol generated during hydrolysis of titanium alkoxide is completely removed (at least 2 times).
- Step 4: The precipitate is then dissolved in 20 ml of aqueous hydrogen peroxide (15%) to get a transparent orange sol of titanium peroxy complex and then diluted with water, after dilution the color of the sol changes from orange to yellow.
- Step 5: Poly(ethylene glycol) (PEG400) was added in order to control morphology of deposited film.
- Step 6: After mixing, the sol should be aged for 5-24 h to form a gel.
- Step 7: The viscous Ti-peroxy complex gel is used for dip coating. For that, a cleaned  $\text{Al}_2\text{O}_3$  substrate is dipped into the  $\text{TiO}_2$  gel and slowly and evenly pulled out of the gel at a uniform rate 1 mm per second. A very thin film of  $\text{TiO}_2$  is formed on the substrate and is first dried in air at room temperature followed by drying at  $100^\circ\text{C}$  for 2 hours in an electric oven. The films formed are further heated at  $400^\circ\text{C}$  for 1 hour in an electric furnace in air.
- Step 8: The remaining gel, which has not been used for dip coating is dried and calcined for XRD and TGA. The XRD and TGA data has been presented in the Appendix. 7.6 in the Fig. A.11 and A.10 respectively. The XRD reveals that the  $\text{TiO}_2$  is 43% rutile and 57% anatase.

The thickness of the  $\text{TiO}_2$  layer depends on the ageing time of the  $\text{TiO}_2$  sol. We have dip coated the ceramic plate after 6 hours which lead to a thickness of 34 nm and after 24 hours to get a thickness of 60 nm.  $\text{TiO}_2$  coated ceramic plates were characterized by

scanning electron microscopy (SEM) to determine the uniformity of coating and to check for the thickness of the coated layer. The SEM images for both 34 nm and 60 nm of  $\text{TiO}_2$  coated plates are shown in Fig. 6.5 and 6.6 respectively. The top view of the SEM images in Fig. 6.5a and 6.6a shows that the coating of the  $\text{TiO}_2$  layer is uniformly covered on the  $\text{Al}_2\text{O}_3$  plates.

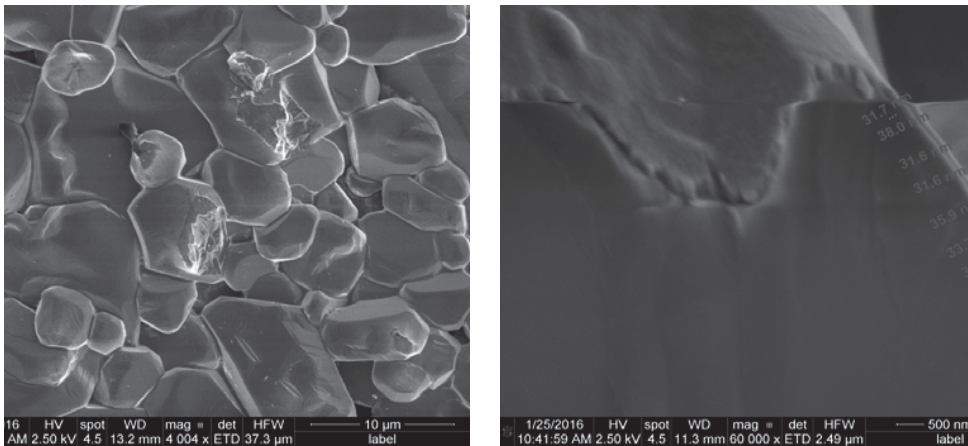


**Figure 6.5** – SEM images of ceramic plate coated with a 34 nm thin layer of  $\text{TiO}_2$  using the sol-gel dip coating technique. (a) is the top view and (b) is the cross-sectional view.

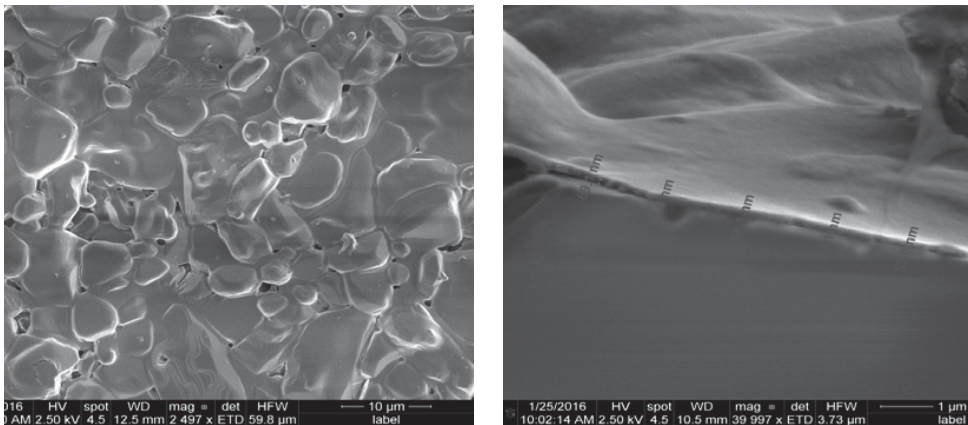


**Figure 6.6** – SEM images of ceramic plate coated with a 60 nm thin layer of  $\text{TiO}_2$  using the sol-gel dip coating technique. (a) is the top view and (b) is the cross-sectional view.

### 6.2.2.2 Design of SDBD plasma-catalytic reactor

The overview of the SDBD reactor is shown in Fig. 6.7. The SDBD plasma-catalytic reactor consists of a casing, having a rectangular section in the middle which is connected to conical input and output loft structures. The length, width and height of the reactor is approximately 470 mm, 118 mm and 109 mm respectively. The rectangular cross-section area of the reactor is provided with grooves of 1.2 mm width at the top and bottom to place the SDBD and the catalyst plates. This design can accommodate up to 20 plates in total. The reactor is constructed with 7 mm thickness of Teflon walls (except on the top of the reactor. This is to avoid short-circuiting issues) around which 1 mm thickness of stainless steel casing is made to give more stability and rigidity. To have an optical view of the plasma, the top of the reactor holds a Polymethyl methacrylate (PMMA) window. High voltage connections to the SDBD plates was realized by a metallic finger-type interface in which the SDBD plates can be inserted. The inlet and outlet gas connections has a diameter of 50 mm which makes it easy to handle large amount of flows up to 100 litres per minute. The loft diameter can be reduced with different reducers to accommodate a variable flow. The lofts at the inlet and outlet can be easily detachable to change or replace the SDBD and catalyst plates. There is a provision to place filters such as activated carbon for the gas to flow through before being exposed to the SDBD and the catalyst plates if the gas stream contains particulate matter.

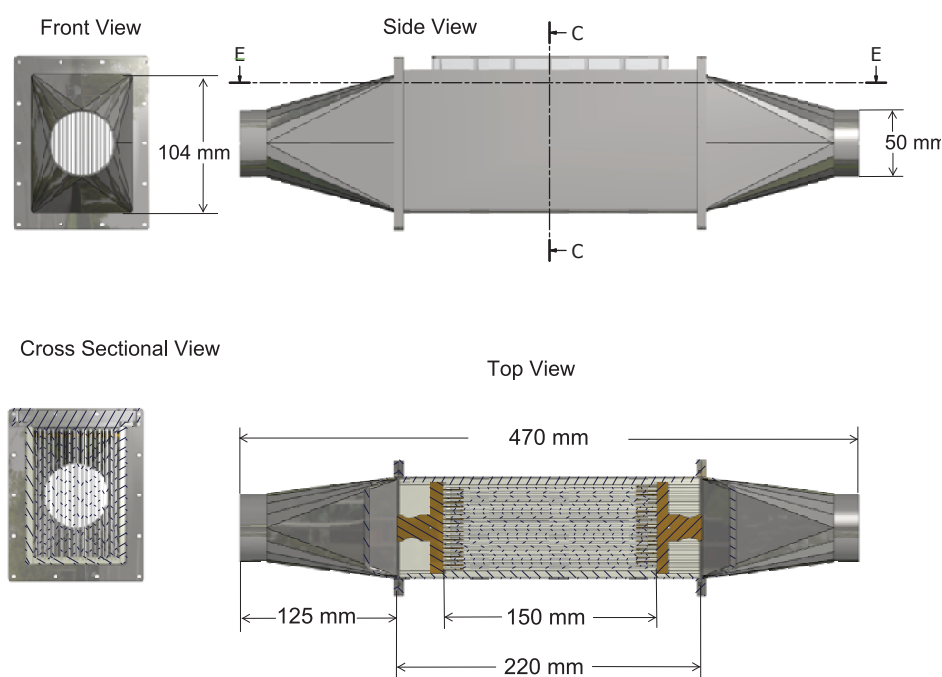


Figure 6.7 – Overview of the SDBD reactor.



## 6.3 Electrical characterization

### 6.3.1 Power modulator Topolgy

A photograph of the SDBD pulsed power modulator is shown in Fig. 6.8 and the detailed description of the solid-state pulse modulator to generate SDBD plasma is mentioned in [148]. A single SDBD modulator is able to generate pulse voltage up to 7-kV with a rise time of approximately  $2\ \mu\text{s}$ . The pulse voltage of 7 kV is limited by the capacitance of the SDBD modulator. A single SDBD modulator can power up to 2 SDBD-plates with dimensions of 100 x 150 mm when connected in parallel.

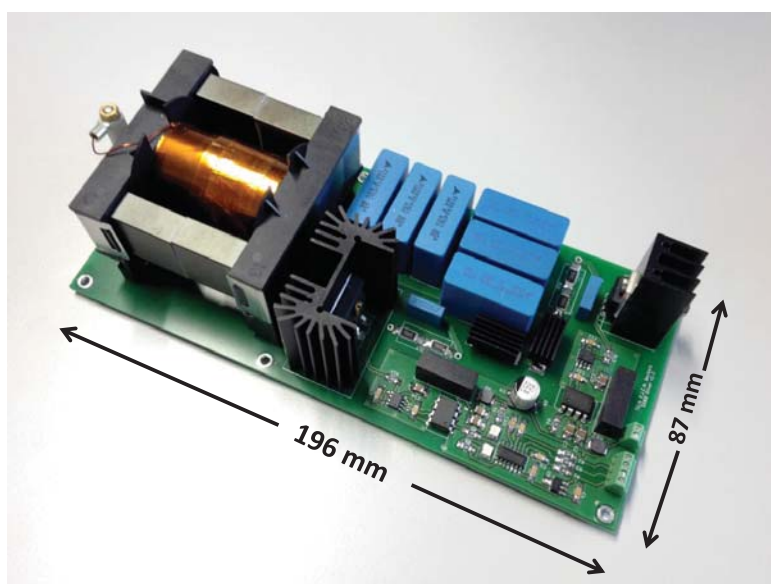


**Figure 6.8** – Photograph of a single pulsed-SDBD power modulator which was used to power the electrode-plate.

### 6.3.2 Modulator specifications

Homogeneous plasma was observed visually when the power modulator was powered by a DC voltage above 200 V. When this power modulator was powered by a DC-voltage between 200-260 V, it is able to generate a high-voltage output pulse over the electrode plate ranging from 5.9 to 7.1 kV. With the change in the DC input-voltage, the energy-per-pulse can be adjusted from 0.8 to 20 mJ. This change in the reactor peak voltage and the energy-per-pulse can be seen in Fig. 6.10. The typical voltage-current waveform and energy per pulse of the pulsed SDBD modulator is shown in Fig. 6.9. The output power to the reactor can be varied up to 120 W. Based on the maximum 120 W output power and with practically

minimum 1 slm volumetric flow rate, a maximum applicable energy density of approximately 120 J/L can be obtained. This data was collected with three pulsed-SDBD power modulators connected in parallel to 6 electrode-plates with an air flow of 10 slm. The pulse repetition rate can be varied from 0-5 kHz.

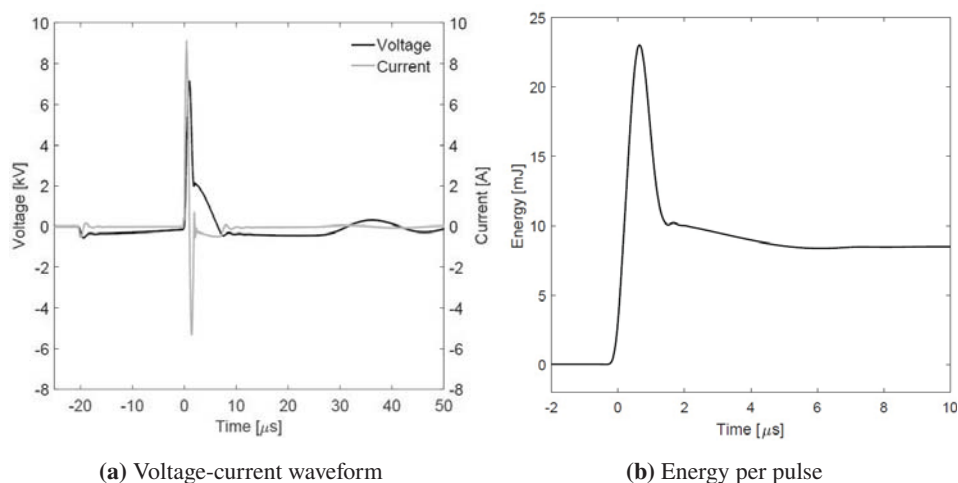


**Figure 6.9** – Typical voltage-current waveform and energy per pulse of the pulsed SDBD modulator.

## 6.4 Chemical characterization

To check the performance of this SDBD reactor, experiments were conducted for NO and VOC removal at various initial concentrations and various flow-rates. We have used ethylene as model compound for the VOC. NO and ethylene removal efficiency and the by-products formation as a function of energy density has been studied for reactor configuration having only 6 SDBD plates and also 7 Al<sub>2</sub>O<sub>3</sub> plates and TiO<sub>2</sub> coated on alumina plates placed in between and parallel to the 6 SDBD plates.

### 6.4.1 NO removal in the pulsed-SDBD reactor

In this section, we present results on NO removal with the SDBD reactor at various initial concentrations and various flow-rates. We have used 1% of NO in N<sub>2</sub> gas and diluted this with synthetic air to get the desired concentrations. All the experiments were conducted at atmospheric conditions. We have studied the NO removal efficiency and by-products formation as a function of energy density.

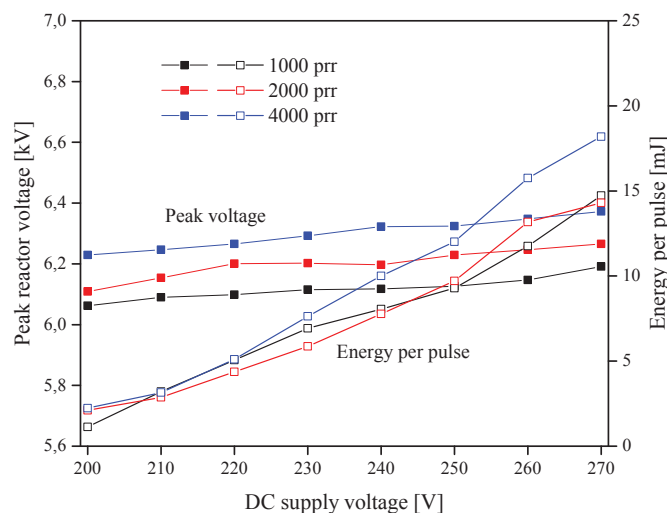


**Figure 6.10** – Reactor-peak-voltage and the energy-per-pulse as a function of the DC-supply-voltage for the three pulsed-SDBD power modulators in parallel to the 6 electrode-plates with an air flow of 10 slm.

#### 6.4.1.1 Effect of NO input concentrations

Figure 6.11 shows the NO and NO<sub>x</sub> conversion as a function of energy density for various NO input concentrations. It can be observed that with increasing NO initial concentrations, the NO conversion decreases. This behaviour was similar to the observations of the experiments conducted using a DBD reactor which were discussed in Chapter 4. NO is completely converted for the input NO concentration of 100 ppm at an energy density of approximately 20 J/L. Whereas for 300 ppm of NO input concentration, the maximum NO conversion is 65% even at high energy density of 120 J/L. It can be observed from Fig. 6.11b that with increasing energy density, NO<sub>x</sub> conversion increases initially and then starts to decrease for all the input NO concentrations. This decrease in NO<sub>x</sub> conversion at high energy densities is due to the increased NO<sub>2</sub> concentrations. With increasing the NO initial concentrations, NO<sub>x</sub> conversion increases up to 200 ppm and then decreases. For 300 ppm of NO input concentration, NO<sub>x</sub> conversion happens to be negative. These negative conversions are due to the increased NO<sub>2</sub> concentrations which contribute to the total NO<sub>x</sub> concentrations. When these NO and NO<sub>x</sub> conversions are compared to the DBD results, DBD showed higher conversions. This trend was also observed by other researchers [149, 150] for the NO<sub>x</sub> as well as for the hydrocarbons removal. It may not be appropriate in our study to quantify the results comparing SDBD and DBD even at the same energy densities because of the

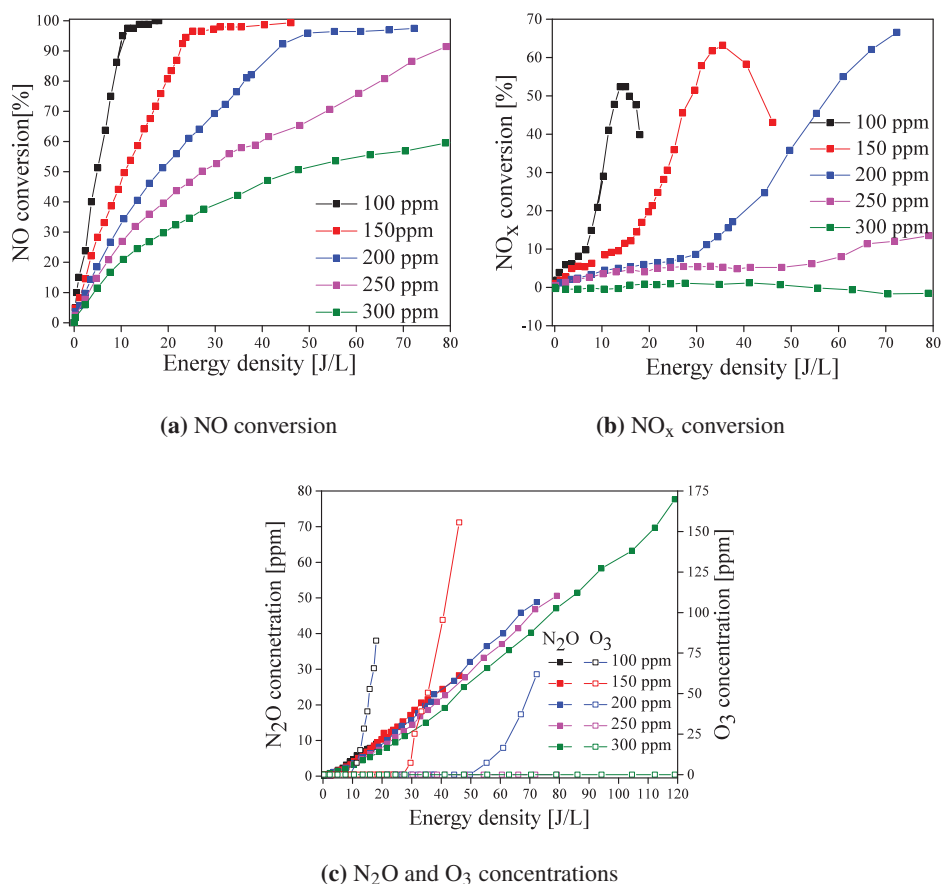


**Figure 6.11** – NO and NO<sub>x</sub> conversion and by-products formation as a function of energy density with 6 SDBD plates at various initial concentrations with the  $\mu$ s-pulsed SDBD driver.

differences in the volume of the reactor and thus the differences in the residence times. From our study on the effect of rise time, which was mentioned in Chapter 3, we observed that the short pulses gives higher removal efficiencies. The nanosecond pulse showed better removal efficiency compared to the micro-second pulse. The power modulator for DBD produced a micro-second pulse with rise-time of approximately  $0.9 \mu$ s whereas the power modulator for SDBD produced a pulse with approximately  $2 \mu$ s rise-time. This difference in the rise-time might have also played a role in the decrease of the NO and NO<sub>x</sub> removal efficiency.

The by-products formation with varying input concentrations can be seen in Fig. 6.11c. It can be observed that the N<sub>2</sub>O concentration increases linearly with energy density. At low energy densities, N<sub>2</sub>O concentrations do not depend significantly on the input NO concentrations but at higher energy densities, the effect of input NO concentrations is

slightly visible.  $O_3$  formation is more prominent for low NO input concentrations. With increasing the NO initial concentrations,  $O_3$  formation decreases. For 100 ppm of NO input concentration,  $O_3$  formation is observed at low energy densities itself. Whereas for the input NO concentration of 300 ppm, no  $O_3$  has been observed. These high  $O_3$  concentrations at low NO input concentration is because of no NO is available to consume the atomic oxygen, as NO is completely converted. The excess atomic oxygen combine with  $O_2$  to form  $O_3$  as mentioned in reaction 3.7. When the  $O_3$  concentration is compared to the DBD for the input NO concentration of 200 ppm, it is evident that SDBD produced higher  $O_3$  for the given energy density.

#### 6.4.1.2 Effect of flow-rate

Here, the effect of flow-rate on NO and  $NO_x$  conversions and the by-products formation is studied. The gas flow-rates were varied from 5 slm to 15 slm. The NO and  $NO_x$  conversion as a function of energy density for various flow-rates can be seen in Fig. 6.12. It is observed that with increasing gas flow, the NO and  $NO_x$  conversion slightly decreases. The gas flow of 10 slm showed minimum NO and  $NO_x$  conversions compared to the 5, 12 and 15 slm flow-rates. But the distinction between the NO and  $NO_x$  conversions is not so obvious as in the effect of initial concentrations. Oda *et al.* in their work on decomposition of gaseous organic contaminants by surface discharge induced plasma chemical processing - SPCP [151], studied the effect of residence time on the removal of acetone as a function of input power for the input concentrations of 100 ppm and 1000 ppm. They varied residence time by varying the flow-rate and observed that the higher conversions are achieved by increasing residence time which showed the same trend as our experiments on  $NO_x$ . On the other hand, the power efficiency is higher at shorter residence time than at longer residence times for 100 ppm input concentration. Whereas for 1000 ppm, the residence time did not show any significant effect on the power efficiency. The by-products formation is more dependent on energy density and less on flow rate as is seen in the Fig. 6.12c. The concentrations of  $N_2O$  and  $O_3$  did not show significant variation with flow rate but their concentrations increased with increasing energy density.

To study the performance of this SDBD plasma reactor combined with catalyst, the  $Al_2O_3$  plates without and with  $TiO_2$  coating were placed alternately to the SDBD plates in a parallel arrangement. Figure 6.13 shows the comparison of the NO and  $NO_x$  conversion with all these three configurations for an initial NO concentration of 200 ppm and at a gas flow-rate of 5 slm. It is observed that the NO conversion is slightly higher and  $NO_x$  conversion slightly lower for just 6 SDBD plates. When these 6 SDBD plates are combined with  $Al_2O_3$  plates with and without  $TiO_2$  coating  $NO_x$  conversions are slightly improved.  $N_2O$  and  $O_3$  concentrations are observed to increase with increasing energy density. This is because, NO is converted to  $NO_2$  which reacts with atomic nitrogen to form  $N_2O$  and atomic oxygen. This atomic oxygen through recombination reaction, produces  $O_3$ . Thus we observe an increasing trend for  $N_2O$  and  $O_3$  concentrations with increase in energy density. It can also be noticed that the by-products formation has been reduced by combining the SDBD plates with catalytic plates. With SDBD plates placed alone in the reactor, the  $N_2O$  concentration

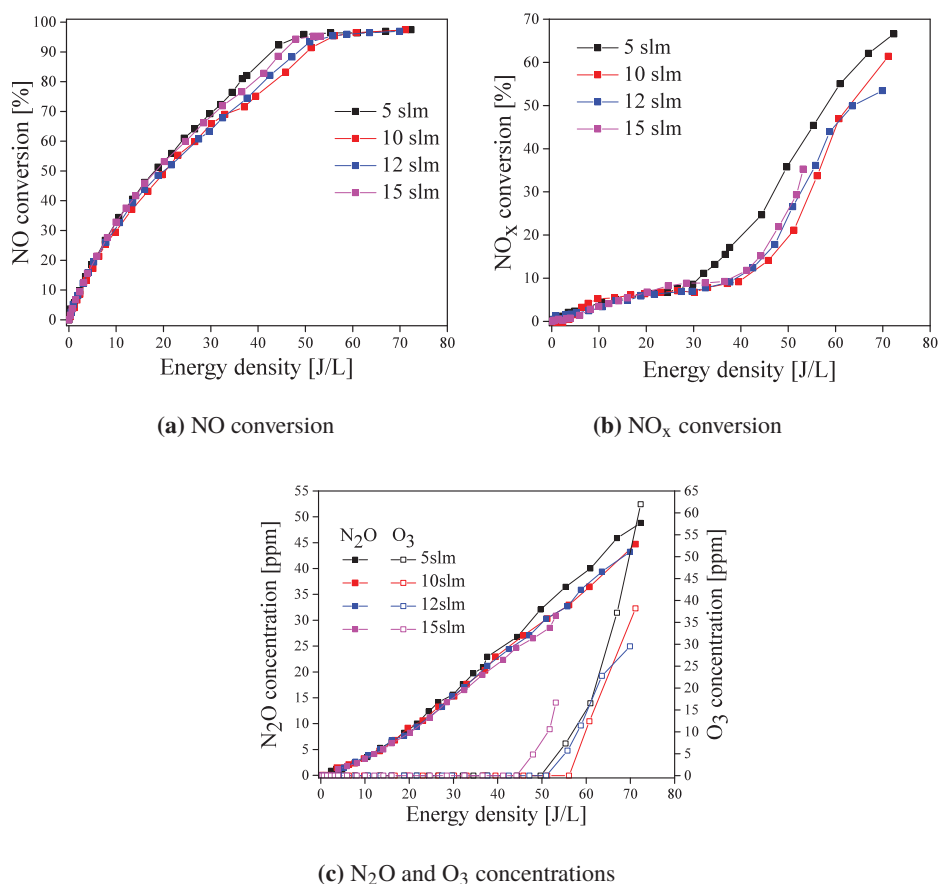


**Figure 6.12** – NO and NO<sub>x</sub> conversion and by-products formation as a function of energy density with 6 SDBD plates at various flowrates with the  $\mu$ s-pulsed SDBD driver.

is observed to be approximately 49 ppm at an energy density of 70 J/L. On the other hand when these SDBD plates are combined with catalytic plates, N<sub>2</sub>O concentrations are reduced to 33 ppm at 70 J/L. With SDBD, dissociation of oxygen is a predominant reaction and thus ozone formation occurs in almost all the experiments. The ozone concentration increases with increasing energy densities irrespective of performing experiments with just SDBD plates or placing alumina plate or TiO<sub>2</sub> coated alumina plates in between the SDBD plates. As long as NO is present in the reactor, the ozone formation will be suppressed. But combining the SDBD plates with catalytic plates showed a significant effect on the O<sub>3</sub> concentrations. O<sub>3</sub> concentrations were reduced from 62 ppm to 25 ppm, which is nearly 2.5 times, by placing the catalytic plates in combination with the SDBD plates. The probable reason for the reduction in by-products formation could be that the active species generated

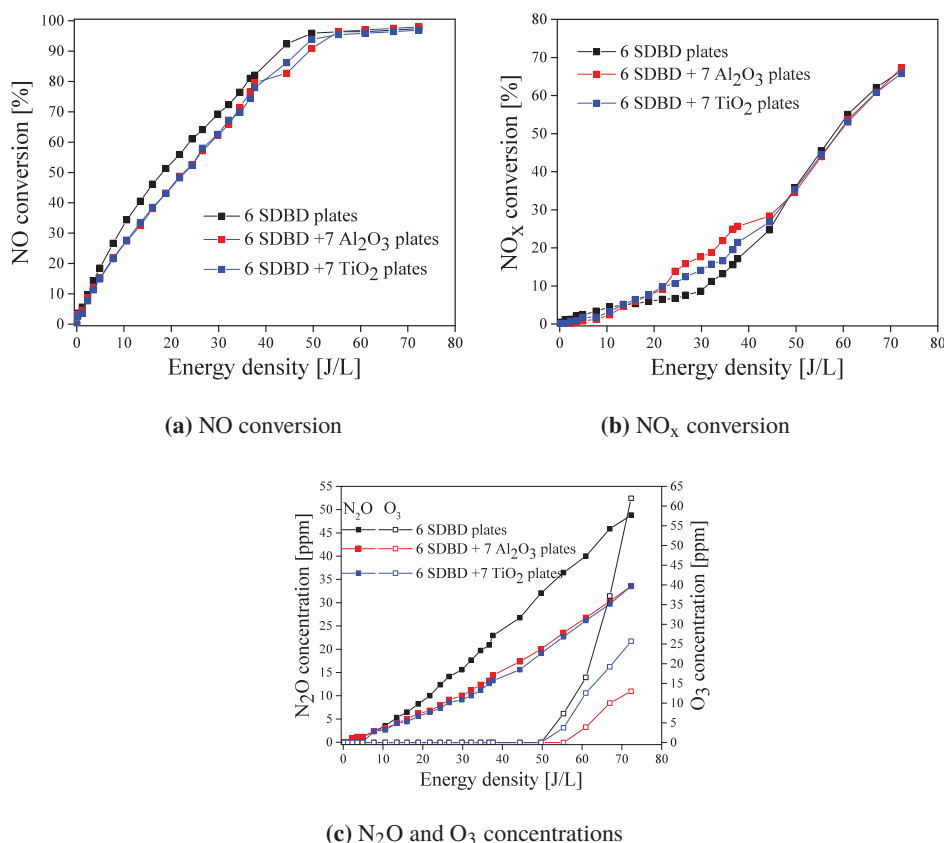


**Figure 6.13** – NO and NO<sub>x</sub> conversion and by-products formation as a function of energy density with catalytic plates placed alternately to the SDBD plates in a parallel arrangement at an input NO concentration of 200 ppm and gas flow-rate of 5 slm.

by the SDBD plasma can travel longer distance before they get quenched when there are no catalyst plates in parallel to the SDBD plates. Thus, there is a probability that more atomic nitrogen are available to react with NO<sub>2</sub> to form N<sub>2</sub>O. This might be the reason why we observed higher N<sub>2</sub>O concentrations with 6 SDBD plates. The same explanation holds good for O<sub>3</sub> as well. When the catalyst plates are placed in parallel to the SDBD plates, the generated atomic oxygen and O<sub>3</sub> collide with the walls of the catalyst plates to form O<sub>2</sub>. So, probably the catalyst plates are just acting like walls to quench the reactions than more of a catalyst. This might also explain why we have not seen any difference in the by-products concentrations of 6 SDBD+7 Al<sub>2</sub>O<sub>3</sub> plates and 6 SDBD+7 TiO<sub>2</sub> plates.

### 6.4.2 Ethylene removal in the pulsed-SDBD reactor

Here, we have evaluated the performance of the SDBD reactor for VOC removal. Ethylene was used as a model compound because of its significant impact in the food industry and in the floral markets. It is relatively simple molecule compared to other VOCs and thus it is easy to destroy with NTP. Experiments were conducted at various input concentrations of ethylene, whereby ethylene removal and CO, CO<sub>2</sub> selectivity is studied as a function of energy density. We have not evaluated the by-products formation in-detail here. The FTIR spectra for C<sub>2</sub>H<sub>4</sub> at an energy density of 50 J/L showing the by-products is shown in the Appendix. 7.6 in the Fig. A.5. The input concentration was varied from 50 ppm to 250 ppm at an interval of 50 ppm. It is observed from Fig. 6.14a that for all the input concentrations 100% conversion can be realized with increasing energy density. This complete removal of ethylene was also reported in [152] and [153]. With increasing the input concentrations, the conversion of C<sub>2</sub>H<sub>4</sub> decreases. 90% conversion of C<sub>2</sub>H<sub>4</sub> was achieved at an energy density 10.5 J/L for input concentration of 50 ppm whereas the 250 ppm obtained 90% conversion with an energy density of 76 J/L. The selectivity towards CO and CO<sub>2</sub> as a function of energy density is shown in Fig. 6.14b. With increasing energy density, the selectivity towards CO is increased. There is remarkably little on the selectivity of CO<sub>2</sub>. The selectivity towards CO is higher than CO<sub>2</sub> which means that the C<sub>2</sub>H<sub>4</sub> is converted more to CO and further oxidation of CO to CO<sub>2</sub> is limited. R.Aerts *et al.* [153] suggested a detailed destruction pathway for C<sub>2</sub>H<sub>4</sub> with dry air and humid air in their work on gas purification by non-thermal plasma: A case study of ethylene. This destruction pathway for dry air could be summarized in four main steps:

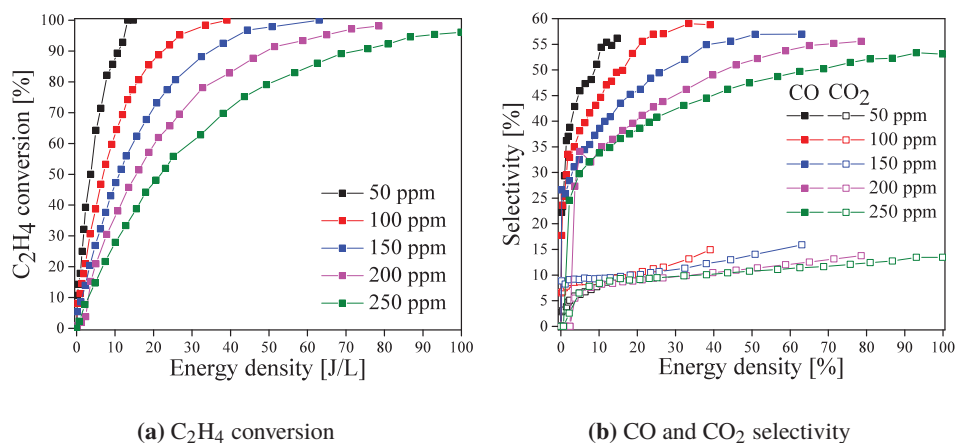


**Figure 6.14** – C<sub>2</sub>H<sub>4</sub> conversion and CO, CO<sub>2</sub> selectivity as a function of energy density with 6 SDBD plates at various C<sub>2</sub>H<sub>4</sub> input concentrations with the  $\mu$ s-pulsed SDBD driver.

Step 1: C<sub>2</sub>H<sub>4</sub> collides with N<sub>2</sub> metastables and with O atoms to produce vinyl radicals



(C<sub>2</sub>H<sub>3</sub>) and acetylene molecules (C<sub>2</sub>H<sub>2</sub>) through the following reactions:



Step 2: C<sub>2</sub>H<sub>3</sub> is oxidized by O<sub>2</sub> to form CHO radicals and HCHO. Formaldehyde is observed as by-product at low energy densities.



Step 3: C<sub>2</sub>H<sub>3</sub> may also reacts with O to form CO and CH<sub>3</sub> or C<sub>2</sub>H<sub>2</sub> and OH. The C<sub>2</sub>H<sub>2</sub> exhibits a high bond energy and also high degree of reactivity. Although its reactions with electrophilic species like OH are strongly exothermic, the formation of the intermediate pi-complex is a slow, rate determining process. Therefore, C<sub>2</sub>H<sub>2</sub> yet can be observed as product.



Step 4: CHO is further oxidized by O, O<sub>2</sub> and OH to form CO and CO<sub>2</sub>



Thus, in the ethylene destruction pathway, CO, CO<sub>2</sub>, HCHO and C<sub>2</sub>H<sub>2</sub> are the main by-products that were produced. In this study, we have studied the CO and CO<sub>2</sub> formations and not the formaldehyde or acetylene because of the limitations to quantify them with the existing experimental setup. With increasing the input concentrations, the selectivity towards CO is increased. There is remarkably little effect on the selectivity of CO<sub>2</sub> as seen Fig. 6.14b. This decrease in selectivity is due to the lower conversion of C<sub>2</sub>H<sub>4</sub> itself. The maximum CO selectivity that is observed here is 60% for an input concentration of 100 ppm.

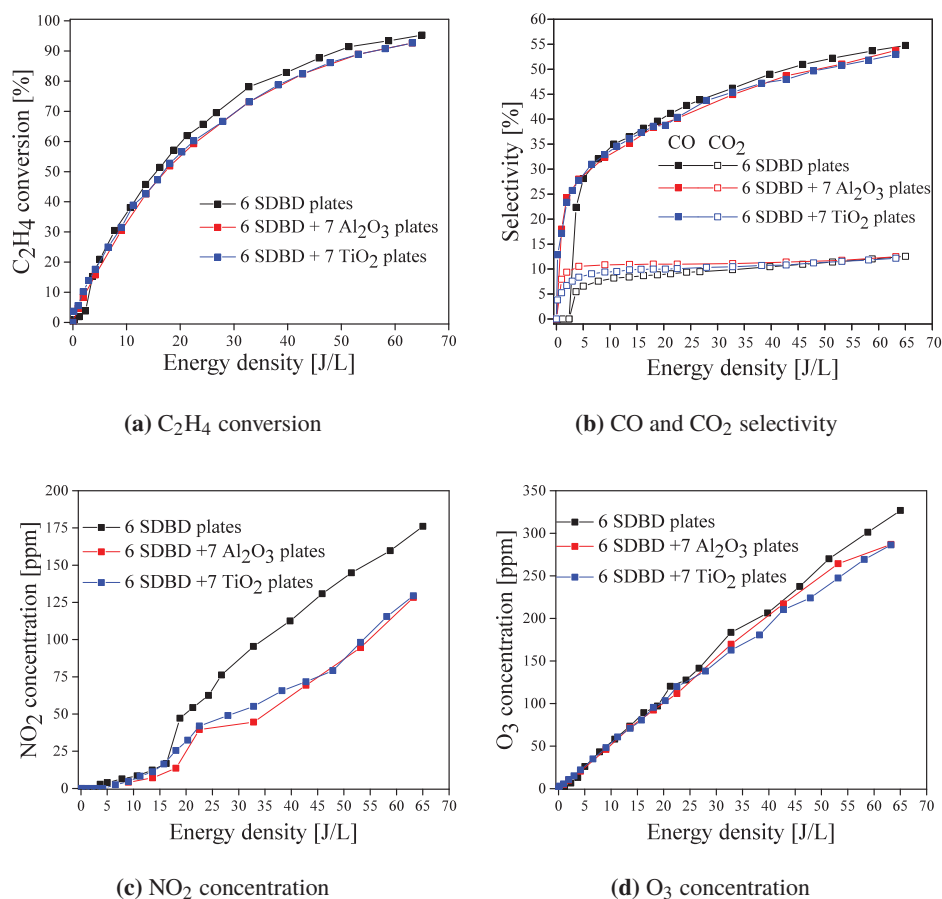


**Figure 6.15** – C<sub>2</sub>H<sub>4</sub> conversion and CO, CO<sub>2</sub> selectivity and NO<sub>2</sub> and O<sub>3</sub> concentrations as a function of energy density with and without catalytic plates placed alternately to the SDBD plates in a parallel arrangement with an input C<sub>2</sub>H<sub>4</sub> concentration of 200 ppm and a gas flow of 5 slm with the  $\mu$ s-pulsed SDBD driver.

The selectivity towards CO<sub>2</sub> is higher for low concentrations because at low concentrations, C<sub>2</sub>H<sub>4</sub> is completely converted to CO at low energy densities and thus the remaining energy is used to oxidize CO to CO<sub>2</sub>. Thus CO is observed as a main by-product for all the concentrations.

In real time applications, CO and HCHO are not the preferred by-products because of their toxic nature and thus we need higher energy densities as mentioned by [152] to oxidize CO and HCHO to CO<sub>2</sub>. Combining plasma with a catalyst is another option to increase the selectivity towards CO<sub>2</sub>. We tried to evaluate the third option by combining SDBD plates with plates coated with TiO<sub>2</sub> and studied the conversion of C<sub>2</sub>H<sub>4</sub>, selectivity towards CO and

CO<sub>2</sub> and other by-products such as O<sub>3</sub> and NO<sub>x</sub>. The effect of placing the catalytic plates on the C<sub>2</sub>H<sub>4</sub> conversion and on CO and CO<sub>2</sub> selectivity can be seen in Fig. 6.15. It is noticed that the C<sub>2</sub>H<sub>4</sub> conversion is slightly higher with just the SDBD plates than combined with the catalytic plates. There is no notable difference in the selectivity towards CO and CO<sub>2</sub>. As the gas mixture consists of N<sub>2</sub> and O<sub>2</sub> because of synthetic air, we also observed NO<sub>2</sub>, O<sub>3</sub> as by-products and the results are presented in Fig. 6.15c and Fig. 6.15d respectively. NO<sub>2</sub> concentration increases with increasing energy density. Harling *et al.* [154] in their work on the novel method for enhancing the destruction of environmental pollutants by the combination of multiple plasma discharges, mentioned that they have not observed any NO and NO<sub>2</sub> concentrations which is in contradiction to our results. R.Aerts *et al.*, [153] also reported very low NO<sub>2</sub> concentrations. This may be because of the high energy densities that they have used where the NO<sub>2</sub> is further converted to N<sub>2</sub>O and HNO<sub>2</sub>. The SDBD plates combined with catalytic plates showed lower NO<sub>2</sub> concentrations and O<sub>3</sub> concentrations. With the TiO<sub>2</sub> sol-gel method that we have used to coat the Al<sub>2</sub>O<sub>3</sub> plates with TiO<sub>2</sub>, we have managed to obtain only a TiO<sub>2</sub> layer thickness of 60 nm. It will be interesting to study the performance of the reactor with the increased thickness of TiO<sub>2</sub> layer which can show increased catalytic activity.

## 6.5 Conclusions

Surface-dielectric-barrier-discharges (SDBDs) have become popular recently due to their ease of generation and their wide range of applications such as ozone generation, surface treatments and air-pollutants removal. In this chapter, we have developed a modular plasma-catalytic surface-dielectric-barrier-discharge (SDBD) reactor to handle large flows which could be scaled-up and scaled-down easily. A SDBD power modulator was developed to generate high-voltage pulses up to 7 kV with microsecond duration that can power two electrode-plates. We have used 3 SDBD power modulators connected in parallel to power up to 6 SDBD plates. The applied power can be controlled by pulse-repetition rate. The electrical and the chemical characterization of the developed SDBD reactor has been done. Reactor performance was analyzed by conducting experiments with NO<sub>x</sub> and ethylene at various input concentrations and various flow-rates and studying the conversions and the by-products formation.

In general, DBD performed better than SDBD with respect to NO and NO<sub>x</sub> conversions despite the SDBD modulator providing higher input energy per pulse. This may be due to the short rise-time pulses created in DBD than in SDBD. With increasing NO initial concentrations, the NO and NO<sub>x</sub> conversion decreases. We have observed negative NO<sub>x</sub> conversion for 300 ppm of NO input concentration. With increasing gas flow, the NO and NO<sub>x</sub> conversion decreases. Thus higher conversion is achieved at longer residence time.

We have evaluated the performance of the SDBD reactor for VOC removal and ethylene was used as a model compound due to its interest in the food and floral industry. 100% conversion of C<sub>2</sub>H<sub>4</sub> was obtained for all the input concentrations. With increasing the input concentrations, the conversion of C<sub>2</sub>H<sub>4</sub> decreases similar to the trend of NO<sub>x</sub> conversion.

With increasing the input concentrations, the selectivity towards CO is observed to decrease while there is no effect on the selectivity towards CO<sub>2</sub>. This decrease in selectivity of CO is due to the lower conversion of C<sub>2</sub>H<sub>4</sub> itself.

To reduce the by-products formation, we were interested to look into the option of combining this SDBD reactor with catalyst. To study the performance of the SDBD plasma reactor combined with catalyst, the Al<sub>2</sub>O<sub>3</sub> plates without TiO<sub>2</sub> coating and with TiO<sub>2</sub> coating were placed alternatively to the SDBD plates in a parallel arrangement. When these 6 SDBD plates are combined with Al<sub>2</sub>O<sub>3</sub> plates with and without TiO<sub>2</sub> coating, C<sub>2</sub>H<sub>4</sub> conversion is marginally improved. The by-products formation have been reduced by combining the SDBD plates with catalytic plates. O<sub>3</sub> concentrations in the NO<sub>x</sub> removal experiments were reduced from 62 ppm to 25 ppm, which is nearly 2.5 times, by placing the catalytic plates in combination with the SDBD plates. There is significant reduction in NO<sub>x</sub> concentration and slight reduction in O<sub>3</sub> concentration in the C<sub>2</sub>H<sub>4</sub> removal experiments. With the sol-gel method that we have used here to coat the Al<sub>2</sub>O<sub>3</sub> plate with TiO<sub>2</sub>, we have managed to obtain the TiO<sub>2</sub> layer with thickness of 60 nm. It will be interesting to study the performance of the reactor with the increased layer thickness of TiO<sub>2</sub> which can show increased catalytic activity. With increased catalytic activity we may obtain higher conversions and low concentrations of by-products. Thus, it will be worthwhile to investigate a better coating technique to get a thicker and a homogeneous deposition of the TiO<sub>2</sub> layer on the Al<sub>2</sub>O<sub>3</sub> plates.



---

## CONCLUSIONS AND RECOMMENDATIONS

---

Non-thermal plasma (NTP) technology has been researched for the past few decades for environmental remediation, bio-medical and surface engineering applications. In this thesis we focussed on combining non-thermal plasma (NTP) technology and catalysts for air purification applications by using a dielectric-barrier-discharge (DBD) reactor. We investigated the effect of various electrical and operational parameters on the performance of the DBD reactor in terms of  $\text{NO}_x$ , by-products concentrations and energy costs. We performed this parametric study systematically using the three reactor configurations: plasma-alone, IPC and PPC configurations. We have also performed screening of the catalytic materials for  $\text{NO}_x$  removal and studied the role of the catalytic material in changing the plasma discharge characteristics. As a part of the environmental sensors for energy efficiency (ESEE)- EU project, we have developed a modular plasma-catalytic surface-dielectric-barrier-discharge (SDBD) reactor to handle large flows which could be scaled-up and scaled-down easily.

### 7.1 Research goals

In this thesis, we have investigated the combination of non-thermal plasma (NTP) technology and catalysts for air purification applications and the effect of various parameters on the plasma and plasma-catalytic processing efficiency.  $\text{NO}_x$  has been taken as target pollutant and the effect of various parameters on its removal efficiency have been researched using a pulsed-DBD (with and without a catalyst) and a SDBD reactor (with and without a catalyst). The main goals of this research were:

- To systematically study the effect of various electrical and operational parameters on  $\text{NO}_x$  removal and to optimize the performance of our DBD configuration.

- To understand the plasma-catalytic interactions by studying the physical interaction of the plasma with the catalyst and to correlate this interaction with the chemical processing efficiency.
- To develop an on-demand air purifier which could be scaled-up and scaled-down easily by using plasma-catalytic technology.

We have achieved the first research goal by two approaches. First, we optimized the plasma reactor for NO<sub>x</sub> removal by varying the electrical parameters, such as applied peak-voltage, pulse polarity and pulse rise-time. This was done for all the three reactor configurations: plasma-alone, in-plasma (IPC) and post-plasma (PPC). We have observed that for waveform with microsecond-pulse duration, with positive polarity and 16-kV applied peak-voltage, gives the most optimum NO<sub>x</sub> conversion. It was also observed that, in comparison with the plasma-alone configuration and the PPC configuration, the IPC configuration performs better with respect to both NO conversion and reducing by-products formation. We used these conditions for further experiments to analyze the effect of operating conditions such as input NO concentrations, gas flow rate and reactor temperature. It was observed that high removal efficiencies were obtained at low input concentrations and low flow rates for all the three configurations. Also it was found that the PPC configuration performed better at increased reactor temperatures.

Secondly, we packed the reactor with various catalytic materials and have tested the NO<sub>x</sub> removal in both IPC and PPC configurations. It was observed that metal oxides loaded on Al<sub>2</sub>O<sub>3</sub> showed better NO<sub>x</sub> removal.

The second research goal was achieved by analyzing the voltage-current waveforms for all the catalytic materials that we have used. The current waveforms provide information on how the discharge varies for different catalytic materials that are placed inside the DBD reactor. We have related the differences in discharge characteristics to the dielectric constants of the materials used. Therefore, the dielectric constants of all the catalytic materials have been measured. We also have done ICCD imaging and correlated the observed plasma intensities with the chemical activity of the plasma-reactor and of the plasma-reactor filled with catalytic materials.

We achieved the third research goal by developing a modular plasma-catalytic surface-dielectric-barrier-discharge (SDBD) reactor to handle large flows. A SDBD power modulator was developed to generate 7-kV high-voltage pulses with microsecond duration that can power two SDBD-reactor plates at a maximum of 5 kHz pulse repetition rate. The electrical, chemical and the reactor characterization of this developed SDBD reactor was done. We studied the performance of the SDBD using NO<sub>x</sub> and ethylene as model compounds. This reactor was developed as a part of EU-funded project Environmental sensors for Energy Efficiency (ESEE) and was successfully demonstrated as a final deliverable in the consortium meeting organized at CIAT, France.

The summary and the main conclusions of this work are organized in line with the chapter titles in this thesis and discussed in the following sections.

## 7.2 Investigation on the effect of electrical parameters on NO<sub>x</sub> removal

In this chapter, we optimized the electrical parameters to obtain energy efficient NO<sub>x</sub> remediation. We have varied electrical parameters such as the applied peak voltage, the pulse polarity and the pulse rise-time, and studied the effect of these parameters on the removal of NO and NO<sub>x</sub>, the by-products formation and the energy consumption. This study was done for all- the three configurations: plasma-alone, in-plasma catalytic configuration(IPC) and post-plasma catalytic configuration (PPC). Commonly used catalyst support materials such as TiO<sub>2</sub>, Al<sub>2</sub>O<sub>3</sub>, zeolites and SiO<sub>2</sub> have been used in the IPC and the PPC configurations. The main conclusion from this chapter are listed below.

- It is observed that the NO conversions and the by-products formation strongly depend on the plasma energy density, and not on the applied peak-voltage. The NO conversion and the formation of by-products increases with increase in the energy density. At higher energy density, the amount of radicals production increases leading to increased conversions and by-products formation. We have shown that the energy deposition per pulse increases with increase in the applied peak-voltage. High energy deposition per pulse leads to increased microdischarges resulting in increased conversions. This increased microdischarge activity also heat up the gas resulting in the energy losses. Therefore the energy costs increases at higher applied peak-voltages.
- The effect of using positive polarity pulses or negative polarity pulses on the NO<sub>x</sub> removal efficiency has been tested. We found that that the positive voltage pulses performed better than negative pulses with respect to NO<sub>x</sub> except for the case that a SiO<sub>2</sub> catalytic support is used in an IPC configuration. There is no significant difference in the by-products formation between the positive and the negative pulses. The reason for the increased conversion with positive pulses might be due to increased reactive species production with positive pulses as compared to the negative pulses. Also, few studies have indicated that the negative polarity pulses produces less streamer volume and thus low production of atomic oxygen.
- We have compared the NO<sub>x</sub> removal efficiency using high-voltage pulses with microsecond pulse rise-time and with nanosecond pulse rise-time. It was observed that the ns pulse showed higher conversions but at the expense of higher by-products formation for the given energy density. At high energy density, both the  $\mu$ s pulse and the ns pulse obtain similar NO conversion but the N<sub>2</sub>O, O<sub>3</sub> and N<sub>2</sub>O<sub>5</sub> concentrations are quite high with the ns pulse. The applied voltage for the ns pulse is approximately 40 kV where as for the  $\mu$ s pulse is approximately 16 kV which means high energy per pulse can be deposited with ns pulse as compared to the  $\mu$ s pulse. This could be a reason that the short rise time pulses showed higher conversions and higher by-products formation. The better performance of the short rise-time pulses for NO conversion is observed in all the three tested reactor configurations.



### 7.3 Investigation on the effect of operational parameters on NO<sub>x</sub> removal

In this chapter, we analyzed the influence of various operational parameters such as input NO concentrations, gas flow-rate, and reactor temperature on the efficiency of NO<sub>x</sub> removal. We have evaluated the performance by considering the increase in the NO<sub>x</sub> removal and the decrease in by-products formation. We have studied the effect of operational parameters with the plasma-alone configuration, with the IPC and with the PPC configuration. For each configuration we investigated the efficiency of NO<sub>x</sub> removal and the by-products formation. Commonly used support materials such as TiO<sub>2</sub>, Al<sub>2</sub>O<sub>3</sub>, zeolites and SiO<sub>2</sub> have been used in the IPC and the PPC configuration. The main observations and conclusions are as follows:

- High NO removal efficiency can be obtained at low NO input concentrations for all the three configurations. Higher input concentrations require higher energy densities to obtain complete conversions. Therefore, the energy deposited in the plasma is used for the NO conversion and thus we observe lower by-products formation at higher input concentrations. The highest NO conversions are obtained with the plasma-alone configuration but at the expense of high NO<sub>x</sub>, N<sub>2</sub>O and O<sub>3</sub> concentrations followed by the IPC configuration and then by the PPC configuration. This is because, the plasma-alone configuration is efficient in converting NO to NO<sub>2</sub> at low energy density and due to this we see higher NO<sub>x</sub> concentrations as NO<sub>x</sub> is the sum of NO and NO<sub>2</sub>. On the other hand, the IPC configuration requires slightly higher energy density to obtain complete NO conversions and thus shows moderate NO<sub>x</sub>, N<sub>2</sub>O and O<sub>3</sub> concentrations.
- High NO removal efficiency can be obtained at low gas flow rates for the plasma-alone and for the PPC configuration. At low gas flow rates, the time spent by a NO molecule increases which increases the probability of collisions between the electrons and gas molecules resulting in higher generation of atomic N and O at a given energy density. With more atomic N and O available, the NO conversion increases at low gas flow rates. The IPC configuration does not show significant dependence of the NO conversion on flow rate up to 5 slm, while at 6 slm, lower NO conversions are observed. This probably could be due to the transport limitation of the catalytic reactions. The higher conversions at lower gas flow rates come at the expense of higher N<sub>2</sub>O and O<sub>3</sub> concentrations.
- With increasing reactor temperature, the NO conversion decreases for the IPC configuration whereas the PPC configuration showed increased NO conversions. This is due to the ease of ozone decomposition at higher temperatures facilitating the back formation of NO in the IPC configuration. The PPC configuration behaviour is similar to the thermal catalysis. Typically above 150 °C, all the catalytic materials showed a distinct behaviour suggesting that the catalytic materials are activated from this temperature. Both the configurations performed better with respect to minimum by-products formation at higher temperatures. This is again due to the ozone decomposition with increasing temperatures.

## 7.4 Screening of catalytic materials for NO<sub>x</sub> removal

In this chapter, we have studied NO<sub>x</sub> removal by loading various metal oxides on TiO<sub>2</sub> and Al<sub>2</sub>O<sub>3</sub> supports, combining them with a pulsed DBD reactor. The metal-oxides that we have used in this study are NiO, MnO, CuO, Fe<sub>3</sub>O<sub>4</sub>, Co<sub>3</sub>O<sub>4</sub>. To understand the effect of support material, we have loaded 3wt% of these metal oxides both on TiO<sub>2</sub> and Al<sub>2</sub>O<sub>3</sub> and compared their NO conversion, NO<sub>x</sub> concentration and by-products formation using both the in-plasma configuration (IPC) and the post-plasma configuration (PPC). We also studied the effect of metal loading, where we have compared the performance of 3wt% and 5wt% of these metal oxides loaded on TiO<sub>2</sub>. Also this comparison was made for both the IPC and the PPC configuration. Finally, in this chapter we studied the effect of the catalytic material on the plasma discharge characteristics by analyzing the voltage-current waveforms and by measuring the dielectric constants of these materials to correlate them to the discharge characteristics. The main conclusions from this chapter are:

- The NO conversion is highest for the plasma-alone configuration, followed by the IPC and then by the PPC configurations. The by-products formation are observed to be less when combining the DBD plasma with catalytic materials. All the catalytic materials significantly suppressed the formation of O<sub>3</sub> which could be due to the insitu decomposition of O<sub>3</sub> to atomic oxygen.
- We correlated the differences in the performance of the various metal oxides loaded on TiO<sub>2</sub> and Al<sub>2</sub>O<sub>3</sub> by looking into the voltage-current waveforms and correlated these parameters to the discharge activity. The plasma-alone configuration showed a current waveform with intense current spikes, indicating intense microdischarge activity. When a catalytic material is introduced into the plasma reactor, the discharge activity is changed significantly. For instance, when Al<sub>2</sub>O<sub>3</sub> is placed inside the reactor, the current waveform shows microdischarge activity but with slightly lower magnitude than for the plasma-alone reactor. Similarly when the DBD reactor is packed with TiO<sub>2</sub>, the current waveform shows less microdischarge activity. This change in the discharge activity could be explained with differences of the dielectric constants of the materials.
- With the increase in the wt% of metal oxide loading on TiO<sub>2</sub>, the NO conversions increase notably. There is also a significant difference in the NO<sub>x</sub> concentration. We have observed that varying the metal-oxide loading varied the discharge activity. With increase in metal oxide loading, the magnitude of the transient spikes in the current waveform is increased, which indicates an increased number and intensity of microdischarges. This increase in microdischarges may lead to an increase in reactive species production. With increased reactive species production, the conversions and by-products formation depend on this as well. This change in discharge behaviour could be due to differences in the dielectric constant for different amounts of metal-oxide loadings. The CuO catalyst with 5wt% loading on TiO<sub>2</sub> performed best for both the NO<sub>x</sub> removal as well with low by-products formation in the IPC configuration.

- The conversion obtained in the PPC configurations are lower than with the plasma-alone and the IPC configurations. However, both the PPC and the IPC configuration resulted in lower by-product formation. In general, if high conversions are required with moderate by-products formation, the IPC configuration is preferred and if the by-products formation is a serious issue then the PPC configuration is a preferred choice.

## 7.5 SDBD reactor for on-demand air purification

In Chapter 6, we have developed a modular plasma-catalytic surface-dielectric-barrier-discharge (SDBD) reactor to handle large flows and which could be scaled-up and scaled-down easily. A SDBD power modulator was developed to generate 7-kV high-voltage pulses with microsecond duration that can power two SDBD-reactor plates at a maximum of 5 kHz pulse repetition rate. The developed reactor can accommodate up to 20 SDBD plates and thus 10 such SDBD driver units are needed to power the entire reactor and to treat larger flows. The electrical and the chemical characterization of this SDBD reactor is discussed in detail in this chapter. The operational efficiency of the developed SDBD has been investigated by studying the removal of both  $\text{NO}_x$  and ethylene. Finally, we combined the SDBD plasma reactor with catalyst by positioning  $\text{Al}_2\text{O}_3$  plates (without or with a  $\text{TiO}_2$  catalytic coating) alternatively to the SDBD plates in a parallel arrangement. The conclusions from this chapter are as follows:

- The dependence on operational parameters of NO and  $\text{NO}_x$  conversions obtained with the SDBD reactor, was comparable to the behaviour of the DBD reactor. In general, the DBD reactor performed better than the SDBD reactor with respect to NO and  $\text{NO}_x$  conversions, despite of the SDBD modulator providing higher input energy per pulse.
- When the SDBD plates are combined with  $\text{Al}_2\text{O}_3$  plates with and without the  $\text{TiO}_2$  catalytic coating, the  $\text{C}_2\text{H}_4$  conversion conversions are marginally improved. The formation of by-products is reduced when combining the SDBD plates with catalytic plates:  $\text{O}_3$  concentrations in the  $\text{NO}_x$  removal experiments were reduced from 62 ppm to 25 ppm, which is nearly 2.5 times, by applying catalytic plates in combination with SDBD plates. There is significant reduction in  $\text{NO}_x$  concentration and slight reduction in  $\text{O}_3$  concentration in the  $\text{C}_2\text{H}_4$  removal experiments by applying catalytic plates in combination with SDBD plates. Although, we observed better performance of the SDBD reactor with the catalytic plates, it is not clear whether the catalytic plates acts more like a catalyst to increase the product selectivity or behave like walls to quench the reactions. Probably, if we can increase the thickness of  $\text{TiO}_2$  coating from 60 nm to few  $\mu\text{m}$  thickness then we can understand the role of these catalytic plates.

## 7.6 Recommendations for future work

We have studied the efficiency of  $\text{NO}_x$  removal in a systematic manner by using various catalytic materials in both the IPC and the PPC configurations, under various electrical and operational conditions. But we realize that this study is not complete yet. There are still some remaining questions for a good understanding of the  $\text{NO}_x$  removal mechanisms.

- In practical applications, the presence of moisture and hydrocarbons in the air flows to be purified, cannot be avoided. Thus, it will be informative if this parametric study could be extended further to study the effect of moisture content and hydrocarbon addition on  $\text{NO}_x$  removal, for the two configurations considered here: the IPC and the PPC configurations. We did the parametric study using model gas compositions, however it will also be worthwhile to do this parametric study for practical exhaust gases from diesel engines, in order to further verify the feasibility to valorize the plasma-catalytic technology.
- We have studied the efficiency of  $\text{NO}_x$  removal by using various metal-oxides on  $\text{TiO}_2$  and  $\text{Al}_2\text{O}_3$  supports using both the IPC and PPC configurations. However, this catalyst screening is far from complete. In all our experiments we have used a particle size of 1-2 mm. When we change the particle size, the void spacing changes, which in-turn affects the residence time distribution and eventually the conversions. It will be interesting to do residence time distribution (RTD) studies with the DBD-plasma reactor and the two plasma-catalytic reactors, to study the effect of void spacing on the residence time. Also, other parameters such as particle size and shape do effect the plasma discharges. Thus, this systematic study could be extended to study the  $\text{NO}_x$  removal efficiency with varying particle size, shape.
- The activity, selectivity and the life-time of the catalyst are determining factors when choosing a catalyst. It will be interesting to study the life-time of the catalyst after plasma exposure and also to study the regeneration of the catalyst using plasma.
- It will be interesting to study the gas-phase and adsorbed-phase-species, by performing adsorption and desorption experiments for all the catalytic materials to deduce plausible surface mechanisms. This can further give information on the difference in the performance of these catalytic materials in both the IPC configuration and the PPC configuration.
- We saw from the spatial development of the discharges that introducing a packing material within the plasma affects the discharge behaviour. Also, the metal-oxide loading affects the plasma dynamics. It will be interesting to study further the effect of various metal-oxides and the effect of various wt% of loadings on the plasma development and intensity. In our study, we could not clearly distinguish whether the discharges are surface discharges, along the catalytic surface or are filamentary discharges, and how the discharge mode depends on the catalytic packing material.

Probably, a more dedicated reactor where we could pack the reactor with only one or very few pellets is needed to study this more in detail.

- We have developed the SDBD reactor and successfully demonstrated pollutant conversions. While discussing the results, the role and functionality of the catalytic plates could not be clarified. Whether these catalytic plates are just acting like a surface to quench the reactions or really contribute to surface reactions remains unclear. To understand this, there is a need to down-scale the existing reactor where we can insert one SDBD plate and one catalytic plate. With this configuration, we will be able to vary the distances between the plates, coating techniques for the catalytic plates and the thickness of the catalytic material. Through this, we can gain more insights in the role of the catalytic plates.

---

# APPENDIX

---

## A1. Supplementary data for the experimental setup

### Characterization of catalytic materials

#### X-ray diffraction patterns for various catalytic materials

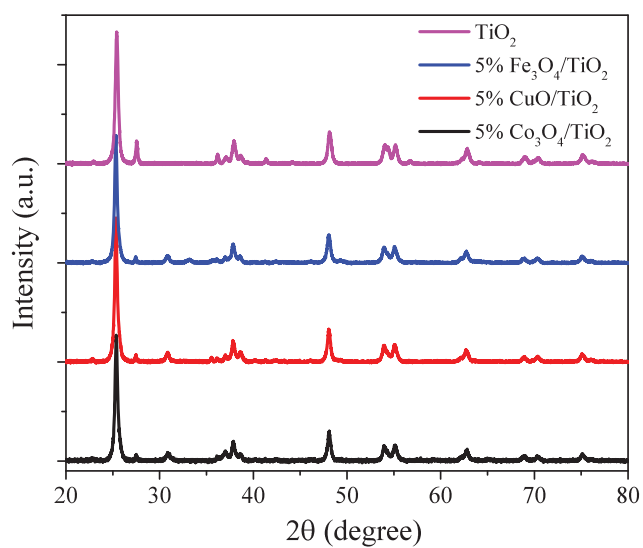


**Figure A.1** – X-ray diffraction patterns for  $\text{TiO}_2$  and metal oxides loaded on  $\text{TiO}_2$ . Baselines are shifted for clarity

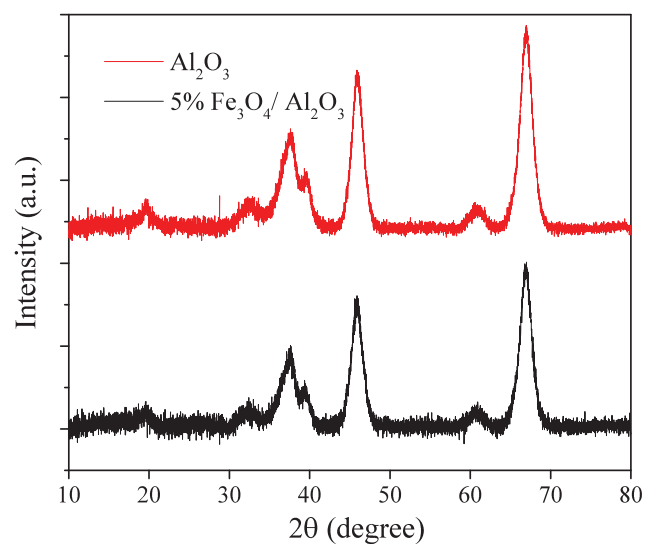
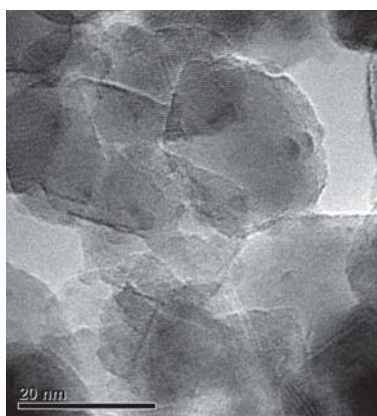
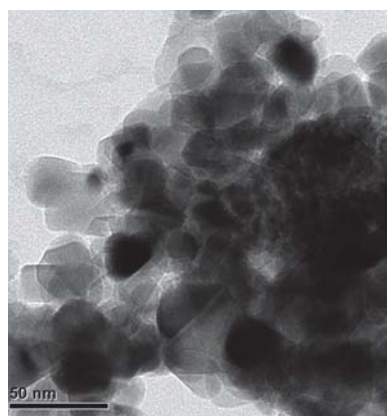


**Figure A.2** – X-ray diffraction patterns for Al<sub>2</sub>O<sub>3</sub> and 5% Fe<sub>3</sub>O<sub>4</sub>/Al<sub>2</sub>O<sub>3</sub>. Baselines are shifted for clarity

### TEM images for various catalytic materials

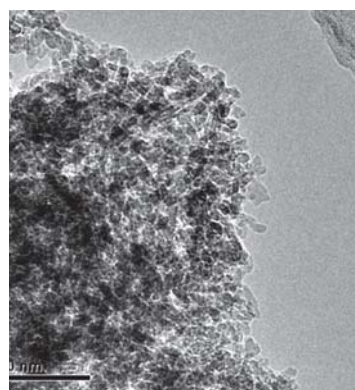


(a) 3% CuO/TiO<sub>2</sub>

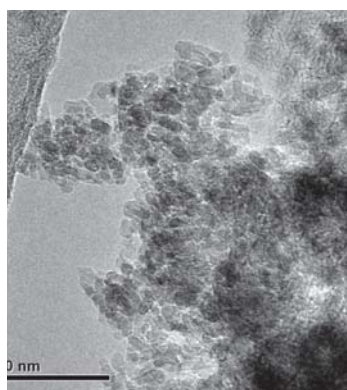


(b) 3% Fe<sub>3</sub>O<sub>4</sub>/TiO<sub>2</sub>

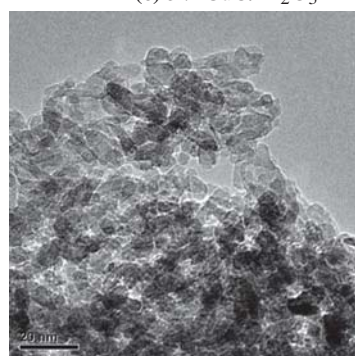
**Figure A.3** – TEM images of the metal oxides loaded on TiO<sub>2</sub> and Al<sub>2</sub>O<sub>3</sub>



(c) 3% CuO/Al<sub>2</sub>O<sub>3</sub>



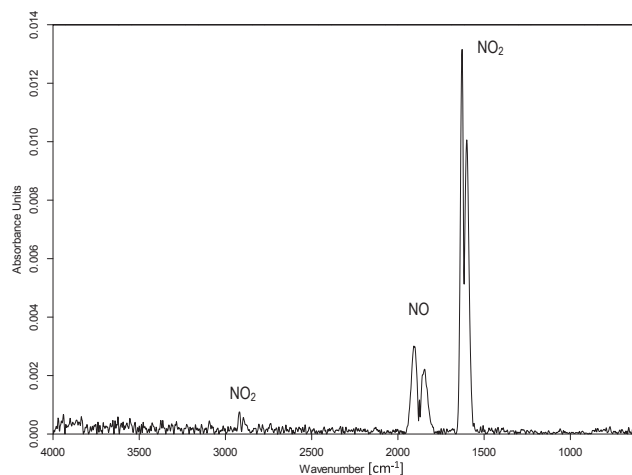
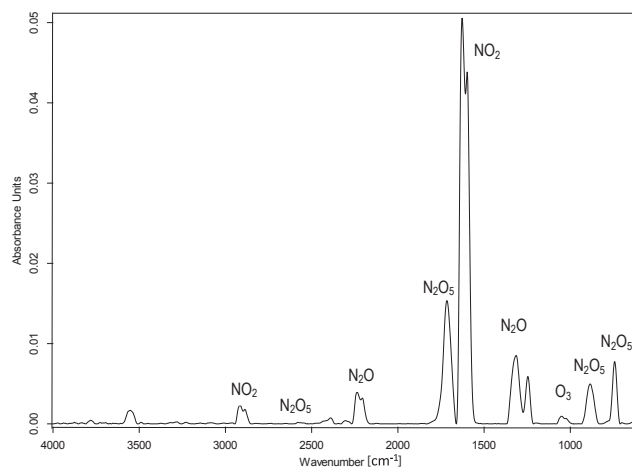
(d) 3% Co<sub>3</sub>O<sub>4</sub>/TiO<sub>2</sub>



(e) 3% Fe<sub>3</sub>O<sub>4</sub>/Al<sub>2</sub>O<sub>3</sub>

**Figure A.3** – TEM images of the metal oxides loaded on TiO<sub>2</sub> and Al<sub>2</sub>O<sub>3</sub>.



**FTIR spectra and calibration****(a) Plasma-off****(b) Plasma-off**

**Figure A.4** – Typical FTIR spectra measured with FTIR spectrometer for (a) NO and NO<sub>2</sub> for plasma-off measurements during the NO-removal experiments and (b) NO<sub>2</sub> and by-products spectra for plasma-on measurements at high energy density where NO is completely converted.

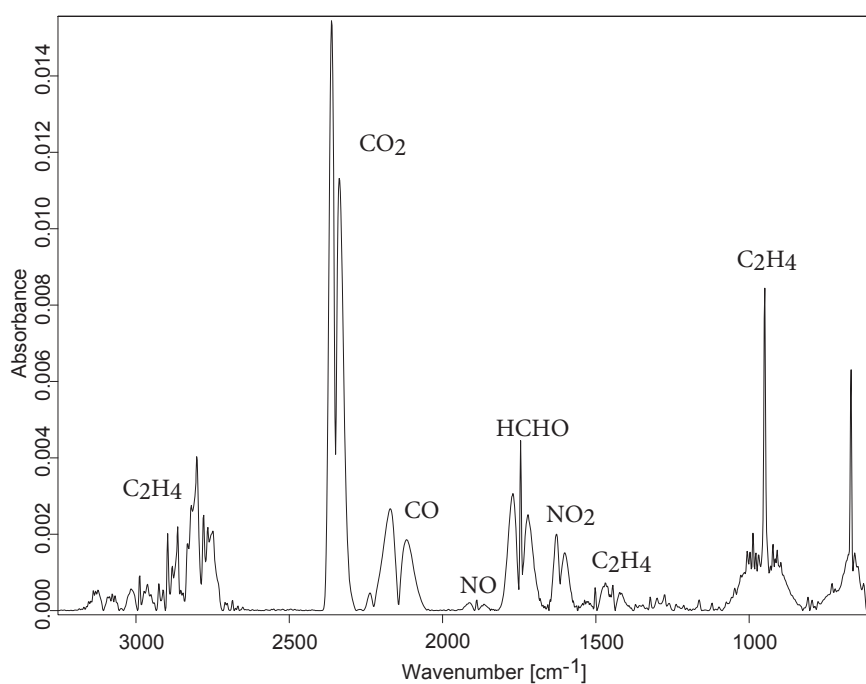
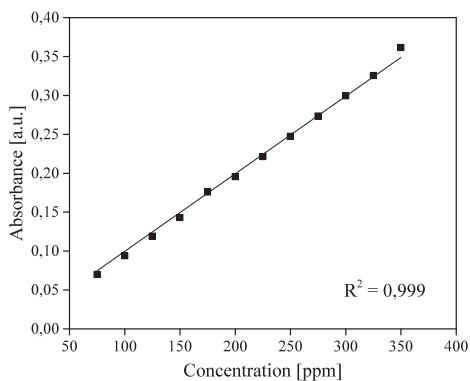
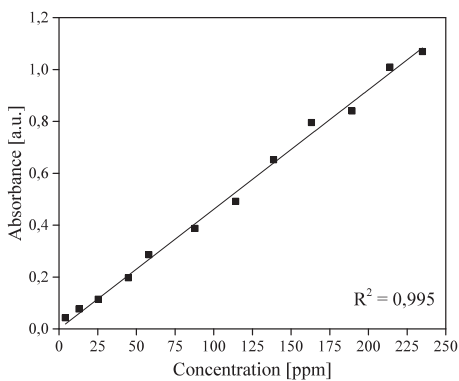


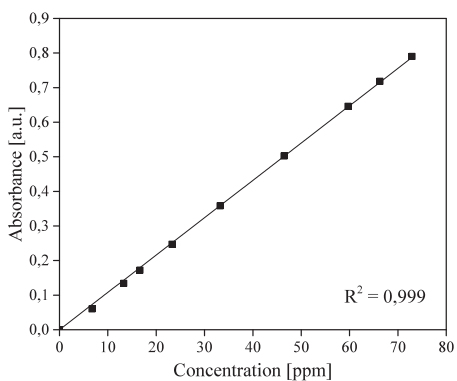
**Figure A.5** – The FTIR spectra measured with FTIR spectrometer for C<sub>2</sub>H<sub>4</sub> at an energy density of 50 J/L showing the by-products.



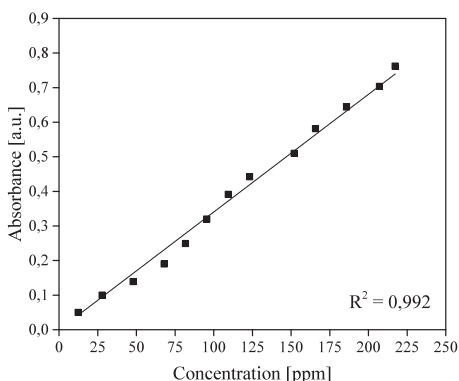
(a) NO



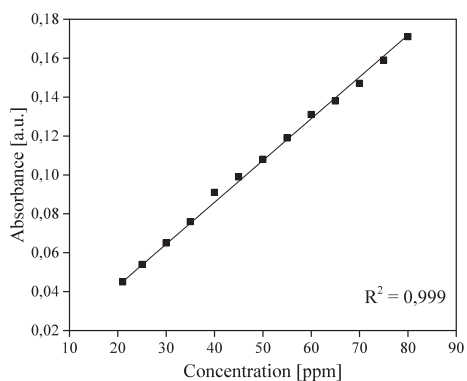
(b) NO<sub>2</sub>



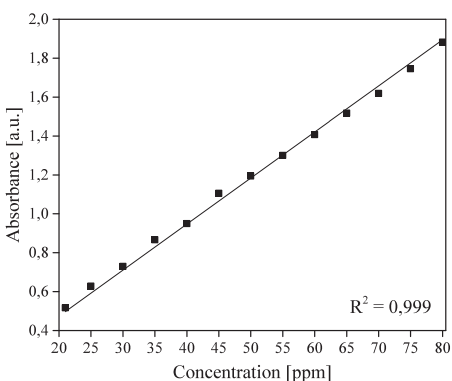
(c) N<sub>2</sub>O



(d) O<sub>3</sub>



(e) CO



(f) CO<sub>2</sub>

**Figure A.6** – Typical FTIR calibration curves for different gases that are used and measured in our experiments.

## A2. Effect of the NO input concentration

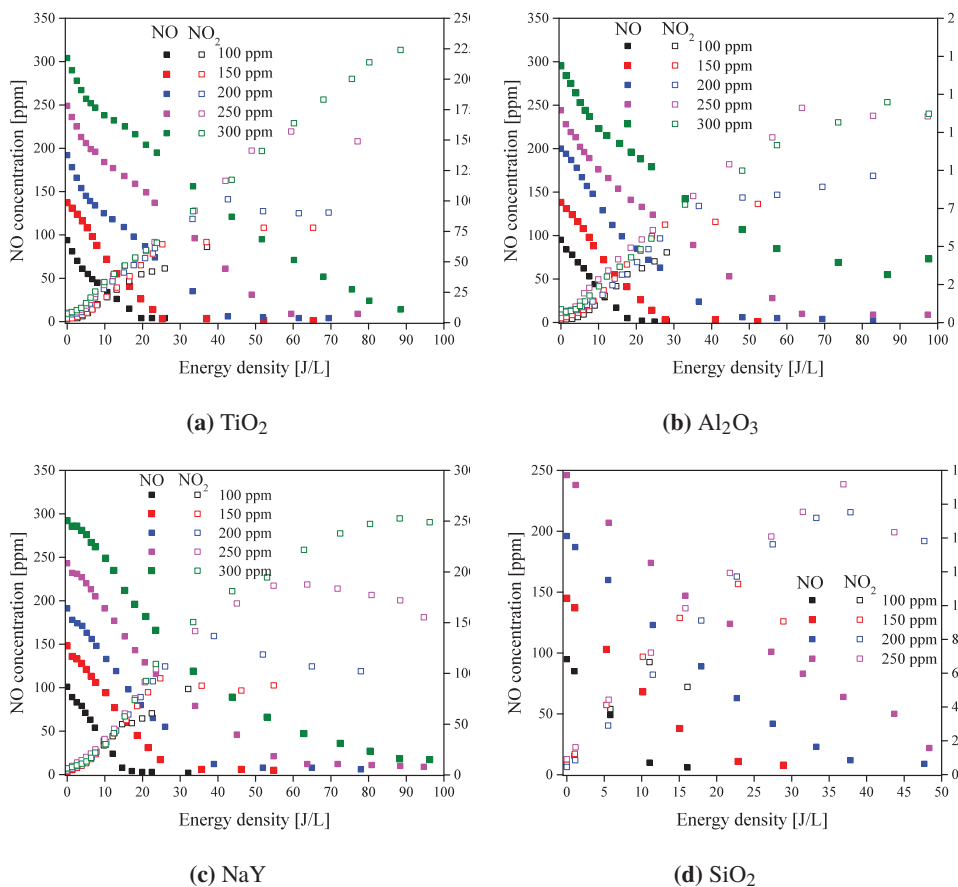


**Figure A.7** – NO and NO<sub>2</sub> concentration as a function of energy density for various input concentrations for all the catalytic materials in the IPC configuration.

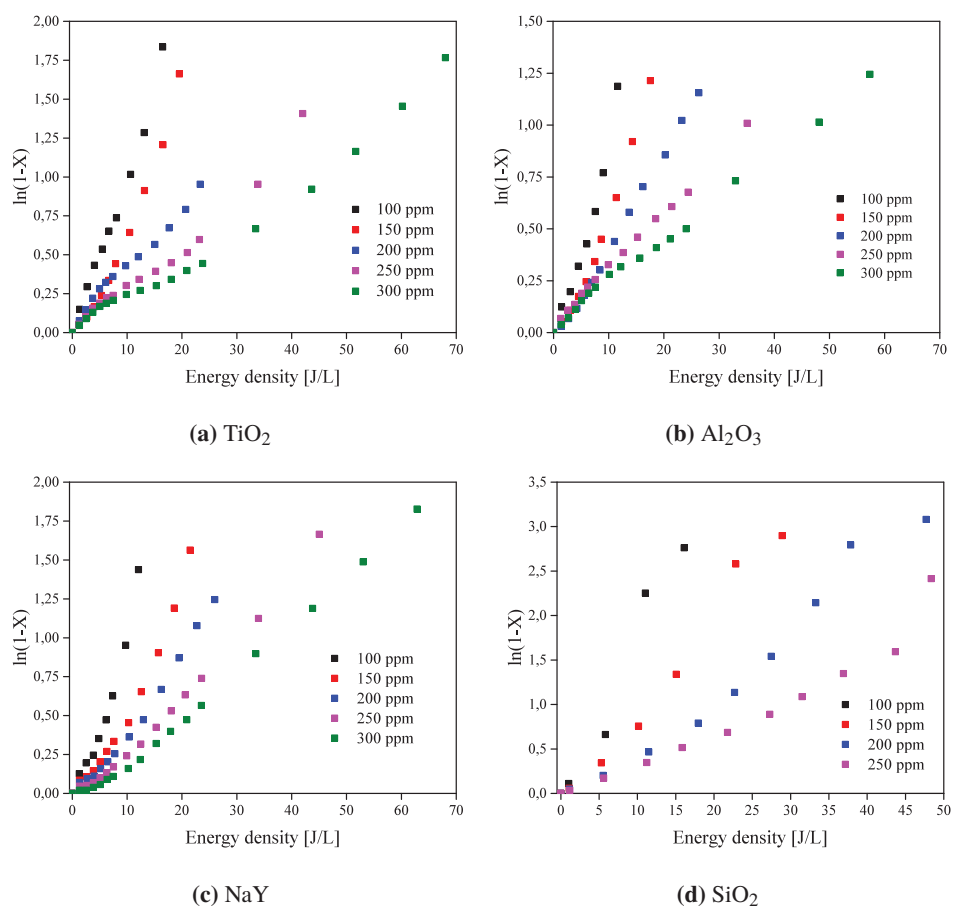


**Figure A.8** – First order kinetic plot to understand the effect of initial concentration on the removal efficiency by calculating the energy constants for IPC configuration.

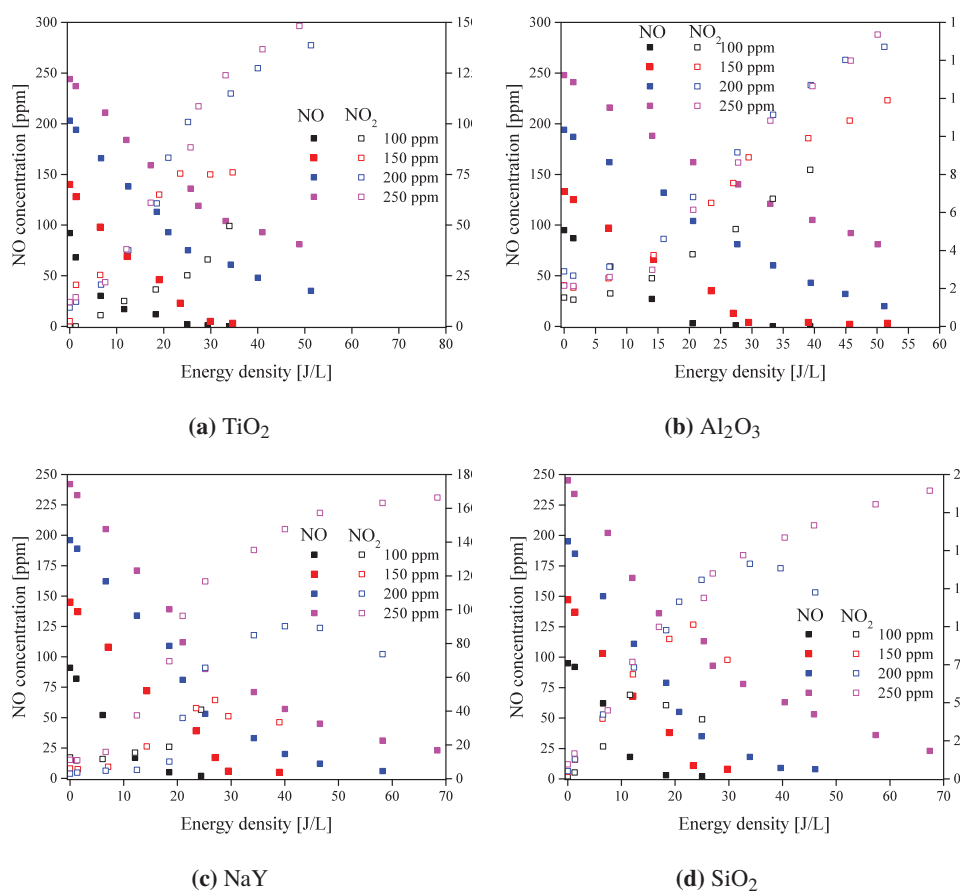


**Figure A.9** – NO and NO<sub>2</sub> concentration as a function of energy density for various input concentrations for all the catalytic materials that we have used in our study in the PPC configuration.

### A3. SDBD reactor for on-demand air purification

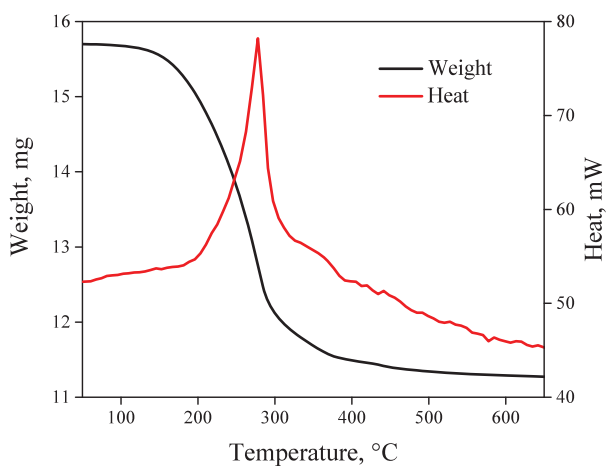


**Figure A.10** – Thermogravimetric analysis (TGA) curve for the remaining sol-gel which has not been used in the dip coating of  $\text{TiO}_2$  catalytic plate. The weight loss in the curve is due to the evaporation of Polyethylene glycol. Above 400 °C, we can see that the polyethylene glycol is completely evaporated and the weight remains almost constant. The carbon is completely removed and thus there exists no carbon deposits on the plate.

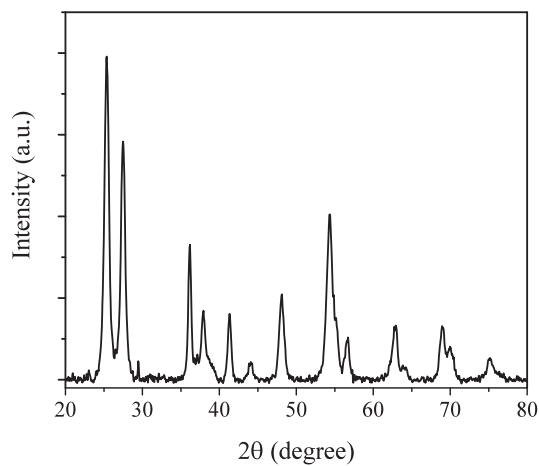


**Figure A.11** – X-ray Diffraction (XRD) pattern for  $\text{TiO}_2$  powder. XRD was done after drying the sol-gel which we have used for dip-coating.

## A4. Plasma-catalytic interactions: Effect of dielectric constant

### Introduction

In the Chapters 3, 4 and 5, we have seen that there is a difference in the performance of the plasma reactor when the electrical and operational parameters are changed. Also, the performance varies largely when the catalytic materials are introduced into the plasma reactor and the performance mainly depends on the type of catalytic material. The way the plasma is generated dictates the plasma chemistry. Thus it is expected that the effectiveness of a plasma-reactor packed with catalytic materials depends on the nature of the catalytic materials under the same conditions.

Hensel *et al.* in their work on electrical and optical properties of AC microdischarges in porous ceramics observed that the pore size of the material influences the mode of discharge [155]. A ceramic material with larger pore size showed microdischarge, while materials having smaller pore size showed surface discharges. They explain that plasma can be generated inside the pores if the pore-size is big enough ( $>100\ \mu\text{m}$  in their work). Kim *et al.* studied the dependence of streamer propagation on the type of the catalytic material and the reactor performance for VOC removal [156–158]. They observed that the presence of catalytic material affects the propagation velocities of the streamers and that active metal-oxides deposited on zeolites significantly change the plasma dynamics.

It will be interesting to study further the effect of various metal-oxides and what will be the effect of the amount of metal-oxide loading on the plasma intensity. From the results in the Chapter 5, we observed that the metal-oxides loaded on  $\text{TiO}_2$  and on  $\text{Al}_2\text{O}_3$  affects discharge behaviour. Therefore in this chapter, we study the effect of the catalysts on the discharge behaviour more in-detail. To study the temporal and spatial behaviour of the discharges, we have used a fast intensified charged coupled device (ICCD) camera. We correlated the changes in discharge behaviour to the dielectric properties of the catalytic materials. The dielectric properties of the packing materials are believed to have influence on the discharge behaviour, since the dielectric constant affects local electric field intensities on the surface of the catalytic material, affecting the presence of possible surface discharges along the dielectric materials. We have measured the dielectric constants of all various materials that we have used in our study and the results will be mentioned in the following sections.

### Experimental setup

In this chapter, time-resolved imaging of the plasma in the packed-bed reactor is done with an ICCD camera and for various packing materials. The schematic representation of the experimental setup is shown in Fig. A.14. The ICCD camera is a 4 Picos-DIG from Stanford Computer Optics [159] and has a minimum exposure time of 200 ps. It has a spatial resolution of  $780 \times 580$  pixels and  $8.3 \times 8.3\ \mu\text{m}$  pixel size. We have used two lens systems in this study. In part of the experiments we have used a Sigma 180-mm F4-5.6 lens for imaging larger areas of  $3 \times 1.5$  cm. Also a microscopic lens was used to focus on one



pellet of the catalyst (approximately  $2\text{ mm} \times 2\text{ mm}$ ), allowing more detailed observations. To protect the camera against electrical interference, it is enclosed in an EMC cabinet. The camera is synchronized with the high-voltage pulsed-power supply and the trigger source. The trigger source that we have used here is a Tektronix CFG250 pulse generator. The trigger signal is also monitored with a digital oscilloscope to check the correct timing of the camera with respect to the pulse source. The gain of the camera was set to 760 V. The power modulator that we used in these experiments is described in Chapter 2 in the section 2.3.1. The schematic representation of the reactor that we have used in these experiments is shown in the Fig. A.13. The reactor has similar dimensions as mentioned in section 2.1.1 except that the reactor is not cylindrical. We have used a rectangular reactor here, to have a better lateral view on the plasma and the catalyst inside the reactor. All the experiments were carried out at room temperature and atmospheric pressure with an input NO concentration of 200 ppm and a gas flow rate of 2 slm. We have used positive polarity pulses for all the experiments.

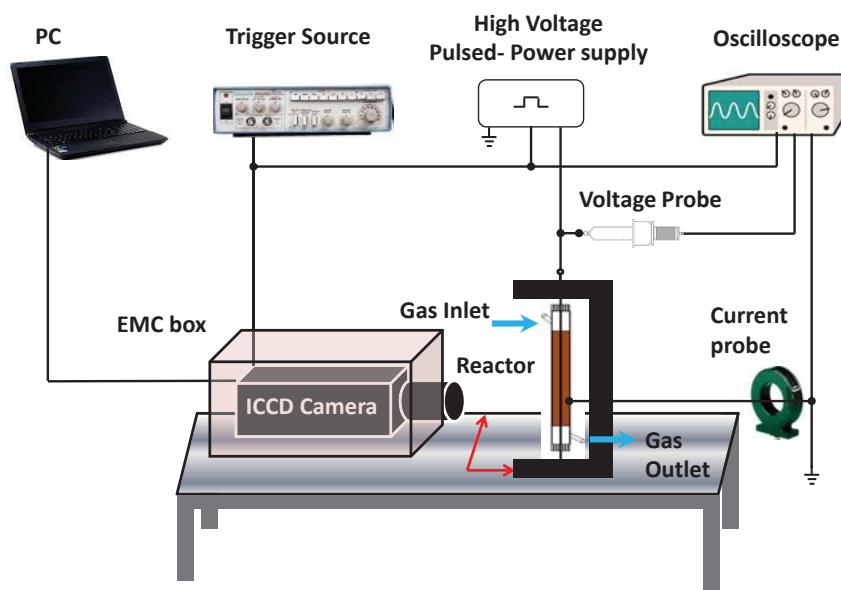


**Figure A.12** – Schematic representation of the experimental setup used for ICCD imaging.

### **Effect of applied peak-voltage on discharge intensity in plasma reactor**

In the section 3.2, we observed that the NO conversion does not depend on the applied peak-voltage but is a function of the plasma energy density. Apparently the amount of radicals generated by the plasma increases with increasing energy density.

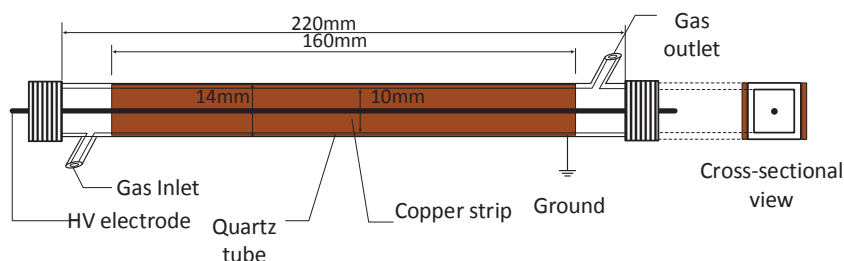


**Figure A.13** – Schematic representation of the DBD-reactor used for ICCD imaging. A rectangular configuration was used to have a better lateral view on the plasma and the catalyst.

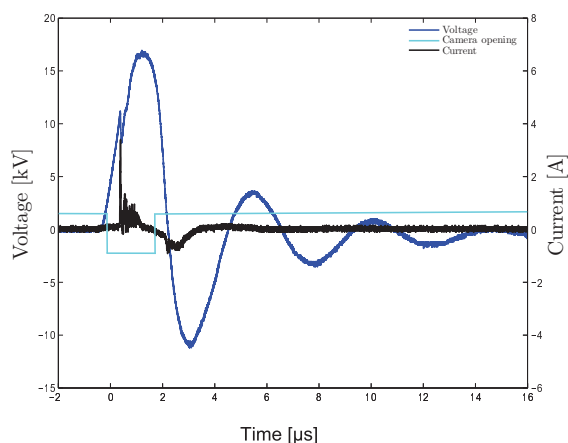


**Figure A.14** – Typical Voltage and current waveform of the pulsed power source used for ICCD imaging. The blue line represents the period when the camera gate was open.

In this section, we have varied the applied peak-voltage from 12 kV to 20 kV to see how the discharge intensity varies. The input NO concentration, the gas flow and the pulse repetition rate were maintained at 200 ppm, 2 slm and 500 Hz respectively. It can be seen from Fig. A.15 that the intensity of the plasma increases with increasing applied peak-voltage. At a peak-voltage of 12 kV, the discharges start to initiate only at one side of the reactor and below 12 kV we have not seen any discharge activity. With further increase in applied peak-voltage, the number of microdischarges increases. This is because, with increase in the applied peak-voltage, there is an increase in the energy-per-pulse deposition

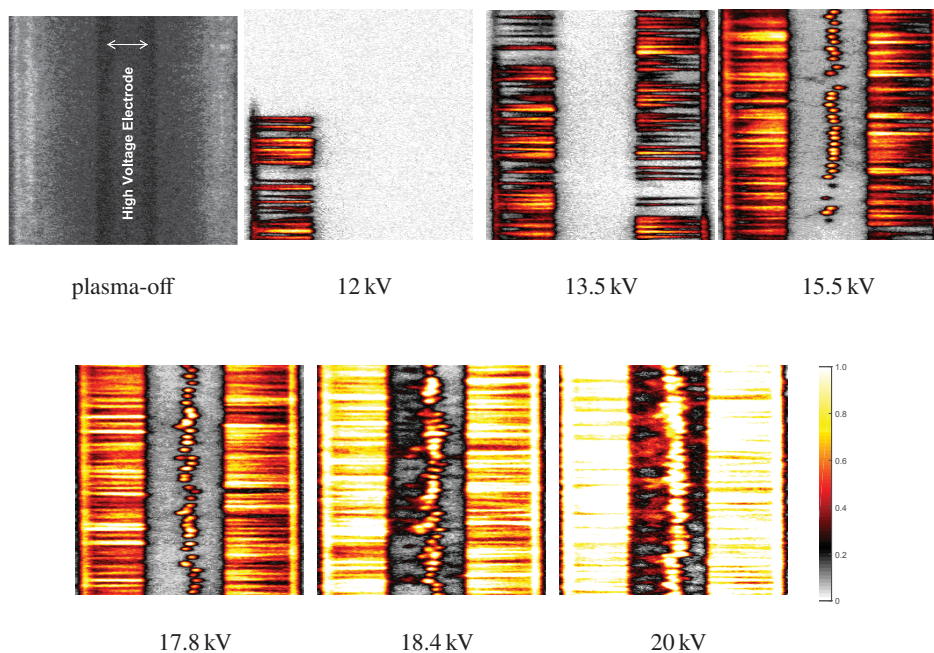


**Figure A.15** – Change in plasma volume as function of applied voltage at the pulse repetition rate of 500 Hz for a gas flow of 2 slm and an input NO concentration of 200 ppm. Exposure time of the camera is  $2\ \mu\text{s}$  and the gain of the camera is 760 V. We have averaged the 50 images at each setting. The colour bar shown in these images will be used in all the images of this chapter.

which in turn increase the plasma energy density. Also, new microdischarges are generated at new locations with increase in applied peak-voltage [160].

From the results in section 3.2, we saw that at a given energy density, higher peak-voltages lead to higher energy costs for NO removal. At high applied peak-voltages, the capacitive current increases leading to the increased energy losses. The energy supplied is used to heat up the gas thus reducing the energy efficiency. At an applied peak-voltage of 15.5 kV and higher, some bright spots can be observed at the high-voltage wire-electrode. This might be due to local field electric enhancements at minor imperfections of the electrode.

### Discharge behaviour in DBD-plasma reactor packed with $\text{TiO}_2$

We have observed that packing the plasma reactor with different catalytic materials lead to different discharge activity and difference in the performance of the reactor. In this part of the study, we analyze the plasma development, using fast ICCD imaging, when catalytic

materials is placed inside the DBD plasma reactor.

We have packed the plasma reactor with  $\text{TiO}_2$  of various packing particle size, and loaded with 5%  $\text{Fe}_3\text{O}_4/\text{TiO}_2$  and 5%  $\text{Co}_3\text{O}_4/\text{TiO}_2$ . For these materials we looked how the intensity of the plasma varies with each material.

### Effect of packing particle size

The packing particle size is one of the important parameters for the performance of packed bed reactors and affecting the discharge activity. We have packed the DBD reactor with particle sizes of respectively 2 mm, 1-2 mm, 0.5-1 mm and 200-500  $\mu\text{m}$ . The packing particle size of 2 mm is cylindrical in shape with a length of approximately 4 mm while the other particle sizes do not have a uniform particle shape.

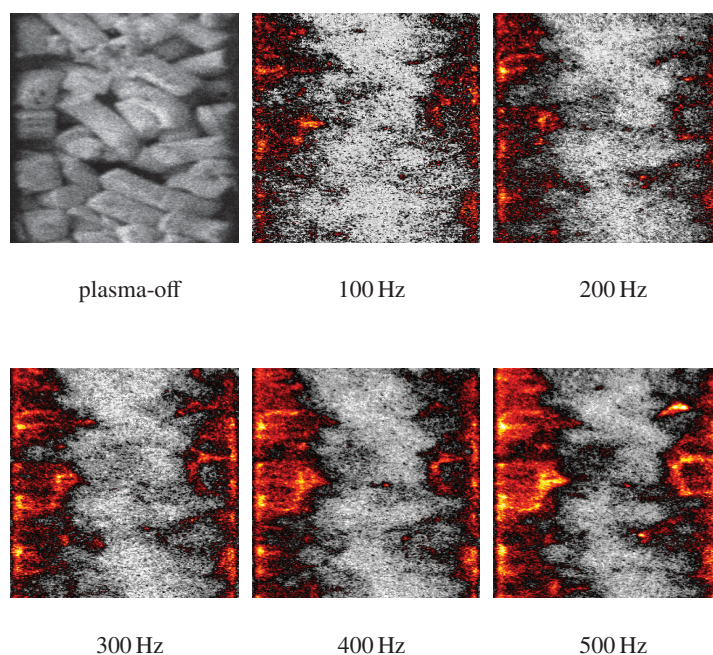


**Figure A.16** – Discharge behaviour for plasma reactor packed with  $\text{TiO}_2$  for particle size 2 mm cylindrical pellets with change in the pulse repetition rate. The  $\text{NO}$  input concentration was 200 ppm and the gas flow rate was 2 slm.

The plasma discharge intensity for the DBD plasma reactor packed with  $\text{TiO}_2$  for particle sizes of 2 mm and of 1-2 mm at various pulse repetition rates (prf) are shown in the figures A.16 and A.18 respectively. The images for a packing particle size of 0.5-1 mm and

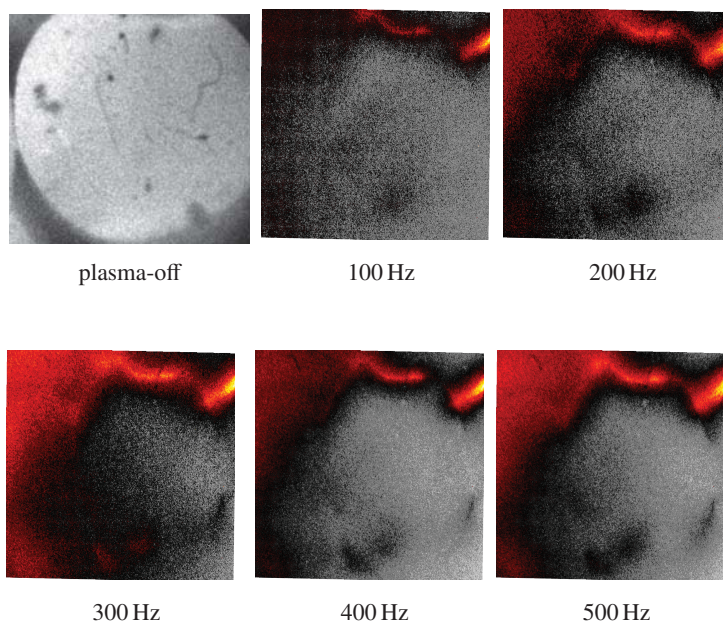


**Figure A.17** – Discharge behaviour for plasma reactor packed with  $\text{TiO}_2$  for particle size 2-3 mm with change in the pulse repetition rate using microscopic lens. The  $\text{NO}$  input concentration was 200 ppm and the gas flow rate was 2 slm.

of 200-500  $\mu\text{m}$  are shown in the figures A.19 and A.20 respectively. The images show that the discharges are mostly present in the space between the catalytic particles. The discharges look different as compared to the situation that only plasma, and no catalyst is present in the reactor. No clear filamentary like discharges can be observed when the plasma-reactor is filled with the catalytic materials. For all the pictures, it can be observed that there is slightly increased discharge activity on the left side of the picture as compared to the right side. This could probably be due to slight movement of the centre electrode towards the left while packing the catalytic materials.

We observed no significant discharge activity at 10 Hz. From 100 Hz, we observe some discharge activity near to the walls of the reactor. With increasing pulse repetition, the energy density increases (at constant flowrate and applied peak-voltage) leading to increased discharge activity. It looks like discharges propagate from the walls of the reactor to the centre electrode. To have a closer look at the discharge propagation, a microscopic lens was used and focussed on a single catalytic pellet as shown in Fig. A.17. We can see that the discharge propagates just in the gas gap between the pellets which can be referred to as a "partial discharge".

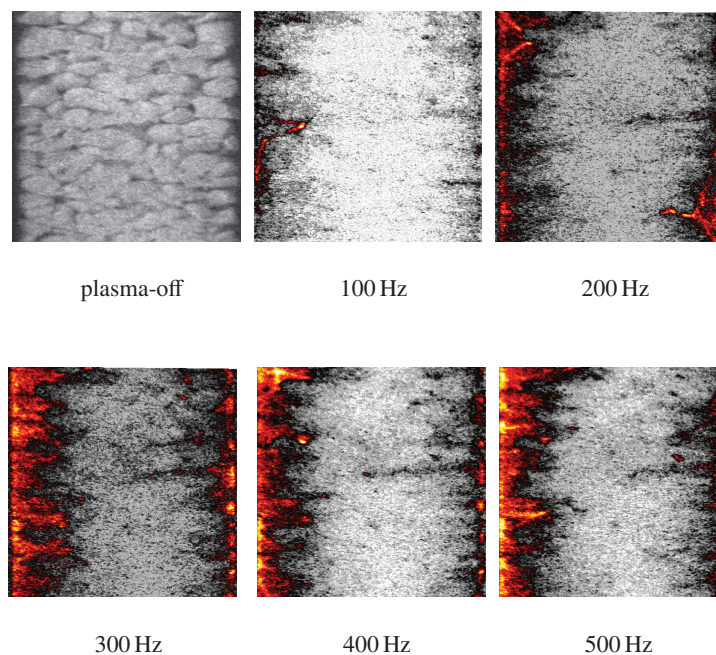


**Figure A.18** – Discharge behaviour for plasma reactor packed with  $\text{TiO}_2$  for particle size 1-2 mm with change in the pulse repetition rate. The NO input concentration was 200 ppm and the gas flow rate was 2 slm.

When we look at the intensity of the plasma for various packing particle sizes, it can be observed by comparing the figures 6.7, 6.10 that the plasma is less intense for the smaller packing particle size. For the  $\text{TiO}_2$  with particle size of 1-2 mm (Fig. 6.10), the plasma intensity is less until a repetition rate of 200 prr, while the intensity increases with repetition rate from 300 prr,

As we have not performed plasma processing experiments with varying packing particle size, it is hard to comment if the particle size affects the NO removal efficiency. In a study by Kim *et al.* [157] on time-resolved imaging of positive pulsed corona-induced surface streamers on  $\text{TiO}_2$  and  $\gamma\text{-Al}_2\text{O}_3$ -supported catalysts, it was observed that the presence of a catalytic materials influences the propagation velocities of the streamers. They stated that the partial discharge served as a starting point for primary streamers, and promote the streamer propagation towards the next catalyst bead which will result in enhanced discharge intensity. That means that for a larger particle size, the probability of partial discharge will increase, resulting in more intense plasma. In our work, we observed that the higher the intensity of the plasma, the less efficient it is. Thus, we may say that decreasing the particle

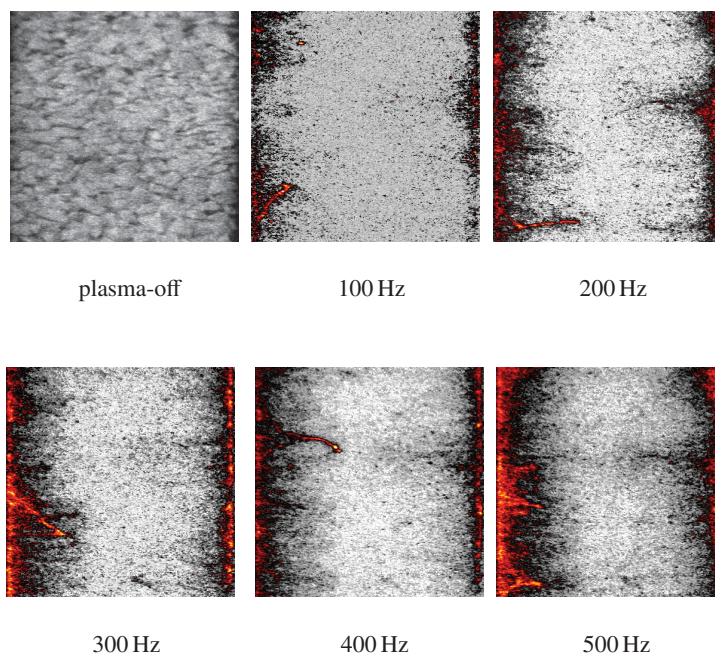


**Figure A.19** – Discharge behaviour for plasma reactor packed with  $\text{TiO}_2$  for particle size 0.5-1 mm with change in the pulse repetition rate. The  $\text{NO}$  input concentration was 200 ppm and the gas flow rate was 2 slm.

size may result in an increase of the efficiency. But, in [161], it is shown that there is an optimum particle size for  $\text{NO}_x$  removal efficiency. In their work on low temperature  $\text{NO}_x$  synthesis in a packed bed reactor Patil *et al.*, observed higher  $\text{NO}_x$  conversion efficiency for lower particle sizes, concluding that lower particles result in higher efficiencies. Though, this work is on  $\text{NO}_x$  synthesis and our work is  $\text{NO}_x$  removal, the main point of citing their work here is to state that the lower particle sizes may lead to improved efficiencies.

#### **Metal-oxides loaded on $\text{TiO}_2$**

In Chapter 5, we have used different metal-oxides loading on  $\text{TiO}_2$  and  $\text{Al}_2\text{O}_3$  to study the performance of plasma-catalytic reactor in both IPC and PPC configurations. The results from this chapter show that different metal-oxides showed different  $\text{NO}$  removal efficiency and that with increase in the metal-oxide loading, the performance of the reactor was improved. It was also observed from the voltage-current waveforms that different materials result in different discharge activity.

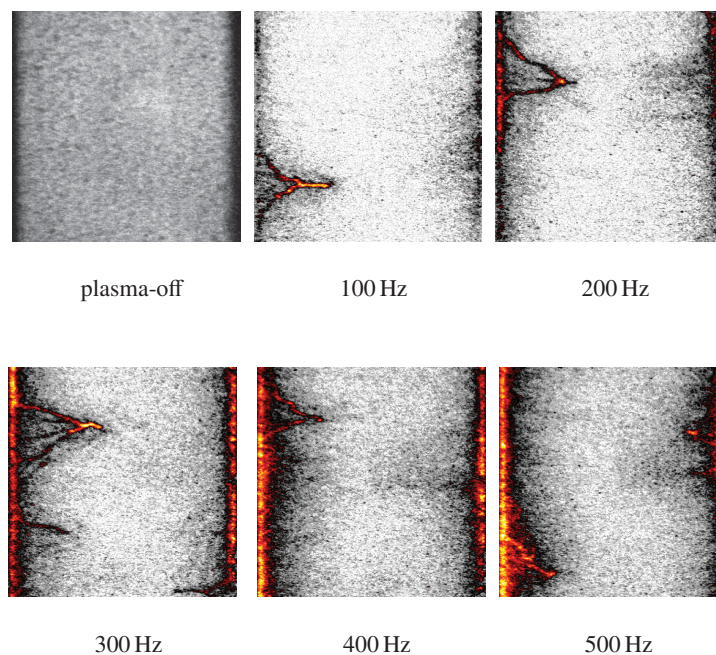


**Figure A.20** – Discharge behaviour for plasma reactor packed with  $\text{TiO}_2$  for particle size 200-500  $\mu\text{m}$  with change in the pulse repetition rate. The NO input concentration was 200 ppm and the gas flow rate was 2 slm.

We have shown in the previous section that the dielectric constant decreases with metal-oxide loading. Literature says that an increase of the dielectric constant of the catalytic material, results in localized electric field enhancement and that the discharges will be concentrated more on the surfaces of the catalytic material [162]. In the case of our system, this would mean that  $\text{TiO}_2$  should show more surface like discharges than metal-oxides loaded on  $\text{TiO}_2$ .

For that reason, in this section we observed the plasma intensity for  $\text{TiO}_2$  with and without metal-oxide loading. ICCD images were taken for  $5\%\text{Fe}_3\text{O}_4/\text{TiO}_2$  and  $5\%\text{Co}_3\text{O}_4/\text{TiO}_2$  for an input NO concentration of 200 ppm and a gas flow rate of 2 slm. The ICCD image of  $\text{TiO}_2$  without a metal-oxide loading is given in Fig. A.18. The ICCD images of  $5\%\text{Fe}_3\text{O}_4/\text{TiO}_2$  and  $5\%\text{Co}_3\text{O}_4/\text{TiO}_2$  are shown in figures A.21 and A.22 respectively. It can be seen that the intensity of the plasma is bit higher in the case that the plasma-reactor is packed with  $\text{TiO}_2$ . For  $5\%\text{Fe}_3\text{O}_4/\text{TiO}_2$  and  $5\%\text{Co}_3\text{O}_4/\text{TiO}_2$ , the intensity is a bit lower. From the plasma processing results for the in-plasma configuration (IPC), as given in Chapter 5,  $5\%\text{Fe}_3\text{O}_4/\text{TiO}_2$  and  $5\%\text{Co}_3\text{O}_4/\text{TiO}_2$  did not show significant difference in their NO



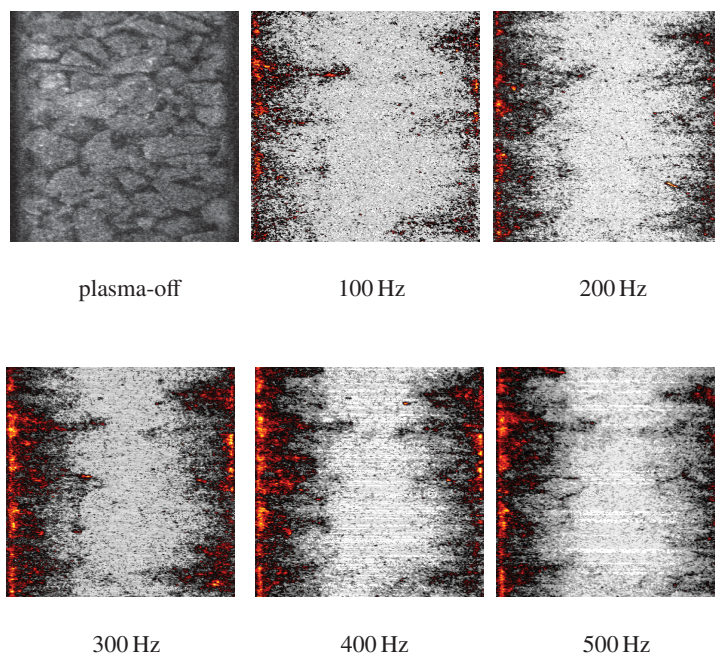


**Figure A.21** – Discharge behaviour for plasma reactor packed with 5%  $\text{Fe}_3\text{O}_4/\text{TiO}_2$  for particle size 1-2 mm with change in the pulse repetition rate. The NO input concentration was 200 ppm and the gas flow rate was 2 slm.

conversion, whereas  $\text{TiO}_2$  showed slightly lower NO conversion as compared to the metal-oxide loaded materials. So apparently the intensity of the plasma can be correlated to its NO removal performance: the more intense plasma results in a lower NO conversion efficiency. This might be due to heating up of the reactor at higher plasma intensity.

From the images that we obtained, it is difficult to comment on whether the discharges are more surface-like or filamentary as we have looked at just the intensity of the plasma. Kim *et al.*, in their study on the microscopic observation of discharge development on the surface of zeolite supported metal nanoparticles [156], observed that the plasma is dense at the contact points of the pellets. The metal nanoparticles supported on the zeolites resulted in less intense plasma, but gave a plasma that was expanded over a wide surface area. Also they observed that the intensity and area of the plasma are higher with Ag than for Cu nanoparticles. Thus the active metal oxide affects the plasma dynamics.

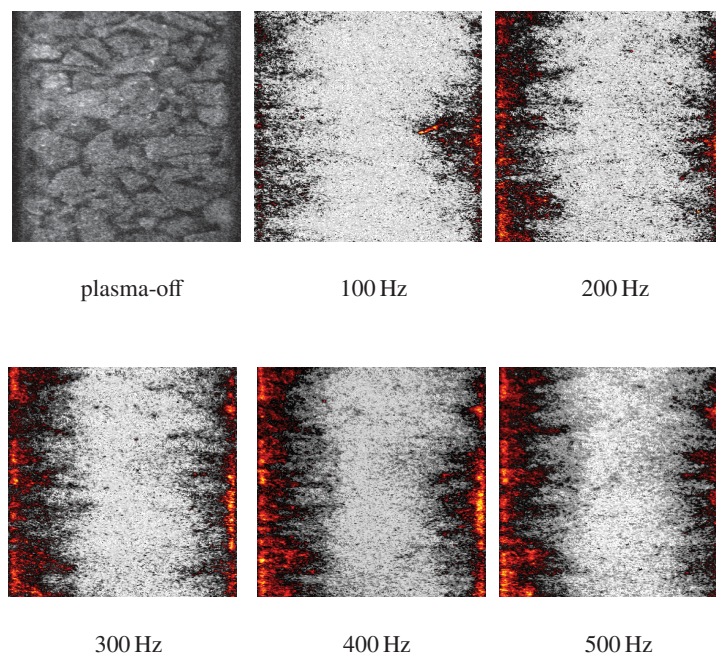


**Figure A.22** – Discharge behaviour for plasma reactor packed with 5%  $\text{Co}_3\text{O}_4/\text{TiO}_2$  for particle size 1-2 mm with change in the pulse repetition rate. The NO input concentration was 200 ppm and the gas flow rate was 2 slm.

## Conclusions

In this appendix, we correlated the chemical activity of the plasma-alone reactor and of the plasma-reactor filled with catalytic materials, to the intensity of the generated plasma. We observed how the plasma development is affected when catalytic material is introduced in the plasma zone. For this purpose, we have used an intensified charged coupled device (ICCD) to record the temporal and spatial development of the discharges.

We have observed that the intensity of the plasma in the DBD reactor increases with increasing applied peak-voltage at a given energy density. This is because, with increase in applied peak-voltage, the number of microdischarges increases. At high intensity of the plasma, the energy costs for NO removal increase and the reactor performance is reduced.

The discharge behaviour changes when the DBD reactor is packed with  $\text{TiO}_2$  pellets. No clear filamentary discharges can be observed. When looked in to the effect of particle size on the discharge activity, the intensity of the plasma increases with increasing particle size due to the availability of larger gas-gap with aids in the formation of partial discharges

between the particles.

Loading metal-oxides on the  $\text{TiO}_2$  resulted in a reduction of the plasma intensity. In conclusion, the nature of the metal-oxide used affects the plasma dynamics. It will be interesting to study further the effect of various metal-oxides and what will be the effect of loading on the plasma intensity. Also the temporal evolution of discharges may give a clue whether the discharges are more like surface discharges or filamentary discharges.

---

---

## BIBLIOGRAPHY

---

- [1] “European environment agency.” <https://www.eea.europa.eu/data-and-maps/indicators/transport-emissions-of-air-pollutants-8/transport-emissions-of-air-pollutants-5>. Accessed: 2017-12-04.
- [2] T. Hammer, T. Kappes, and M. Baldauf, “Plasma catalytic hybrid processes: gas discharge initiation and plasma activation of catalytic processes,” *Catalysis Today*, vol. 89, no. 1, pp. 5–14, 2004.
- [3] Y. S. Mok, C. M. Nam, M. H. Cho, and I.-S. Nam, “Decomposition of volatile organic compounds and nitric oxide by nonthermal plasma discharge processes,” *IEEE Transactions on Plasma Science*, vol. 30, no. 1, pp. 408–416, 2002.
- [4] J. S. Chang, “Recent development of plasma pollution control technology: a critical review,” *Science and Technology of Advanced Materials*, vol. 2, no. 3, pp. 571–576, 2001.
- [5] S. Müller and R.-J. Zahn, “Air pollution control by non-thermal plasma,” *Contributions to Plasma Physics*, vol. 47, no. 7, pp. 520–529, 2007.
- [6] A. Mizuno, “Industrial applications of atmospheric non-thermal plasma in environmental remediation,” *Plasma Physics and Controlled Fusion*, vol. 49, no. 5A, p. A1, 2007.
- [7] L. A. Rosocha, “Nonthermal plasma applications to the environment: gaseous electronics and power conditioning,” *IEEE transactions on plasma science*, vol. 33, no. 1, pp. 129–137, 2005.
- [8] H.-H. Kim, Y. Teramoto, A. Ogata, H. Takagi, and T. Nanba, “Plasma catalysis for environmental treatment and energy applications,” *Plasma Chemistry and Plasma Processing*, vol. 36, no. 1, pp. 45–72, 2016.

- [9] V. R. Chirumamilla, W. F. L. M. Hoeben, F. J. C. M. Beckers, T. Huiskamp, E. J. M. Van Heesch, and A. J. M. Pemen, "Experimental investigation on the effect of a microsecond pulse and a nanosecond pulse on NO removal using a pulsed DBD with catalytic materials," *Plasma Chemistry and Plasma Processing*, vol. 36, pp. 487–510, Mar 2016.
- [10] B. Penetrante, M. Hsiao, B. Merritt, G. Vogtlin, and C. Wan, "Plasma-assisted heterogeneous catalysis for NO<sub>x</sub> reduction in lean-burn engine exhaust," tech. rep., DTIC Document, 1997.
- [11] B. M. Penetrante, R. M. Brusasco, B. T. Merritt, and G. E. Vogtlin, "Environmental applications of low-temperature plasmas," *Pure and Applied Chemistry*, vol. 71, no. 10, pp. 1829–1835, 1999.
- [12] M. Sun and V. Ravi, "Role of Oxygen in the Plasma Catalytic Removal of NO<sub>x</sub>," *VIVECHAN IJR*, vol. 1, no. 2, pp. 1–9, 2010.
- [13] F. Beckers, W. Hoeben, A. Pemen, and E. Van Heesch, "Low-level NO<sub>x</sub> removal in ambient air by pulsed corona technology," *Journal of Physics D: Applied Physics*, vol. 46, no. 29, p. 295201, 2013.
- [14] E. Neyts and A. Bogaerts, "Understanding plasma catalysis through modelling and simulation : a review," *Journal of Physics D: Applied Physics*, vol. 47, no. 22, p. 224010, 2014.
- [15] V. I. Pârvulescu, M. Magureanu, and P. Lukes, *Plasma chemistry and catalysis in gases and liquids*. John Wiley & Sons, 2012.
- [16] T. Nozaki and K. Okazaki, "Non-thermal plasma catalysis of methane: Principles, energy efficiency, and applications," *Catalysis today*, vol. 211, pp. 29–38, 2013.
- [17] U. Roland, F. Holzer, and F.-D. Kopinke, "Improved oxidation of air pollutants in a non-thermal plasma," *Catalysis Today*, vol. 73, no. 3, pp. 315–323, 2002.
- [18] A. M. Vandenbroucke, R. Morent, N. De Geyter, and C. Leys, "Non-thermal plasmas for non-catalytic and catalytic VOC abatement," *Journal of hazardous materials*, vol. 195, pp. 30–54, 2011.
- [19] T. Yamamoto, M. Okubo, K. Hayakawa, and K. Kitaura, "Towards ideal NO<sub>x</sub> control technology using a plasma-chemical hybrid process," *IEEE Transactions on Industry Applications*, vol. 37, no. 5, pp. 1492–1498, 2001.
- [20] H. Conrads and M. Schmidt, "Plasma generation and plasma sources," *Plasma Sources Science and Technology*, vol. 9, no. 4, pp. 441–454, 2000.
- [21] C. Tendero, C. Tixier, P. Tristant, J. Desmaison, and P. Leprince, "Atmospheric pressure plasmas: A review," *Spectrochimica Acta - Part B Atomic Spectroscopy*, vol. 61, no. 1, pp. 2–30, 2006.

- [22] B. M. Penetrante and S. E. Schultheis, *Non-thermal plasma techniques for pollution control: part b: electron beam and electrical discharge processing*, vol. 34. Springer Science & Business Media, 2013.
- [23] U. Kogelschatz, "Dielectric-barrier discharges: their history, discharge physics, and industrial applications," *Plasma chemistry and plasma processing*, vol. 23, no. 1, pp. 1–46, 2003.
- [24] M. B. Chang and S. C. Yang, "NO/NO<sub>x</sub> removal with C<sub>2</sub>H<sub>2</sub> as additive via dielectric barrier discharges," *AIChE journal*, vol. 47, no. 5, pp. 1226–1233, 2001.
- [25] A. Mizuno, R. Shimizu, A. Chakrabarti, L. Dascalescu, and S. Furuta, "NO<sub>x</sub> removal process using pulsed discharge plasma," *IEEE Transactions on industry applications*, vol. 31, no. 5, pp. 957–962, 1995.
- [26] M. Moscoca-Santillan, A. Vincent, E. Santirso, and J. Amouroux, "Design of a DBD wire-cylinder reactor for NO<sub>x</sub> emission control: experimental and modelling approach," *Journal of Cleaner Production*, vol. 16, no. 2, pp. 198–207, 2008.
- [27] T. Hammer and S. Bröer, "Plasma enhanced selective catalytic reduction of NO<sub>x</sub> for diesel cars," tech. rep., SAE Technical Paper, 1998.
- [28] C.-L. Chang and T.-S. Lin, "Decomposition of toluene and acetone in packed dielectric barrier discharge reactors," *Plasma chemistry and plasma processing*, vol. 25, no. 3, pp. 227–243, 2005.
- [29] N. Blin-Simiand, S. Pasquiers, F. Jorand, C. Postel, and J. Vacher, "Removal of formaldehyde in nitrogen and in dry air by a DBD: importance of temperature and role of nitrogen metastable states," *Journal of Physics D: Applied Physics*, vol. 42, no. 12, p. 122003, 2009.
- [30] H. M. Lee and M. B. Chang, "Gas-phase removal of acetaldehyde via packed-bed dielectric barrier discharge reactor," *Plasma chemistry and plasma processing*, vol. 21, no. 3, pp. 329–343, 2001.
- [31] J.-O. Chae, "Non-thermal plasma for diesel exhaust treatment," *Journal of electrostatics*, vol. 57, no. 3, pp. 251–262, 2003.
- [32] G. Xiao, W. Xu, R. Wu, M. Ni, C. Du, X. Gao, Z. Luo, and K. Cen, "Non-thermal plasmas for VOCs abatement," *Plasma Chemistry and Plasma Processing*, vol. 34, no. 5, pp. 1033–1065, 2014.
- [33] V. Puchkarev and M. Gundersen, "Energy efficient plasma processing of gaseous emission using a short pulse discharge," *Applied physics letters*, vol. 71, no. 23, pp. 3364–3366, 1997.

- [34] T. Yamamoto, S. Member, C.-I. Yang, M. R. Beltran, and Z. Kravets, "Plasma-assisted chemical process for NO<sub>x</sub> control," *Industry Applications, IEEE Transactions on*, vol. 36, no. 3, pp. 923–927, 2000.
- [35] T. Oda, "Non-thermal plasma processing for environmental protection: Decomposition of dilute VOCs in air," *Journal of Electrostatics*, vol. 57, no. 3-4, pp. 293–311, 2003.
- [36] S. Samukawa, M. Hori, S. Rauf, K. Tachibana, P. Bruggeman, G. Kroesen, J. C. Whitehead, A. B. Murphy, A. F. Gutsol, S. Starikovskaia, U. Kortshagen, J.-P. Boeuf, T. J. Sommerer, M. J. Kushner, U. Czarnetzki, and N. Mason, "The 2012 Plasma Roadmap," *Journal of Physics D: Applied Physics*, vol. 45, no. 25, p. 253001, 2012.
- [37] J. C. Whitehead, "Plasma catalysis: A solution for environmental problems," *Pure and Applied Chemistry*, vol. 82, no. 6, pp. 1329–1336, 2010.
- [38] H. L. Chen, H. M. Lee, S. H. Chen, M. B. Chang, S. J. Yu, and S. N. Li, "Removal of volatile organic compounds by single-stage and two-stage plasma catalysis systems: A review of the performance enhancement mechanisms, current status, and suitable applications," *Environmental Science and Technology*, vol. 43, no. 7, pp. 2216–2227, 2009.
- [39] J. Jolibois, K. Takashima, and A. Mizuno, "Application of a non-thermal surface plasma discharge in wet condition for gas exhaust treatment: NO<sub>x</sub> removal," *Journal of Electrostatics*, vol. 70, pp. 300–308, June 2012.
- [40] H. Miessner, K.-P. Francke, and R. Rudolph, "Plasma-enhanced HC-SCR of NO<sub>x</sub> in the presence of excess oxygen," *Applied Catalysis B: Environmental*, vol. 36, pp. 53–62, Feb. 2002.
- [41] R. McAdams, P. Beech, and J. T. Shawcross, "Low temperature plasma assisted catalytic reduction of NO<sub>x</sub> in simulated marine diesel exhaust," *Plasma Chemistry and Plasma Processing*, vol. 28, pp. 159–171, Feb. 2008.
- [42] D. Tran, C. Aardahl, K. Rappe, P. Park, and C. Boyer, "Reduction of NO<sub>x</sub> by plasma-facilitated catalysis over In-doped  $\gamma$ -alumina," *Applied Catalysis B: Environmental*, vol. 48, pp. 155–164, Mar. 2004.
- [43] H. H. Kim, K. Takashima, S. Katsura, and A. Mizuno, "Low-temperature NO<sub>x</sub> reduction processes using combined systems of pulsed corona discharge and catalysts," *Journal of Physics D: Applied Physics*, vol. 34, no. 4, p. 604, 2001.
- [44] S. Bröer and T. Hammer, "Selective catalytic reduction of nitrogen oxides by combining a non-thermal plasma and a V<sub>2</sub>O<sub>5</sub>-WO<sub>3</sub>/TiO<sub>2</sub> catalyst," *Applied Catalysis B: Environmental*, vol. 28, no. 2, pp. 101–111, 2000.

- [45] T. Oda, T. Kato, T. Takahashi, and K. Shimizu, "Nitric oxide decomposition in air by using nonthermal plasma processing with additives and catalyst," *Industry Applications, IEEE Transactions on*, vol. 34, no. 2, pp. 268–272, 1998.
- [46] A. Nasonova, H. C. Pham, D.-J. Kim, and K.-S. Kim, "NO and SO<sub>2</sub> removal in non-thermal plasma reactor packed with glass beads-TiO<sub>2</sub> thin film coated by PCVD process," *Chemical Engineering Journal*, vol. 156, pp. 557–561, Feb. 2010.
- [47] T. Oda, T. Kato, T. Takahashi, and K. Shimizu, "Nitric oxide decomposition in air by using non-thermal plasma processing - with additives and catalyst," Oct. 1997.
- [48] I. Jōgi, K. Erme, A. Haljaste, and M. Laan, "Oxidation of nitrogen oxide in hybrid plasma-catalytic reactors based on DBD and Fe<sub>2</sub>O<sub>3</sub>," *The European Physical Journal Applied Physics*, vol. 61, no. 02, p. 24305, 2013.
- [49] J. H. Kwak, J. Szanyi, and C. H. Peden, "Nonthermal plasma-assisted catalytic NO<sub>x</sub> reduction over Ba-Y,FAU: the effect of catalyst preparation," *Journal of Catalysis*, vol. 220, pp. 291–298, Dec. 2003.
- [50] Y. Lee, J. Chung, Y. Choi, J. Chung, M. Cho, and W. Namkung, "NO<sub>x</sub> removal characteristics in plasma plus catalyst hybrid process," *Plasma Chemistry and Plasma Processing*, vol. 24, no. 2, pp. 137–154, 2004.
- [51] Y. S. Mok, D. J. Koh, D. N. Shin, and K. T. Kim, "Reduction of nitrogen oxides from simulated exhaust gas by using plasma-catalytic process," *Fuel Processing Technology*, vol. 86, no. 3, pp. 303–317, 2004.
- [52] Y. S. Mok, D. J. Koh, K. T. Kim, and I.-S. Nam, "Nonthermal plasma-enhanced catalytic removal of nitrogen oxides over V<sub>2</sub>O<sub>5</sub>/TiO<sub>2</sub> and Cr<sub>2</sub>O<sub>3</sub>/TiO<sub>2</sub>," *Industrial & engineering chemistry research*, vol. 42, no. 13, pp. 2960–2967, 2003.
- [53] R. G. Tonkyn, S. E. Barlow, and J. W. Hoard, "Reduction of NO<sub>x</sub> in synthetic diesel exhaust via two-step plasma-catalysis treatment," *Applied Catalysis B: Environmental*, vol. 40, no. 3, pp. 207–217, 2003.
- [54] A. Srinivasan and B. Rajanikanth, "Nonthermal-plasma-promoted catalysis for the removal of NO<sub>x</sub> from a stationary diesel-engine exhaust," *IEEE Transactions on Industry Applications*, vol. 43, no. 6, pp. 1507–1514, 2007.
- [55] J.-H. Niu, A.-M. Zhu, C. Shi, H.-Y. Fan, X.-M. Chen, and X.-F. Yang, "The reactions and composition of the surface intermediate species in the selective catalytic reduction of NO<sub>x</sub> with ethylene over Co-ZSM-5," *Research on Chemical Intermediates*, vol. 33, no. 6, pp. 549–566, 2007.
- [56] J. H. Kwak, J. Szanyi, and C. H. Peden, "Nonthermal plasma-assisted catalytic NO<sub>x</sub> reduction over Ba-Y, FAU: the effect of catalyst preparation," *Journal of Catalysis*, vol. 220, no. 2, pp. 291–298, 2003.



- [57] Y. Nie, J. Wang, K. Zhong, L. Wang, and Z. Guan, "Synergy study for plasma-facilitated C<sub>2</sub>H<sub>4</sub> selective catalytic reduction of NO<sub>x</sub> over Ag/ $\gamma$ -Al<sub>2</sub>O<sub>3</sub> catalyst," *IEEE transactions on plasma science*, vol. 35, no. 3, pp. 663–669, 2007.
- [58] Z. Liu, K. Yan, A. Pemen, G. Winands, and E. Van Heesch, "Synchronization of multiple spark-gap switches by a transmission line transformer," *Review of scientific instruments*, vol. 76, no. 11, p. 113507, 2005.
- [59] G. J. J. Winands, "Efficient streamer plasma generation," PhD Thesis, Eindhoven University of Technology, 2007, ISBN 978-90-386-1040-5.
- [60] T. Huiskamp, "Nanosecond pulsed power technology for transient plasma generation," PhD Thesis, Eindhoven University of Technology, 2015, ISBN 978-94-6259-776-1.
- [61] F. Beckers, "Pulsed power driven industrial plasma processing," PhD Thesis, Eindhoven University of Technology, 2015, ISBN 978-90-386-3982-6.
- [62] *Dielectric constant probe-Keysight Technologies*, 2018 (accessed January 2, 2018). <https://www.keysight.com/en/pd-1000000046%3Aeapsg%3Apro-pn-16451B/dielectric-test-fixture?cc=US&lc=eng>.
- [63] E. Hioki, "Hioki 3532–50 lcr hitester instruction manual," *JAPAN. HIOKI EE CORPORATION*, 2001.
- [64] D. Ghodgaonkar, V. Varadan, and V. Varadan, "Free-space measurement of complex permittivity and complex permeability of magnetic materials at microwave frequencies," *IEEE Transactions on instrumentation and measurement*, vol. 39, no. 2, pp. 387–394, 1990.
- [65] J. W. Lamb, "Miscellaneous data on materials for millimetre and submillimetre optics," *International Journal of Infrared and Millimeter Waves*, vol. 17, no. 12, pp. 1997–2034, 1996.
- [66] G. Jiang, W. Wong, E. Raskovich, W. Clark, W. Hines, and J. Sanny, "Open-ended coaxial-line technique for the measurement of the microwave dielectric constant for low-loss solids and liquids," *Review of scientific Instruments*, vol. 64, no. 6, pp. 1614–1621, 1993.
- [67] W. Hu, L. Li, W. Tong, and G. Li, "Supersaturated spontaneous nucleation to TiO<sub>2</sub> microspheres: synthesis and giant dielectric performance," *Chemical Communications*, vol. 46, no. 18, pp. 3113–3115, 2010.
- [68] A. A. Gafoor, M. Musthafa, and P. Pradyumnan, "AC conductivity and diffuse reflectance studies of Ag-TiO<sub>2</sub> nanoparticles," *Journal of electronic materials*, vol. 41, no. 9, pp. 2387–2392, 2012.

- [69] J. Hwang, K. Lee, Y. Jeong, Y. U. Lee, C. Pearson, M. C. Petty, and H. Kim, "UV-assisted low temperature oxide dielectric films for tft applications," *Advanced Materials Interfaces*, vol. 1, no. 8, 2014.
- [70] L. A. Rosocha and R. A. Korzekwa, "First report on non-thermal plasma reactor scaling criteria and optimization models," tech. rep., LAWRENCE LIVERMORE NATIONAL LAB CA, 1998.
- [71] C. R. McLarnon and B. M. Penetrante, "Effect of reactor design on the plasma treatment of NO<sub>x</sub>," tech. rep., SAE INTERNATIONAL WARRENDALE PA, 1998.
- [72] K. Takaki, M. Shimizu, S. Mukaigawa, and T. Fujiwara, "Effect of electrode shape in dielectric barrier discharge plasma reactor for NO<sub>x</sub> removal," *IEEE Transactions on Plasma Science*, vol. 32, no. 1, pp. 32–38, 2004.
- [73] T. Huiskamp, W. Hoeben, F. Beckers, E. van Heesch, and A. Pemen, "(sub) nanosecond transient plasma for atmospheric plasma processing experiments: application to ozone generation and NO removal," *Journal of Physics D: Applied Physics*, vol. 50, no. 40, p. 405201, 2017.
- [74] A. C. Gentile and M. J. Kushner, "Reaction chemistry and optimization of plasma remediation of N<sub>x</sub>O<sub>y</sub> from gas streams," *Journal of applied physics*, vol. 78, no. 3, pp. 2074–2085, 1995.
- [75] S. G. Jeon, K.-H. Kim, D. H. Shin, N.-S. Nho, and K.-H. Lee, "Effective combination of non-thermal plasma and catalyst for removal of volatile organic compounds and NO<sub>x</sub>," *Korean Journal of Chemical Engineering*, vol. 24, no. 3, pp. 522–526, 2007.
- [76] B. Adelman, G.-D. Lei, and W. Sachtler, "Co-adsorption of nitrogen monoxide and nitrogen dioxide in zeolitic de-NO<sub>x</sub> catalysts," *Catalysis letters*, vol. 28, no. 2, pp. 119–130, 1994.
- [77] W. Addison and R. Barrer, "Sorption and reactivity of nitrous oxide and nitric oxide in crystalline and amorphous siliceous sorbents," *Journal of the Chemical Society (Resumed)*, pp. 757–769, 1955.
- [78] S. Masuda and H. Nakao, "Control of NO<sub>x</sub> by positive and negative pulsed corona discharges," *IEEE Transactions on Industry Applications*, vol. 26, no. 2, pp. 374–383, 1990.
- [79] M. A. Jani, K. Takaki, and T. Fujiwara, "Streamer polarity dependence of NO<sub>x</sub> removal by dielectric barrier discharge with a multipoint-to-plane geometry," *Journal of Physics D: Applied Physics*, vol. 32, no. 19, p. 2560, 1999.
- [80] T. Huiskamp, W. Sengers, F. Beckers, S. Nijdam, U. Ebert, E. Van Heesch, and A. Pemen, "Spatiotemporally resolved imaging of streamer discharges in air generated in a wire-cylinder reactor with (sub) nanosecond voltage pulses," *Plasma Sources Science and Technology*, vol. 26, no. 7, p. 075009, 2017.

- [81] R. Hackam and H. Aklyama, "Air pollution control by electrical discharges," *IEEE Transactions on Dielectrics and Electrical Insulation*, vol. 7, no. 5, pp. 654–683, 2000.
- [82] P. Vitello, B. Penetrante, and J. Bardsley, "Simulation of negative-streamer dynamics in nitrogen," *Physical Review E*, vol. 49, no. 6, p. 5574, 1994.
- [83] C. Subrahmanyam, "Catalytic non-thermal plasma reactor for total oxidation of volatile organic compounds," *Indian Journal of Chemistry*, vol. 48, no. August, pp. 1062–1068, 2009.
- [84] N. Blin-Simiand, P. Tardiveau, A. Risacher, F. Jorand, and S. Pasquiers, "Removal of 2-heptanone by dielectric barrier discharges - The effect of a catalyst support," *Plasma Processes and Polymers*, vol. 2, no. 3, pp. 256–262, 2005.
- [85] T. Namihira, S. Tsukamoto, D. Wang, S. Katsuki, R. Hackam, H. Akiyama, Y. Uchida, and M. Koike, "Improvement of NO<sub>x</sub> removal efficiency using short-width pulsed power," *IEEE Transactions on Plasma Science*, vol. 28, no. 2, pp. 434–442, 2000.
- [86] Y. S. Mok, M. Dors, and J. Mizeraczyk, "Effect of reaction temperature on NO<sub>x</sub> removal and formation of ammonium nitrate in nonthermal plasma process combined with selective catalytic reduction," *IEEE transactions on plasma science*, vol. 32, no. 2, pp. 799–807, 2004.
- [87] A. Khacef and J. M. Cormier, "Pulsed sub-microsecond dielectric barrier discharge treatment of simulated glass manufacturing industry flue gas: removal of SO<sub>2</sub> and NO<sub>x</sub>," *Journal of Physics D: Applied Physics*, vol. 39, no. 6, p. 1078, 2006.
- [88] H. Kim, K. Takashima, S. Katsura, and A. Mizuno, "Low-temperature NO<sub>x</sub> reduction processes using combined systems of pulsed corona discharge and catalysts," *Journal of Physics D: Applied Physics*, vol. 34, no. 4, p. 604, 2001.
- [89] H. H. Kim, G. Prieto, K. Takashima, S. Katsura, and A. Mizuno, "Performance evaluation of discharge plasma process for gaseous pollutant removal," *Journal of electrostatics*, vol. 55, no. 1, pp. 25–41, 2002.
- [90] K. Takaki, T. Sato, S. Mukaigawa, and T. Fujiwara, "Influence of NO initial concentration on removal efficiency in dielectric barrier discharge reactor," in *Pulsed Power Conference, 2007 16th IEEE International*, vol. 1, pp. 399–402, IEEE, 2007.
- [91] B. Penetrante, M. Hsiao, J. Bardsley, B. Merritt, G. Vogtlin, A. Kuthi, C. Burkhart, and J. Bayless, "Identification of mechanisms for decomposition of air pollutants by non-thermal plasma processing," *Plasma sources science and technology*, vol. 6, no. 3, p. 251, 1997.

- [92] H.-H. Kim, "Nonthermal plasma processing for air-pollution control: a historical review, current issues, and future prospects," *Plasma Processes and Polymers*, vol. 1, no. 2, pp. 91–110, 2004.
- [93] X. Zhu, X. Gao, X. Yu, C. Zheng, and X. Tu, "Catalyst screening for acetone removal in a single-stage plasma-catalysis system," *Catalysis Today*, vol. 256, pp. 108–114, 2015.
- [94] S. Delagrangé, L. Pinard, and J.-M. Tatibouët, "Combination of a non-thermal plasma and a catalyst for toluene removal from air: Manganese based oxide catalysts," *Applied Catalysis B: Environmental*, vol. 68, no. 3, pp. 92–98, 2006.
- [95] H.-H. Kim, S.-M. Oh, A. Ogata, and S. Futamura, "Decomposition of gas-phase benzene using plasma-driven catalyst (PDC) reactor packed with Ag/TiO<sub>2</sub> catalyst," *Applied Catalysis B: Environmental*, vol. 56, no. 3, pp. 213–220, 2005.
- [96] T. Namihira, S. Tsukamoto, D. Wang, H. Hori, S. Katsuki, R. Hackam, H. Akiyama, M. Shimizu, and K. Yokoyama, "Influence of gas flow rate and reactor length on NO removal using pulsed power," *IEEE Transactions on Plasma Science*, vol. 29, no. 4, pp. 592–598, 2001.
- [97] T. Hammer, T. Kishimoto, H. Miessner, and R. Rudolph, "Plasma enhanced selective catalytic reduction: kinetics of NO<sub>x</sub>-removal and byproduct formation," tech. rep., SAE Technical Paper, 1999.
- [98] T. Yamamoto, M. Okubo, K. Hayakawa, and K. Kitaura, "Towards ideal NO<sub>x</sub> control technology using a plasma-chemical hybrid process," *Industry Applications, IEEE Transactions on*, vol. 37, no. 5, pp. 1492–1498, 2001.
- [99] A. Ogata, K. Saito, H.-H. Kim, M. Sugasawa, H. Aritani, and H. Einaga, "Performance of an ozone decomposition catalyst in hybrid plasma reactors for volatile organic compound removal," *Plasma Chemistry and Plasma Processing*, vol. 30, no. 1, pp. 33–42, 2010.
- [100] S. Futamura, A. Zhang, H. Einaga, and H. Kabashima, "Involvement of catalyst materials in nonthermal plasma chemical processing of hazardous air pollutants," *Catalysis Today*, vol. 72, no. 3, pp. 259–265, 2002.
- [101] N. Blin-Simiand, F. Jorand, Z. Belhadj-Miled, S. Pasquiers, and C. Postel, "Influence of temperature on the removal of toluene by dielectric barrier discharge," *International Journal of Plasma, Environmental Science and Technology*, vol. 1, no. 1, 2007.
- [102] A. M. Harling, H.-H. Kim, S. Futamura, and J. C. Whitehead, "Temperature dependence of plasma-catalysis using a nonthermal, atmospheric pressure packed bed; the destruction of benzene and toluene," *The Journal of Physical Chemistry C*, vol. 111, no. 13, pp. 5090–5095, 2007.

- [103] V. Ravi, Y. S. Mok, B. Rajanikanth, and H.-C. Kang, "Temperature effect on hydrocarbon-enhanced nitric oxide conversion using a dielectric barrier discharge reactor," *Fuel Processing Technology*, vol. 81, no. 3, pp. 187–199, 2003.
- [104] T. Wang, H. Liu, X. Zhang, H. Xiao, and B. Sun, "NO and SO<sub>2</sub> removal using dielectric barrier discharge plasma at different temperatures," *Journal of Chemical Engineering of Japan*, vol. 50, no. 9, pp. 702–709, 2017.
- [105] Y. Takahara, A. Ikeda, M. Nagata, and Y. Sekine, "Low-temperature NO decomposition in humidified condition using plasma–catalyst system," *Catalysis today*, vol. 211, pp. 44–52, 2013.
- [106] A. G. Panov, R. G. Tonkyn, M. L. Balmer, C. H. Peden, A. Malkin, and J. Hoard, "Selective reduction of NO<sub>x</sub> in oxygen rich environments with plasma-assisted catalysis: the role of plasma and reactive intermediates," tech. rep., SAE Technical Paper, 2001.
- [107] E. Filimonova, Y. ho Kim, S. H. Hong, and Y.-H. Song, "Multiparametric investigation on NO<sub>x</sub> removal from simulated diesel exhaust with hydrocarbons by pulsed corona discharge," *Journal of Physics D: Applied Physics*, vol. 35, no. 21, p. 2795, 2002.
- [108] B. Rajanikanth, A. Srinivasan, and V. Ravi, "Discharge plasma treatment for NO<sub>x</sub> reduction from diesel engine exhaust: a laboratory investigation," *IEEE Transactions on Dielectrics and Electrical Insulation*, vol. 12, no. 1, pp. 72–80, 2005.
- [109] G. B. Fisher, C. L. DiMaggio, and J. W. Sommers, "NO<sub>x</sub> reactivity studies of prototype catalysts for a plasma–catalyst aftertreatment system," tech. rep., SAE Technical Paper, 1999.
- [110] J. C. Whitehead, "Plasma–catalysis: the known knowns, the known unknowns and the unknown unknowns," *Journal of Physics D: Applied Physics*, vol. 49, no. 24, p. 243001, 2016.
- [111] H. Miessner, K.-P. Francke, R. Rudolph, and T. Hammer, "NO<sub>x</sub> removal in excess oxygen by plasma-enhanced selective catalytic reduction," *Catalysis today*, vol. 75, no. 1, pp. 325–330, 2002.
- [112] R. Atkinson, D. Baulch, R. Cox, R. Hampson, J. Kerr, and J. Troe, "Evaluated kinetic and photochemical data for atmospheric chemistry: Supplement III," *International journal of chemical kinetics*, vol. 21, no. 2, pp. 115–150, 1989.
- [113] J. Brian and A. Mitchell, "The dissociative recombination of molecular ions," *Physics reports*, vol. 186, no. 5, pp. 215–248, 1990.
- [114] Y. Itikawa, "Cross sections for electron collisions with nitrogen molecules," *Journal of physical and chemical reference data*, vol. 35, no. 1, pp. 31–53, 2006.

- [115] R. Dorai and M. J. Kushner, "Effect of multiple pulses on the plasma chemistry during the remediation of NO<sub>x</sub> using dielectric barrier discharges," *Journal of Physics D: Applied Physics*, vol. 34, no. 4, p. 574, 2001.
- [116] M. Nahavandi, "Selective catalytic reduction (SCR) of no by ammonia over V<sub>2</sub>O<sub>5</sub>/TiO<sub>2</sub> catalyst in a catalytic filter medium and honeycomb reactor: A kinetic modeling study," *Brazilian Journal of Chemical Engineering*, vol. 32, no. 4, pp. 875–893, 2015.
- [117] R. Q. Long, R. T. Yang, and R. Chang, "Low temperature selective catalytic reduction (scr) of NO with NH<sub>3</sub> over Fe–Mn based catalysts," *Chemical Communications*, no. 5, pp. 452–453, 2002.
- [118] G. Qi and R. T. Yang, "Low-temperature selective catalytic reduction of NO with NH<sub>3</sub> over iron and manganese oxides supported on titania," *Applied Catalysis B: Environmental*, vol. 44, no. 3, pp. 217–225, 2003.
- [119] D. A. Peña, B. S. Uphade, and P. G. Smirniotis, "TiO<sub>2</sub>-supported metal oxide catalysts for low-temperature selective catalytic reduction of NO with NH<sub>3</sub>: I. evaluation and characterization of first row transition metals," *Journal of catalysis*, vol. 221, no. 2, pp. 421–431, 2004.
- [120] V. Demidyuk and J. C. Whitehead, "Influence of temperature on gas-phase toluene decomposition in plasma-catalytic system," *Plasma chemistry and plasma processing*, vol. 27, no. 1, pp. 85–94, 2007.
- [121] M. Wojciechowska and S. Lomnicki, "Nitrogen oxides removal by catalytic methods," *Clean Technologies and Environmental Policy*, vol. 1, no. 4, pp. 237–247, 1999.
- [122] T. Batakliiev, V. Georgiev, M. Anachkov, and S. Rakovsky, "Ozone decomposition," *Interdisciplinary toxicology*, vol. 7, no. 2, pp. 47–59, 2014.
- [123] S. Walia, S. Balendhran, H. Nili, S. Zhuiykov, G. Rosengarten, Q. H. Wang, M. Bhaskaran, S. Sriram, M. S. Strano, and K. Kalantar-zadeh, "Transition metal oxides—thermoelectric properties," *Progress in Materials Science*, vol. 58, no. 8, pp. 1443–1489, 2013.
- [124] A. Clark, "Oxides of the transition metals as catalysts," *Industrial & Engineering Chemistry*, vol. 45, no. 7, pp. 1476–1480, 1953.
- [125] H. H. Kung, *Transition metal oxides: surface chemistry and catalysis*, vol. 45. Elsevier, 1989.
- [126] W. Oelerich, T. Klassen, and R. Bormann, "Metal oxides as catalysts for improved hydrogen sorption in nanocrystalline Mg-based materials," *Journal of Alloys and Compounds*, vol. 315, no. 1, pp. 237–242, 2001.

- [127] K.-P. Francke, H. Miessner, and R. Rudolph, "Plasmacatalytic processes for environmental problems," *Catalysis Today*, vol. 59, no. 3, pp. 411–416, 2000.
- [128] M. Magureanu, N. Mandache, E. Gaigneaux, C. Paun, and V. Parvulescu, "Toluene oxidation in a plasma-catalytic system," *Journal of applied physics*, vol. 99, no. 12, p. 123301, 2006.
- [129] S. Futamura, H. Einaga, H. Kabashima, and L. Y. Hwan, "Synergistic effect of silent discharge plasma and catalysts on benzene decomposition," *Catalysis Today*, vol. 89, no. 1, pp. 89–95, 2004.
- [130] S. Bröer and T. Hammer, "Selective catalytic reduction of nitrogen oxides by combining a non-thermal plasma and a  $V_2O_5$ - $WO_3$ / $TiO_2$  catalyst," *Applied Catalysis B: Environmental*, vol. 28, no. 2, pp. 101–111, 2000.
- [131] J. Wu, Y. Huang, Q. Xia, and Z. Li, "Decomposition of toluene in a plasma catalysis system with NiO,  $MnO_2$ ,  $CeO_2$ ,  $Fe_2O_3$ , and CuO catalysts," *Plasma Chemistry and Plasma Processing*, vol. 33, no. 6, pp. 1073–1082, 2013.
- [132] X. Fan, T. Zhu, Y. Sun, and X. Yan, "The roles of various plasma species in the plasma and plasma-catalytic removal of low-concentration formaldehyde in air," *Journal of hazardous materials*, vol. 196, pp. 380–385, 2011.
- [133] S. Yamamoto, S. Yao, S. Kodama, C. Mine, and Y. Fujioka, "Investigation of transition metal oxide catalysts for diesel PM removal under plasma discharge conditions," *Open Catal. J.*, vol. 1, pp. 11–16, 2008.
- [134] B. Halpern and J. Germain, "Thermodesorption of oxygen from powdered transition metal oxide catalysts," *Journal of Catalysis*, vol. 37, no. 1, pp. 44–56, 1975.
- [135] T. Butterworth and R. Allen, "Plasma-catalyst interaction studied in a single pellet DBD reactor: dielectric constant effect on plasma dynamics," *Plasma Sources Science and Technology*, vol. 26, no. 6, p. 065008, 2017.
- [136] D. Mei, X. Zhu, Y.-L. He, J. D. Yan, and X. Tu, "Plasma-assisted conversion of  $CO_2$  in a dielectric barrier discharge reactor: understanding the effect of packing materials," *Plasma Sources Science and Technology*, vol. 24, no. 1, p. 015011, 2014.
- [137] H.-H. Kim and A. Ogata, "Nonthermal plasma activates catalyst: from current understanding and future prospects," *The European Physical Journal Applied Physics*, vol. 55, no. 1, p. 13806, 2011.
- [138] H. Huang, D. Ye, and X. Guan, "The simultaneous catalytic removal of VOCs and  $O_3$  in a post-plasma," *Catalysis Today*, vol. 139, no. 1, pp. 43–48, 2008.
- [139] F. Beckers, "Pulsed operation of a SDBD plasma reactor," Master Thesis, Eindhoven University of Technology, 2008.

- [140] S. Pekárek, "Experimental study of surface dielectric barrier discharge in air and its ozone production," *Journal of Physics D: Applied Physics*, vol. 45, no. 7, p. 075201, 2012.
- [141] N. Mastanaiah, P. Banerjee, J. A. Johnson, and S. Roy, "Examining the role of ozone in surface plasma sterilization using dielectric barrier discharge (DBD) plasma," *Plasma Processes and Polymers*, vol. 10, no. 12, pp. 1120–1133, 2013.
- [142] K. Nassour, M. Brahami, S. Nemnich, N. Hammadi, N. Zouzou, and A. Tilmatine, "New hybrid surface–volume dielectric barrier discharge reactor for ozone generation," *IEEE Transactions on Industry Applications*, vol. 53, no. 3, pp. 2477–2484, 2017.
- [143] M. A. Malik, K. H. Schoenbach, and R. Heller, "Coupled surface dielectric barrier discharge reactor-ozone synthesis and nitric oxide conversion from air," *Chemical Engineering Journal*, vol. 256, pp. 222–229, 2014.
- [144] S. Portugal, S. Roy, and J. Lin, "Functional relationship between material property, applied frequency and ozone generation for surface dielectric barrier discharges in atmospheric air," *Scientific reports*, vol. 7, no. 1, p. 6388, 2017.
- [145] T. Huiskamp, W. Brok, A. Stevens, E. van Heesch, and A. Pemen, "Maskless patterning by pulsed-power plasma printing," *IEEE Transactions on Plasma Science*, vol. 40, no. 7, pp. 1913–1925, 2012.
- [146] S. Voeten, F. Beckers, E. Van Heesch, and A. Pemen, "Optical characterization of surface dielectric barrier discharges," *IEEE Transactions on Plasma Science*, vol. 39, no. 11, pp. 2142–2143, 2011.
- [147] A. Balamurugan, S. Kannan, and S. Rajeswari, "Evaluation of TiO<sub>2</sub> coatings obtained using the sol–gel technique on surgical grade type 316l stainless steel in simulated body fluid," *Materials Letters*, vol. 59, no. 24, pp. 3138–3143, 2005.
- [148] A. Pemen, E. van Heesch, and F. Beckers, "Quasi resonant pulse modulator for surface-dielectric-barrier discharge generation," Proceedings of the 4<sup>th</sup> Euro-Asian Pulsed Power Conference (EAPPC-2012), 30 September - 4 October, pp. 1-4, 2012.
- [149] J. Jolibois, K. Takashima, and A. Mizuno, "NO<sub>x</sub> removal using a wet type plasma reactor based on a three-electrode device," in *Journal of Physics: Conference Series*, vol. 301, p. 012011, IOP Publishing, 2011.
- [150] H. Zhang, K. Li, C. Shu, Z. Lou, T. Sun, and J. Jia, "Enhancement of styrene removal using a novel double-tube dielectric barrier discharge (DDBD) reactor," *Chemical Engineering Journal*, vol. 256, pp. 107–118, 2014.



- [151] T. Oda, R. Yamashita, I. Haga, T. Takahashi, and S. Masuda, "Decomposition of gaseous organic contaminants by surface discharge induced plasma chemical processing-spcp," *IEEE Transactions on Industry Applications*, vol. 32, no. 1, pp. 118–124, 1996.
- [152] S. Chavadej, K. Saktrakool, P. Rangsunvigit, L. L. Lobban, and T. Sreethawong, "Oxidation of ethylene by a multistage corona discharge system in the absence and presence of Pt/TiO<sub>2</sub>," *Chemical engineering journal*, vol. 132, no. 1, pp. 345–353, 2007.
- [153] R. Aerts, X. Tu, W. Van Gaens, J. Whitehead, and A. Bogaerts, "Gas purification by nonthermal plasma: a case study of ethylene," *Environmental science & technology*, vol. 47, no. 12, pp. 6478–6485, 2013.
- [154] A. M. Harling, D. J. Glover, J. C. Whitehead, and K. Zhang, "Novel method for enhancing the destruction of environmental pollutants by the combination of multiple plasma discharges," *Environmental science & technology*, vol. 42, no. 12, pp. 4546–4550, 2008.
- [155] K. Hensel, V. Martišovitš, Z. Machala, M. Janda, M. Leštinský, P. Tardiveau, and A. Mizuno, "Electrical and optical properties of AC microdischarges in porous ceramics," *Plasma Processes and Polymers*, vol. 4, no. 7-8, pp. 682–693, 2007.
- [156] H.-H. Kim, J.-H. Kim, and A. Ogata, "Microscopic observation of discharge plasma on the surface of zeolites supported metal nanoparticles," *Journal of Physics D: Applied Physics*, vol. 42, no. 13, p. 135210, 2009.
- [157] H.-H. Kim, Y. Teramoto, and A. Ogata, "Time-resolved imaging of positive pulsed corona-induced surface streamers on TiO<sub>2</sub> and  $\gamma$ -Al<sub>2</sub>O<sub>3</sub>-supported Ag catalysts," *Journal of Physics D: Applied Physics*, vol. 49, no. 41, p. 415204, 2016.
- [158] H.-H. Kim, N. Hwang, A. Ogata, and Y.-H. Song, "Propagation of surface streamers on the surface of HSY zeolites-supported silver nanoparticles," *IEEE Transactions on Plasma Science*, vol. 39, no. 11, pp. 2220–2221, 2011.
- [159] "4Picos ICCD camera," accessed January 2, 2018. <http://stanfordcomputeroptics.com/products/picosecond-iccd.html>.
- [160] U. Kogelschatz, "Filamentary, patterned, and diffuse barrier discharges," *IEEE Transactions on plasma science*, vol. 30, no. 4, pp. 1400–1408, 2002.
- [161] M.-G. Chen, A. Mihalcioiu, K. Takashima, and A. Mizuno, "Catalyst size impact on non-thermal plasma catalyst assisted deNO<sub>x</sub> reactors," in *Electrostatic Precipitation*, pp. 681–684, Springer, 2009.

- 
- [162] H. L. Chen, H. M. Lee, S. H. Chen, and M. B. Chang, "Review of packed-bed plasma reactor for ozone generation and air pollution control," *Industrial & Engineering Chemistry Research*, vol. 47, no. 7, pp. 2122–2130, 2008.



---

---

## LIST OF PUBLICATIONS

---

### Journal Publications

- V.R. Chirumamilla, W.F.L.M. Hoeben, F.J.C.M. Beckers, T. Huiskamp, E.J.M. van Heesch, A.J.M. Pemen, “Experimental investigation on the effect of a microsecond pulse and a nanosecond pulse on NO removal using a pulsed DBD with catalytic materials,” *Plasma Chem. Plasma Proc.*, vol.36, pp.487–510, 2016.
- A.J.M. Pemen, V.R. Chirumamilla, F.J.C.M. Beckers, W.F.L.M. Hoeben, T. Huiskamp, “An SDBD plasma catalytic system for on-demand air purification ,” *IEEE T. Plasma Sci.*, 2018, submitted
- V.R. Chirumamilla, A.J.M. Pemen, “Effect of applied peak-voltage and polarity on NO<sub>x</sub> removal in plasma-catalytic pulsed-DBD reactor- an experimental study,” *Plasma Chem. Plasma Proc.*, 2018, to be submitted
- V.R. Chirumamilla, A.J.M. Pemen, “Effect of operational parameters on NO<sub>x</sub> removal in plasma-catalytic pulsed-DBD reactor- an experimental study,” *Plasma Chem. Plasma Proc.*, 2018, to be submitted
- V.R. Chirumamilla, A. Parastaev, E. Hensen, A.J.M. Pemen, “Screening of catalytic materials for NO<sub>x</sub> removal by combining a pulsed-DBD reactor with catalytic materials,” *Plasma Chem. Plasma Proc.*, 2018, to be submitted

### Conference contributions

- V.R. Chirumamilla, W.F.L.M. Hoeben, F.J.C.M. Beckers, E.J.M. van Heesch and A.J.M. Pemen, “Indoor air cleaning by plasma-assisted catalysis,” *26<sup>th</sup> symposium on Plasma Physics and Radiation Technology (26 NNV)*, 11-12 March 2014, Lunteren, The Netherlands.

- V.R. Chirumamilla, W.F.L.M. Hoeben, F.J.C.M. Beckers, E.J.M. van Heesch and A.J.M. Pemen, "Removing NO<sub>x</sub> in indoor air by combining pulsed dielectric barrier discharges with CuO-MnO<sub>2</sub>/TiO<sub>2</sub> catalyst," *14<sup>th</sup> International Symposium on High Pressure Low Temperature Plasma Chemistry (HAKONE XIV)*, 21-26 September 2014, Zinnowitz, Germany.
- V.R. Chirumamilla, W.F.L.M. Hoeben, F.J.C.M. Beckers, T. Huiskamp and A.J.M. Pemen, "Experimental investigation on NO<sub>x</sub> removal with pulsed DBD in combination with catalysts," *Proceedings of the 22<sup>nd</sup> International Symposium on Plasma Chemistry (ISPC 22)*, July 5-10, 2015, Antwerp, Belgium.
- V.R. Chirumamilla, W.F.L.M. Hoeben, F.J.C.M. Beckers, E.J.M. van Heesch and A.J.M. Pemen, "Effect of pulse rise-time on NO<sub>x</sub> removal in a hybrid plasma-catalytic system", *6<sup>th</sup> Central European Symposium on Plasma Chemistry (CESPC-6)*, September 6-10, 2015, Bressanone, Italy (awarded with a best poster award).
- V.R. Chirumamilla, W.F.L.M. Hoeben, F.J.C.M. Beckers and A.J.M. Pemen, "Effect of initial concentration on NO<sub>x</sub> removal using pulsed dielectric barrier discharges", *International Workshop on Plasmas for Energy and Environmental Applications (IWPEEA-2016)*, 21- 24 August 2016, Liverpool, United Kingdom.
- V. R. Chirumamilla and A.J.M. Pemen, "Kinetics studies on NO<sub>x</sub> removal in a pulsed DBD catalytic reactor", *29<sup>th</sup> symposium on Plasma Physics and Radiation Technology (29 NNV)*, 7-8 March 2017, Lunteren, the Netherlands.

---

---

## ACKNOWLEDGEMENTS

---

After a slightly longer amazing journey of four and half years, today is the day, It is done! It has been a very challenging period for me not only in the scientific area but also on personal front. Scripting this dissertation has had a big influence on myself. I would take this opportunity to reflect on everyone: my colleagues, friends and family who have supported and helped me throughout this journey.

Firstly, I would like to express my sincere gratitude to my promotor and supervisor, prof. Guus Pemen for the continuous support during my Ph.D study. Thank you Guus for believing in me and giving me this opportunity. It was your invaluable support which has motivated me to complete this thesis.

I would like to convey my thanks to dr. Tom Huiskamp who kindly accepted to be my supervisor at the very last minute. Thank you very much for your critical reviews on my thesis. I have learnt a lot from you both professionally and personally. You gave me a lot of positive energy especially when I was emotionally down.

I would like to thank the rest of my thesis committee : prof.dr. J.C. Whitehead (The University of Manchester), prof.dr. C. Paradisi (University of Padova), prof.dr. V. Hessel, dr.ir. W.F.L.M. Hoeben, and dr. R.A.H. Engeln, not only for their insightful comments and encouragement, but also for the hard questions which incited me to widen my research content. A very special thanks to all the sponsors of the Eniac JU project who extended their financial support and sponsored this research.

I should definitely convey my gratitude to dr. Frank Beckers. Frank, I should accept that I could not have finished my thesis without your contribution. It is amazing that you have a solution for every problem and fix anything in the lab. Although you wanted to follow your three commandments : “I don’t know; I don’t care ; It’s your project”, you always come to help me in the lab after seeing my pathetic face.

My sincere appreciation goes to dr. Wilfred Hoeben for introducing me to all our colleagues and giving me a short lab trip on my first day at TU/e. Your help to build my first small set-up in the corona lab and your coordination of new experimental infrastructure in

the HV lab in Flux building steered me in the direction I am in today.

Alexander Parastaev, I always admire your passion for research and keen eye for detail. Without your contribution, chapter 5 would not have existed. I very much enjoyed our short discussions related to both Ph.D and other interesting issues. I wish you all the very best with your thesis completion.

I would like to thank Jovita Morales, Frans Kuijpers, Paul Bijer, Paul Anderoemer, Harry te laat, Ruud de Regt from EPC for their willingness to help me in building my setup or to fix the things that I used to break.

Thank you Herman for your patience in dealing with my gas bottle ordering and most of the time bringing and fitting the gas cylinders for my lab work. I would like to thank dr. Jan Bernards and Jan van Lierop from Thin Films and Functional Materials laboratory at Fontys, Eindhoven for giving me an opportunity to try the sputtering technique at Fontys.

I am privileged to meet few wonderful people during the course of my PhD who became good friends. Lei and Jin: I cannot thank you enough for all the help and support you have offered me. Jin, you gave me tons and tons of motivation throughout the thesis period. I am truly blessed to have a friend like you. Sharmistha and Raja: You are such an inspirational couple. Thank you for being there when I needed the most.

Ananthi and Praveena: how can I say just thank you to both of you? You guys are truly amazing. Both of you were there with me during my ups and downs. In the past few years, there isn't anything that happened in my life without you two. But all of it would not have been possible if Ashok and Sundar were not supportive and caring as they are.

I would like to thank Alexander, Merce, Armand, Siddharth, Hasan, Bart, Pavlo, Anna, Rene, Marcel, Hennie, Annemie, Annemarie, Mansoor, Samina, Elena, Babar, Gu, Ballard and many other colleagues from EES-group for creating a pleasant work environment and continuous support. Annemarie, you were always there for me when I need some help both at TU/e and outside TU/e.

I would also like to thank Gertjan and Yvonne, Martin kok, Reju and Bindu, Dewi and Inge for making our stay pleasant at our new place. I would also like to thank my friends Nagarjuna, Arun and Anita, Bhaskar Patil, Shariar, Samaneh for their friendly talks, lunches and dinners.

This thesis would not have been possible without the love and support from my parents. I am indebted to them for their belief and allowing me to do what I wish in my life. I am indebted to my mother-in-law and father-in-law for their understanding and for standing besides me during every aspect of my life. Your prayer for me was what sustained me this far. The greatest strength comes from my sister, Vijji and my brother, Amar. Though, we miss the regular conversations, I always cherish those moments that we have spent together. It will be incomplete if I miss to thank my aunts and uncles, sister-in-laws and brother-in-laws, cousins, nieces and nephews; thank you family.

Finally, I would like to acknowledge the most important persons in my life: My husband Srini and my daughter Akshaya. Thank you Srini for your unconditional love, infinite patience, unimaginable support and ofcourse for wonderful morning coffees!. You and our cute little angel Akshaya have been by my side in all happy and sad moments of this expedition. Your love and trust in me made it possible for me to finish what I started.

---

---

## CURRICULUM VITAE

---

Vindhya Rani Chirumamilla was born on August 10, 1983 in Guntur, Andhra Pradesh, India. She obtained her bachelor of technology in chemical engineering from Jawaharlal Nehru Technology University, India in 2004. She received her master of technology in mineral process engineering from Andhra University in 2006. While pursuing her masters she also worked as an engineer at Indian Ordnance factory services, Itarsi, India. She also received joint M.Sc. degree in Management and Engineering of Environment and Energy (ME3) from Ecole des Mines de Nantes, France and Universidad Politecnica de Madrid in 2009. Later on she worked as a researcher at Tata steel R&D, Jamshedpur, India. In 2013 she joined Electrical Energy Systems group at Eindhoven University of Technology, as a PhD candidate under the supervision of prof.dr.ing. A.J.M. Pemen which resulted in this thesis. During her PhD project she received a best poster award at 6<sup>th</sup> Central European Symposium on Plasma Chemistry, Bressanone (Italy), 2015.